High Pressure Studies of Iron-Based Superconductors

Zachary Zajicek

Somerville College
University of Oxford

A thesis submitted for the degree of Doctor of Philosophy

Trinity 2022

Abstract

Unconventional superconductors are promising systems that can be used in practical applications, due to their large critical temperature, critical current densities and upper critical fields. This thesis investigates the electronic and superconducting behaviour of a new family of unconventional iron-chalcogenide superconductors tuned by applied hydrostatic pressure. I will present transport measurements, at low temperatures and high magnetic fields of different single crystals of the FeSe family, to understand their complex electronic phase diagrams under pressure. The parent compound shows an unexpected fourfold increase in superconductivity under pressure, whereas as a monolayer on a substrate it displays superconductivity above the liquid nitrogen temperature. Furthermore, bulk FeSe has an unusual electronic nematic phase, but applied pressure stabilises an additional magnetic order which manifests as an upturn in resistivity.

Firstly, I report the effect of impurity scattering on the electronic behaviour induced by copper substitution in the conducting iron planes. This substitution is strongly disruptive to the nematic and superconducting phases which are quickly suppressed. The enhanced impurity scattering leads to a marked increase in resistivity and strongly reduced charge carrier mobilities, as determined from magnetotransport measurements. As the amount of impurities increases, both the suppression of critical temperatures and the temperature dependence of the upper critical field are consistent with a superconductor having a sign changing order parameter. In a subsequent study of $Fe_{1-x}Cu_xSe$ under pressure I find that, even in the presence of a small amount of Cu impurity, the high-T_c high pressure superconducting phase is robust. Surprisingly, no signatures of the pressure stabilised magnetic order are found in zero field, only in strong magnetic fields.

In the next chapters, I investigate the phase diagrams of systems with isoelectronic substitution of sulphur for selenium outside of the iron planes. The first system, $FeSe_{0.82}S_{0.18}$, explores the electronic structure in the absence of nematicity, which displays a threefold enhancement in the superconducting transition temperature in the high pressure phase. Quantum oscillations in high magnetic fields and simulations probe the expansion and topology of the large Fermi surface under pressure. Despite the enhanced critical temperature under pressure, the quasiparticle effective masses are almost pressure independent. Notably, the quantum oscillations of a different system, $FeSe_{0.96}Se_{0.04}$, only display small frequencies in the high pressure phase. I find its phase diagram shows no signature of magnetic order outside of the nematic phase in zero field, but upturns in resistivity are observed inside the nematic phase in zero field and at high pressures in strong magnetic fields. Overall, the high pressure phase of all systems investigated display an enhanced superconducting phase, and highlight the sensitivity of the magnetic phase to chemical substitution and magnetic fields.

High Pressure Studies of Iron-Based Superconductors

Zachary Zajicek

Somerville College

University of Oxford

A thesis submitted for the degree of

Doctor of Philosophy

Trinity 2022

Acknowledgements

Personal

The last four years have been *unprecedented* times, and I owe a lot to many for their help and support during this time, without which this thesis would not exist.

This is a firmly experimental thesis, and there are many contributors to thank for their practical and experimental support and help. The largest being all the staff at the Clarendon Laboratory, especially the workshop who are able to make or fix parts at a moments notice enabling experiments to continue. In particular, thank you to Kieran for the endless chats about sport and the advise to not drink coffee before preparing samples, I found the opposite stopped the jitters! Further afield, I was fortunate to work with Alix McCollam performing three experiments at the HFML in Nijmegen, I must thank her for her expertise and endless energy. Similarly, I am indebted to David Graf for measurements he performed on our behalf in Tallahassee when travel restrictions prevented in person attendance. Finally, without the high quality single crystals grown by Shiv Singh and Amir Haghighirad there would have been no results to present, thank you for these.

The Coldea group is small at the core, but the influx of MPhys and summer students each year has been an endless source of ideas and enthusiasm, thank you. Thank you to Pascal Reiss for his guidance, assistance and teaching of sample preparation. From being scared of the prospect of working on such small scales, to taking pride in my experimental ability. I have Pascal to thank, who showed me that with sample preparation, the next attempt will always be the one that works. Thank you also to Matthew Bristow for his guidance and help at the state of my DPhil. I hope I have managed to pay this forward to Archie Morfoot, who I'd also like thank for his support and an excellent trip to APS in Chicago. Most importantly, I cannot thank Amalia Coldea enough for her supervision and support. Your endless energy and boundless knowledge were of tremendous help.

I would like to thank both my parents and sister for their support and encouragement always. Finally, I thank Lara for her love, support and endless patience. This thesis would not be complete without her.

Abstract

Unconventional superconductors are promising systems that can be used in practical applications, due to their large critical temperature, critical current densities and upper critical fields. This thesis investigates the electronic and superconducting behaviour of a new family of unconventional iron-chalcogenide superconductors tuned by applied hydrostatic pressure. I will present transport measurements, at low temperatures and high magnetic fields of different single crystals of the FeSe family, to understand their complex electronic phase diagrams under pressure. The parent compound shows an unexpected fourfold increase in superconductivity under pressure, whereas as a monolayer on a substrate it displays superconductivity above the liquid nitrogen temperature. Furthermore, bulk FeSe has an unusual electronic nematic phase, but applied pressure stabilises an additional magnetic order which manifests as an upturn in resistivity.

Firstly, I report the effect of impurity scattering on the electronic behaviour induced by copper substitution in the conducting iron planes. This substitution is strongly disruptive to the nematic and superconducting phases which are quickly suppressed. The enhanced impurity scattering leads to a marked increase in resistivity and strongly reduced charge carrier mobilities, as determined from magnetotransport measurements. As the amount of impurities increases, both the suppression of critical temperatures and the temperature dependence of the upper critical field are consistent with a superconductor having a sign changing order parameter. In a subsequent study of $Fe_{1-x}Cu_xSe$ under pressure I find that, even in the presence of a small amount of Cu impurity, the high-T_c high pressure superconducting phase is robust. Surprisingly, no signatures of the pressure stabilised magnetic order are found in zero field, only in strong magnetic fields.

In the next chapters, I investigate the phase diagrams of systems with isoelectronic substitution of sulphur for selenium outside of the iron planes. The first system, $FeSe_{0.82}S_{0.18}$, explores the electronic structure in the absence of nematicity, which displays a threefold enhancement in the superconducting transition temperature in the high pressure phase. Quantum oscillations in high magnetic fields and simulations probe the expansion and topology of the large Fermi surface under pressure. Despite the enhanced critical temperature under pressure, the quasiparticle effective masses are almost pressure independent. Notably, the quantum oscillations

of a different system, $FeSe_{0.96}Se_{0.04}$, only display small frequencies in the high pressure phase. I find its phase diagram shows no signature of magnetic order outside of the nematic phase in zero field, but upturns in resistivity are observed inside the nematic phase in zero field and at high pressures in strong magnetic fields. Overall, the high pressure phase of all systems investigated display an enhanced superconducting phase, and highlight the sensitivity of the magnetic phase to chemical substitution and magnetic fields.

Contents

1 Superconductivity and Electronic Structure **1**

1.1 Introduction to superconductivity 1
1.2 Superconducting Properties 3
1.2.1 Abrikosov-Gor'kov Model 6
1.2.2 Upper Critical Field 7
1.3 Iron-Based Superconductors 10
1.3.1 Iron Chalcogenides: FeSe 14
1.3.2 Effect of Applied Pressure 16
1.3.3 Effect of Chemical Pressure 18
1.4 Transport Properties 18
1.4.1 Non-interacting Free Electron Models 19
1.4.2 Fermi Liquid Theory 22
1.4.3 Magnetotransport Properties 24
1.5 Quantum Oscillations 28
1.5.1 Lifshitz-Kosevich Formalism 31
1.5.2 Landau Fan Diagrams 33
1.5.3 Damping Terms 33

2 Experimental Methods and Techniques **38**

2.1 Transport Measurements 38
2.1.1 Sample Preparation 38
2.1.2 Magnetotransport measurements 43
2.1.3 Local resistivity exponent 44
2.2 Pressure Techniques 45
2.2.1 Piston Cylinder Cells 45
2.2.2 Anvil Cells 48
2.2.3 Pressure calibration 49
2.3 Low Temperature Techniques 52
2.3.1 Flow cryostat 52
2.3.2 Physical Properties Measurement System (PPMS) 53
2.3.3 High Magnetic Fields 53
2.3.4 Temperature Extrapolation in High Magnetic Fields 55

2.4 Other Techniques . . . 56
2.4.1 Tunnel Diode Oscillator (TDO) . . . 56
2.4.2 Energy Dispersive X-ray (EDX) . . . 57
2.4.3 X-ray Diffraction . . . 58

3 The effects of impurity scattering in $Fe_{1-x}Cu_xSe$ 60
3.1 Introduction . . . 61
3.2 Experimental details . . . 62
3.3 Transport properties of Cu-FeSe . . . 64
3.4 Magnetotransport behaviour . . . 67
3.5 Mobility analysis . . . 69
3.6 Normal electronic behaviour at low temperatures . . . 71
3.7 Upper critical fields . . . 75
3.8 Discussion . . . 79
3.9 Conclusions . . . 82
3.10 Additional Figures . . . 83

4 Pressure effects in $Fe_{1-x}Cu_xSe$ 85
4.1 Introduction . . . 86
4.2 Methods . . . 87
4.3 Transport studies under applied pressure . . . 88
4.4 The high-pressure electronic phase in high magnetic fields . . . 92
4.5 Magnetotransport behaviour . . . 92
4.6 Upper critical field . . . 98
4.7 The pressure-temperature p-T phase diagrams . . . 100
4.8 Discussion . . . 103
4.9 Conclusions and Outlook . . . 104
4.10 Additional Figures . . . 106

5 Signatures of the high-pressure phase of $FeSe_{1-x}S_x$ 109
5.1 Introduction . . . 110
5.2 Materials and Methods . . . 112
5.3 Temperature dependence of resistivity with applied pressure . . . 114
5.4 Magnetotransport . . . 117
5.5 The evolution of the Fermi surface with pressure. . . . 122
5.5.1 Quasiparticle masses . . . 127
5.5.2 Fermi surface simulations . . . 129
5.6 Discussion . . . 131
5.7 Conclusions . . . 136
5.8 Additional Figures and Tables . . . 137

6 Interplay between different phases in $FeSe_{0.96}S_{0.04}$ under pressure 143
6.1 Introduction . . . 144
6.2 Methods . . . 145
6.3 Transport behaviour . . . 148
6.4 Magnetotransport and the Magnetic Phase . . . 151
6.5 Charge Carrier Mobilities . . . 157
6.6 Upper Critical Field . . . 161
6.7 Quantum Oscillations in High Magnetic Fields . . . 165
6.8 Discussion . . . 173
6.9 Conclusions and Outlook . . . 177

7 Concluding Remarks 180

8 Publications 183

References 185

1 Superconductivity and Electronic Structure

In this first chapter I will introduce relevant theoretical aspects. Firstly, I discuss the basic properties of superconductors and the theoretical understanding of conventional superconductors in which the pairing of electrons in Cooper pairs is mediated by electron-phonon coupling. Secondly, I will introduce the generic phase diagrams of iron-based superconductors, and specifically the characteristics of the iron chalcogenide superconductors. Thirdly, I introduce the principle of the electronic transport and magnetotransport in multi-band systems, which enables the determination of the relevant charge carrier densities and mobilities. Lastly, quantum oscillations in high magnetic fields are introduced, and I describe how the information about Fermi surface orbits, quasiparticle effective masses, and scattering times is determined from analysis of these oscillations.

1.1 Introduction to superconductivity

Superconductivity was discovered over a century ago, and has progressed from an interesting effect only found at low temperatures, to a multitude of systems of superconducting families with higher and higher critical transition temperatures. The discovery that pure mercury has zero electrical resistance below 4.2 K by

Kammerlingh Onnes in 1911 began this long journey. Whilst this was not a particularly high temperature by recent standards, it opened the door for new possibilities. In the following decades, superconductivity was found in many metallic elemental and compound systems at low temperatures only. In 1957, the very successful Bardeen Cooper Schriffer theory (BCS) explained the mechanism behind the superconductivity for, what are now known as, conventional superconductors [1, 2]. At the time, this was believed to place a limit on the critical temperature that below which the system is a superconductor, T_c, around 30 K. The first high-temperature superconductor was discovered in 1986 with La-Ba-Cu-O (LBCO) by Georg Bednorz and Karl Alex Müller, a monumental discovery credited with a Nobel prize in physics the next year in 1987 [3]. This ignited the discovery of more cuprate superconductors, which eventually lead to a record T_c of 133 K (and 156 K under high pressure) in mercury barium calcium copper oxide [4, 5]. A different group of unconventional superconductors emerged with the heavy fermion superconductors, first with $CeCu_2Si_2$ [6]. This family of superconductors is characterised by very large effective masses, but superconductivity only exists at low temperatures [7].

There are many practical uses for these materials, particularly because they can superconduct at temperatures above the boiling point of liquid nitrogen (77 K), such as superconducting wires capable of carrying large amounts of current without dissipation. A notable use of such wires for measurements in this work, is being used to make coils and produce high magnetic fields, and thus use significantly less energy than a conventional resistive magnet. However, driven by the prospect of room temperature superconductivity thousands of research papers are published each year to extend this field of research. More recently, a class of unconventional superconductors was discovered that includes the materials presented in this thesis, that of the iron-based superconductors (FeSCs). This began with LaFePO in 2006 with $T_c \sim 4$ K [8], and subsequently as high-T_c superconductors when $LaFeAsO_{1-x}F_x$ was discovered with $T_c = 26$ K in 2008 [9]. The highest T_c in FeSCs is with monolayer FeSe epitaxially grown on $SrTiO_3$, found to be upwards of 65 K, and potentially reaching 100 K [10–12]. Most recently, the limit on T_c imposed by the BCS theory

has been overcome in certain conventional superconductors by using extremely high pressures on hydride systems to reach superconducting transition temperatures tantalisingly close to room temperature, with the caveat of several hundred giga Pascals of pressure [13–15]. However, it is not just conventional superconductors where pressure plays a prominent role in leading the drive towards enhanced superconductivity. In both the cuprates and iron-based superconductors some of the largest recorded T_c are found under hydrostatic pressure [5, 16, 17].

Motivation to investigate FeSCs includes the possibility to make practicable high-T_c superconducting wires, owing to the less brittle nature compared to the ceramic cuprate superconductors, as well as their ability to hold very large current densities [18]. From a physics perspective, the family of FeSCs opened up a new class of unconventional superconductors, in which the Cooper pairs have zero angular momentum (s-wave), compared to the traditional cuprates with a d-wave superconducting state.

1.2 Superconducting Properties

There are two key features to define the superconducting state in a system. First, the superconductor has zero resistance in the superconducting state. Second, the superconductor will expel all magnetic flux below T_c, known as the Meissner effect. This is different to a perfect conductor which would not necessarily expel all magnetic flux on cooling below T_c, instead it would allow preexisting flux to remain inside the conductor. The superconducting state is entered below the critical temperature, T_c. However, this term is often reported in zero magnetic field, and if for transport, a general applied current. The value of T_c is influenced by both the applied magnetic field and the current density. Hence, the superconductivity can be suppressed by increasing the temperature above the critical temperature $T_c(H, J)$, applying a magnetic field of sufficient strength, above the critical field $H_c(T, J)$, or by increasing the current density past the critical current density $J_c(T, H)$. For future applications, J_c and T_c are the key parameters in superconducting wires, but

increases in one of these critical values typically increases the others too. Type-I superconductors are perfect diamagnets below H_c, and the superconductivity is destroyed above this. Interestingly, some superconductors allow some flux to penetrate into the system at magnetic fields above where it is a perfect diamagnet, H_{c1}. This larger critical field is called the upper critical field, H_{c2}, and between these two critical fields the system is in the vortex phase (also called the mixed phase), and retains superconducting properties. Such systems are called type-II. Here, the flux penetrates the system through the core of vortices. A vortex is non-superconducting and a current circulates the core to screen the system from the magnetic flux. The core has a size given by the coherence length, ξ, whilst the current decays over a length scale of the penetration length, λ. A system is a type-II superconductor if $\lambda/\xi > 1/\sqrt{2}$. The systems investigated in this work are all type-II.

Superconductors can be classified as either conventional and unconventional superconductors. Conventional superconductors follow BCS theory (or extensions of this theory), where the superconductivity is mediated by phononic interactions. They are well understood, and display the isotope effect and exponential heat capacity at low temperature. Systems which do not follow this mechanism are labelled unconventional superconductors, and include the highest T_c superconductors for ambient pressures to date [4]. One of the first considerations for newly discovered superconductors is to assess results against BCS theory, to determine if the superconductivity is likely phonon mediated or not.

BCS Theory

BCS theory describes how a weak attractive potential between electrons can lead to the formation of Cooper pairs, which are composed of two electrons with equal and opposite momentum and spin. In this scenario, the fermionic particles pair up to form the Cooper pairs in the superconducting condensate, and these Cooper pairs are able to be in the same ground state, like Bosonic particles. The typical mechanism for conventional superconductors involves a coupling to the lattice, through electron-phonon interactions, and thereby being labelled phonon mediated.

An energy gap, 2Δ, resulting from the energy gain in forming a Cooper pair, arises at T_c, and grows as $T/T_c \to 0$. The energy gap can be considered as the energy required to break a Cooper pair. By minimising the energy from the BCS Hamiltonian, which can be explored in more detail in [19, 20], the excitation energy, $E_{\mathbf{k}}$, and the BCS gap equation at $T = 0$ are given by:

$$E_{\mathbf{k}} = \sqrt{(\epsilon_{\mathbf{k}} - \mu)^2 + |\Delta|^2} \tag{1.1}$$

$$\Delta = |g_{\text{eff}}|^2 \sum_k \frac{\Delta}{2E_{\mathbf{k}}} \tag{1.2}$$

where, for phonon mediation, the electron-phonon coupling parameter is $\lambda = |g_{\text{eff}}|^2 g(E_F)$ and $g(E_F)$ is the density of states at E_F. Hence, equations 1.1 and 1.2 can be combined, now integrating over possible energy states, to give:

$$\Delta = \lambda \int_0^{\hbar\omega_D} \frac{\Delta}{\sqrt{\Delta^2 + \epsilon^2}} d\epsilon = \lambda\Delta \sinh^{-1}\Big(\frac{\hbar\omega_D}{\Delta}\Big) \tag{1.3}$$

As the gap is small, $\Delta \ll \hbar\omega_D$, this can be approximated as:

$$1 \approx \lambda \ln\Big(\frac{2\hbar\omega_D}{\Delta}\Big) \tag{1.4}$$

$$\Delta = 2\hbar\omega_D \exp(-1/\lambda) \tag{1.5}$$

This is the BCS gap equation in the limit towards zero temperature ($T \to 0$), describing conventional superconductors with (weak) electron-phonon coupling. As the electron-phonon coupling constant is small ($\lambda \ll 1$ for the BCS weak coupling limit), the superconducting gap is typically smaller than the Debye frequency and is of overall small magnitude. Meanwhile, for finite temperatures, the Fermi-Dirac distribution, $f_{\text{FD}}(E_{\mathbf{k}})$, governs the occupation of each quasiparticle state with energy E_k. The temperature dependence alters the gap equation, equation 1.2, with an additional factor of $(1-2f_{\text{FD}}(E_{\mathbf{k}}))$, which is equivalent to $\tanh(E_{\mathbf{k}}/2)$, and results in:

$$\frac{1}{\lambda} = \int_0^{\hbar\omega_D} \frac{\tanh(\frac{\sqrt{\Delta^2+\epsilon^2}}{2k_BT})}{\sqrt{\Delta^2 + \epsilon^2}} d\epsilon \tag{1.6}$$

At $T = T_c$, the gap is necessarily zero, and the above equation can be used to relate T_c to the strength of the attractive interaction, here the electron-phonon coupling constant:

$$k_B T_c = 1.13\hbar\omega_D \exp^{-1/\lambda} \tag{1.7}$$

By substituting equations 1.5 into 1.7, the following relationship emerges between T_c and the superconducting gap:

$$2\Delta(T \to 0) = 3.528 k_B T_c \tag{1.8}$$

Recently, systems have been found with T_c approaching room temperature [13–15]. These are based around various hydride systems exhibiting large density of states at the Fermi level at extremely high pressures (several hundred GPa), which can lead to a high-T_c according to modified forms of equation 1.7 in strong coupling limits for conventional superconductors [21]. Unconventional superconductors have a different pairing mechanism, not mediated by phonons in the weak limit, so do not follow BCS theory, and hence are not found to follow this relationship.

1.2.1 Abrikosov-Gor'kov Model

Theoretical models can predict the behaviour of T_c in different systems as expected for different pairing mechanisms. Anderson's theorem describes how superconductivity is robust to non-magnetic disorder in convential superconductors [22]. Also, magnetic impurities in conventional superconductors will suppress superconductivity according to the Abrikosov-Gor'kov (AG) model [23], as the impurities act as pair breakers. For unconventional superconductors, nonmagnetic impurities can also cause pair breaking. The AG model can describe the suppression of superconductivity as the presence of non-magnetic impurities increases in FeSCs when mediated by a sign reversal $s_\pm$ superconducting state. The general form of the suppression of T_c formula in the AG model is:

$$\ln\left(\frac{T_c}{T_{c,0}}\right) = \Psi\left(\frac{1}{2}\right) - \Psi\left(\frac{1}{2} + \frac{\hbar}{4\pi\tau k_B T_c}\right) \tag{1.9}$$

where $T_{c,0}$ is T_c of the pristine system, Ψ is the digamma function, and τ is the scattering time. The changes in scattering time at low temperatures due to the impurities are compared to the suppression of the superconducting transition temperature. In Section 1.4.1 an estimation of an average scattering time using transport measurements is discussed. In Chapter 3 this model is used to examine the pairing symmetry in FeSe through the substitution of copper for iron in $Fe_{1-x}Cu_xSe$.

1.2.2 Upper Critical Field

With a strong enough external magnetic field applied to a superconductor, the superconducting state is suppressed and the systems enters its normal state. There are various upper critical field values and definitions that are useful, depending on the type of superconductor. For a type-I superconductor, the critical field $\mu_0 H_c$ is typically small ($\sim 10^{-2}$ T). For type-II superconductors the upper critical field $\mu_0 H_{c2}$ can be much larger ($10^0 - 10^2$ T) because of the vortex phase. In the vortex phase, magnetic flux is able to pass through the system through vortices, whilst the system still has zero resistance. We will briefly cover several models for the temperature dependence of the upper critical field and other parameters that can be extracted for useful insights into the superconducting state.

Coherence Length

The coherence length is a measure of how far magnetic flux penetrates into a superconductor. This is relevant throughout superconductors: at the surface, at any defect points or interfaces, and through vortices. In type II superconductors, the core of a vortex has a size of the coherence length, ξ, where a supercurrent exists which induces a magnetic field with flux equal to that of a single flux quantum, Φ_0. In an anisotropic superconductor the upper critical field will vary as the angle of the applied magnetic field is rotated. Hence, an anisotropy can be determined from the change in upper critical field along different directions. This introduction will focus on the high symmetry axes in-plane and out-of-plane, such that $H||c$ and $H||(ab)$, for the systems measured here.

The coherence length is one of the characteristic length scales of superconductors. In BCS theory, the coherence length is associated to the physical size of a single Cooper pair. More generally through the Ginzburg-Landau model (GL), the coherence length is a length scale of the distance from the surface that the order parameter recovers back to its bulk value. In the GL model, the coherence lengths can be calculated through the upper critical field [19]. If the upper critical fields

are measured to the lowest temperatures, then the GL equations for coherence length with $H||c$ is given by:

$$\xi_{ab} = \left(\frac{\Phi_0}{2\pi\mu_0 H_{c2}^c}\right)^{0.5} \tag{1.10}$$

The in-plane coherence length ξ_{ab} is only dependent upon the upper critical field with $H||c$. In contrast, the inter-plane coherence length, ξ_c, contains both inter-plane and in-plane screening contributions and therefore $\mu_0 H_{c2}^{ab}$ is dependent on both ξ_{ab} and ξ_c. Using the form of ξ_{ab} in equation 1.10, ξ_c can be written as:

$$\xi_c = \left(\frac{\mu_0 H_{c2}^c}{\mu_0 H_{c2}^{ab}} \frac{\Phi_0}{2\pi\mu_0 H_{c2}^{ab}}\right)^{0.5} \tag{1.11}$$

Whether a system is in the clean or dirty limit can be determined by comparing the coherence length (ξ) to the mean free path (ℓ). A system is in the clean limit when $\xi \ll \ell$, and in the dirty limit when $\xi \gg \ell$. The mean free path can be estimated from Drude theory (equation 1.18).

Orbital and Pauli Pair Breaking

The experimentally observed upper critical field is subject to orbital and Pauli paramagnetic limiting. Orbital pair breaking is driven by the Lorentz force. The orbital limit upper critical field ($\mu_0 H_{c2}^{orb}$) is that at which vortices begin to overlap and the vortex lattice breaks down. Meanwhile, Pauli pair breaking is driven by Zeeman splitting. As the magnetic field increases in magnitude, it will become favourable for one of the spins in a Cooper pair to flip and break the pair. This is given as $\mu_0 H_{c2} = \mu_0 H^{orb}/\sqrt{1+\alpha_M^2}$, where $\alpha_M = \sqrt{2}\mu_0 H_{c2}^{orb}/\mu_0 H_{c2}^P$ is the Maki parameter [24], and $\mu_0 H_{c2}^P$ the Pauli field. The Maki parameter relates the orbital and Pauli limits for a value of the paramagnetic contribution. In the anisotropic layered systems considered here, the paramagnetic pair breaking is minimal along $H||c$, where α_M is small, but is relevant for $H||(ab)$, where α_M is larger.

$$\mu_0 H_{c2}^P = \sqrt{2}\Delta/g\mu_B \tag{1.12}$$

The WHH model describes the upper critical field of single band superconductors, developed by Wethamer, Helfand and Hohenber [25, 26]. In the absence of orbital

and Pauli pair breaking effects, a simple relation is found for the zero temperature upper critical field, $\mu_0 H_{c2}(0\,\mathrm{K})$:

$$\mu_0 H_{c2}(0\,\mathrm{K}) = -0.73 T_c \left.\frac{\mathrm{d}\mu_0 H_{c2}}{\mathrm{d}T}\right|_{T_c} \tag{1.13}$$

The pre-factor is that for the clean limit, whereas it is -0.69 for systems in the dirty limit. For multi-band systems the situation is more complex due to inter-band and intra-band couplings, but these effects can be acccounted for by using models such as those developed by Gurevich [27].

The next model for behaviour of the upper critical field is considered for a two band system developed by Kogan and Prozorov [28]. As the upper critical field is the point where vortices begin to overlap and so is the point of pair breaking, relations can be derived between the upper critical field and parameters related to the quasiparticles and Fermi surface. In the clean limit, the slope of the upper critical field near T_c is affected by orbital pair breaking, and the superconducting energy gap, whilst Pauli pair breaking is minimal. For a two band system with cylindrical or 2D Fermi surfaces, this slope of the upper critical field is given by [27, 28]:

$$-\left.\frac{\mu_0}{T_c}\frac{\mathrm{d}H_{c2}}{\mathrm{d}T}\right|_{T_c} = \frac{16\pi k_B^2 \phi_0}{7\zeta(3)\hbar^2(n_1\lambda_{11}\langle v_1^2\rangle + n_2\lambda_{22}\langle v_2^2\rangle)} \tag{1.14}$$

where v_i is the Fermi velocity, λ_{11} and λ_{22} are normalised coupling constants, n_i is the density of states of each carrier (N_i/N_{total}), ϕ_0 is the quantum flux, and $\zeta(\mathrm{x})$ is the Riemann zeta function at x. The density of states, n_i, is related to the Fermi surface by the Fermi wavevector, $k_{\mathrm{F,i}}$, and effective mass, m_i^*. One can consider the single band case by setting λ_{22} to 0, and a relation is found for the effective mass to the slope by:

$$-\left.\frac{\mu_0}{T_c}\frac{\mathrm{d}H_{c2}}{\mathrm{d}T_c}\right|_{T_c} \propto v_F^{-2} \propto (m^*)^2 \tag{1.15}$$

Whilst reasonable estimations of Fermi velocities can be learned from quantum oscillations or ARPES measurements, and averaged for each Fermi surface, the coupling constants are harder. The normalised slope of the $\mu_0 H_{c2}(T)$ near T_c can be linked to changes in the effective mass, and variations, such as with pressure, reveal insights to the Fermi surface evolution with applied pressure.

1.3 Iron-Based Superconductors

The focus now shifts to the high-T_c superconductors family of iron-based superconductors. A common feature of the FeSCs is the crystallographic structure. The basis being a plane of Fe atoms in a square lattice, with chalcogenide or pnictogen atoms above and below the Fe-plane to form tetrahedral arrangements around each Fe. The full structure is built from repeating layers, in combination with other spacer layers (which can be grouped into different families). There are several families of FeSCs based on their stoichiometry, in particular: '11' (FeSe, FeTe), '111' (XFeAs, X = Li, Na, Eu), '122' (XFe_2As_2, X = Ba, Ca, K) as examples. This thesis will focus on the structurally simplest FeSe, but first a general introduction to FeSCs.

The phase diagrams of FeSCs are complex, containing many different competing phases, similar to the cuprate superconductors. At high temperatures the system is (often) tetragonal and so fourfold symmetric, then at a lower temperature enters a different ordered phase, often antiferromagnetic (AFM). This ordered phase is suppressed with a tuning parameter, for example chemical doping, charge doping, or applied pressure, and a dome of superconductivity emerges around the point of full suppression. Perhaps the best example is $BaFe_2As_2$, and a schematic phase diagram as a function of electron and hole doping, and for isovalent substitution, is shown in Figures 1.1a and b, containing examples of how the superconducting domes emerge.

There are four distinct phases that, in general, form the phase diagrams of FeSCs: tetragonal at high temperatures, antiferromagnetic (AFM, spin density wave), nematic, and superconducting. The parent compound $BaFe_2As_2$ is paramagnetic at high temperatures, and has a Néel temperature of 140 K, below which the system is antiferromagnetic in a spin density wave (SDW) phase [29, 30]. For most systems, a nearby or concomitant structural transition is found, in $BaFe_2As_2$ the second-order structural transition closely preceeds the first-order AFM phase transition. The structural transition from a tetragonal to orthorhombic phase, breaking the C_4 rotational symmetry, then defines the boundary of the nematic phase. The nematic phase is believed to be electronic driven, in which the electronic degrees of freedom couple to the lattice to induce the rotational symmetry breaking

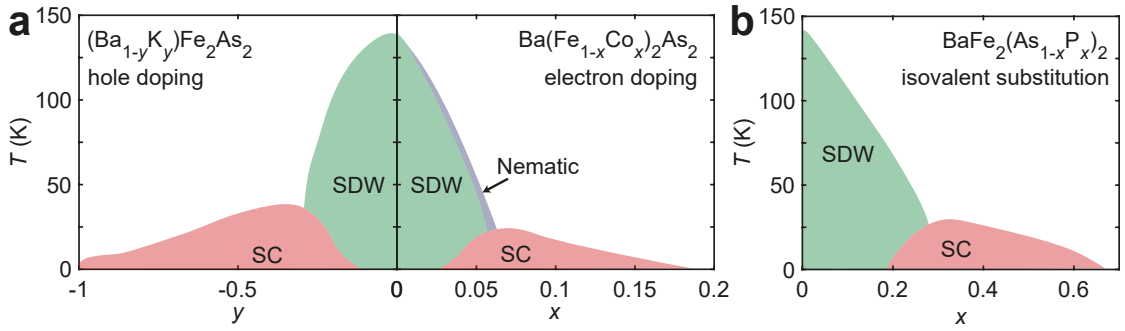

Figure 1.1: Phase diagrams of substituted $BaFe_2As_2$. (a) A schematic phase diagram for $BaFe_2As_2$ for both electron and hole doping, based off [29] and [30] respectively. (b) Schematic phase diagram for the isovalent substitution of $BaFe_2(As_{1-x}P_x)_2$, adapted from [36] and [32].

[31]. With electron doping, the difference in temperature between the nematic and AFM phase transitions increases [29]; however, with hole doping and isovalent substitution the structural and AFM transitions are found to be concomitant [30, 32]. Furthermore, the isovalent substitution with P in $BaFe_2(As_{1-x}P_x)_2$ reveals a quantum critical point [33]. A link has been suggested empirically between the height of the anion, $h = zc$, above the Fe-plane (this definition is highlighted in Figure 1.3c) and T_c for FeSCs generally [34]. With applied pressure, the anion height should generally decrease, therefore suggesting pressure, up to a point, will enhance superconductivity in many of these systems [35].

It is worth considering the similarities and differences between the two main high-T_c families of superconductors, the cuprates and iron-based superconductors. Both families are layered systems, with either layers of CuO_2 or Fe ions arranged on a square lattice. Each high-T_c family is comprised of systems with different combinations of ions above and/or below the CuO_2 or Fe layers. Additionally, electron correlations are believed to play a key role in the properties of these (and heavy Fermion) systems for the normal and superconducting states. Both families exhibit rich phase diagrams; however, the phase diagrams of the cuprates superconductors typically contain a Mott insulator phase suppressed through hole or electron doping, the presence of a pseudogap, and charge density waves [37], that are yet to be widely realised in FeSCs. A crucial difference arises from the single band nature of cuprates superconductors, in contrast to typically multiband (and

compensated) FeSCs. For the cuprate superconductors, there exists a single d-orbital per Cu site. Perhaps more interestingly, there are six electrons of the $3d$ Fe orbitals, where all Fe $3d$ orbitals are occupied and relevant (d_{xz}, d_{yz}, d_{xy}, $d_{x^2-y^2}$, and d_{z^2}).

The electronic structure of FeSCs contains both electron and hole bands crossing the Fermi level, see a schematic of the band structure near the Fermi energy in Figure 1.2a. The systems are compensated metals in the stoichiometric states, although many parent compounds may require doping to reveal a superconducting phase, such as $BaFe_2As_2$ [38] or LaFeAsO [9]. The Fermi surfaces are typically quasi-two dimensional, owing to the layered structure and weak interlayer coupling, which leads to many anisotropic effects in FeSCs. In the iron chalcogenides, there are weak van-der Waals bonds between layers. The Fermi surface, in the typical 2-Fe Brillouin zone, has hole pocket(s) at the centre and electron pocket(s) at the corners. The Fermi surfaces are small, and thus are very sensitive to changes in the environment, which explains the tunability of these systems. Both the nematic and magnetic transitions are associated with significant changes to the Fermi surface. Firstly, the nematic transition, from a tetragonal to orthorhombic sturcture, breaks the four-fold rotational symmetry and induces elongation of the Fermi surface. More drastically, a Fermi surface reconstruction occurs across the magnetic phase transition, such as in $BaFe_2As_2$ where the charge carrier density is noticeably reduced across the magnetic transition [39]. Additionally, there is orbital character differentiation on the Fermi surfaces, where different orbitals experience different correlations effects [40]. Figure 1.2b shows schematically a cut of the Fermi surface at the high symmetry points for FeSCs in the tetragonal phase. Furthermore, the multiband nature of interband and intraband interactions must be considered. Theoretically, DFT calculations overestimate the size of the Fermi surface, but do capture the overall shape, as compared to techniques such as ARPES (Angle resolved photoemission spectroscopy), and quantum oscillations [41].

The different suggestions of pairing mechanisms in unconventional superconductors include: spin fluctuations [40, 42], orbital fluctuations [43–45], charge-transfer superexchange [46, 47], and nematic fluctuations [48]. For FeSCs, nematic

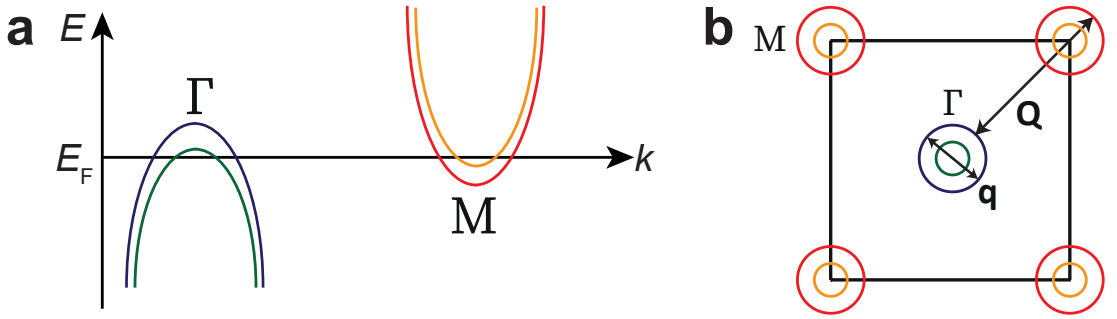

Figure 1.2: Fermi surface of iron-based superconductors. (a) Schematic band structure around the Γ and M points for iron-based superconductors. (b) Schematic Fermi surface of FeSCs at $k_z = 0$. Possible scattering vector **Q** for AFM nesting, and **q** for typical electron-phonon coupling, and/or nematic fluctuations.

fluctuations, orbital fluctuations and spin fluctuations are the most reported possible superconducting mechanisms. The nematic fluctuations and spin fluctuations are suggested due to the emergence of superconducting domes as the nematic and magnetic phase transition temperatures approach zero for many FeSCs. The close nature of these two phases adds a complication to assigning the role of the attractive pairing interaction to one set of fluctuations over the other, or indeed accepting both as leading contributors. There are 5 d orbitals from the Fe ions, and thus an orbital fluctuations regime is proposed, in particular because this would support a pairing interaction where the sign of the superconducting gap is preserved, the s_{++} state. In that scenario, a consequence is the robustness of the superconducting phase to impurities, and T_c should show an almost invariance to moderate levels of impurities [49]. STM measurements in particular have investigated the orbital characters on each band, and their involvement in superconductivity, for example in FeSe showing orbitally-selective Cooper pair preferentially arising from the Fe d_{yz} orbitals [50]. Alternatively, spin fluctuations could arise from nesting between the hole and electron-like Fermi surfaces (intraorbital) [51, 52]. Such a scenario favours a sign changing superconducting pairing ($s_{\pm}$). A significant difference between the s_{++} and $s_{\pm}$ gap symmetries arises in the response to disorder, with $s_{\pm}$ being highly sensitive to nonmagnetic impurities [42, 53]. This will be discussed in chapter 3 in relation to Cu substituted FeSe.

1.3.1 Iron Chalcogenides: FeSe

The iron chalcogenides can be split into two main groups. There are the structurally simple Fe(Se,S,Te) systems, where the chalcogenides sits above and below the Fe plane, with weak van der Waals bonds between layers, see Figure 1.3. These systems are mostly superconducting at low temperatures, up to 15 K [54–57]. In addition, intercalated systems of the form $A_xFe_{2-y}Se_2$ (A = K, Rb, Cs, Tl, etc) can reach values of T_c in the range of 30 K [58]. The intercalated A can dope the system, and these latter systems can be considered similar to electron doped FeSe.

Unlike most FeSCs, FeSe does not magnetically order at any temperature [54]. The system undergoes a structural phase transition from a high temperature tetragonal structure (P4/nmm) to an orthorhombic structure (Cmma) at T_s = 90 K, entering the electronic nematic phase [59]. As with FeSCs in general, this nematic phase breaks the C_4 rotational symmetry of the lattice, to C_2, which is possibly induced from orbital ordering of the bands that leads to band shifting and in-plane elongation of the electronic pockets [60]. Upon further cooling, a rather low superconducting transition temperature of T_c = 9 K is found in the absence of any magnetic order transitions. FeSe is an ideal candidate to investigate the superconductivity of FeSCs in a clean nematic state, as it is a highly tunable system, and does not exhibit magnetic order at ambient pressures. Additionally, due to the relatively low T_c of 9 K, the normal electronic state to lowest temperatures can be accessed with only modestly high magnetic fields, and thus more readily probe the system.

Perhaps the most noteworthy discovery related to FeSe thus far is in FeSe monolayers, specifically when grown epitaxially on $SrTiO_3$. In the right conditions, values of T_c reach 65 K, and potentially upwards of 100 K [10–12]. The compensated aspect of FeSCs no longer holds for monolayer FeSe, where only electron-like surfaces remain and the main hole band has moved substantially below the Fermi energy, effectively appearing as electron doped [62, 63]. In addition, intercalation of FeSe with spacer layers has shown the ability to enhance T_c above 40 K [64].

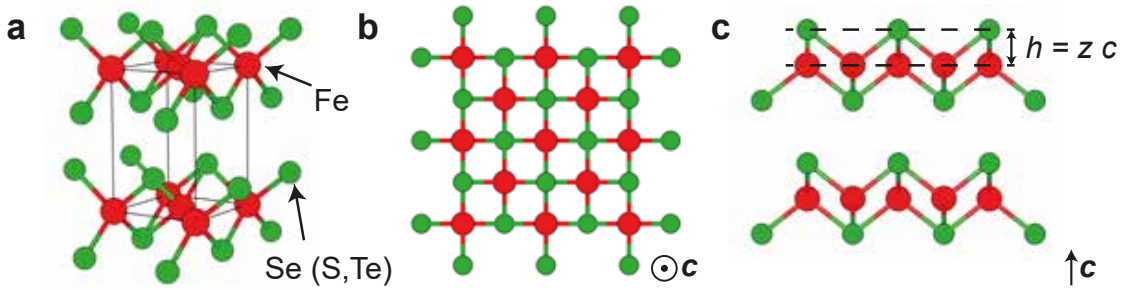

Figure 1.3: Crystal structure of FeSe. (a) View of the unit cell, where red spheres are Fe, and green spheres are Se. The black cube is the unit cell. A view looking (b) along the c-axis and (c) perpendicular to the c-axis. The height of the anion above the Fe-plane is $h = z\,c$. All images produced in VESTA [61].

The normal and superconducting states properties stem from the Fermi surface and electronic structure. ARPES measurements on bulk FeSe have investigated the Fermi surface at high temperatures in the tetragonal phase, and low temperatures in the nematic phase. Owing to the orthorhombicity of the nematic phase, detwinning of the crystals is required to resolve different domains [65, 66]. The tetragonal Fermi surface is a single hole pocket at the centre and two electron pockets centered at the corners of the Brillouin zone [60]. The Fermi surfaces are quasi-two dimensional and are relatively small. From the band structure at low temperatures inside the nematic phase, a second hole pocket lies just below the chemical potential [60], and small shifts could raise this band above the Fermi energy. In $FeSe_{1-x}S_x$ one such Lifshitz transition occurs around $x \approx 0.11$ [67]. The small Fermi energies can be attributed to Fermi surface shrinking from strong electronic correlations found in FeSe [68].

In FeSe, chemical substitution of different ions can replace either the Fe, or the Se ions. The isovalent substitution with S or Te takes place outside of the Fe-plane, with minimal effects related to impurity scattering. As the S(Te) ions are smaller(larger) than the Se ions, this substitution acts as a chemical pressure. Conversely, substitution inside the Fe-plane by replacing Fe ions with transition metals can introduce significant impurity scattering, and should dope the system - with holes or electrons depending on the transition metal. Examples include the substitution of Fe for Co, Ni, Mn, Cu [72–76]. Furthermore, the

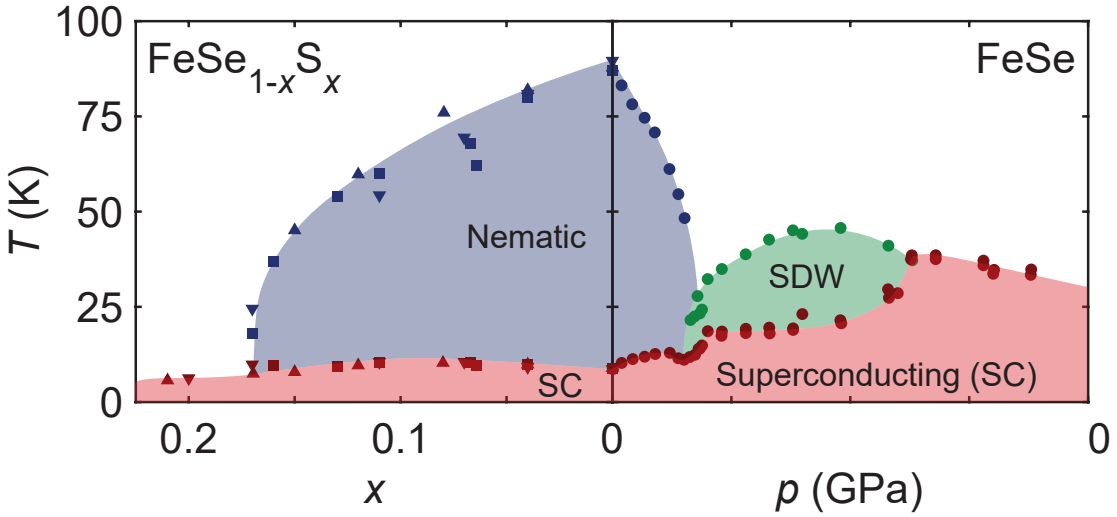

Figure 1.4: Phase diagrams of FeSe. (left) $FeSe_{1-x}S_x$ doping temperature phase diagram and (right) FeSe pressure-temperature phase diagram. The structural transition points are blue, superconducting transition points red and magnetic transition points green. Circles are from [69], squares from [67], triangles from [70], and upside down triangles from [71].

superconductivity is also reduced as the thickness of thin flakes FeSe is decreased as the disorder increases [77].

Beyond the discussed phases of FeSe, in strong magnetic fields at low temperatures, it is suggested that FeSe provides access to the FFLO state (Fulde-Ferrell-Larkin-Ovchinnikov), where Cooper pairs exist with nonzero total momentum and the order parameter is spatially modulated [78, 79]. This state has previously been proposed to be present only in a few heavy fermion and organic superconductors [80, 81]. In addition, $FeTe_{1-x}Se_x$ has recently been a leading system in the research of topological superconductors [82].

1.3.2 Effect of Applied Pressure

FeSe provides clean access to the nematic phase at ambient pressure, in the clear absence of a magnetically ordered phase. This is perhaps unusual, as FeSe has a rather large total fluctuating magnetic moment (60% larger than $BaFe_2As_2$) [83]. Inelastic neutron-scattering experiments concluded that there are strong spin fluctuations in FeSe of both Néel and stripe type, and competition between these instabilities prevents the long-range magnetic order [83, 84].

Figure 1.4 presents the phase diagram of FeSe under pressure [16, 69, 85–89]. Applied pressure enhances superconductivity in FeSe, with a peak value of T_c = 36.7 K around 6.4 GPa [16, 69, 72, 85, 90–92]. Interestingly, FeSe under pressure does not only enhance superconductivity, but it is suggested that under pressure a spin-density wave phase exists over a large pressure regime [69]. More recently, a detailed high-energy x-ray diffraction study on the evolution of the crystal structure of FeSe under applied pressure identifies the different structural transitions from the nematic phase at low pressures, and the magnetic phase at high pressures [89, 93]. In contrast, the nematic transition from a tetragonal to orthorhombic structure shows a smooth change to the lattice constants, indicative of a second-order phase transition. Meanwhile, at higher pressures there is a discontinuous shift to the a and b lattice parameters which persists to much higher pressures (∼6.6 GPa), which is a clear indicator of a first-order phase transition. This first-order phase transition occurs at the same temperatures as the magnetic order transition found in other measurement techniques [69, 94]. In transport measurements, the signature of this magnetic order has been linked to an upturn in the resistivity which occurs at the same temperature even in strong magnetic fields [69, 95, 96], because this anomaly occurs at the same temperatures where magnetic order is found through the techniques discussed above. Furthermore, quantum oscillations observed in this phase are significantly reduced in frequency compared to ambient pressure, as expected for a Fermi surface reconstruction with a spin-density wave [87]. Comparing to $Ba(Fe_{1-x}Co_x)_2As_2$ where the magnetic and structural transition are separated in temperature, the signature of the magnetic transition in resistivity manifests as either a downturn or upturn in resistivity [29]. Thus, resistivity measurements can be used to probe the magnetic transition in FeSe-based systems. Concerning the local magnetic order, μSR studies on FeSe under applied pressure found static magnetic order at temperatures above T_c for $p > 0.8$ GPa [86]. For all pressures the superconducting volume fraction is close to 100%, and the magnetic volume fraction continuously increases with pressure up to 90% at 14 kbar, suggesting coexistence of superconductivity and magnetism in FeSe under pressure [86, 97]. A follow up study with μSR for FeSe at 19 kbar finds

the magnetic order in FeSe to correspond most likely to single-stripe (collinear) [98]. The striped antiferromagnetic order is also consistent with NMR [99].

1.3.3 Effect of Chemical Pressure

Chemical pressure in FeSe has some similarities to the effects of applied pressure. The isovalent substitution with S in $FeSe_{1-x}S_x$ suppresses the nematic phase to zero temperature at the nematic end point, close to $x = 0.18$, as shown in Figure 1.4a [67]. The superconductivity forms a small dome inside the nematic phase, with a maximum T_c of 11 K around $x = 0.1$, and shows a significant drop across the nematic phase boundary [55]. For larger S substitution superconductivity remains present at low temperatures in the tetragonal phase all the way to FeS with a $T_c \sim 4$ K [57, 100]. The high quality single crystals of $FeSe_{1-x}S_x$ are widely grown using the chemical vapour transport technique [101, 102], as were the single crystals used in this thesis. The community has struggled to produce single crystals with $x \gtrapprox 0.25$ using this method. Recently, a hydrothermal method has mapped out the full phase diagram from FeSe to FeS [57]. The phase diagrams of single crystals from both methods are in broad agreement, although the residual resistivity is significantly higher using the hydrothermal method. Additional differences arise in the sign of the Hall coefficient at low temperatures for FeSe, which remain unexplained [103]. Interestingly, by applying pressure to different compositions of $FeSe_{1-x}S_x$, the signatures in transport associated with the magnetic order are shifted to higher pressures for higher sulphur substitution [104]. This means that the two overlapping nematic and magnetic phases can be decoupled to identify their role on superconductivity and explore the region of a potential quantum nematic phase transition [105–107].

1.4 Transport Properties

The main experimental techniques used in this thesis to probe the various electronic phases are electrical transport and magnetotransport. To explore these phases, the measurements examine the response of the system to varying the temperature, external magnetic field and increasing applied hydrostatic pressure. The temperature

and magnetic field dependences of the resistivities (along different directions of the conducting *ab*-plane) can reveal more about the electronic structure and the dominant scattering channels. Additionally, different transitions can be identified in resistivity. Resistivity measurements are a powerful technique to detect different electronic transitions, such as the superconducting transition from finite to zero resistance, the structural transition that is associated with a kink in the resistivity, a magnetic transition, or a metal-to-insulator transition. The low temperature absolute resistivity provides useful information for understanding the impurities in a system, and, relatively, how this changes with chemical doping.

1.4.1 Non-interacting Free Electron Models

Drude Model

A simple non-interacting model of electron behaviour in metals is that of Drude theory, which assumes no quantum phenomena and considers the electrons classically. The electrons are assumed as being mobile objects which classically collide with immobile positive ions, making this an application of kinetic theory. Three key assumptions are made. The electrons have a scattering time, τ. After each scattering event, the electron momentum is reset, $\boldsymbol{p} = 0$. As the electrons are (negatively) charged particles, they also respond to external electric and magnetic fields as expected. The equation of motion for a system in both an electric and a magnetic field is given by:

$$\frac{\mathrm{d}\mathbf{p}}{\mathrm{d}t} = -e(\mathbf{E} + \mathbf{v} \times \mathbf{B}) - \frac{\mathbf{p}}{\tau} \tag{1.16}$$

In steady state, $\frac{\mathrm{d}\mathbf{p}}{\mathrm{d}t} = 0$, and as the current density, for a single band system, is $\mathbf{j} = -ne\mathbf{v}$, the momentum can be shown as $\mathbf{p} = m\mathbf{v} = -\frac{m}{ne}\mathbf{j}$ to give:

$$0 = -e\mathbf{E} + \frac{1}{n}(\mathbf{j} \times \mathbf{B}) + \frac{m}{ne\tau}\mathbf{j} \tag{1.17}$$

In the absence of a magnetic field ($\mathbf{B} = 0$), then according to Ohm's law $\mathbf{j} = \sigma_0\mathbf{E}$, the conductivity at zero temperature is given by:

$$\sigma_0 = \frac{ne^2\tau}{m} \tag{1.18}$$

This is the inverse of the zero-temperature resistivity, $\rho_0 = 1/\sigma_0$. From this expression the mean free path, $\ell = v_F\tau$, can also be calculated, where v_F is the Fermi velocity.

In a multi-dimensional system, the resistivity tensor is used to describe the transport along different directions, and is given by equation 1.19.

$$\rho = \begin{pmatrix} \rho_{xx} & \rho_{xy} & \rho_{xz} \\ \rho_{yx} & \rho_{yy} & \rho_{yz} \\ \rho_{zx} & \rho_{zy} & \rho_{zz} \end{pmatrix} \tag{1.19}$$

In the quasi-two dimensional iron-based superconductors the (ab) plane is along the conducting Fe-plane and the c axis is perpendicular to the layers. Throughout this thesis, the measurements are considered with the current applied along the (ab) axis, and the magnetic field parallel to c. In particular, the different layers of the samples are short-circuited together with current contacts on either end of the single crystal. This allows a simplification to treat the system as quasi-two dimensional, since no inter-plane resistance is measured. Symmetry also dictates, $\rho_{xx} = \rho_{yy}$ and $\rho_{xy} = -\rho_{yx}$.

Hall effect

In the presence of an applied magnetic field the Lorentz force acts on charged particles in a plane perpendicular to the field, see the **B** term in equation 1.16. Whilst there is a contribution to the longitudinal resistivity, ρ_{xx}, there is also a transverse contribution, ρ_{xy}, known the Hall effect (named after Edwin Hall who discovered this in 1879). The Hall coefficient, R_H, is a measure of the strength of the Hall effect and is given by:

$$R_H = \frac{E_y}{j_x B_z} \tag{1.20}$$

Using equation 1.17, and considering the resistivity matrix, one can find:

$$R_H = -\frac{1}{ne} \tag{1.21}$$

Thus, in a single band system, measuring the Hall coefficient measures the density of charge carriers, and depending on the sign of R_H, the charge of the charge carrier (the above has assumed electrons, thus $q = -e$).

Sommerfeld Free Electron Model

The Sommerfeld model applies Fermi-Dirac statistics to Drude theory. Instead of assuming the distribution of velocities for electrons is governed by the Maxwell-Boltzmann distribution, the Pauli exclusion principle prevents identical states being occupied. Now, the ground state of the system consists of electrons filling from the lowest available energy state. The highest occupied energy state defines the Fermi energy, and higher energy states will remain unfilled. More strictly, the Fermi energy is the chemical potential at $T = 0$. This introduces the notion of the Fermi surface, which is the boundary between occupied and unoccupied states in k-space. The Fermi energy can be calculated for a three dimensional system with an electron carrier density n by:

$$E_{\mathrm{F}} = \frac{\hbar^2(3\pi^2 n)^{2/3}}{2m} \tag{1.22}$$

In the two-dimensional case the density of states function is energy independent ($g(E) = m/\pi\hbar^2$), which leads to a different form of the Fermi energy at zero temperature $E_{\mathrm{F}}^{\mathrm{2D}} = \hbar^2\pi n/m$.

Average scattering time from transport measurements

In order to compare the AG model from equation 1.9 to experimental measurements, τ must be related to the residual resistivity. To estimate an average scattering time from measurable values, the nearly free electron model is used to express the total conductivity, assuming a constant effective mass for each Fermi surface, by:

$$\sigma = \sum_i \eta_i e^2 \tau_i, \quad \text{where } \eta_i = n_i/m_i \tag{1.23}$$

By taking an average of the scattering times, weighted by the effective mass and carrier density through η_i:

$$\tau_{\mathrm{avg}} = \frac{\sum_i \eta_i \tau_i}{\sum_i \eta_i} \tag{1.24}$$

$$\frac{1}{\rho_0} = \sigma = \sum_i \eta_i e^2 \tau_{\mathrm{avg}} \tag{1.25}$$

This can be substituted into equation 1.9 for the average scattering time to produce a form of the equation more directly relevant to parameters in transport measurements:

$$\ln\left(\frac{T_c}{T_{c,0}}\right) = \Psi\left(\frac{1}{2}\right) - \Psi\left(\frac{1}{2} - \frac{\hbar e^2 \rho_0 \sum_i \eta_i}{4\pi k_B T_c}\right) \tag{1.26}$$

Thus, by using measurements of the carrier densities and effective masses for η_i of each surface, a relation is found between ρ_0, indicating the impurity increase in the system, and the superconducting transition temperature, T_c.

1.4.2 Fermi Liquid Theory

The previous models considered the set of electrons as noninteracting. However, there are clearly scenarios where electron-electron interactions are inevitable due to Coulomb's law, and can not be negated. Fermi Liquid theory, developed by Lev Landau, considers the effect of introducing (adiabatically) interactions between electrons [108, 109]. One of the results of this theory is that when electron-electron interactions dominate, the scattering rate, $1/\tau$, has a quadratic temperature dependence. These interactions do not contribute significantly at high temperatures, but the relaxation time will increase as $1/T^2$ and thus will be most relevant at low temperatures. Hence, for a Fermi liquid the resistivity follows a quadratic temperature dependence at low temperatures, given by:

$$\rho(T) = \rho_0 + AT^2 \tag{1.27}$$

where ρ_0 is the resistivity at zero temperature, and $A \propto (m^*/m_e)^2$ is a coefficient linked to the strength of electronic correlations through the effective masses, m^*. Typically, electron-phonon scattering will dominate at high temperature to give linear temperature dependence, whereas at very low temperatures electron-phonon interactions have a T^5 contribution to the resistivity. Materials where electron-electron interactions are strongest are called strongly correlated systems, often found in unconventional superconductors like the heavy fermion systems.

Non-Fermi liquids

Where a quadratic temperature dependence is not recovered at low temperatures, the system is not governed by Fermi liquid theory. Deviations from T^2 are referred to as non-Fermi liquid behaviour. A notable case is that of a strictly linear temperature dependence in high-T_c systems, which are often called strange metals [110, 111]. To identify deviations from Fermi-liquid behaviour, a modified form of equation 1.27 is used instead, where the exponent, n, can vary:

$$\rho = \rho_0 + \alpha T^n \tag{1.28}$$

In this thesis, the resistivity exponent will be explored in several systems displaying non-Fermi liquid behaviour, and where some recover Fermi-liquid behaviour at low low temperatures. The value of the exponent, and any changes with different tuning parameters, can hint at the dominant scattering terms. For example, in the vicinity of a quantum critical point non-Fermi liquid behaviour is found, which is recovered when moving away from the critical point, such as with $BaFe_2(As_{1-x}P_x)_2$ [112], or in heavy fermion systems like $CeCoIn_5$ [113]. Theoretically, low temperature values of n are expected to differ from Fermi liquid in many scenarios [114–116].

Impurity Scattering

Towards zero temperature the scattering becomes dominated by impurities and defects, and this dictates the residual resistivity, ρ_0. The residual resistivity is particularly hard to determine in superconductors, and requires high magnetic fields to suppress the superconductivity and reveal the normal state to lower temperatures. From the residual resistivity, an estimate of the mean free path can be made, which can be used to determine if the system is in the clean ($\xi \ll \ell$) or dirty limit ($\xi \gg \ell$). When multiple scattering channels are present, Matthiessen's rule states mobilities from different sources can be inversely summed together to calculate an overall mobility, we can extend this argument to scattering times too [20]. However, this remains true only when the individual scattering times/rates, such as concerning impurities or phonon scattering, have probabilities independent of each other [117].

Throughout this work, the determination of ρ_0 and subsequent analysis is paramount for determining the disorder in systems, the power laws concerning Fermi liquid (or not) behaviour, and electronic correlations.

1.4.3 Magnetotransport Properties

The resistivity will exhibit magnetoresistance when an external magnetic field is applied. With an applied magnetic field, charged particles are affected by the Lorentz force through $\mathbf{F} = q\mathbf{v} \times \mathbf{B}$ (see equation 1.16 for the equation of motion in electric and magnetic fields), which alters the velocity of the particle towards circular/helical motion. Interestingly, the field dependence of the resistivity can be used to determine the behaviour of the charge carrier densities and mobilities, the size and shape of Fermi surfaces through quantum oscillations and angular dependent magnetoresistance oscillations (AMRO) [118], and the behaviour of the upper critical field with temperature.

Let us consider an isotropic system with a spherical Fermi surface in the presence of both an electric and magnetic field. The electric field, $\mathbf{E}$, is applied along $\mathbf{x}$, and a magnetic field $\mathbf{B}$ applied along $\mathbf{z}$. For a general $\mathbf{E}$, the current density, $\mathbf{J}$, is given by:

$$\mathbf{J} = \sigma\mathbf{E} = \begin{pmatrix} \sigma_{xx} & \sigma_{xy} & 0 \\ \sigma_{yx} & \sigma_{yy} & 0 \\ 0 & 0 & \sigma_{zz} \end{pmatrix} \mathbf{E} \tag{1.29}$$

The components of σ can be deduced from the equation of motion (equation 1.16) and noting that $\mathbf{J} = -ne\mathbf{v}$. This results in, for the scenario described above:

$$\sigma_{xx} = \frac{\sigma_0}{1 + \omega_c^2\tau^2} \tag{1.30}$$

$$\sigma_{xy} = \frac{\sigma_0\omega_c\tau}{1 + \omega_c^2\tau^2} \tag{1.31}$$

where $\sigma_0 = ne^2\tau/m^*$, as found in the absence of a magnetic field, and $\omega_c = eB/m^*$ being the cyclotron frequency. A more practical form for transport measurements is the resistivity components, found by inverting the conductivity tensor ($\boldsymbol{\rho} = 1/\boldsymbol{\sigma}$), such that:

$$\rho_{xx} = \rho_{yy} = \frac{\sigma_{xx}}{\sigma_{xx}^2 + \sigma_{xy}^2} \tag{1.32}$$

and

$$\rho_{xy} = -\rho_{yx} = \frac{\sigma_{xy}}{\sigma_{xx}^2 + \sigma_{xy}^2} \tag{1.33}$$

Hence, for a monovalent isotropic system, with a spherical Fermi surface, ρ_{xx} is field independent, and no magnetoresistance is found (it is zero). In an anisotropic system, then $\sigma_{xx} \neq \sigma_{yy}$, and $\sigma_{xy} \neq \sigma_{yx}$, and magnetoresistance is not zero.

A notable case is metals with a single carrier species and a single isotropic scattering time. In this case, the magnetoresistance is proportional to the amount of cyclotron orbits made before scattering and follows Kohler's rule [119, 120]. The change in resistivity with magnetic field is given by Kohler's rule as:

$$\frac{\Delta\rho_{xx}(H)}{\rho_{xx}(H=0)} \propto \Big(\frac{\mu_0 H}{\rho_{xx}(H=0)}\Big)^2 \tag{1.34}$$

Hence, a strictly quadratic field dependence, which can be scaled (Kohler's scaling) for different temperatures, is an indication that the scattering is dominated by a single scattering time. Violations of Kohler's rule can indicate the presence of more than one carrier species, anisotropic effects or temperature dependent electronic structure quantities. Further modifications can be made to Kohler's rule to seek out scaling laws, such as with the Hall angle θ_H and an energy-field scaling law, and will be introduced when used in later chapters.

Magnetoresistance in multi-carrier systems

The magnetoresistivity can be modelled successfully with multicarrier models. Starting with a single band system, with a simple spherical Fermi surface, the conductivities σ_{xx} and σ_{xy} are given by [120]:

$$\sigma_{xx}(B) = \frac{en\mu}{1 + \mu^2 B^2} \tag{1.35}$$

$$\sigma_{xy}(B) = \frac{en\mu^2 B}{1 + \mu^2 B^2} \tag{1.36}$$

However, FeSCs are typically compensated metals, and therefore multi-band systems. The conductivities from multiple charge carriers can be added together, as so

for i hole like carriers and j electron like carriers the longitudinal and Hall conductivities are given by:

$$\sigma_{\mathrm{xx}}(B) = \sum_i \frac{q_i n_i \mu_i}{1+\mu_i^2 B^2} + \sum_j \frac{q_j n_j \mu_j}{1+\mu_j^2 B^2} \tag{1.37}$$

$$\sigma_{\mathrm{xy}}(B) = \sum_i \frac{q_i n_i \mu_i B}{1+\mu_i^2 B^2} - \sum_j \frac{q_j n_j \mu_j B}{1+\mu_j^2 B^2} \tag{1.38}$$

where each carrier may have its own charge, q_i, carrier density, n_i, and mobility, μ_i. The treatment can be extended to any number of charge carriers, and so one can calculate the dependency of ρ_{xx} and ρ_{xy} as a function of the carrier density and mobility of each carrier. As an example, the two carrier model, after inverting the conductivity tensor is given by (assuming one hole, h, and one electron, e):

$$\rho_{\mathrm{xx}} = \frac{(\sigma_h+\sigma_e)+\sigma_h\sigma_e(\sigma_h R_h^2+\sigma_e R_e^2)B^2}{(\sigma_h+\sigma_e)^2+\sigma_h^2\sigma_e^2(R_h+R_e)^2B^2} \tag{1.39}$$

$$\rho_{\mathrm{xy}} = \frac{(\sigma_h^2 R_h+\sigma_e^2 R_e)+\sigma_h^2\sigma_e^2 R_h R_e(R_h+R_e)B^2}{(\sigma_h+\sigma_e)^2+\sigma_h^2\sigma_e^2(R_h+R_e)^2B^2}B \tag{1.40}$$

where σ_i and R_i are the conductivity and Hall coefficient for each carrier. Taking the conductivities as $\sigma = n_i q_i \mu_i$ and the Hall coefficients as $R_i = 1/(n_i e)$. A simplification can be made if the system is compensated, where the total charge carrier densities add to zero (positive for holes, negative for electrons). For the two band compensated model with one hole-like and one electron-like carrier, $n_h = n_e = n$:

$$\rho_{\mathrm{xx}} = \frac{1+\mu_e\mu_h B^2}{e\, n(\mu_h+\mu_e)} \tag{1.41}$$

$$\rho_{\mathrm{xy}} = \frac{\mu_h-\mu_e}{e\, n(\mu_h+\mu_e)}B \tag{1.42}$$

Based on these equations for a two carrier compensated system, the longitudinal resistivity should have a quadratic field dependence, whilst the Hall resistivity is strictly linear in magnetic field. In this thesis, compensated two carrier and compensated three carrier models are used to investigate the behaviour of charge carriers in $FeSe_{0.82}S_{0.18}$, $FeSe_{0.96}S_{0.04}$ and $Fe_{1-x}Cu_xSe$ under pressure. The compensation removes one parameter in the model, but nevertheless even for a two carrier model the starting point for each variable is important.

Sometimes the two-band model used for ρ_{xx} can be simplified from equation 1.39 into a two parameter form to minimise the number of fit parameters as:

$$\rho_{xx} = \rho_0 + \frac{\alpha\mu_0 H^2}{1 + \beta\mu_0 H^2} \tag{1.43}$$

where α and β are functions of the carrier density and mobility of each carrier. From the forms of equation 1.41 and 1.42, it is clear that a linear field dependence of ρ_{xx}, or a non-linear H dependence for ρ_{xy} is not captured in the compensated two-band model. Deviations from this model may require investigations into the compensation or number of charge carriers, such as with a three carrier model [121, 122]. The next section introduces a different method to understand the number of charger carriers and their mobilities.

Mobility Spectrum

To further analyse the mobility of charge carriers mobility spectrum analysis is employed. This technique was first used for semiconductors by McClure [123] and Beck and Anderson [124], but recently has been used in semimetals [125, 126] and iron-based superconductors [127–130]. The method implemented by Humphries [129] and Huynh [127, 128] builds upon the work and ideas of Beck [124] using techniques from Krein and Ahiezer [131]. The conductivity is calculated by solving the Boltzmann equation in the relaxing time approximation, and subsequently using a Kronig-Kramer transformation to find the mobility spectrum as a function of mobility.

$$\hat{\sigma}(B) = \sigma_{xx} + i\sigma_{xy} = \int_{-\infty}^{\infty} \frac{s(\mu)(1 + i\mu B)}{1 + \mu^2 B^2} d\mu \tag{1.44}$$

where the mobility spectrum is $s(\mu) = e\, n(\mu)\, \mu$. This defines the carrier densities as a function of the mobility, note that hole-like carriers have $\mu > 0$, whilst electron-like carriers have $\mu < 0$. The spectrum therefore contains peaks at mobilities where carriers are most likely found. The mobility spectrum technique is used on the magnetoresistance of the longitudinal and Hall resistivities together to determine starting points for mobility fits (such as with equations 1.39 and 1.40) through

the number of carriers, and their respective mobility and carrier density. This method requires a sufficiently large separation of the hole and electron mobilities away from $\mu = 0$ for the resolution allowed by the magnetic field window of the measurements. To contribute to the conductivity and for well-defined peaks, it is also necessary that $\mu B \ll 1$ [126].

1.5 Quantum Oscillations

When placed in a magnetic field the k-space orbits are confined to planes perpendicular to the magnetic field. This restricts the quasiparticle orbits to quantised states that exist on concentric Landau tubes of constant energy, with the axis parallel to the applied magnetic field, see Figure 1.5. The area between the Landau tubes is quantised, so as the magnetic field strength increases, the tubes expand. As these tubes cross the Fermi surface at the chemical potential, the density of states fluctuates periodically. These periodical changes in the density of state are termed quantum oscillations, and can be measured in any property that couples to the density of states at the Fermi level. Examples include, but are not limited to, oscillations in resistivity (Shubnikov de-Haas effect, SdH), and magnetic susceptibility (de Haas-van Alphen effect, dHvA).

Landau Tubes

Quantum oscillations appear in measurements when an external magnetic field magnitude is varied. In a magnetic field charged particles experience the Lorentz force perpendicular to the applied field. If we consider an electron with momentum $\boldsymbol{p}$ in a magnetic field $\boldsymbol{B} = (0, 0, B)$, the Hamiltonian is:

$$\hat{H} = \frac{p_x^2}{2m_1} + \frac{(p_y + eBx)^2}{2m_2} + \frac{p_z^2}{2m_3} \tag{1.45}$$

Using that $p_y = \hbar k_y$, and $p_z = \hbar k_z$:

$$\hat{H} = \frac{p_x^2}{2m_1} + \frac{(\hbar k_y + eBx)^2}{2m_2} + \frac{\hbar^2 k_z^2}{2m_3} \tag{1.46}$$

$$\hat{H} = \frac{1}{2m}\left(p_x^2 + m^2\omega_c^2(x - x_0)^2\right) + \frac{\hbar^2 k_z^2}{2m_3} \tag{1.47}$$

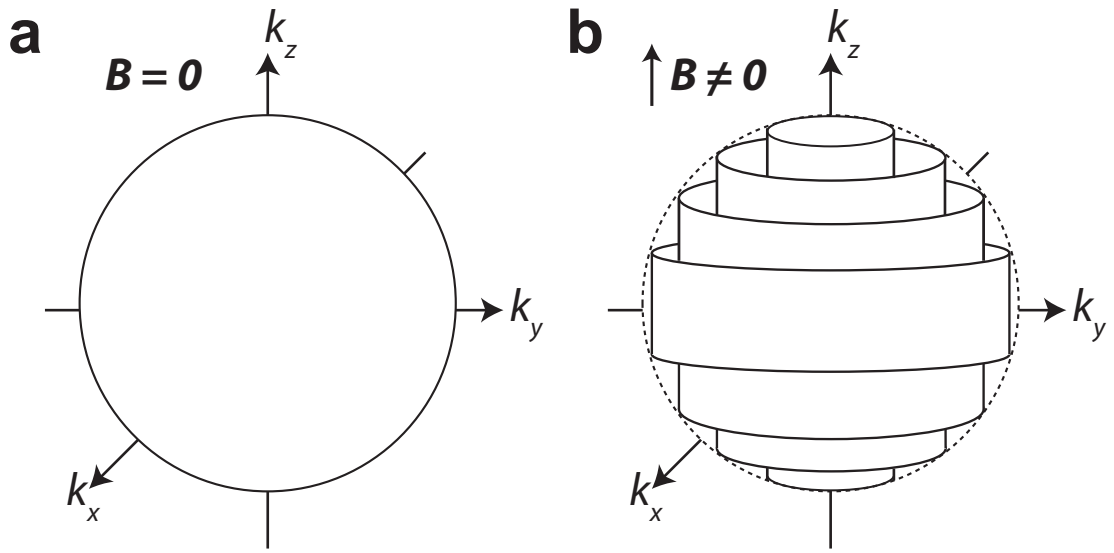

Figure 1.5: Landau Tubes. (a) A spherical Fermi surface of occupied states in the absence of an applied magnetic field. (b) Quantised energy states in an applied magnetic field ($B||k_z$), forming Landau tubes below the Fermi energy, for an example spherical Fermi surface.

where $m = m_1$, the cyclotron frequency $\omega_c = eB/\sqrt{m_1 m_2}$, and $x_0 = -\hbar k_y/eB$. This takes the classic form of a simple harmonic oscillator, with a shift in x by x_0 and 1D motion along $\hat{z}$. Therefore, the energy can be quantised to give:

$$E(n, B, k_{||}) = \hbar\omega_c(n + 1/2) + \frac{\hbar^2 k_{||}^2}{2m_3} \tag{1.48}$$

The electron motion due to the magnetic field then becomes helical, with the axis parallel to the magnetic field, **B**, with quantised energies. This confines the states into concentric cylinders parallel to the magnetic field in reciprocal space, with the allowed quantised energy levels called Landau levels. The difference in energy between each level, ΔE, is given by:

$$\Delta E = E(n+1, B, k_{||}) - E(n, B, k_{||}) = \hbar\omega_c = \hbar\Big(\frac{eB}{m^*}\Big) \tag{1.49}$$

Now, since the cyclotron frequency can be expressed in terms of an effective mass, m^*, which is given by the in-plane area $A(E, k_{||})$ through:

$$m^* = \frac{\hbar^2}{2\pi}\frac{\partial A(E, k_{||})}{\partial E} \tag{1.50}$$

then substitution of equation 1.49 into the above for m^* gives:

$$\frac{\hbar eB}{\Delta E} = \frac{\hbar^2}{2\pi}\frac{\partial A(E, k_{||})}{\partial E} \tag{1.51}$$

From here, the differential can be approximated as the difference in A and E between the n and $n+1$ levels, thus:

$$\frac{\hbar eB}{\Delta E} \approx \frac{\hbar^2}{2\pi}\frac{A(n+1, E, k_{||}) - A(n, E, k_{||})}{E(n+1, B, k_{||}) - E(n, B, k_{||})} \tag{1.52}$$

Noting that $\Delta E = E(n+1, B, k_{||}) - E(n, B, k_{||})$, this then gives the quantised areas of orbits in reciprocal space as:

$$A(n, E, k_{||}) = \frac{2\pi eB}{\hbar}(n + \lambda) \tag{1.53}$$

and the difference in area between adjacent Landau tubes as:

$$\Delta A(E, k) = \frac{2\pi eB}{\hbar} \tag{1.54}$$

where λ is a fixed phase. Figure 1.5a shows an example of the allowed energy states in zero magnetic field for a spherical Fermi surface. Figure 1.5b shows the Landau tubes of allowed energy states in a magnetic field. For the n^{th} Landau tube, as B increases, the area will increase until $A = A_{\text{F}}$ where that tube passes through the Fermi surface. This will lead to oscillations that are periodic in $1/B$, with a frequency, F:

$$F = \frac{1}{\Delta(1/B)} = \left(\frac{1}{B_{n+1}} - \frac{1}{B_n}\right)^{-1} = \frac{\hbar}{2\pi e}A \tag{1.55}$$

This is known as the Onsager relation, relating the frequency of quantum oscillations to the Fermi surface area [132, 133]. Extending the treatment to non-spherical Fermi surfaces, then as B increases, the Landau tubes will cross the E_{F} for different B at different points in reciprocal (k-) space. Integrating over the contributions from all $k_{||}$ in the first Brillouin zone results in destructive interference of all contributions, except for the orbits of extremal area (minimum and maximum) which will have a net contribution. The quantum oscillations are a direct measure of the cross-sectional area of the extremal areas of the Fermi surface perpendicular to the applied magnetic field, for closed orbits. By varying the angle of the applied field, the Fermi surface shape can be investigated further. There will be a contribution to the oscillatory signal from the extremal orbits of each Fermi surface to create a superposition of various frequencies, amplitudes and phases.

1.5.1 Lifshitz-Kosevich Formalism

The Lifshitz-Kosevich equation has been developed to be able to extract relevant parameters from quantum oscillations. A brief description follows of the general form of the equation, followed by the relevant damping terms and the electronic properties revealed by each term.

The grand thermodynamic potential of a system with chemical potential μ is given by the Lifshitz-Kosevich equation [133]:

$$\begin{aligned}\tilde{\Omega} = \frac{e^{5/2}VB^{5/2}}{2^{3/2}m_e\hbar^{1/2}\pi^{7/2}} \sum_{\text{orbits } i} \left|\frac{\partial^2 A_{k,i}}{\partial k_\parallel^2}\right|^{-1/2} \\ \sum_{p=1}^{\infty} p^{-5/2} R_T R_D R_S \cos\left[2\pi p\left(\frac{F_i}{B} - \frac{1}{2}\right) \pm \frac{\pi}{4}\right].\end{aligned} \tag{1.56}$$

The first sum extends over all extremal Fermi surface areas $A_{k,i}$ perpendicular to the applied field, and is referred to as the curvature factor. The second sum runs over the harmonics p of each fundamental oscillation frequency. The prefactors include various damping terms, R_T, R_D and R_S. The $\pm\pi/4$ phase arises in three-dimensional Fermi surfaces. The curvature factor $((\frac{\partial^2 A}{\partial k_{||}^2})^{-1/2})$ will be small for an extremal orbit where the Fermi surface area hardly changes. In that case, many more states will contribute to the orbit amplitude than an orbit with a sharply changing area.

Shubnikov-De Haas Oscillations

Strictly speaking, as transport is not a thermodynamic probe oscillations in the resistivity cannot be derived from the free energy. Oscillations of the conductivity (resistivity) are a result of oscillations in the density of states. This can be derived by considering the contributions from 2D slices of k-space and if the energy of that Landau level is above or below a certain energy. An indepth explanation is available in Shoenberg's book [133], and a full derivation from Adams and Holstein [134]. The result of this experssion is that the oscillatory part of the density of states is proportional to that of the contribution to the grand thermodynamic potential [133]:

$$\tilde{D}(\zeta) \propto \frac{\mathrm{d}\tilde{M}}{\mathrm{d}B} \propto \frac{\mathrm{d}}{\mathrm{d}B}\left(\frac{\mathrm{d}\tilde{\Omega}}{\mathrm{d}B}\right) \tag{1.57}$$

where $\tilde{D}(\zeta)$ is the oscillatory part of the density of states at the Fermi energy, ζ, and $\tilde{M}$ is the oscillatory magnetic moment. Hence, the form of the density of states can be found form the grand thermodynamic potential. The density of states is still affected by both level broadening (R_D) and spin splitting (R_S) but not by thermal damping (R_T) as that does not affect the states but only the occupation distribution. As such, the full density of states is:

$$\begin{aligned}\tilde{D}(\zeta) = \left(\frac{2eB}{c\hbar}\right)^{1/2} \frac{mV}{\pi^{3/2}\hbar^2} \sum_{\text{orbits } i} \left|\frac{\partial^2 A_{k,i}}{\partial k_\parallel^2}\right|^{-1/2} \\ \sum_{p=1}^{\infty} p^{-1/2} R_D R_S \cos\left[2\pi p\left(\frac{F_i}{B} - \frac{1}{2}\right) \pm \frac{\pi}{4}\right]\end{aligned} \tag{1.58}$$

The full oscillatory resistivity of a multi-band system will be complex with contributions from each Fermi surfaces. The conductivity can be estimated from the relation [133]:

$$\frac{\tilde{\sigma}}{\sigma} \sim R_T \frac{\tilde{D}(\zeta)}{D_0(\zeta)} \tag{1.59}$$

where the oscillatory part of the conductivity is $\tilde{\sigma}$, and D_0 is the total density of states for all sheets of the Fermi surface and $\tilde{D}(\zeta)$ only refers to one sheet. The thermal damping, R_T, affects the conductivity directly, not the density of states. Considering a spherical Fermi surface, one can find [133]:

$$\begin{aligned}\frac{1}{R_D R_S}\frac{|\tilde{D}(\zeta)|}{D_0(\zeta)} &= \left(\frac{eB}{c\hbar k_F^2}\right)^{1/2} \\ &= \left(\frac{\pi eB}{c\hbar A}\right)^{1/2} \\ &= \left(\frac{B}{2F}\right)^{1/2}\end{aligned} \tag{1.60}$$

Now, by combining equations 1.59 and 1.60 the amplitude of oscillations of each orbit, A_i, can be expressed as:

$$A_i \sim A_i^0 R_{T,i} R_{D,i} R_{S,i} \left(\frac{B}{2F_i}\right)^{1/2} \tag{1.61}$$

where A_i^0 is an overall amplitude term. Therefore, the normalised oscillatory resistivity includes the above amplitude expression with the $\cos(f(F))$ term (with

a single phase δ_i to capture the non F dependent terms), with contributions from each orbit:

$$\rho_{\text{osc}} \propto \sum_i A_i^0 R_{T,i} R_{D,i} R_{S,i} \left(\frac{B}{2F_i}\right)^{1/2} \cos\left(2\pi \frac{F_i}{B} + \delta_i\right) \tag{1.62}$$

where the sum is over different Fermi surface orbits.

1.5.2 Landau Fan Diagrams

Next, we will briefly discuss methods to determine the frequencies in the quantum oscillations. For transport, the resistivity will contain a contribution from both the background and the oscillatory signal. To isolate the oscillatory signal, the background signal is approximated with a polynomial. This typically uses the low field dependence, where the oscillations amplitude are negligible, and extrapolating to higher fields where the oscillations are large. Once the oscillatory signal is isolated, one can attempt a direct fitting to equation 1.62, encompassing the damping terms, number of extremal orbits and correct powers to model the precise oscillatory signal[1]. A second method takes the oscillatory signal and applies a fast Fourier transform (FFT) to produce a frequency spectrum. A third technique uses a Landau fan diagram, assigning the minima and maxima to Landau levels with index, n, to plot $1/B$ against n. The positions of the Landau levels with the minimum and maximums in field can then be fitted such that: $n = c_1/B + c_0$, where the frequency $F = c_1$. This technique works well for a single dominating frequency, although for two closely spaced frequencies a beat pattern may still be visible.

1.5.3 Damping Terms

The next several sections expand on the damping terms in the Lifshitz-Kosevich equation (Equation 1.58), and the quasiparticle parameters that can be extracted from each term.

[1]Not recommended if the signal contains several frequencies as there will be too many variables to constrain.

Temperature Damping Factor

As discussed earlier, the oscillations were assumed at $T = 0$, and the first damping term arises from thermal effects. At $T = 0$ the Fermi-Dirac distribution (equation 1.63) of the quasiparticles would be a perfect step function at the Fermi energy, whereas at any non-zero temperature a distribution of occupied energies will develop over a range given by $k_{\mathrm{B}}T$. Figure 1.6a shows the broadening effect as the temperature increases for a given chemical potential, μ.

$$n_{\mathrm{i}} = \frac{1}{e^{(\epsilon_{\mathrm{i}}-\mu)/k_{\mathrm{B}}T}+1} \tag{1.63}$$

At non-zero temperature, the Fermi surface is no longer a single well defined separation between occupied and unoccupied states. Therefore, each occupied energy level corresponds to a slightly different frequency, which from integration over all occupied energy levels at a particular temperature will result in a reduced total amplitude. The thermal damping, R_{T}, is given by:

$$\begin{aligned} R_{\mathrm{T}} &= \frac{\chi}{\sinh(\chi)} \\ \chi &= \frac{2\pi^2 k_B T\, p m^*}{e\hbar B} \end{aligned} \tag{1.64}$$

where m^* is the quasiparticle effective mass that is renormalized by both electron-electron and electron-phonon interactions, and p is the p^{th} harmonic. Thermal damping is large when the thermal broadening is at least comparable to the energy difference between Landau levels, this is minimised with low temperatures and high magnetic fields ($\chi \propto T/B$) and is where oscillations are best observed. The only temperature dependence of the resistivity oscillations, equation 1.61, is contained in R_{T}. Thus, by fitting the temperature dependence of the amplitude of a frequency to equation 1.64 at a fixed field, the quasiparticle effective mass, m^* can be extracted. Figure 1.6b is an example of the damping rate for various effective masses. For lighter masses, around $1m_e$, the amplitude will persist appreciably up to around 4 K, whilst for heavier masses lower temperatures are required to follow the amplitude decrease with temperature.

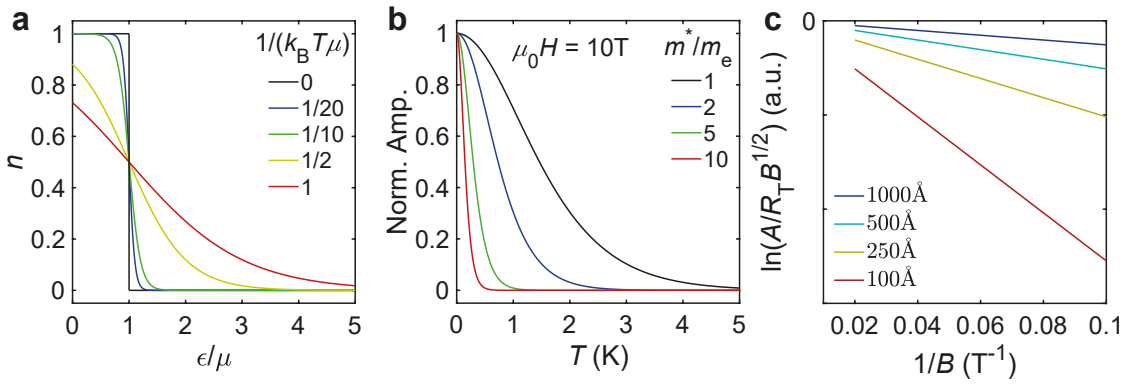

Figure 1.6: Damping effects in quantum oscillations. (a) The Fermi-Dirac distribution (equation 1.63) shown at increasing temperatures from $T = 0$. (b) The thermal damping effect on amplitude due to increased effective masses, m^*, according to equation 1.64. (c) A Dingle plot of the log of the amplitude against inverse field for several example mean free paths, ℓ, according to equation 1.67.

Impurity Scattering Factor

The second damping term is the Dingle term R_D which arises from impurity scattering of the electrons. As the electrons have a finite relaxation time, the quantum levels are broadened into Lorentzian distributions with a finite width. Similar to the thermal damping, this broadening reduces the amplitude of any quantum oscillations. As before, a spread of frequencies F are found for a spread of Fermi energies. The resulting damping is given by:

$$R_{\mathrm{D}} = \exp\left(-\frac{\pi p m_b}{eB\tau}\right) = \exp\left(-\frac{2\pi^2 p m_b k_B T_D}{e\hbar B}\right), \tag{1.65}$$

where τ is the scattering time, m_b is the band (cyclotron) mass, and $T_D = \hbar/2\pi k_B\tau$ is the Dingle temperature. For free electrons we can use the fact that $m_b v_F = \hbar k_F$ and $\ell = \tau v_F$ in equation 1.65 to relate the damping term to the mean free path, ℓ. Therefore, using the Onsager relation and if a circular orbit is assumed: $A_i = \pi k_F^2 = \frac{2\pi eF}{\hbar}$

$$R_{\mathrm{D}} = \exp\left(-1140\frac{\sqrt{F}}{\ell B}\right) \tag{1.66}$$

where the frequency, F, is in Tesla and the mean free path, ℓ is in Angstroms. Additionally, damping is more significant for larger orbit sizes.

From this term one can determine the scattering time of an orbit by analysing the amplitude. Using 1.61, we can rearrange for the B and T dependence and take the logarithm to find this relationship:

$$\ln\left[A\left(\frac{1}{B^{1/2}R_{\mathrm{T}}}\right)\right] = \ln\left[R_{\mathrm{D}}\right] + \text{constants} \tag{1.67}$$

where χ is as defined in equation 1.64, and A is the oscillation amplitude. The constant terms are collected together. Therefore, using the exponential form of the Dingle damping term from equation 1.66 the mean free path ℓ can be found from the slope of a linear fit of equation 1.67 against inverse magnetic field. An example of the effect of varying the mean free path on the so called Dingle plot is shown in Figure 1.6c. This method is used in Chapter 5.

Spin Splitting Factor

Finally, for completeness, the spin splitting factor R_{S} accounts for the Zeeman splitting of Landau levels. In a magnetic field, the spin degeneracy of energy levels is lifted as they change in energy by $\pm\frac{1}{2}g\mu_B B$, where g is the spin splitting factor and μ_B the Bohr magneton. For free electrons, $g \simeq 2$. Over a full oscillation this energy difference is equivalent to a phase difference $2\pi\Delta E/(\hbar\omega_c)$ between the spin up and spin down electrons. The superposition of the two orbits leads to a reduction in the amplitude by a factor R_{S}:

$$R_{\mathrm{S}} = \cos\left(\frac{p\pi g m_s}{2m_e}\right) \tag{1.68}$$

where m_s accounts normally for renormalization by electron-electron interactions, but not electron-phonon interactions like the effective cyclotron mass term in the thermal damping term, R_{T}. The spin mass is angle dependent, and this induces the notion of 'spin-zeros' where the oscillation amplitude goes to zero for a particular angle such that m_s/m_e is an odd integer. This term is both temperature and magnetic field independent, and angular dependence is required to learn about the value of gm_s. Hence, this may become an avenue of research in the future with rotatable pressure cells to explore the particularly high-T_{c} regions of iron-based superconductors under pressure.

As we know, it is the extremal orbits perpendicular to the applied magnetic field on a Fermi surface that are picked up in quantum oscillations. Therefore, even for a Fermi surface that is nearly spherical, the angular dependence of the oscillations can be used to learn more about the exact Fermi surface shape, dimensionality and distortions. However, angular dependence in pressure cells in high magnetic fields at low temperatures was not possible with the pressure cell used extensively in this thesis. For many surfaces, especially distorted cylinders, as the angle between the axis of the Fermi surface and the applied magnetic field increases, the area of the maximal and minimal orbits will tend towards each other. The angle at which the maximal and minimal orbit areas are equal is the Yamaji angle. At the Yamaji angle, a peak in the resistivity arises due to a minimum in the conductivity as the curvature of the Fermi surface is minimised.

Other damping contributions

Further damping contributions can arise, but in the circumstances here are negligible. One contribution could be field inhomogeneity, leading to phase smearing, if the value of the applied magnetic field varies across the area of the sample. This effect is given by $R_{\Delta\mu_0 \mathrm{H}} = \sin(\lambda)/\lambda$, where $\lambda = \pi p F \Delta\mu_0 H/(\mu_0 H)^2$ [133]. Thus, this factor is minimal if $\Delta\mu_0 H \ll (\mu_0 H)^2/\pi p F$. For a orbit with $F = 200\,T$, in the 41.5 T resistive magnet in Tallahassee measuring at 20 T (the lower range where the quantum oscillations are observed in these systems) then $\Delta\mu_0 H \ll 0.159\,\mathrm{T}$. For this magnet, the field homogeneity is far greater, with $\Delta\mu_0 H = 0.028\,\mathrm{T}$ at 20 T when 1 cm away from the field centre for the 41.5 T resistive magnet, and thus this effect can be counted as negligible here [135].

2

Experimental Methods and Techniques

This chapter presents details about the experimental methods employed for the work presented in this thesis. Firstly, I will discuss the principles of the transport measurements, related to the steps involved in the preparation and the measurement of the electrical resistivity, and the concepts of the resistivity tensor in magnetic fields. Secondly, I introduce details of the two types of pressure cells: the piston cylinder cell suitable for low pressure experiments, and anvil cells capable of reaching higher pressures. Thirdly, I will discuss the different systems used to measure the samples at low temperatures and high magnetic fields in these experiments. Finally, I will briefly introduce other techniques used sometimes for complementary studies, or to characterise the quality and suitability of samples to be used in measurements.

2.1 Transport Measurements

2.1.1 Sample Preparation

The single crystals used in measurements for this thesis were grown in Oxford by Shiv Singh and Amir-Abbas Haghighirad via the $KCl/AlCl_3$ chemical vapour transport method [101, 102]. The typical size of crystals in transport measurements was from 250 to 2000 μm by 100 to 500 μm by 10 to 100 μm. The crystals grow with the thickness aligning with the c axis, and the plane corresponds to the ab plane.

Crystals were cut to thin cuboidal shapes, to provide cleaner surfaces for electrical contacts, or to fit inside measurement spaces, and to allow a good understanding of the distances between contacts for resistivity conversions.

Typical samples have resistivity values of $<1\,\mathrm{m\Omega cm}$ at room temperature, and as the crystals are small the measured resistances are small. Therefore the standard four-point technique is used to measure a small resistance. An alternating current is passed down a wire to the sample, across a contact between the wire and sample, through the sample itself, onto a second contact and finally down a second wire back to the measuring instrument. If just two contacts measure both the current and voltage then the wire and contact resistances would dominate the signal. By using four wires, two for current and two for voltage, the measurement is isolated to the resistance of the sample. The alternating current is applied to the sample through the current contacts covering the ends of the sample, and the potential difference between the two voltage contacts is measured using a lock-in amplifier. The current is passed through the lock-in amplifier to determine the frequency. As the signals are small on a large background, from wires of several metres passing from the instruments to the bottom of the cryostat and back, the lock-in amplifier measures only the signal with the input frequency, removing any noise. The wires used between the sample and the instruments are twisted together in pairs (current wires together, voltage wires together), such that the overall magnetic field around the pair of current carrying wires is cancelled out.

As both longitudinal and Hall resistivities were of interest, typically measurements were taken in a 5 point configuration. Figure 2.1 shows an example configuration, with a spare (6th) contact. Contacts are made using indium solder with the soldering iron at 230°C. As measurements are measuring in the conducting Fe-plane, along the *ab* plane, contacts cover the sides of the sample as opposed to the top or bottom. The wires are either gold (25μm thick) or platinum (15 or 10μm thick), with the latter favoured for the pressure experiments due to its malleability. To enable safe movement of prepared samples to different probes and for storage, samples were prepared on quartz pieces. This allows the wires to be anchored at the

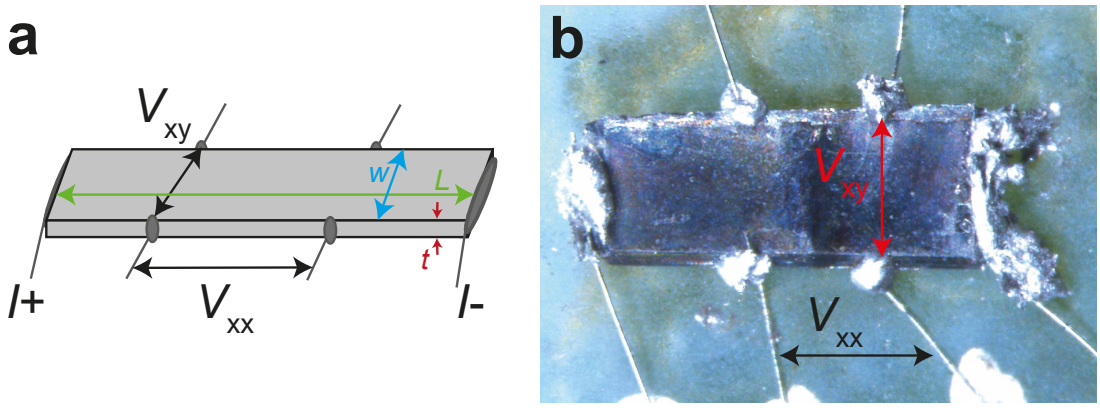

Figure 2.1: Transport measurements of single crystals. (a) A schematic and (b) an example of the contact configuration of a single crystal for a transport measurement. All contacts short circuit the layers of the crystal by covering the full thickness. Each current contact covers fully an end of the crystal. The longitudinal voltage contacts are on one side of the crystal, and the Hall voltage contacts are opposite each other. One contact would typically be used simultaneously in both the longitudinal and Hall voltage measurements.

edge of the quartz with a drop of silver paint, making it easier to solder the wire to the sample without the wire moving. Whilst early samples were stuck to the quartz piece using Loctite Double Bubble Epoxy, the majority of samples in this work were never stuck to a quartz piece. This allows transfer into a pressure cell without damaging the sample, and removes the risk of induced strain effects from the epoxy. The voltage contacts were ensured to cover the full height of the sample, and current contacts cover the entire area of the end of the sample. Due to the weak van der Waals forces between the layers, the inter-layer resistance can be quite large, and this method short-circuits the conducing layers to only prove the in-plane signal (ρ_{ab}).

The resistance ($R = V/I$) measured is converted to resistivity using the standard formula $\rho = RA/l$, where A is the cross sectional area between the two voltage contacts, perpendicular to the current path, and l is taken as the minimum distance between the contacts. However, the sample is not typically a perfect cuboid, and so distances would be averaged for the thickness (t), width (w) and lengths (L). For the longitudinal resistivity the conversion from the measured (symmetrised) resistance is: $\rho_{xx} = R_{xx}(wt/l_{xx})$, where l_{xx} is the minimum distance between the two finite sized voltage contacts parallel to the current path. Similarly, for the Hall resistivity the

conversion from the (anti-symmetrised) resistance is: $\rho_{xy} = R_{xy}(Lt/l_{xy})$, where L is the length of the sample, and l_{xy} is the distance between the contacts perpendicular to the current path and often taken as w. Additionally, an error in the absolute value of resistivity comes from errors in the value of the thickness, width, and distance between contacts added in quadrature, and found to be typically between 10 to 15% of the absolute resistivity.

The resistance of samples was measured using lock-in amplifiers, usually a Stanford Research Systems SR830. Typically, the current was supplied from a Keithley 6221 AC/DC current source with an alternating current of up to 2 mA RMS, at a low frequency in the range of 10 to 40 Hz (avoiding integer fractions of 50 Hz[1]), to maintain a low impedance and a frequency independent resistance. Alternatively, when a separate current source was not available, the current was provided by the SR830 through its voltage source and a resistor of approximately 1 kΩ to produce a current on the order of 1 mA. Low noise transformers (Princeton Applied Research 1900 low noise transformers) were used to increase signal sizes and match the low impedance of the measured samples to the higher impedances of the lock-in amplifiers. The gain factor from each transformer was set to 100, but was verified at room temperature to calculate the actual gain factor, which was typically around 99.

There are three electronic phase transitions that are defined consistently in this work. The superconducting phase is characterised in transport by the zero resistivity. Figures 2.2a and b show how the transition temperature can be defined in multiple ways: the onset temperature, T_{on}, the midpoint temperature, T_{mid}, the offset temperature, T_{off}, and at absolute zero resistance, T_0. The midpoint temperature is defined through the peak of the derivative, although for superconducting transitions which are not smooth this can be poorly defined. A linear fit is applied through the transition, and a second linear fit for temperatures a few K above the superconducting transition. The intercept between these two lines is taken as T_{on}. The offset, T_{off}, can be defined through the intercept of the linear fit through the superconducting transition, with zero resistivity. The final

[1]The frequency of UK mains supply.

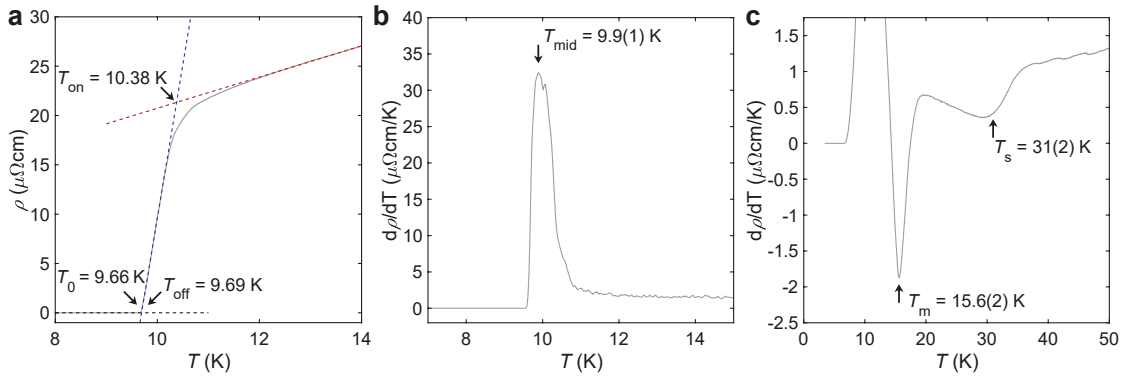

Figure 2.2: Transition definitions in transport. (a) Resistivity temperature dependence through the superconducting transition. Linear fits above (red, dashed) and through (blue, dashed) the superconducting transition, used to define T_{on} and T_{off}. T_0 is defined as the highest temperature at zero resistance. (b) Derivative of (a), used to define T_{mid} from the peak. (c) The structural transition T_{s} is defined through linear fits around the minimum in the derivative, the error is such to include the actual position of the minimum. Likewise, the magnetic transition T_{m}, is also defined through the minimum in the derivative.

definition is the highest temperature where the resistivity is absolute zero, given as T_0. Typically the absolute zero transition temperature is used in this thesis. Except in Chapter 5 where, due to the inconsistent rounding for the final ∼10% of the superconducting transition at different pressures, the extrapolated offset value T_{off} is used. Additionally, other transitions are defined through the derivative of the resistivity, either using the minimum or the maximum, see Figure 2.2c.

Multiple crystals were screened to identify high quality single crystals before measurements in high magnetic fields and under applied pressure. Crystals would be chosen based on the (relative) superconducting transition width, superconducting critical temperature, and the residual resistivity ratio, defined as:

$$RRR = \frac{\rho(300\,\mathrm{K})}{\rho(T_{\mathrm{on}})} \tag{2.1}$$

In non superconducting systems, it is usual to take the ratio as the resistivity at room temperature (300 K or so) to that extrapolated at 0 K. However, in superconducting systems the resistivity at the onset of superconductivity is used for a more consistent measure of sample qualities when comparing crystals of similar systems. It should be noted that ρ_0 can be estimated using measurements in high magnetic fields to suppress superconductivity to base temperature, and then extrapolate the resistivity

temperature dependence to 0 K. However, as T_c increases, stronger magnetic fields are required to suppress superconductivity to base temperature, and thus estimating ρ_0 accurately becomes harder and more inaccurate. A system with a larger residual resistivity indicates more impurity scattering, and therefore a lower RRR.

2.1.2 Magnetotransport measurements

In principle, with point like voltage contacts and perfectly aligned contacts, both the longitudinal and Hall voltage magnetic field dependence could be accurately measured with one magnetic field measurement. However, there is often a non-zero contribution from both ρ_{xx} and ρ_{xy} in either voltage measurement. In order to isolate the longitudinal ρ_{xx} and Hall ρ_{xy} components of the resistivity tensor in magnetic field sweeps, one must either symmetrise (equation 2.2) or anti-symmetrise (equation 2.3) using data from measurements performed at the same temperature using both positive and negative magnetic fields.

$$\rho_{xx} = \frac{1}{2}\Big[\rho(\mu_0 H > 0) + \rho(\mu_0 H < 0)\Big] \tag{2.2}$$

$$\rho_{xy} = \frac{1}{2}\Big[\rho(\mu_0 H > 0) - \rho(\mu_0 H < 0)\Big] \tag{2.3}$$

This is because the Hall effect will reverse if the magnetic field direction is reversed (as it is antisymmetric with respect to magnetic field), whereas the longitudinal contribution will be symmetric. Figure 2.3 shows an example of (a) the raw resistance in positive and negative magnetic fields, which is then (b) symmetrised and (c) anti-symmetrised to isolate R_{xx} and R_{xy} respectively. To convert from resistance to resistivity, one must be careful in ensuring the values of A and l in $\rho = R\,A/l$ are accurate for that contact configuration and component (See Figure 2.1). In theory, with $H||c$, the longitudinal resistivity may not need to be measured in both positive and negative polarity, provided there is a minimal Hall contribution. When $H||(ab)$, the Hall contribution is zero, as the magnetic field and electrical current are parallel to each other, and measurements need only be taken in one polarity.

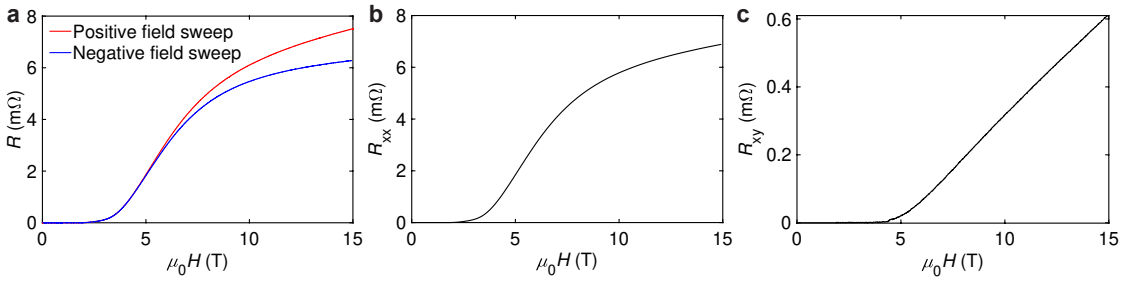

Figure 2.3: Isolating resistivity components in high magnetic fields. An example of isolating the mixed R_{xx} and R_{xy} components in high magnetic fields for a single crystal of $Fe_{1-x}Cu_xSe$, $x = 0.0025$, at 17 kbar and 12 K. (a) The resistance measured in two opposite magnetic field orientations defined as positive and negative. (b) R_{xx} and (c) R_{xy} field dependence from symmetrising and anti-symmetrising the curves from (a). Conversions to resistivity can be made using the correct conversion factors for that particular component, with A being the cross-sectional area perpendicular to the component in question ($\rho = RA/l$).

2.1.3 Local resistivity exponent

One model for the resistivity in metals at low temperatures is Fermi liquid theory, which describes interacting fermions (as discussed in Chapter 1), from which the resistivity should have a quadratic temperature dependence. Therefore, it is useful to calculate the resistivity exponent as a function of temperature, especially for regions which display non-Fermi liquid-like behaviour. In order to extract information about the deviation from the Fermi liquid behaviour one can consider the resistivity to be of the form:

$$\rho(T) = \rho_0 + AT^n \tag{2.4}$$

where n is the local resistivity exponent, and ρ_0 the resistivity at $T = 0$ K. This can be rearranged to isolate n by taking the logarithm of the equation and using the multiplicative and exponential property of logarithms to separate A and T^n:

$$\ln(\rho(T) - \rho_0) = \ln(A) + n\ln(T) \tag{2.5}$$

By taking the derivative with respect to $\ln(T)$ and rearranging, we are left with:

$$n = \frac{\mathrm{d}[\ln(\rho(T) - \rho_0)]}{\mathrm{d}\ln(T)} \tag{2.6}$$

The crux in this method is determining ρ_0, which can heavily influence the calculated values of n, especially for small resistivities (clean metallic systems).

For superconducting systems, the accessible normal state is only available down to the onset of superconductivity. By using high magnetic fields at fixed temperatures below the superconducting transition temperature, the superconductivity can be suppressed to reveal the low temperature-high field normal state. Extrapolations are then made from the high field regime to determine a normal state resistivity value at fixed low temperatures. Ideally, these will be with $H||(ab)$ with a linear extrapolation, although the anisotropic upper critical field ($\mu_0 H_{c2}^{ab} > \mu_0 H_{c2}^{c}$) in these systems then requires very high magnetic fields. Finally, the extrapolated low temperature resistivities can be used with a form of equation 2.4 to estimate ρ_0.

2.2 Pressure Techniques

There are many different pressure cell designs available to achieve high pressure in hydrostatic conditions. I will discuss piston cylinder cells, used extensively in the work presented throughout this thesis, and anvil cells, in which I was involved in the stages of the preparation of, and I performed measurements on prepared cells for TDO measurements used in other studies.

2.2.1 Piston Cylinder Cells

Piston cylinder cells derive their name from the mechanism used to increase and maintain hydrostatic pressure. Figure 2.4a is a schematic of the pressure cell used for measurements performed in Oxford, which constitute the main results of Chapters 4-6. At the centre of the pressure cell is the sample space. Wires connect the samples inside the cell to the outside instruments. The sample space is enclosed by a Teflon cap, a BeCu anti-extrusion ring, and a feedthrough. The feedthrough passes any wires out of the sample space, and is filled with stycast to seal the sample space and secure the wires. At the base of the pressure cell is a backup to the feedthrough and a backing nut to lock the bottom of the cell securely, with a hole for wires to extend out of the cell, to the probe and instruments. A second BeCu anti-extrusion ring is placed between the top of the Teflon cap and the first tungsten carbide piston,

followed by a backup disc on top of the piston. The backup disc is recessed in the top nut that can screw into the cell body to lock the system in at a certain pressure.

To change the pressure, a hydraulic press is used with a pressurising piston and backup to squeeze the Teflon cap and reduce the volume of the pressure cell. Reducing the volume increases the pressure inside the Teflon cap, and the pressurising medium ensures homogeneous hydrostatic pressure conditions throughout the sample space. The top nut is used to ensure the piston and backup are locked in place when the hydraulic press pressure is removed. The pressure can be estimated from the load applied by the press by comparing the cross-sectional areas of the hydraulic press and the sample space ($P = F/A$).

The pressurising medium should be chosen depending on its hydrostaticity limit, the maximum pressure of the cell itself, any discontinuous pressure jumps through solidification and any potential reactions with samples being measured. To this end, Daphne oil 7373 was used in pressure experiments in Oxford, whilst Daphne oil 7575 was used in Tallahasee. Both remain hydrostatic in the pressure range being measured (up to 21 kbar and 22 kbar respectively) [136, 137]. Additionally, there is no discontinuous pressure drop through solidification, which can risk damaging the sample [138]. For pressure experiments to higher pressures, pressurising mediums with a higher hydrosatic limit are required, such as glycerol, nitrogen (gas), argon (gas), or 4:1 Methanol:Ethanol [139, 140].

The careful preparation of all aspects for piston cylinder cells is paramount to ensuring the safety and longevity of the cell, especially at higher pressures. The feedthrough plugs the sample space shut, and passes wires from inside the sample space to the outside instruments, such as copper wires or fibre optic wires. The stycast used to fill feedthroughs was stycast 2850 FT with catalyst 24LV. Typically ~ 6 g would be prepared in the ratio (by weight) of 100:8 to ensure sufficient volume to mix evenly. The feedthrough, with wires, was placed on to a pump chamber as mixed stycast 2850 FT (with catalyst 24LV) was applied to the top of the feedthrough. The wires are pushed through the feedthrough slightly at this point to pull the stycast in to the feedthrough central hole, and pumping on this removes

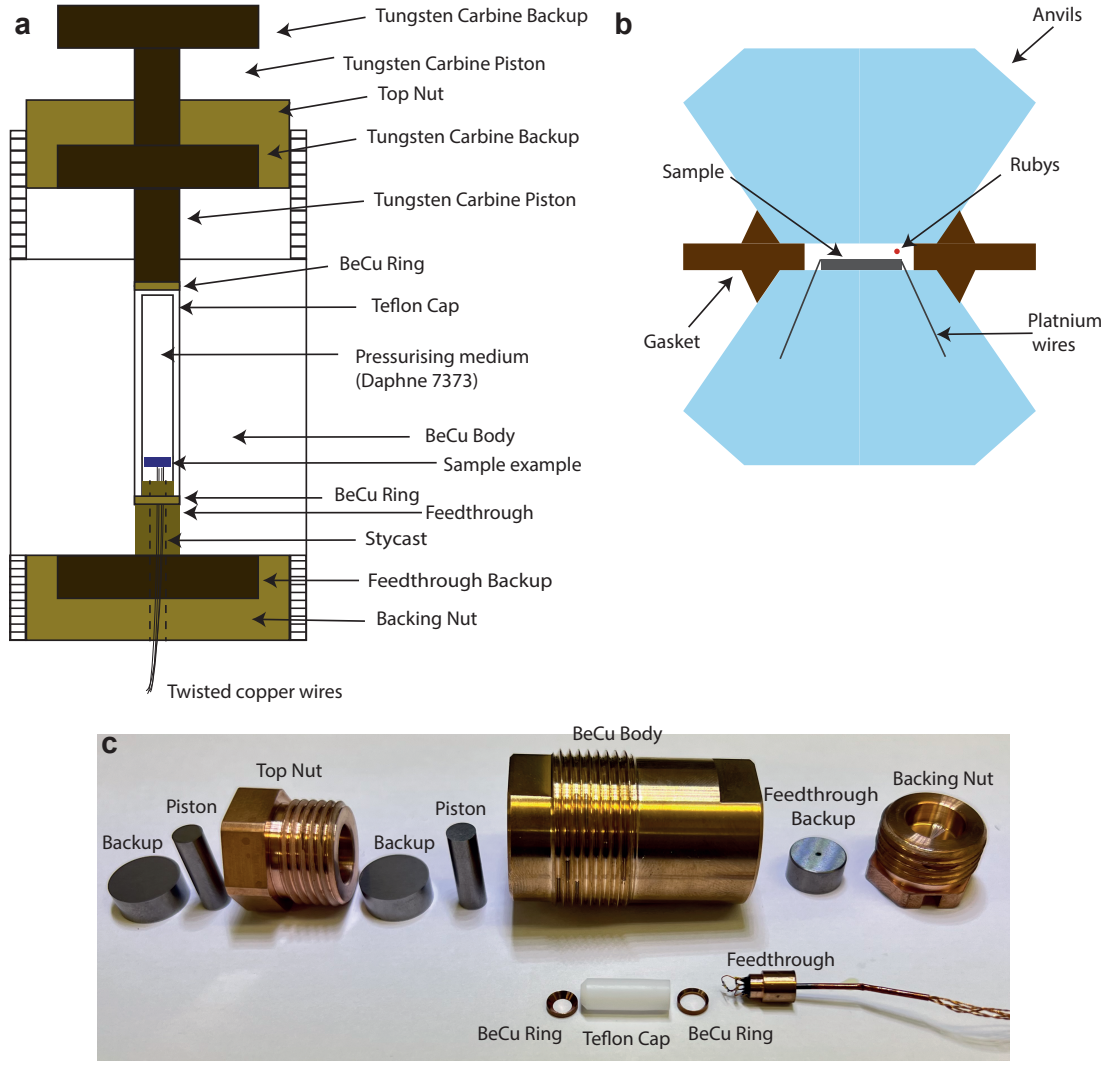

Figure 2.4: Pressure cell diagrams. Schematic cross sectional views of a (a) piston cylinder cell and (b) anvil cell. The sample space diameter for the piston cylinder cell is around 2 mm, with a height available of a few cm. For the anvil cells, the diameter available is typically around 250-300 μm, with a height of around 80 μm. (c) An exploded view of the Quantum Design piston cylinder cell used in Oxford with all components labelled.

any air pockets and ensures the stycast fills and seals this space. During this, one must ensure the insulation of the wires is not scratched, which can short the wire(s) to the cell body. The sealant is then cured at room temperature for >24 hours. It can be advantageous to protect the wires where they leave the stycast with tubing to prevent breakages during the cell preparation.

In this thesis, work is presented from seven piston cylinder cell pressure experi-

ments. Five of these used a commercially available Quantum Design pressure cell in Oxford. The other two were measured at the National High Magnetic Field laboratory in Tallahassee, one to 45 T, and the other 41 T. Further efforts were made on a different piston cylinder cell in Oxford in an attempt to measure crystals from the same batch with transport and TDO simultaneously, and the pressure verified with a ruby, but no results are presented from this work.

2.2.2 Anvil Cells

In order to achieve pressures above a few GPa the cell must be scaled down, and the material strength increased. Thus, anvil cells are used to reach higher pressures of tens to hundreds of GPa. These are often moissanite (more readily available), or for the highest pressure, diamond anvils. A schematic of an anvil cell is shown in Figure 2.4b.

The sample space is formed between the two flat and parallel culets of diamond anvils, and walled by a gasket, typically made of heat-hardened BeCu. The sample space is filled with a pressurising medium and the samples to be measured. The gasket must first be indented to sit neatly between the two diamond anvils. This requires placing the fresh gasket between the anvils and slowly increasing the applied load to squeeze the gasket. The gasket will flow outwards and the area between the anvils will decrease, increasing the pressure. A thinner gasket is capable of reaching higher pressures before deforming too much and the sample space increasing past the culet diameter. The maximum pressure depends also on the position of the sample space, gasket material, culet size and the sample space size. Next, the centre of the indented region is drilled to between 1/3 and 1/2 of the diameter of the culets, and the drilled hole cleaned of any scraps. If using BeCu, the gasket must be heat hardened at 325°C for 15 minutes.

Insulation is required on the gaskets to prevent the wires being shorted to the gasket and cell body. Insulation was prepared using stycast 1266 (28:100 of parts B:A as per manufacturers instructions), which is chosen as it is transparent, whereas the black stycast 2850 FT is perfectly suitable for piston cylinder cells, allowing some

visibility of the pre-drilled hole on the gasket later in the preparation process. The mixed stycast is used fresh, so as to be very runny, when it is mixed with Alumina power in the ratio 57:43 (Alumina powder:stycast 1266). All weight measurements were measured with an analytical balance, in order to achieve the desired ratios with a high precision. A good method for the mixing of powder and stycast is to use a toothpick or small needle to massage small amounts of powder at a time into the mixture. This helps to minimise the formation of lumps and produce an overall smoother consistency, packing as much powder into the stycast as needed.

A thin layer of insulation is applied such that the drilled hole is packed, and the indented region is covered in a thin layer that extends just over the lip of the indent. The gasket with fresh insulation is cured inside the pressure cell under an applied load of 2800 N, with liquid PTFE sprayed on to the anvils to prevent the insulation sticking to the anvils instead of the gasket. This is cured at 120°C for at least 1 hour. Finally, the insulated gasket has to be drilled again to create the sample chamber. A smaller drill bit (around 25μm is sufficient if performed carefully) creates this chamber, insulated around the perimeter. Under a microscope, it can be possible to see where the hole is through the insulation, which can assist in aligning the drill.

2.2.3 Pressure calibration

The pressure inside the cell is detemined by the superconducting transition of a sample of high purity tin inside the cell. At ambient pressures, tin has a superconducting transition of $T_c = 3.72\,\mathrm{K}$ [142] and decreases with pressure according to $\frac{dT_c}{dP} = -0.0489\,\mathrm{K/kbar} = -0.489\,\mathrm{K/GPa}$ [141]. Figure 2.5a shows for two experiments the relationship between applied load on the piston to increase the pressure, and the pressure as determined via the change in the superconducting transition temperature of the tin. In the first case[2] (red crosses) the applied load was continuously increased up to a maximum (a load of 300 bar for a pressure of 20.1(3) kbar), whereas in the second case (blue circles) the applied load was increased and then decreased several times. The figure shows how the applied load

[2]This is typically the case for most pressure cell experiments presented here

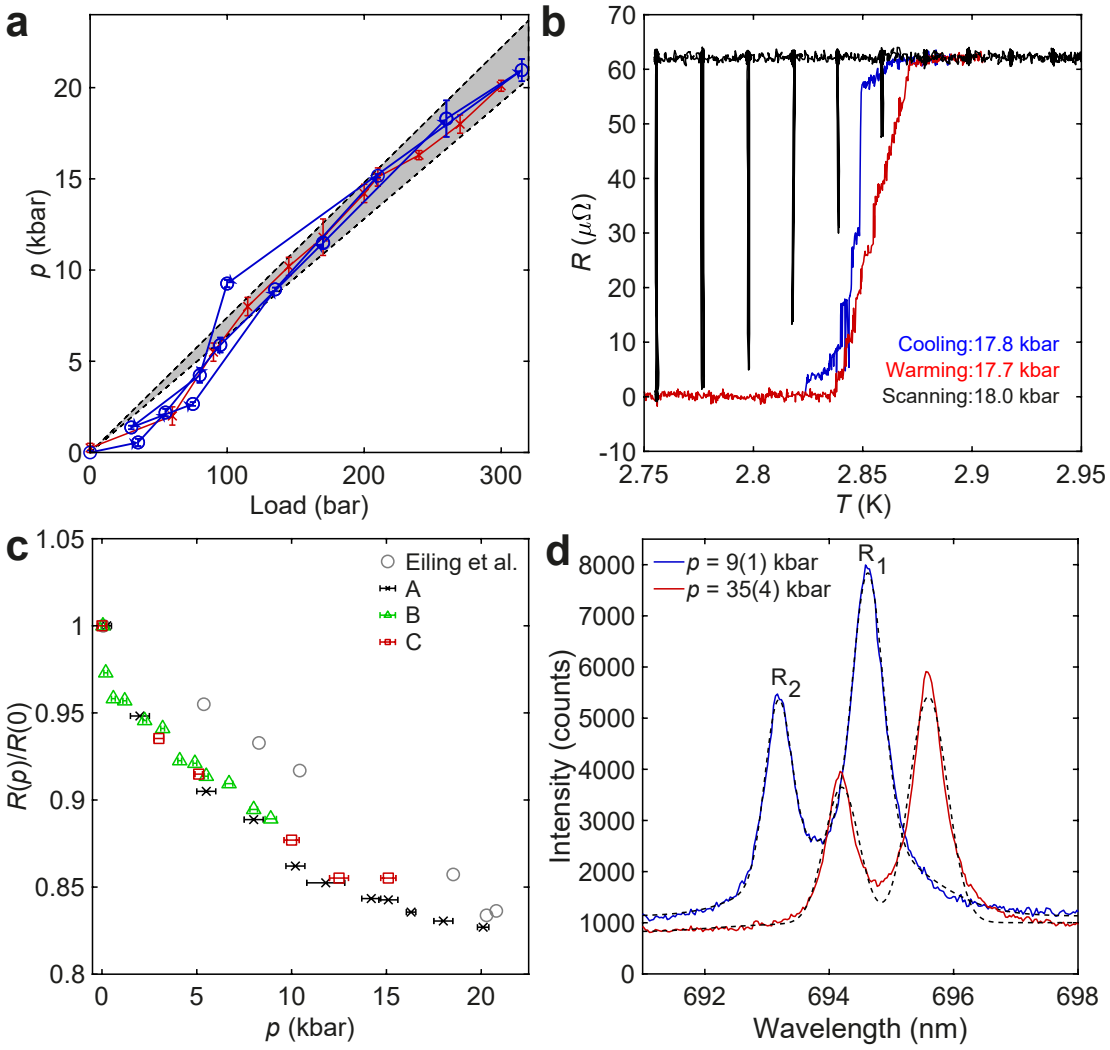

Figure 2.5: Pressure calibration. (a) Applied load from the hydraulic press to the piston cylinder cell and the corresponding low temperature pressure from measurements of the change in tin superconducting transition temperature. The shaded region is marked out by the expected pressure for an applied load in theory ($p = 74\times$ load) and the in practice value provided by the manufacturer ($p = 64\times$ load). The red markers are from a pressure run with Cu-FeSe (Chapter 4) where the applied load was continuously increased. The blue markers are from $FeSe_{0.82}S_{0.18}$ sample S1 (Chapter 5), arrows denote the order of pressure runs. (b) Resistance temperature dependence of the tin manometer from Chapter 4. The cooling(warming) data is in blue(red) taken at 0.02 K/min, whilst the scanning measurements sweep the field from −100 Oe to 100 Oe every 0.02 K in black. (c) Variation in the tin manometer resistance at room temperature as the pressure increases. Three pressure experiments are included (A, B and C). Grey circles are data about Sn adapted from Eiling et al. [141]. (d) Example ruby spectra taken at room temperature in a diamond anvil cell. The dashed lines show a fit to three Gaussian peaks (R_1, R_2, and a wide small amplitude background) to determine the position of the R_1 peak shift.

maps well to the low temperature pressure with a linear behaviour. When the direction of load change is reversed, a *lag* appears which is then corrected over the next few pressure changes. Additionally, at low pressures when the load is first applied, the actual pressure is much lower than expected. This is due to the pressure cell overcoming initial internal friction, and once this is complete the actual pressure then recovers to the expected pressure from the linear dependence. The shaded region in Figure 2.5a denotes the theoretical conversion (74 times) and the manufacturer supplied conversion (64 times). I found these to be a good estimate of the actual pressure, after the initial lag is overcome.

Due to the tin being high purity, there is a very low residual resistivity and almost no temperature dependence to the resistivity at low temperatures. Hence, in order to obtain a large signal and sharp transition a long thin slice of tin is prepared ($R = \rho l/A$). Figure 2.5b shows an example transition from an $Fe_{1-x}Cu_xSe$ measurement, corresponding to a pressure of 18.0(3)kbar. For each measurement, the pressure is checked by sweeping, in zero-field, the temperature in cooling and warming at 0.02 K/min through the transition to check for hysteresis. Next, to account for any remanent magnetic field, a method is used where at fixed temperatures (every 0.01-0.02 K) the field would oscillate between ± 100 Oe to remove the effect of any remanent magnetic field, seen in Figure 2.5b.

The room temperature resistivity of the tin decreases with pressure, and thus can be used as a proxy for the pressure at high temperatures [141]. Figure 2.5c shows the reduction in the room temperature resistivity for the tin manometer from three separate experiments, and from literature [141]. There is a small difference compared to literature, this is attributed to the pressure values from literature being determined at room temperature, whereas the pressure from the experiments here are the low temperature values. The low temperature pressure values are reduced compared to room temperature estimates through solidification of the pressurising medium. Other suitable metals for an in-situ manometer, if tin is not available, with slightly different T_c ranges would be lead or zinc.

A second method to determine the pressure in-situ is from the fluorescence spectrum of ruby, when illuminated by a laser light (a 532 nm green laser was used in Oxford). Two strong lines appear in the spectrum, R_2 and R_1 (where R_1 has a larger intensity, and a longer wavelength), owing to the de-excitation of excited electrons after being energised by laser light. The wavelength of theses lines are strongly pressure, and temperature, dependent. The pressure dependence at room temperature fits the empirical formula:

$$p = \frac{a}{b}\left[\left(\frac{\lambda}{\lambda_0}\right)^b - 1\right] \tag{2.7}$$

with a and b constants [143, 144], λ the wavelength of R_1 at applied pressures, and λ_0 the wavelength of R_1 measured in ambient conditions as this can vary slightly per ruby. At low temperatures, small differences in the pressure change from shifts in R_1 require accounting for compared to room temperature [145]. This technique requires optical access to the sample space, either directly or with a fibre optic cable (as is required for a piston cylinder cell). A particular benefit of this technique is that, for a diamond anvil cell for example, multiple rubies can be placed inside to verify (or not) uniform hydrostatic conditions across the sample space.

2.3 Low Temperature Techniques

2.3.1 Flow cryostat

In order to screen single crystals of new materials with transport measurements, I often used a flow cryostat for the measurement. The principle of a flow cryostat is that a pump is used inside the cryostat which pulls helium from a dewar into the sample space and cools the sample, down to 4.2 K (or slightly lower with pumping on the sample space thus lowering the pressure and therefore temperature). The rate of pumping is controlled such that the cooling is performed slowly and improves thermalisation of samples during the measurement. At low temperatures, the rate of cooling/warming was controlled by restricting the pumping on the cryostat. The warming above ∼30 K is performed with no pumping, and instead only from thermalisation with the atmosphere. Hence, the rate of change in temperature

is smoother and slower for warming[3], therefore the warming measurements are utilised for determining sample quality and properties. The temperature would be determined using a 4 point resistance measurement of a cernox thermometer on the probe, and a Lakeshore 340 temperature controller to convert the resistance to a temperature using that specific thermometers calibration curve.

2.3.2 Physical Properties Measurement System (PPMS)

I performed many experiments using the Quantum Design Physical Property Measurement System [146]. This is a cryostat with control over temperature (down to 2 K) and magnetic field (up to 16 T, both polarities). The system uses a variable temperature insert (VTI) which sits in a liquid helium bath and inside a superconducting magnet made of Nb_3Sn. The temperature is controlled through a needle valve connecting the sample chamber and helium bath. Heaters and sensors are used to balance the flow rate of He to set the temperature.

The conditions in the cryostat were controlled using the PPMS MultiVu software provided by the manufacturer, which displays the current state of the system. The cryostat is controlled directly by the Model 6000 PPMS controller. List of instructions (a sequence) can be issued from MultiVu to the controller to execute on the PPMS. The sequence is executed in order using wait commands to ensure a certain time, field, or temperature is reached. For the pressure cell experiments, MultiVu is used to control the cryostat conditions, but a second thermometer next to the pressure cell is simultaneously measured to more accurately measure the temperature of the sample. In addition, slow temperature sweep rates of typically 0.5 K/min were used as this was sufficiently slow to observe no lag in the temperature of both thermometers.

2.3.3 High Magnetic Fields

One of the most useful tools in the exploration of superconductors is magnetic fields. A magnetic field can suppress the superconductivity to reveal the normal state at

[3]Typically around 10 hours for warming to room temperature without a heater, although this value is seasonal.

low temperatures and access quantum oscillations. The magnetic fields are also used to explore the magnetotransport of a system above the superconducting state, and therefore probe the charge carrier densities and mobilities, to understand the scattering processes. Additionally, quantum oscillations can be measured in high magnetic fields at low temperatures to directly probe the Fermi surface.

In this thesis, measurements have been taken in a variety of instruments hosting magnetic fields. Much of the fine-detailed pressure work, amongst others, used a 16 T Quantum Design Physical Property Measurement System (PPMS), down to 2 K. User facilities allowed access to higher magnetic fields, where quantum oscillations can then be measured. The user facilities at the National High Magnetic Field Laboratory, NHMFL, Tallahassee, Florida were used for a 45 T hybrid resistive magnet, and a 41 T fully resistive magnet, both operating with ^{3}He cryostats down to 0.35 K. Slightly closer to Oxford, other measurements used fully resistive 35 T magnets at the High Magnetic Field Laboratory (HMFL), Nijmegen, Netherlands.

Magnetic fields are generated by passing a current through wires in the shape of a solenoid. Measurements here have used both superconducting and resistive Bitter magnets to generate high magnetic fields continuously. The Bitter magnets are more conventional, and often made of multiple concentric coils connected in series though which large currents are passed to generate the magnetic field. Each coil is made up of layers of Bitter plates, conductive plates the current passes through, and separated by insulating spacer layers, which are designed to extend the current path around the plate on each layer. The plates are designed with holes across the surface for cooling water to pass through. These require a large cooling power, up to 33 MW for the Tallahassee 41 T fully resistive magnet, which is typically provided with high pressure cold water continuously cooling the magnets. Meanwhile, superconducting magnets are made with superconducting wires, which instead need to be kept cold to maintain their superconducting properties. This is typically done by immersing the magnet in liquid ^{4}He. Finally, the largest continuous DC field hybrid magnet uses a combination of an 11.5 T superconducting

magnet and a 33.5 T resistive magnet to achieve up to 45 T, at the National High Magnetic Field Laboratory, NHMFL, Tallahassee Florida.

Superconducting magnets often retain a non-zero remanent field when the current is removed, owing to trapped flux inside the magnet. This is of particular concern for measurements intended to be taken in zero-field, such as cool-downs and the tin manometers inside the pressure cell where accurate measurements of T_c are needed to accurately determine the pressure (tin is a type I superconductor with a $\mu_0 H_{c2}$ around 0.03 T [147]). Thus, as discussed earlier, the superconducting transition temperature of tin is checked by oscillating the magnetic field between -100 and 100 Oe at low temperatures to account for this remanent field.

Whilst advantageous time-wise to fit as many samples on to a single probe during experiments, care must be taken to account for any offset away from the field centre, and any significant distances between thermometers and samples. In addition, the thermal load from multiple transport samples can cause issues with stabilising temperatures, particularly at the lowest temperatures. Checks were performed for temperature lag on each sample in high field experiments, and transport values (T_c, resistivity at specific temperatures and/or fields) compared to resistivity curves performed from screening in Oxford.

2.3.4 Temperature Extrapolation in High Magnetic Fields

For the experiments in the 45 T hybrid magnet the field range accessible in each field sweep is only 11.5 to 45 T. As the resistance of the thermometers have field dependence, in addition to the temperature dependence, mapping the temperature from both resistance and field would require extensive calibration. Instead, the temperature is calculated from using two thermometers with opposite magnetoresistance to extrapolate a 0 T temperature value from the field dependence of the resistors. One Cernox and one RuOx thermometers are used, because they have a positive and negative magnetoresistance respectively. A second order polynomial is fitted over a suitable field window for each thermometer,

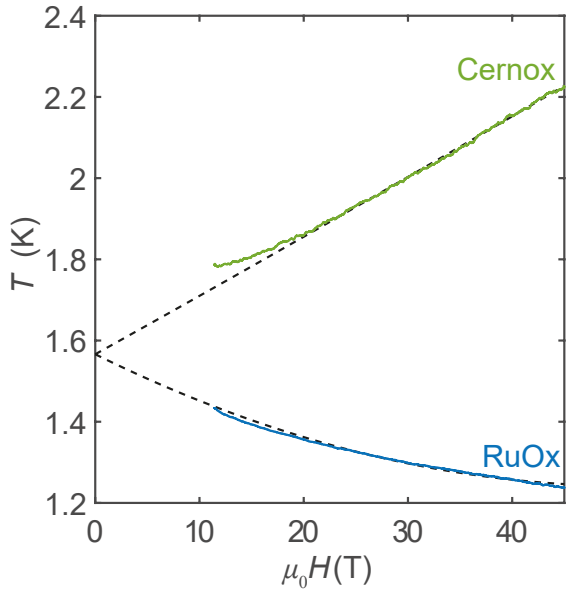

Figure 2.6: High magnetic field temperature extrapolation. A second order polynomial is used to extrapolate the 0 T temperature from both a cernox and a RuOx thermometer nearby to the sample to a common value.

and simultaneously extrapolated to 0 T such that there is agreement. Figure 2.6 is an example extrapolation of the temperature unaffected by high magnetic fields.

2.4 Other Techniques

I will briefly discuss other techniques that have been used for measuring and characterising single crystals.

2.4.1 Tunnel Diode Oscillator (TDO)

The tunnel diode oscillator technique is used in this thesis in Chapter 6 for measurements up to 41 T in Tallahassee. The technique utilises a tunnel diode as part of an LC circuit for a contactless probe with high resolution [148]. Tunnel diodes are heavily doped semiconductor diodes with a small gap junction between the position (P) and negative (N), where the valence band holes on the P side are aligned with the conduction band electrons on the N side to allow for quantum tunnelling. The sample is placed inside a coil which acts as an inductor, L, at the end of the circuit, in parallel with a capacitor, C, which produce an oscillating current with a DC voltage. The tunnel diode counteracts the positive resistance of

the circuit to prevent power loss and damping of the oscillations. The frequency of the oscillations can be approximated close to a simple LC circuit, which would be:

$$F = \frac{1}{2\pi\sqrt{LC}} \tag{2.8}$$

The inductance, L, of a coil depends on the length, l, number of turns, N, and cross sectional area, A:

$$L = \frac{\mu_0 \mu_r N^2 A}{l} \tag{2.9}$$

Crucially, the inductance is proportional to the relative permeability of the space in the volume of the coil ($\mu_r = 1 + \chi$). The skin depth of the sample is given by $\delta = \sqrt{\rho/(\pi\mu F)}$, with μ the magnetic susceptibility of the sample. Hence, the skin depth will decrease as the resistivity decreases, and/or as the susceptibility increases. Therefore, as the skin depth decreases, the inductance will decrease and thus the oscillation frequency F will increase. Inside the superconducting phase, the penetration depth from the magnetic field is measured. The frequency of the oscillations $F \propto L^{-1/2}$ will respond to such changes, particularly phase transitions. Experimentally, the frequency measured includes a background contribution, which is field and temperature dependent, and increasing the filling factor of the sample (relative to A) in the coil will increase the relative size of transitions. Typically the background frequency is on the order of tens of MHz, and changes through transitions on the order of 0.01-1 MHz. However, when set-up correctly there is very good sensitivity and stability to changes in the inductance, allowing accurate measurements of small changes. Hence, in the systems investigated here the phase transitions for the nematic, magnetic (SDW), and superconducting phases can be probed.

2.4.2 Energy Dispersive X-ray (EDX)

Energy Dispersive X-ray analysis (EDX) is a common way to measure the composition of different elements of crystals. The principle idea is to measure x-rays emitted from the sample when a beam of electrons is shone on to the sample to

remove inner shell electrons, and then when a higher energy shell electron fills the vacancy a photon is emitted for the energy difference. The energy of these x-rays produces a different spectrum for each chemical element. Software can be used to then determine the relative abundance of each element, based on the intensity and position of peaks in the emission spectrum and calibration of the instrument against a well known source.

For a batch of new crystals, multiple sample crystals would be measured with EDX to produce an average and spread of the composition in that batch. For chapter 3, the nominal 0.25% composition of copper, relative to the Fe, was impossible to verify beyond a trace amount. In addition, as the nematic transition, T_s, is sensitive to the composition, this can be used as an indirect measure when compared with other crystals in $FeSe_{1-x}S_x$ and $Fe_{1-x}Cu_xSe$ here.

2.4.3 X-ray Diffraction

X-ray diffraction (XRD) was used for the determination of the crystal structure, lattice parameters, and the degree of mosaicity of the crystals. In particular, lattice parameters can be used as a proxy to identity the composition of crystals when isoelectronic substitution is the tuning parameter. XRD works because when a periodic array of atoms is exposed to a monochromatic source, in this case X-rays as this wavelength is most comparable to the space between scatterers (the atoms), spherical diffracted waves will be emitted. For most angles, the waves will destructively interfere, except for points which fulfil the Bragg condition where constructive interference occurs and produces a Bragg peak. Analysis of these peaks reveals the unit cell and symmetries of the system. The XRD instrument used for measurements in this thesis was an Agilent Supernova Single Crystal X-ray diffractometer.

The crystal used in a TDO experiment in Chapter 6 is presented with corresponding Bragg peaks along high symmetry planes in Figure 2.7. The Bragg peaks are point like, and the peaks are compared to the expected points of each crystal structure (in this case 347 out of 351 peaks matched), indicating this is a single

crystal. The measurements confirm the crystal is tetragonal (with lattice constants: $a = b = 3.7747\,\text{Å}$ and $c = 5.5030\,\text{Å}$) with space group P4/nmm.

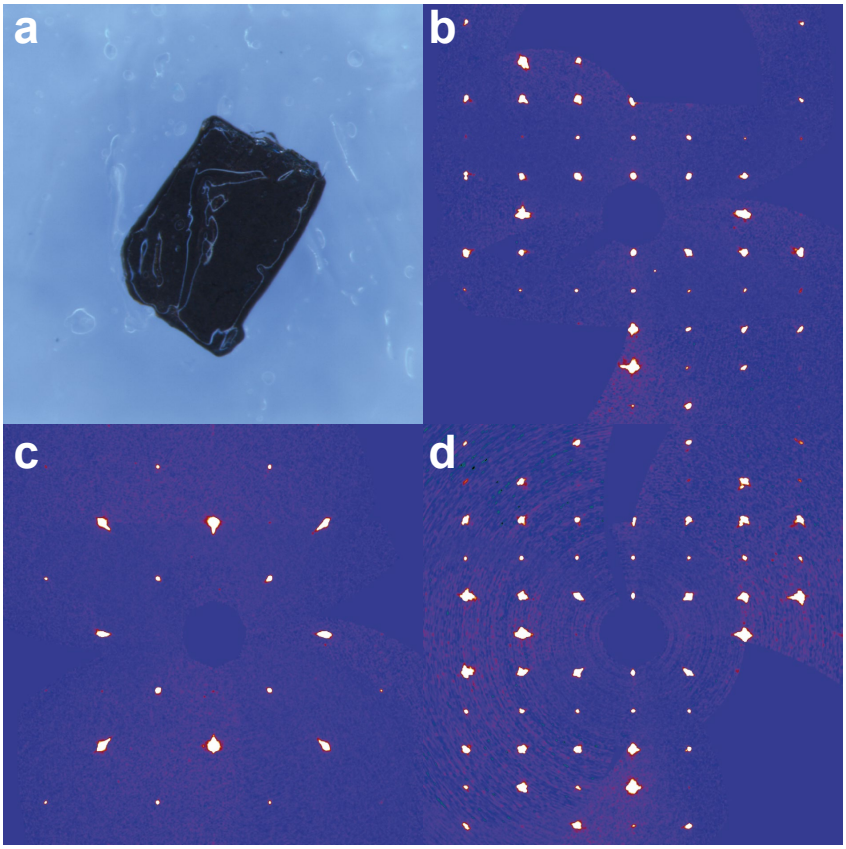

Figure 2.7: X-ray diffraction results. (a) Single crystal of $FeSe_{0.96}S_{0.04}$ (sample E). The Bragg peaks are along (b) [h 0 l] (c) [h k 0] and (d) [0 k l]. As this crystal is tetragonal at this temperature (300 K), (b) and (d) look effectively the same by symmetry. Lattice parameters are: $a = b = 3.7747\,\text{Å}$ and $c = 5.5030\,\text{Å}$.

3

The effects of impurity scattering in $Fe_{1-x}Cu_xSe$

This chapter reports on a study into the effect of chemical substitution in the Fe-plane of FeSe using copper ions in $Fe_{1-x}Cu_xSe$, up to $x = 0.02$. In this study, the incredibly small Cu substitution amounts allow a sensitive investigation of the effects of controlled disorder in the FeSe system (the lowest being where 1 of every 400 Fe sites are replaced with Cu). The substitution of Cu introduces a strong impurity potential in the Fe-plane, significantly affecting the electronic and superconducting properties of these single crystals. Both the nematic and superconducting phases are suppressed remarkably quickly, requiring only 2% Cu to suppress the superconductivity fully. The residual resistivity is continuously increased with the amount of Cu, due to enhanced impurity scattering. In addition, I find a strong correlation between T_c and T_s. I will use magnetotransport measurements up to 35 T on a very low substitution, $Fe_{0.9975}Cu_{0.0025}Se$ ($x = 0.0025$), to show a reduction in the charge carrier mobilities by a factor of ~ 3 as compared to FeSe, whilst the charge carrier densities remain unaltered. As the hole-like carriers remain more mobile than the electron-like carriers, a positive Hall coefficient is found, in contrast to the negative coefficients of FeSe and Co-substituted FeSe single crystals. At low temperatures a linear in temperature resistivity is found, as is a $H^{1.6}$ magnetic field dependence of

the magnetoresistance, identifying additional signatures of anisotropic scattering. The suppression of superconductivity with the Cu substitution can be described by the Abrikosov-Gor'kov formula for a sign-changing order parameter in the presence of non-magnetic impurities. Additionally, the upper critical field behaviour follows similar trends to FeSe, where all curves collapse onto a single curve in reduced units of $\mu_0 H_{c2}/T_c$, but for $H||(ab)$ no low temperature upturn is detected, as found in FeSe[1].

3.1 Introduction

Perhaps the most explored tuning parameter of iron-based superconductors is chemical substitution. The substitution of transition metals in iron-based superconductors, such as in $BaFe_2As_2$, suppresses the structural and magnetic transitions and stabilises a dome of superconductivity [29, 38]. Not all transition metals are equal. Some, like Co or Ni, can stabilise superconductivity in FeSCs [38, 150]. Meanwhile, Cu substitution displays unusual behaviour as sometimes being a dopant of electrons or of holes [38, 151, 152], causing major changes in transport behaviour and local magnetism [153]. In NaFeAs, Cu substitution increases the resistivity and induces a metal-to-insulator transition [153, 154], leading to a decreasing in the spectral weight [151]. Such a transition has been linked to a Mott-like insulator phase, raising the possibility that Cu substitution can be a tuning parameter towards strong correlations [152, 153].

FeSe enters a nematic electronic phase below 90 K, but unlike most iron-based superconductors, no long-range spin-density wave is stabilised at any temperature for ambient pressure [155]. Nevertheless, a large range of spin excitations are present [156], and these low-energy spin fluctuations can stabilize the anisotropic superconductivity in FeSe, as observed in scanning tunnelling microscopy (STM) [50], and influence the low temperature normal state transport properties [71]. Isovalent substitution of Se with S or Te occurs outside the Fe-plane and has moderate effects with nematicity slowly suppressed and superconductivity quite

[1]This chapter is adapted from work published in Physical Review B **105**, 115130 [149]

robust [55, 56]. In contrast, substitution of Fe using transition metals in the Fe-plane leads to the suppression of both nematicity and superconductivity [72–76]. Further Cu substition in FeSe induces a metal-to-insulator transition even for small substitutions ($x = 0.04$) [74, 75, 157], and even higher substituions can induce local magnetism around the Cu sites [75]. The insulating behaviour is suppressed and the superconductivity restored with applied pressure, although with a reduced superconducting fraction [158–160]. This highlights how Cu substitution in FeSe is a prime system for investigating the normal and superconducting states, and if an insulating state can be tuned into a high-T_c superconductor with applied pressure in iron-based superconductors. Furthermore, the strong impurity scattering effects induced by the substitution of various transition metal ions in the Fe plane can be compared with those induced by electron irradiation, where superconductivity of FeSe was found to be enhanced by defects [161], thus raising further questions about its pairing symmetry in the presence of disorder.

3.2 Experimental details

The single crystals of $Fe_{1-x}Cu_xSe$, with nominal compositions of $x = 0.0025$ to 0.02, in this chapter were grown by Shiv Singh using the $KCl/AlCl_3$ chemical vapour transport method and the same growth conditions for all compositions [102, 162]. The batch of single crystals with the lowest nominal composition, $x = 0.0025$ was measured using EDX by Jason Brown, indicating a small variation in composition of $x = 0.0029$, from measurements of three unique crystals. The ratio of (Fe+Cu)/Se was found to be around 0.95, suggesting a small excess of Se (or deficit of Fe/Cu). Table 3.1 details transport parameters of single crystals from several batches of different nominal composition. Across all batches, more than 20 samples were measured with transport, the residual resistivity ratio was found to be smaller than in FeSe (≈ 7.5 compared to 25-30). Notably, the absolute resistivity varied more for larger substitution values, x, within each batch, as a result of inhomogeneous distributions of copper.

Table 3.1: Sample details for single crystals of $Fe_{1-x}Cu_xSe$. Parameters extracted from transport measurements of the crystals from different batches of $Fe_{1-x}Cu_xSe$.

Batch	Sample	T_s (K)	T_c^{on} (K)	T_c^{mid} (K)	T_c^{off} (K)	RRR	ρ_0 ($\mu\Omega$cm)	ρ_{300} ($\mu\Omega$cm)
SS13	ZP1 - S1	76(1)	7.5	6.6	6.2	7.8	59	581
$x = 0.0025$	ZP2 - S2	74(2)	6.6	6.0	5.4	7.5	65	542
	ZZ5 - S3	79(1)	7.3	7.0	6.0	7.5	60	533
	ZZ3 - S4	81(1)	7.3	6.1	6.0	7.3	68	598
	ZZ6 - S5	76(2)	7.5	5.0	4.8	5.7	63	419
	ZZ1	76(2)	6.5	5.1	5.0	6.3	50	388
	ZZ4	81(2)	6.8	6.0	5.7	6.8	40	339
	ZZ7	78(1)	5.9	5.0	4.8	6.3	52	371
	HJ2	74(1)	7.4	6.7	5.9	7.2	70	570
	HJ3	74(1)	8.6	7.4	5.9	7.0	92	743
SS10	ZZ1	72(1)	5.3	4.0	2.9	4.7	94	473
$x = 0.005$	ZZ2	72(1)	4.7	4.3	3.2	4.9	123	623
SS9	MB1	51(1)	3.2	<2	<0.3	2.2	211	463
$x = 0.01$								
SS12	HJ1	50(1)	3.1	N/A	N/A	N/A	397	933
$x = 0.02$	ZZ3	63(2)	5.3	N/A	N/A	2.9	456	1348
	ZZ4	29(1)	N/A	N/A	N/A	N/A	343	558
	ZZ5	34(3)	N/A	N/A	N/A	N/A	465	805
	ZZ6	48(3)	3.0	N/A	N/A	2.3	213	493
	ZZA1	N/A	N/A	N/A	N/A	N/A	740	1161

Transport measurements were always performed with the current applied in-plane ($I||(ab)$). The single crystals were prepared as detailed in Chapter 2 with indium solder. The maximum a.c. current applied was 1 mA RMS. Low field transport measurements were taken in a 16 T Quantum Design PPMS in Oxford. Additional high (d.c.) field measurements were performed in a variable temperature cryostat up to 35 T and down to 0.38 K on samples S2, S3 and S4. The magnetic field was mostly applied along the c-axis, but measurements with the field parallel to the conducting plane ($H||(ab)$) are also reported. The polarity of the applied magnetic field was reversed to allow measurements in positive and negative fields for later (anti)symmetrising to isolate ρ_{xx} and ρ_{xy}. Finite solder contact sizes result in errors on the absolute value of the resistivity on the order of 13% for each sample. The high field measurements in 35 T were performed at the High Magnetic Field Laboratory in Nijmegen by Pascal Reiss, owing to travel restrictions during the Covid-19 pandemic.

From Table 3.1 the crystals SS13 HJ2, SS13 HJ3, and SS12 HJ1 were prepared and measured by Helen Jones, and SS9 MB1 was prepared by Matthew Bristow, parameters are shown to further indicate the range of parameters in each batch. All analysis and figures presented in this chapter are that of the author.

3.3 Transport properties of Cu-FeSe

Figure 3.1a shows the temperature dependence of resistivity for single crystals of $Fe_{1-x}Cu_xSe$ for different compositions up to $x = 0.02$ (0.0025, 0.005, 0.01, 0.02). Upon cooling, a strong kink is identified at T_s, the structural transition temperature. Below T_s the system is in the electronic nematic phase, which is driven by electronic correlations and orbital-ordering effects and an associated coupling to the lattice induces a structural transition from a tetragonal to an orthohombic strucutre [155]. The typical metallic-like behaviour of the temperature dependence of the resistivity of FeSe changes to an almost invariant temperature dependence below 100 K with Cu substitution (see $x = 0.02$ in Figure 3.1a). This is accompanied by an increasing residual resistivity at low temperatures, as expected from Matthiessen's rule in the presence of strong impurity scattering. Larger Cu substitutions ($x > 0.02$) show the trend continues with a temperature independence becoming insulating-like ($d\rho/dT < 0$) for $x = 0.2$ with a factor of 100 increase in resistivity at low temperature, as reported by Williams et al. [75, 163]. The resistivity displays an unusual linear temperature dependence for the low Cu substitution of $x = 0.0025$, up to 60 K near T_s. Figure 3.1a also shows a similar linear behaviour for higher substitutions too, albeit for a smaller temperature range. This behaviour of the resistivity in the normal state is often a signature of a system close to an antiferromagnetic critical point in the presence of disorder [164].

In addition to the increased resistivity from the introduction of Cu in the Fe-plane, the superconductivity is strongly suppressed such that a zero resistance state is not measured down to 0.3 K for $x = 0.01$. Compared to FeSe, the superconducting transition becomes broader, $\Delta T \sim 1.5 - 2$ K, which indicates the Cu substitution leads to a more inhomogeneous electronic structure, even with substitutions on

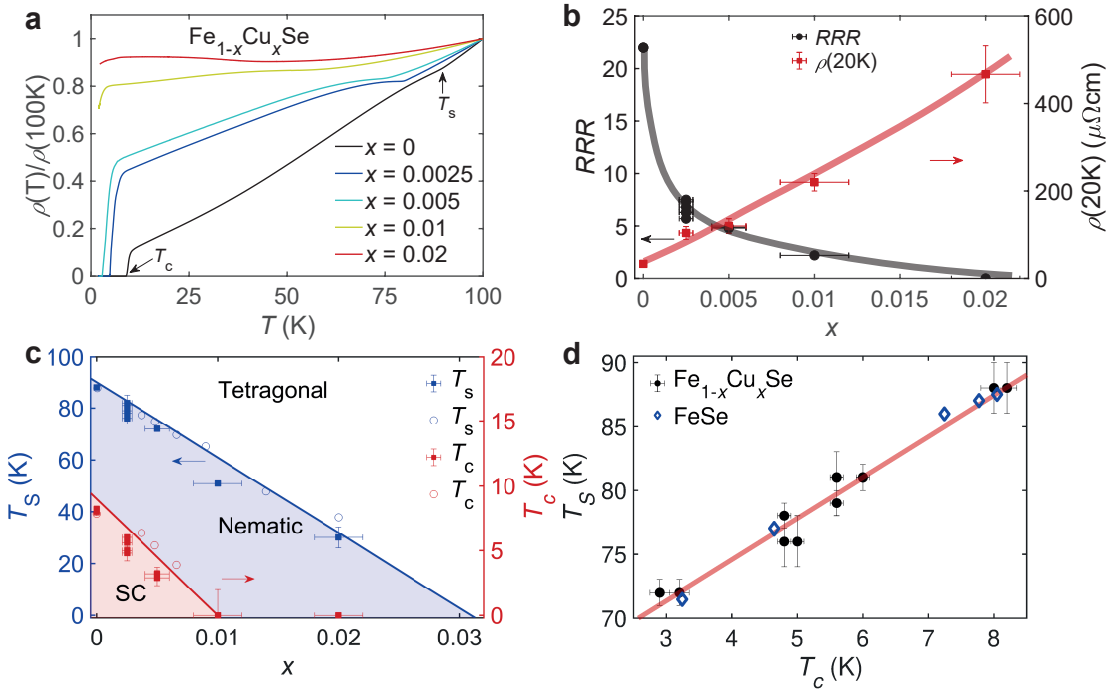

Figure 3.1: Transport behaviour for single crystals of $Fe_{1-x}Cu_xSe$. (a) Temperature dependence of the resistivity as a function of Cu doping, normalised at 100 K. (b) The evolution of the residual resistivity ratio, *RRR*, (defined as the ratio of the resistivity at 300 K to that at the onset of superconductivity) and that of the resistivity at 20 K with different Cu substitution. (c) Temperature-doping phase diagram for $Fe_{1-x}Cu_xSe$. Open symbols correspond to data previously reported in reference [76]. (d) The linear dependence between the nematic transition T_s and T_c caused by the Cu substitution. The blue open diamonds represent data from FeSe single crystals grown using different temperature gradients that can lead to the formation of defects in the crystals by Böhmer et al. [102].

the order of 1 in every few hundred atoms. Indeed, the superconducting fraction is reduced with Cu substitution, shown in Figure 3.1a. Meanwhile, Figure 3.1b shows the resistivity at 20 K, just above the onset of superconductivity, increases with increasing x. For higher x the resistivity at low temperatures is only reduced partially in response to an applied magnetic field, as if the system is not fully superconducting (see Figures 3.7c and d in Section 3.10). This suggests that Cu substitution promotes the formation of isolated clusters of superconductivity. If such clusters cannot act as a full percolating path in a parallel network resistor to contribute significantly to the total conductivity, then this results in the zero resistivity at low temperatures being suppressed. At higher doping, these effects

also lead to increased variation in crystal quality and transport values between individual samples from the same batch (see Table 3.1).

The nematic phase is suppressed from 87 K for $x = 0$, to 29 K for $x = 0.02$, and the structural transition becomes increasingly broader in temperature, similar to effects influencing the superconducting transition. No structural transition or superconductivity is detected in powder samples with $x \geq 0.03$ [74, 163], these transitions would not be expected if the transition continued to be suppressed linearly, as shown schematically in Figure 3.1c. As the resistivity temperature dependence weakens with increased Cu doping, the residual resistivity ratio, RRR, defined here as the ratio of resistivity at 300 K and onset temperature, drops from 30 for FeSe [71] towards 7.5 and lower, as shown in Figure 3.1b. The (decreased) RRR is a measure of the effect of disorder in each system, similar to previous reports on single crystals of $Fe_{1-x}Cu_xSe$ [76, 163], powder samples of Cu-substituted FeSe [75] and Co and Ni doping [165]. Additionally, the full temperature dependence, from 2 to 300 K, for each substitution is shown in Figure 3.4a, with a drastic increase in the high temperature resistivity for larger x. The residual resistivity increases faster with Cu doping than with Co doping, for the same amount of substitution [73, 165], suggesting that Cu produces a larger impurity scattering potential and/or may not provide additional charge carriers. However, all substitutions on the Fe conducting plane lead to the suppression of superconductivity [165], in contrast to other iron-based superconductors in which the electron doping with Co normally leads to an enhancement in superconductivity [38]. Moreover, this in-plane substitution of FeSe has a faster, more disruptive, effect as compared with isoelectronic substitution outside the plane with S or Te for Se [55, 56].

Figure 3.1c shows the phase diagram of $Fe_{1-x}Cu_xSe$ and comapres to previous work on single crystals [76] and powder samples [75]. Notably, a linear correlation between T_s and T_c persists across all the superconducting compositions, similar to studies on single crystals of FeSe grown in different conditions that have a different degree of disorder [102], shown in Figure 3.1d. In both of these circumstances, the correlation is likely induced by strong impurity scattering due to reduced

values of RRR. Similar trends have also been observed for FeSe thin flakes, with RRR reducing as the thickness is reduced, suggesting that disorder may also play a role in those systems [166]. In contrast, FeSe tuned by uniaxial strain shows behaviour where the nematic state is suppressed but the superconductivity is enhanced for compressive strain [167].

3.4 Magnetotransport behaviour

The magnetotransport behaviour is studied extensively for the lowest Cu concentration of $x = 0.0025$ to understand the impact of the impurity scattering on the nematic electronic phase in the presence of anisotropic spin fluctuations [168, 169]. Figures 3.2a and b show the magnetic field dependence of ρ_{xx} and ρ_{xy} respectively for a sample S1 measured in magnetic fields up to 15 T. Similarly, Figures 3.2c and d show the resistivities for sample S2 measured up to 35 T, all with the magnetic field applied perpendicular to the conducting plane ($H||c$). The transition from superconducting to normal state broadens in magnetic field at low temperatures ($\Delta\mu_0 H \sim 10$ T) as compared with FeSe, even for this small substitution. The zero resistivity is used to define the critical field, $\mu_0 H_{c2}$. Firstly, at higher temperatures inside the normal state, the longitudinal resistivity, ρ_{xx}, shows little field dependence, and the Hall resistivity has a quite linear field dependence, as is expected for a two-band compensated metal. At lower temperatures, below 60 K, the Hall resistivity develops a non-linear magnetic field dependence (see the derivatives showing field dependence in Figure 3.8d in Section 3.10). Notably, no sign change from positive to negative is found, which is the case for FeSe inside the nematic phase at low temperatures [170]. The magnetotransport close to T_c is shown for a sample of each composition in Figures 3.7a-d (Section 3.10), notably highlighting the reduced superconducting fraction in $x = 0.01$ and 0.02.

The Hall coefficient, R_H, a measure of the transverse resistivity, can be extracted from the low field regime ($\mu_0 H < 1$ T) from the field dependence of ρ_{xy} by assuming a linear field dependence at low fields for the curves in Figure 3.2b. Figure 3.2f shows the temperature dependence of R_H for both Cu and Co substituted FeSe as a

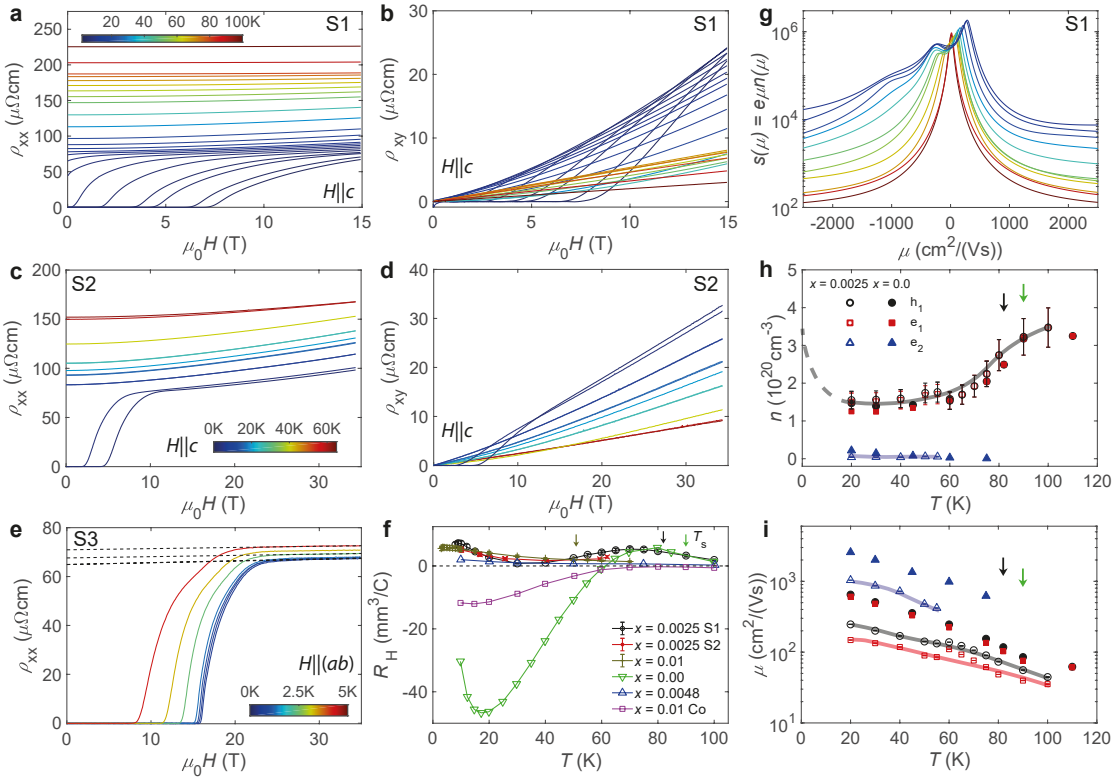

Figure 3.2: Magnetotransport results for $Fe_{1-x}Cu_xSe$ with $x = 0.0025$. The field dependence of the longitudinal resistivity, ρ_{xx}, and Hall resistivity, ρ_{xy}, for sample S1 in magnetic fields up to 15 T in (a) and (b), and for sample S2 measured in magnetic fields up to 35 T in (c) and (d) respectively. The measurements were performed with the magnetic field along c axis ($H||c$) and at different constant temperatures. (e) The longitudinal resistivity, ρ_{xx}, for the sample S3 was measured with $H||(ab)$ up to 35 T at temperatures below 5 K. The positions of T_s for different compositions are indicated by arrows of corresponding colours. (f) The temperature dependence of the Hall coefficient, R_H, for Cu-substituted FeSe compared with FeSe [171] (down open triangle), $x = 0.0048$ (up open triangle) from [76], and Co substitution $x = 0.001$ (open square) from [73]. (g) The mobility spectrum generated from the field sweeps in (a) and (b) using an approach developed in Ref. [129]. (h) Carrier densities and (i) mobilities of charge carriers as a function of temperature extracted considering a compensated two-band model at higher temperatures and a compensated three-band model at lower temperatures below 60 K. Data for FeSe are taken from [170]. The solid lines are a guide to the eye. The dashed line indicates the expected low temperature value from quantum oscillations data [55, 170]. This apparent drop in the carrier number inside the nematic phase is a consequence of the anisotropic scattering, as found for FeSe [170].

function of the amount of substitution [73, 76, 163, 171]. For the lowest Cu doping of $x = 0.0025$, R_H remains positive at lowest temperatures, but the magnitude demonstrates a weak temperature dependence with a local peak around 75 K and a local minimum around 40 K. At a higher substitution of $x = 0.01$, R_H remains

positive at lowest temperatures, increases slowly as the temperature decreases, and displays no minimums or maximums in the measured range from 70 to 2 K. In FeSe, R_H changes sign below 70 K with a positive local maximum around 80 K, for a T_s of 90 K [71, 73, 163, 170, 171]. No negative values of R_H are found across different compositions of Cu-doped FeSe systems inside the nematic phase [76, 163], which is in contrast to Co-doped FeSe where R_H remains negative at low temperatures for all measured samples up to $x_{Co} = 0.075$ [73]. Hence, this suggests that although the Cu and Co substitution both cause strong impurity scattering in the Fe plane, they behave differently with respect to the doping of electrons, with Co being a more significant donor of electrons as shown by the negative Hall coefficient [73]. If the Cu substitution donated electrons to the systems, then a similar response would be expected in R_H as found with Co doping. Although, through isoelectronic substitution in $FeSe_{1-x}S_x$ the Hall coefficient at low temperatures does change sign and becomes positive for higher x, as the distortion of the Fermi surface is suppressed and the anisotropy scattering reduced [55, 71, 171]. Overall, between the different substitution methods, R_H has shown marked sensitivity that likely arises from the different combinations and balances of impurity scattering and anisotropic scattering for this multiband system.

3.5 Mobility analysis

Next, effects on the charge carriers are investigated through simultaneously fitting the longitudinal and Hall resistivity components to extract the carrier density and mobility of each charger carrier for Cu substituted FeSe. Figure 3.2g shows the mobility spectrum of charge carriers at a range of temperatures, using the method detailed in Chapter 1. At high temperatures only one peak can be resolved, centred around $\mu = 0$, which is expected to be a combination of holes (positive mobility) and electrons (negative mobility) with low mobilities. Upon cooling, two peaks develop in the mobility spectrum which are fairly symmetrical around zero, with one electron and one hole peak. As the temperature decreases inside the nematic phase, both the hole and electrons become more mobile. At lower temperatures inside the

normal state, below 60 K, an additional local peak develops in the mobility spectrum which would correspond to a second electron-like carrier, this one of higher mobility.

The peak positions in the mobility spectrums, and the corresponding carrier densities ($n = s/e\mu$), are then used as starting points for the simultaneous fits of ρ_{xx} and ρ_{xy}. The models used assume charge compensation, as the Cu-substitution does not appear thus far to be doping the system with holes or electrons, as is the case with Co doping. Concerning any doping effects, Cu has been suuggested to be an electron dopant for Cu-FeSe from DFT [172] and ARPES [173], but for this low concentration of $x = 0.0025$, any excess of electrons or holes is negligible. Moreover, the Hall coefficient becomes positive by Cu substitution, which is in contrast to Co substitution and the expected changes in a basic Drude model [73]. Therefore, to analyse the magnetotransport data a compensated two-band model at high temperatures and a three-carrier model at low temperatures are used (see equations 1.39 and 1.40 for the two band case), similar to the approach used in FeSe [87, 170]. Examples of the fits are shown in Figures 3.8e and f, in Section 3.10. Figures 3.2h and i present the carrier density and mobility for each charge carrier as a function of temperature for both Cu-FeSe with $x = 0.0025$, and, for comparison, FeSe [170]. For the charge carrier densities, no significant changes are found compared to FeSe, as expected with such a small change in the composition. Firstly, through the nematic transition, at T_s, a smooth reduction in the carrier density of both the dominant hole and electron carriers (n_h and n_{e1}) is found, comparable to bulk FeSe [87, 170]. Sudden drops in carrier density are likely related to Fermi surface reconstructions, however the apparent reduction in the nematic phase here is likely a product of the anomalous transport present in the nematic phase from anistropic scattering [71, 170], which persists in the presence of small Cu substitution and strong impurity scattering. As the temperature is reduced, the mobilities increase for all charger carriers. Compared to FeSe, the mobilities for all charge carriers in Cu-FeSe are reduced by a factor ~ 3. This can be attributed to an increase in the scattering rate, $\mu = e\tau/m^*$, from Cu ions acting as strong scattering centers [172]. At low temperatures a divergence occurs in the

behaviour of the hole and electron mobilities, where the electron mobilities become less temperature dependent below 50 K, which is similar to the behaviour found in thin flake devices of FeSe [130]. For the low temperature regime, the impurity scattering dominates the changes in spectrum, as seen with the increased values of ρ_0, and similar reductions were observed for higher Cu doping at 10 K [76].

3.6 Normal electronic behaviour at low temperatures

The normal state resistivity, above T_c, in zero-magnetic field for Cu-doped FeSe displays linear in temperature behaviour with this increase in disorder, as shown in Figures 3.1a and 3.4b, consistent with previous reports [76]. This behaviour of $\rho \propto T^1$ was also noticed in samples with smaller RRR values in FeSe and $FeSe_{1-x}S_x$ inside the nematic phase [71, 174]. To investigate the temperature dependence of the normal state to lowest temperatures, going below T_c, high magnetic fields are employed to suppress the superconductivity. The high field, normal state, resistivity can be extrapolated to determine a zero-field value for the normal state at low temperatures. Two approaches are made for this method, varying the orientation of the magnetic field ($H||(ab)$ and $H||c$) to the current ($I||(ab)$). For $H||(ab)$, the in-plane longitudinal resistivity can be extrapolated with a linear dependence, because such an orientation eliminates orbital effects, as shown for sample S3 in Figure 3.2e. Switching the orientation such that $H||c$ requires a suitable choice of power law field dependence for the orbital magnetoresistance. Figure 3.3a demonstrates in this system a power law of $\sim H^{1.6}$ works well, similar to the dependence found for FeSe [71]. Combining the zero-field resistivity measurements, with the extrapolated zero-field resistivity points, the linear temperature dependence is found to extend to the lowest measured temperatures, giving access to the zero-temperature resistivity ρ_0, presented in Figure 3.3c.

The zero temperature resistivity can be used in determining the value of the local resistivity exponent, n, from the relationship $\rho = \rho_0 + AT^n$. This method follows that described in Section 2.1.3, and is applied to the data in

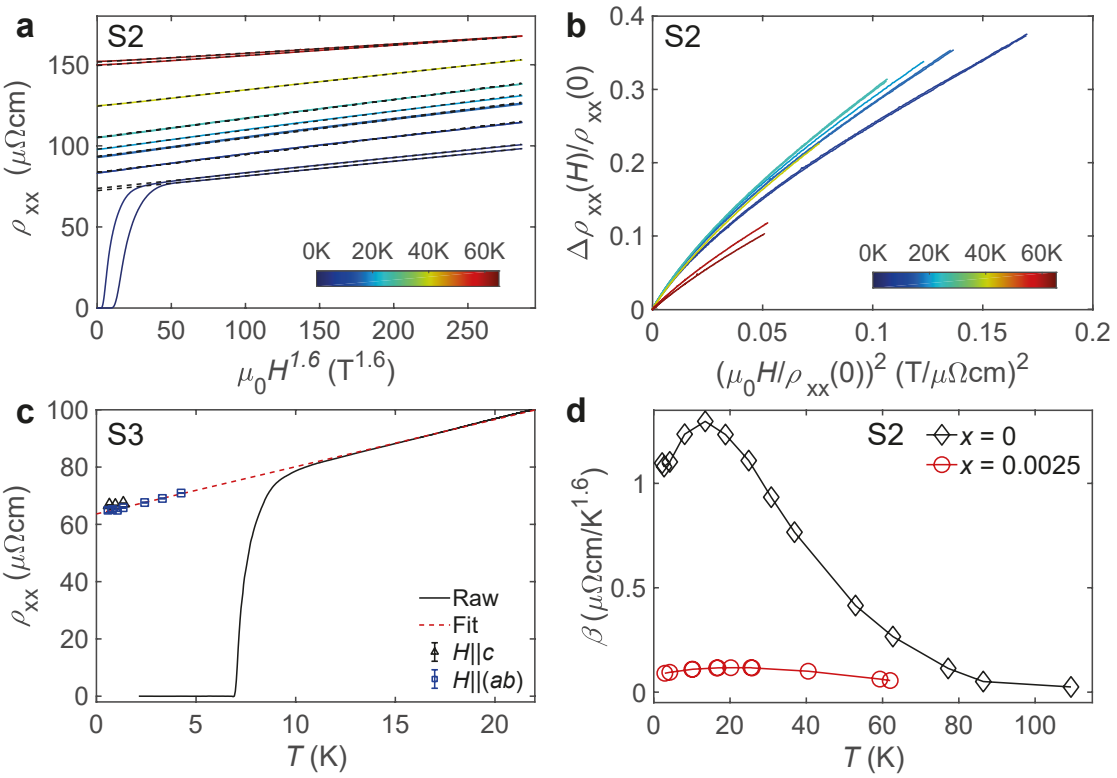

Figure 3.3: Normal electronic state of Cu-substituted FeSe with $x = 0.0025$. (a) Longitudinal resistivity versus $(\mu_0 H)^{1.6}$ for sample S2 inside the nematic phase at constant temperatures (represented in the colour bar) for $H||c$. The dashed lines are linear fits to the curves. (b) Kohler's scaling applied to the data in (a), where $\Delta\rho_{xx} = \rho_{xx}(\mu_0 H, T) - \rho(0, T)$. (c) The low-temperature zero field resistivity, with 0 T resistivity (black, solid line), and low temperature extrapolated values from high field measurements with $H||(ab)$ (blue squares) and from $H||c$, as extrapolated in (a) (black triangles). The red dashed line is a fit to the low temperature $H||(ab)$ points. (d) The slope of the $(\mu_0 H)^{1.6}$ magnetoresistance, β, extracted from (a), as a function of temperature. The black points are taken from a similar field dependence of FeSe from Ref. [71].

Figure 3.4a. Figure 3.4b shows how n varies with temperature for each composition of $Fe_{1-x}Cu_xSe$ measured. Hence, in the presence of strong impurity scattering the linear temperature dependence in Cu-FeSe extends through the entire nematic phase to the lowest temperatures, which is consistent with the existence of strong antiferromagnetic critical fluctuations in the presence of disorder [175]. In contrast, the close to linear resistivity found in FeSe and $FeSe_{1-x}S_x$ in clean systems eventually enters a crossover regime to Fermi liquid behaviour ($n = 2$) [71, 105, 110]. A similar crossover occured in thin flakes of FeSe which are in the presence of strong two-dimensional fluctuations and disorder [130].

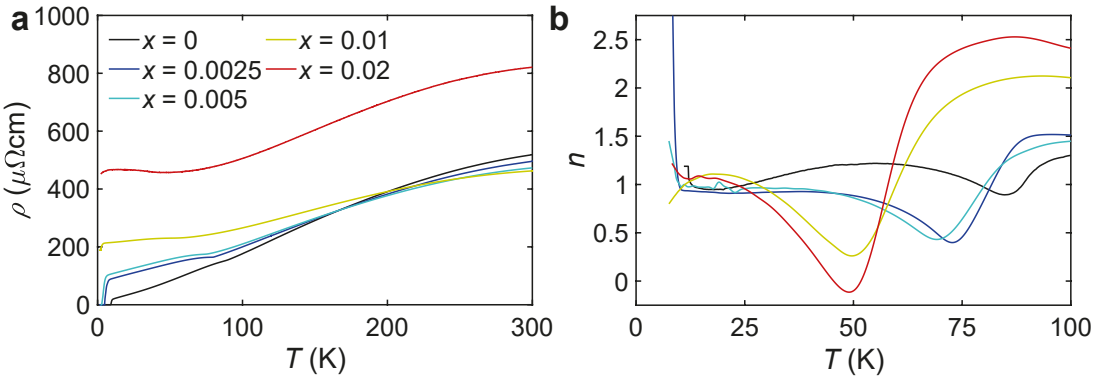

Figure 3.4: Transport of Cu-substituted FeSe. (a) Resistivity temperature dependence for single crystals with different Cu substitutions, x. (b) The temperature dependence of the local resistivity exponent, n, of the zero field resistivity data in zero-magnetic field, $\rho(T) = \rho(0) + \alpha T^n$, calculated from (a).

Furthermore, ρ_0 can be used to estimate the mean free path at low temperatures for the multiband FeSe, assuming the Fermi surface consists of two-dimensional cylinders with a compensated hole and two electron pockets ($k_F \sim 0.1\,\text{Å}^{-1}$), such that $\ell = \frac{\pi c\hbar}{Ne^2 k_F \rho_0}$ [78]. For FeSe, a clean system with a typical value around $\rho_0 \sim 5\,\mu\Omega\text{cm}$ corresponds to a mean free path of $\ell \sim 712\,\text{Å}$ [71]. With the lowest Cu substitution, the mean free path[2] is reduced by a factor 10 towards $\ell \sim 55(5)\,\text{Å}$ due to the increased residual resistivity. Furthermore, the scattering time is estimated by using the mobilities extracted from the magnetotransport earlier. For the three pockets at low temperatures, the scattering time varies between 0.6 - 1.2 ps, which is a factor of 3 shorter, resulting in more frequent scattering, than for FeSe [170]. The increase in residual resistivity with increasing Cu substitution naturally leads to the mean free path reaching the limit where $\ell \sim a$, corresponding to the average distance a quasiparticle travels between collisions approaching the interatomic spacing. The system then reaches the Mott-Ioffe-Regel limit [176] where the coherent quasi-particle motion vanishes and the electron scattering rate τ^{-1} becomes comparable to the Fermi energy $E_F/\hbar$ [177]. With increasing Cu substitution, this limit is reached for very low substitution at low temperatures, and consequently systems will become insulating above $x > 0.02$.

[2]With the small substitution of $x = 0.0025$ here, c, N, and k_F are assumed to not significantly change from FeSe.

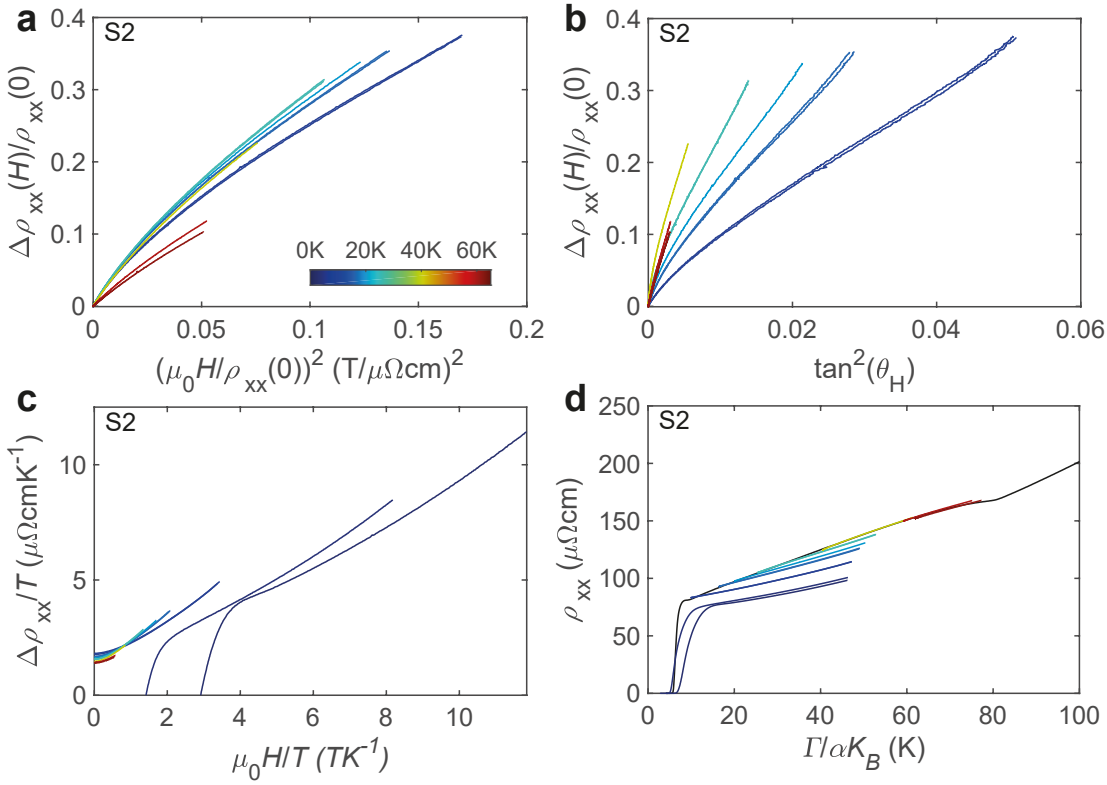

Figure 3.5: Scaling of the longitudinal magnetoresistance of Cu-substituted FeSe with $x = 0.0025$ ($H||c$). (a) Kohler's rule scaling $\Delta\rho_{xx}(\mu_0 H)/\rho_{xx}(0) \sim (\mu_0 H/\rho_{xx}(\mu_0 H = 0))^2$, where $\Delta\rho_{xx}(\mu_0 H, T) = \rho_{xx}(\mu_0 H, T) - \rho_{xx}(0, T)$. (b) Modified Kohler's rule scaling using the Hall angle, $\tan\theta_H = \rho_{xy}/\rho_{xx}$. (c) $\mu_0 H$-T scaling of $\Delta\rho_{xx}(\mu_0 H)/\rho_0 \sim \mu_0 H/T$, where $\Delta\rho_{xx}(\mu_0 H) = \rho_{xx}(\mu_0 H) - \rho_0$ and ρ_0 is the zero-temperature zero-field resistivity. (d) Energy scaling of resistivity as Γ, where $\Gamma = \alpha k_B T\sqrt{1 + (\beta/\alpha)^2(\mu_B\mu_0 H/(k_B T))^2}$ using $\alpha = 1$ and $\beta = 1$. This data does not follow the proposed energy scaling, similar to $FeSe_{1-x}S_x$ [71]. This magnetoresistance scaling was used to describe the antiferromagnetic critical region in $BaFe_2(As_{1-x}P_x)_2$ [178].

The classic magnetoresistance and symmetry conditions in a tetragonal system lead to a quadratic dependence of the electrical resistivity, $\Delta\rho/\rho$, on magnetic field $(\mu_0 H)^2$ in the low-field limit [179]. For $FeSe_{1-x}S_x$ this result is followed in the tetragonal phase outside the nematic phase, whereas inside the nematic phase the in-plane Fermi surface distortion and the anisotropic spin fluctuations alter the observed power law dependence, found to be $\sim H^{1.55}$ [71]. For Cu substituted FeSe of $x = 0.0025$ a similar power law of $H^{1.6}$ is found to best describe the magnetotransport, with the resistivity shown against $H^{1.6}$ in Figure 3.3a. To compare with FeSe, the amplitude of the power law (that is β for $\rho(\mu_0 H, T) = \rho(0, T) + \beta\mu_0 H^{1.6}$) is shown

for both FeSe and Cu-substituted FeSe in Figure 3.3d. Both measurements are in the same field regime, up to 35 T, with the FeSe data adapted from reference [71]. A significant reduction is found by a factor of 10 compared to FeSe, which is close to the expected change due to the factor of 3 reduction in mobilities found earlier.

Next, scaling laws are briefly considered which might be expected in different regimes, and the implications from violations of such scaling laws. Firstly, it might be expected that Kohler's rule would be obeyed where the Cu substitution helps to impose a single dominant scattering process. In such a case the magnetoresistance is scaled with $\Delta\rho_{xx}/\rho_{xx}(0) \sim (\mu_0 H/\rho_{xx}(0))^2$. However, Figure 3.5a shows that deviations from Kohler's law remain (as they did in bulk FeSe [71]), despite the fact that the impurity scattering increases. Other considerations arise from the linear temperature dependence in the resistivity. A modified Kohler's rule unsuccessfully uses the Hall angle as scaling, $\tan\theta_H = \rho_{xy}/\rho_{xx}$, in Figure 3.5b. Simlarly, a $\mu_0 H$-T scaling is attempted in Figure 3.5c. Finally, an energy scaling which successfully described the antiferromagnetic critical region of $BaFe_2(As_{1-x}P_x)_2$ [178] does not scale the low temperature resistivity of Cu substituted FeSe in Figure 3.5d. To summarise, these various proposals for scaling of the magnetoresistance cannot successfully describe the behaviour for $Fe_{1-x}Cu_xSe$, $x = 0.0025$, which matches that found for $FeSe_{1-x}S_x$ inside the nematic phase [71].

3.7 Upper critical fields

Figures 3.6a and b show the temperature dependence of the upper critical magnetic field, $\mu_0 H_{c2}$, with the magnetic field orientated with $H||c$ and $H||(ab)$ respectively. The results are shown for two single crystals (S3 and S4) of $Fe_{1-x}Cu_xSe$, $x = 0.0025$, and compared to bulk FeSe (adapted from references [78, 79]). The most notable feature is that at the lowest temperatures the upper critical field of FeSe shows an unusual upturn in critical field for $H||(ab)$, which has been associated to the stabilisation of an FFLO state [78], magnetic field-induced transitions [79] or simply the manifestation of multi-band effects on the upper critical field [180]. For the Cu substituted systems, no such upturn region is identified for $H||(ab)$, similar

again to the disordered systems of thin flakes FeSe [166]. To account for small variation in the value of T_c between samples, which then continues into shifts in $\mu_0 H_{c2}$, both the upper critical field and temperature are reported in reduced units, that being $\mu_0 H_{c2}/T_c$ and T/T_c using the offset temperature of superconductivity. In Figure 3.6c with reduced units, all curves collapse onto a single dependence, except for the low temperature upturn in $H||(ab)$ of FeSe. This indicates that the superconducting pairing mechanism does not change significantly for low Cu substitution, and meanwhile the low temperature upturn for $H||(ab)$ is smeared out. These small changes in the upper critical field behaviour of $Fe_{1-x}Cu_xSe$ could be a consequence of changes in pairing due to the presence of impurities that promote intraband pairing over interband pairing. Interestingly, in the case of single crystals of FeSe with small amounts of disorder (RRR reduced from 30 to 12 and T_c reduced from 9.1 to 7.2 K) the slight upturn in upper critical field $H||(ab)$ was found to be robust [174]. This prompted suggestions the high field phase of FeSe is not a conventional FFLO state [174]. Whilst these features are smeared out for further enhanced disorder in Cu substituted FeSe, the temperature dependence can still be described by a similar multi-band model suitable for FeSe corresponding to an $s_{\pm}$ pairing, but with a reduced velocity anisotropy [180].

The first model to describe the behaviour of the upper critical field is the standard three-dimensional Werthamer-Helfand-Hohenberg (WHH) model [25], describing the low temperature orbitally limited critical fields and determining the value of the Maki parameter. Orbital pair breaking alone determines the temperature dependence of $\mu_0 H_{c2}$ for $H||c$, with a slope of $H'_{c2} \sim -1.7(1)$ T/K, similar to FeSe (-1.84 T/K) [180]. Switching orientation to $H||(ab)$ requires introducing a Pauli pair breaking contribution which reduces the orbital-limited critical field at low temperatures. Close to T_c the slope is $H'_{c2} \sim -4.7(1)$ T/K, which corresponds to an orbital value of 19.2 T, larger than the experimental value of 15.8 T at 0.6 K, attributed to Pauli paramagnetic effects. For FeSe, the expected Pauli paramagnetic limit field, based on the values of different band gaps, can vary between 4.8 T to

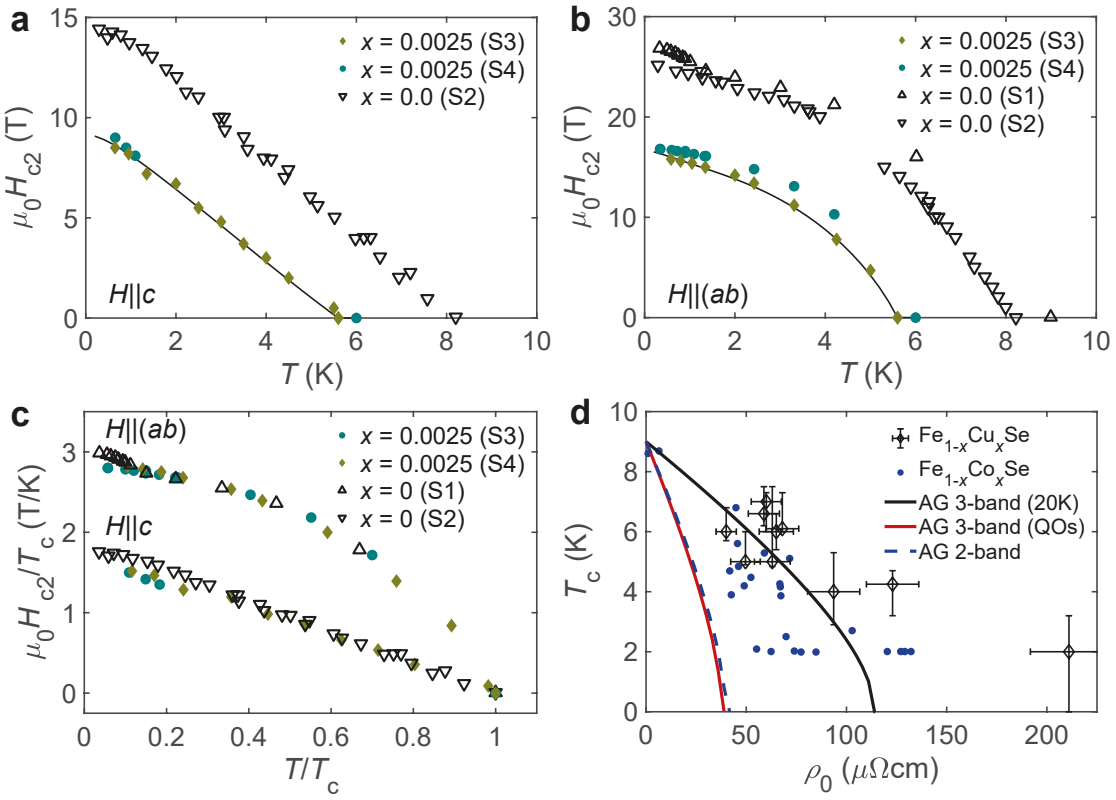

Figure 3.6: Superconducting properties of Cu-substituted FeSe. Upper critical field-temperature phase diagram of Cu-substituted FeSe for $x = 0.0025$ and FeSe for $H||c$ in (a) and $H||ab$ in (b), respectively. The position of $\mu_0 H_{c2}$ is defined as the offset of superconductivity at the zero resistance temperature. Data for FeSe are from Ref. [79] in (a) and Ref. [78] in (b). The data are described by a two-band model using similar parameters to those for FeSe [180] but with reduced η anisotropy factor, which corresponds to an $s_{\pm}$ pairing. (c) The reduced upper critical field, $\mu_0 H_{c2}/T_c$, versus reduced temperature, T/T_c, for two orientations in magnetic field using the data from (a) and (b). (d) The suppression of the superconducting transition temperature, T_c, form the impurity scattering expressed by the zero temperature residual resistivity ρ_0 of Cu-substituted FeSe (open diamonds) and Co-substituted FeSe (solid circles) [73]. The solid red line is a 3-band AG formalism as seen in [73] using parameters from quantum oscillations and previous magnetotransport studies [60, 170]. The effective masses used are: $m_{h1} = 4.5\ m_e$, $m_{e1} = 7\ m_e$, $m_{e2} = 1.5\ m_e$. The carrier densities used for the three band model are estimated from quantum oscillations at the lowest temperatures (low T) (red solid line): $n_h = 3.75 \times 10^{20}$ cm^{-3}, $n_{e1} = 4.33 \times 10^{20}$ cm^{-3} and $n_{e2} = 0.78 \times 10^{20}$ cm^{-3} and those from magnetotransport analysis at $T = 20$ K [170] (grey solid line) are: $n_1 = 1.45 \times 10^{20}$ cm^{-3}, $n_2 = 1.25 \times 10^{20}$ cm^{-3}, $n_1 = 0.22 \times 10^{20}$ cm^{-3}. The dashed line is a 2-band AG formalism reported previously by Urata et al. [73].

28 T [180], for which the Maki parameter would vary between 1-1.5 for the hole and electron pocket, increasing to 5.7 for smallest gap [180].

To further describe the temperature dependence of the upper critical field, a two-

band model in the clean limit is used (justified as the coherence length for $x = 0.0025$ is $\xi = 3.4\,\mathrm{nm} \ll \ell$). A model is chosen that is similar to those employed for thin flakes and bulk FeSe [166, 180]. Figures 3.6a and b show the fitted data[3] described by the following coupling parameters for both orientations using $\lambda_{11} = 0.81$, $\lambda_{22} = 0$, $\lambda_{12} = \lambda_{21} = 0.5$, $\eta = 0.025$ with $\alpha_1 = 1.6$ and $\alpha_2 = 0$ for $H||(ab)$. The coupling parameters are similar to FeSe, whereas the velocity anisotropy, η, is slightly larger than for the highly anisotropic FeSe [180]. This suggests that the Cu substitution, due to the increase in impurity scattering, is smearing the superconducting gap.

As many single crystals have been measured across the different batches of $Fe_{1-x}Cu_xSe$ the relationship between changes in T_c and the residual resistivity are considered here. Comparisons are made with results reported for Co substitution [73] and previous Cu-substituted FeSe [76]. Normally, the suppression of T_c by nonmagnetic impurities in iron-based superconductors with $s_\pm$ sign reversal superconducting states would obey the Abrikosov-Gor'kov (AG) formula [23], similar to a magnetic impurity in a single-band conventional BCS superconductor. A model specific to FeSe implies a full suppression of superconductivity when the residual resistivity is close to $4\,\mu\Omega$cm [73]. The general form of the AG formula requires knowledge of the scattering time in the system, τ. Here, the average scattering time is estimated using contributions of each band to the total conductivity in a parallel resistor network. Due to the magnetoresistance analysis reported earlier (Section 3.4) and the presence of an additional small electron pocket, a three-band model of the Fermi surface for FeSe is used. The effective masses and charge carrier densities are taken from quantum oscillations and magnetotransport studies at low temperatures in literature from reference [60, 170]. The estimate for an average scattering time then follows the method described in section 1.4.1. Three scenarios are considered and presented in Figure 3.6d:

[3]The software used to model the upper critical field was developed by Matthew Bristow and Alex Gower.

1. A three band model using the charge carrier density and mobility from quantum oscillations at the lowest temperature, values taken from reference [60] (red solid line, AG 3-band (QOs)).

2. A three band model as in (1), but now using the estimates of the charge carrier density and mobility at 20 K, values taken from reference [170] (grey solid line, AG 3-band (20K)).

3. A two band AG formalism for FeSe reported previously in reference [73] (blue dashed line, AG 2-band).

Figure 3.6d presents the variation of T_c with the residual resistivity for both Cu and Co substituted FeSe [73]. The errorbars for $Fe_{1-x}Cu_xSe$ are from errors in estimating the contact size (resistivity) and superconducting transition width (ΔT_c). Indeed, the suppression in superconductivity obeys the AG formula with the carrier density and mobility considered at 20 K (scenario (2)). On the other hand, for the other scenarios with the low temperature values (scenario (1)) and two band formalism (scenario (3)) require a stronger suppression rate. The decrease in carrier densities at 20 K are likely to be a consequence of very anisotropic scattering inside the nematic phase, whereas the low temperature values are from a regime of more dominant isotropic scattering. This finding is consistent with an $s_{\pm}$ pairing symmetry in FeSe, and emphasizes the importance of the anisotropic scattering inside the nematic phase and its effect on the anomalous magnetotransport. Such a pairing symmetry is in agreement with the finding from scanning tunnelling microscopy of FeSe [50].

3.8 Discussion

The focus of this study is understanding the role of the Cu substitution in FeSe, in particular on the changes of the electronic and superconducting behaviour that occur for small substitutions. Normally, the substitution with a metal-transition ion, such as Co, adds additional electrons into the Fe plane and affects its spin state [73], but Cu substitution is found to act mainly as a source of impurity, at least

for low substitutions [153]. As a result, the superconductivity is suppressed and resistivity increased. However, the field-induced magnetotransport power law and the upper critical field behaviour inside the nematic phase have surprisingly similar trends to FeSe. If Cu is an electron dopant, similar behaviour to the Co substitution would be expected, but is not observed for these low subsitutions. Recent ARPES studies find that only large Cu substitution in FeSe potentially dope the system with electrons [173], as long as the surface of the sample is not charging during photoemission studies of non-metallic samples. For Cu-doped NaFeAs, doping drives the system towards a more correlated Mott-like state due to strong electron-electron correlations and therefore localization of electrons [152], .

Superconductivity of FeSe is strongly suppressed in the presence of either Cu or Co [73, 76], as compared with the isoelectronic substitution of S and Te [55, 56]. Spin fluctuations, with potential orbitally-dependent character, are likely responsible for the superconducting pairing in the FeSe family, and remain unchanged with increasing S, but are strongly suppressed by Co substitution [181]. This would lead to an $s_{\pm}$ pairing mechanism supporting both nodeless and nodal states, and would stabilize highly anisotropic superconducting gaps on both electron and hole pockets [50]. The presence of such nodes or gap minima are found in crystals of higher quality only, with a small amount of disorder being sufficient to smear out the small gap in more isotropic lower quality crystals of FeSe [182]. The Cu substitution, which introduces a significant amount of impurity scattering, leads to a suppression of velocity anisotropy, as detected from the parametrization of the upper critical field (Figure 3.6). The suppression of superconductivity with Cu and Co impurity substitution is consistent with sign changing $s_{\pm}$ pairing, described by the AG formula. However, the effect of anisotropic scattering can affect the apparent drop in the carrier density inside the nematic phase [170] and consequently requires consideration in an extended AG formula.

Next, I compare the effect of impurities induced by Cu in FeSe to those introduced by electron irradiation (2.5 MeV) [161]. Interestingly, the superconducting transition temperature is slightly enhanced by the point-like disorder induced by electron

irradiation, and it was suggested that the irradiation-induced Frenkel defects enhance the pair interaction, in turn enhancing the spin fluctuations [161]. This modest increase in T_c of 0.4 K is accompanied by a decrease in the nematic temperature T_s of 0.9 K. The small change in T_c could be related to the relatively low concentration of radiation defects, as well as the location of these defects in the conducting Fe layers or outside in the van der Waals gaps of FeSe. Therefore, the small changes in the transition temperatures with electron irradiation do not follow the trends observed by Cu-doping, but are closer to the behaviour of FeSe substituted with S outside the Fe plane [55], as well as FeSe under the effect of small applied pressure [87] or uniaxial strain [167]. The variation in the response of superconductivity to different kinds of impurities suggests that the pairing mechanism has a strong three-dimensional dependence that needs to be taken into account, as suggested by k_z dependent ARPES studies [183].

The precise power law of the temperature dependence of resistivity is often influenced by the nature of the critical fluctuations, its dimensionality, the presence of disorder and its proximity to quantum critical points. At lowest temperatures, the resistivity of $FeSe_{1-x}S_x$ displays a Fermi-liquid-like behaviour ($\rho \sim T^2$), whereas inside the nematic phase a regime of linear resistivity was associated with the presence of spin fluctuations [71, 105]. Interestingly, in FeSe samples with larger amounts of disorder (smaller RRR values) the resistivity seems to display linear behaviour at the lowest temperatures. This behaviour was found in FeSe crystals with small RRR values [71, 174], Cu-substituted FeSe in this work, and thin flakes of FeSe [130]. In the vicinity of an itinerant antiferromagnetic quantum critical point, as proposed for FeSe [184], the resistivity is strongly affected by small amounts of disorder. Strongly anisotropic scattering due to spin fluctuations in the presence of disorder would generate an anomalous temperature dependence of resistivity with exponents varying between $n = 1$ and 1.5 [164]. Here, the linear T resistivity persists over a large temperature regime, to the lowest temperatures, but is superimposed on a large background caused by the resistance of the channel dominated by impurity scattering. For higher Cu substitution, the Mott-Ioffe-Regel limit is reached, in which

the usual description of a metal in terms of ballistically propagating quasiparticles is no longer valid, and this could lead to suppression of spin fluctuations and enhanced local magnetism that would lead to the disappearance of superconductivity.

3.9 Conclusions

In summary, this study has presented conclusively the effect of impurity scattering induced by low level Cu substitution on the electronic and superconducting properties of FeSe. The introduction of Cu rapidly suppresses both the nematic and superconducting phases, whilst increasing the impurity scattering in the system. Detailed studies for a very low concentration ($x = 0.0025$) investigated the suppression of superconductivity, the upper critical fields, and magnetotransport in high magnetic fields. In particular, both the suppression of superconductivity and the behaviour of the upper critical field can be accounted for by taking into account the multi-band effects in the sign-reversal symmetry ($s_{\pm}$) of the order parameter. This is true for the relationship between reduction in T_c and increase in residual resistivity described by the AG formula when anisotropic scattering effects reducing the charge carrier density inside the nematic phase are considered. The magnetotransport studies reveal suppression of the charge carrier mobilities, and a reduction in the magnetoresistance, due to the increase in the scattering rate in Cu-substituted FeSe. However, the power law of resistivity ($H^{1.6}$) seems to have a similar field dependence to FeSe, suggesting the electron-electron collisions remain unaltered by the electron-impurity collisions for low Cu substitutions. This study raises questions about the universality of impurities through in-plane doping, the effect of irradiation, sample thickness in thin flakes, and growth conditions in suppressing the superconductivity of FeSe.

3.10 Additional Figures

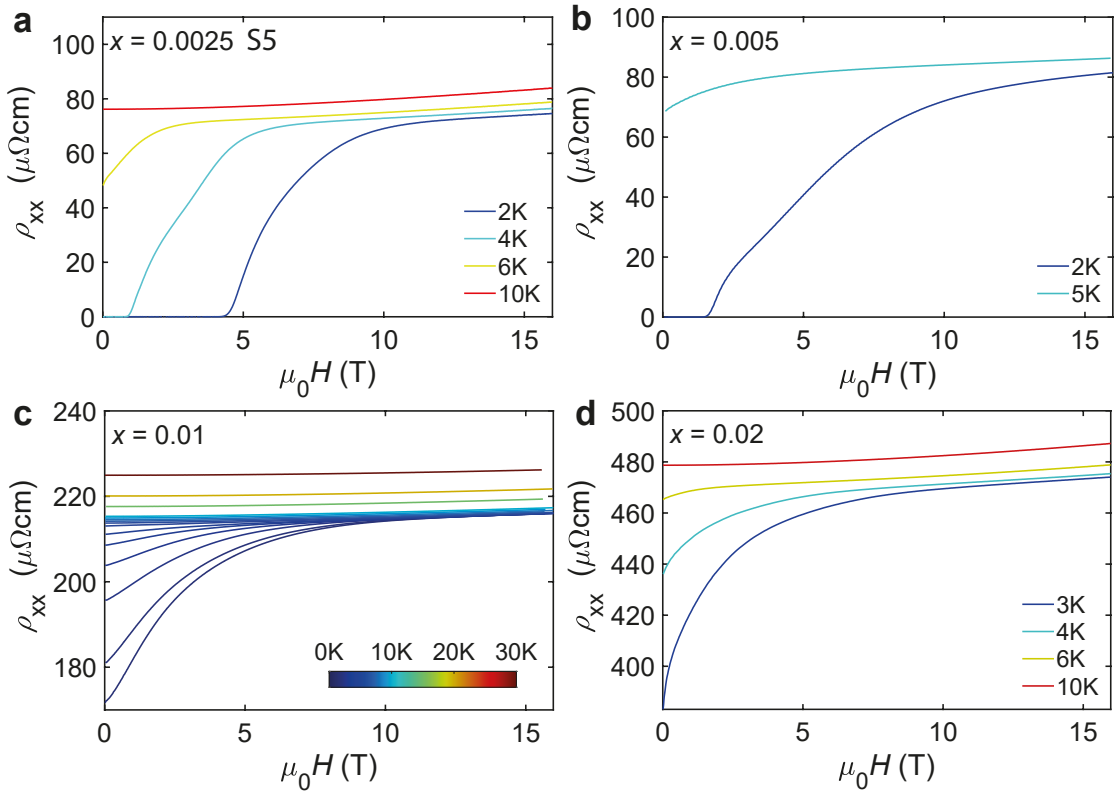

Figure 3.7: Magnetotransport of Cu-substituted FeSe. Longitudinal resistivity, ρ_{xx}, as a function of magnetic field up to 16 T at constant temperatures for different Cu substitutions: (a) $x = 0.0025$, (b) $x = 0.005$, (c) $x = 0.01$, (d) $x = 0.02$.

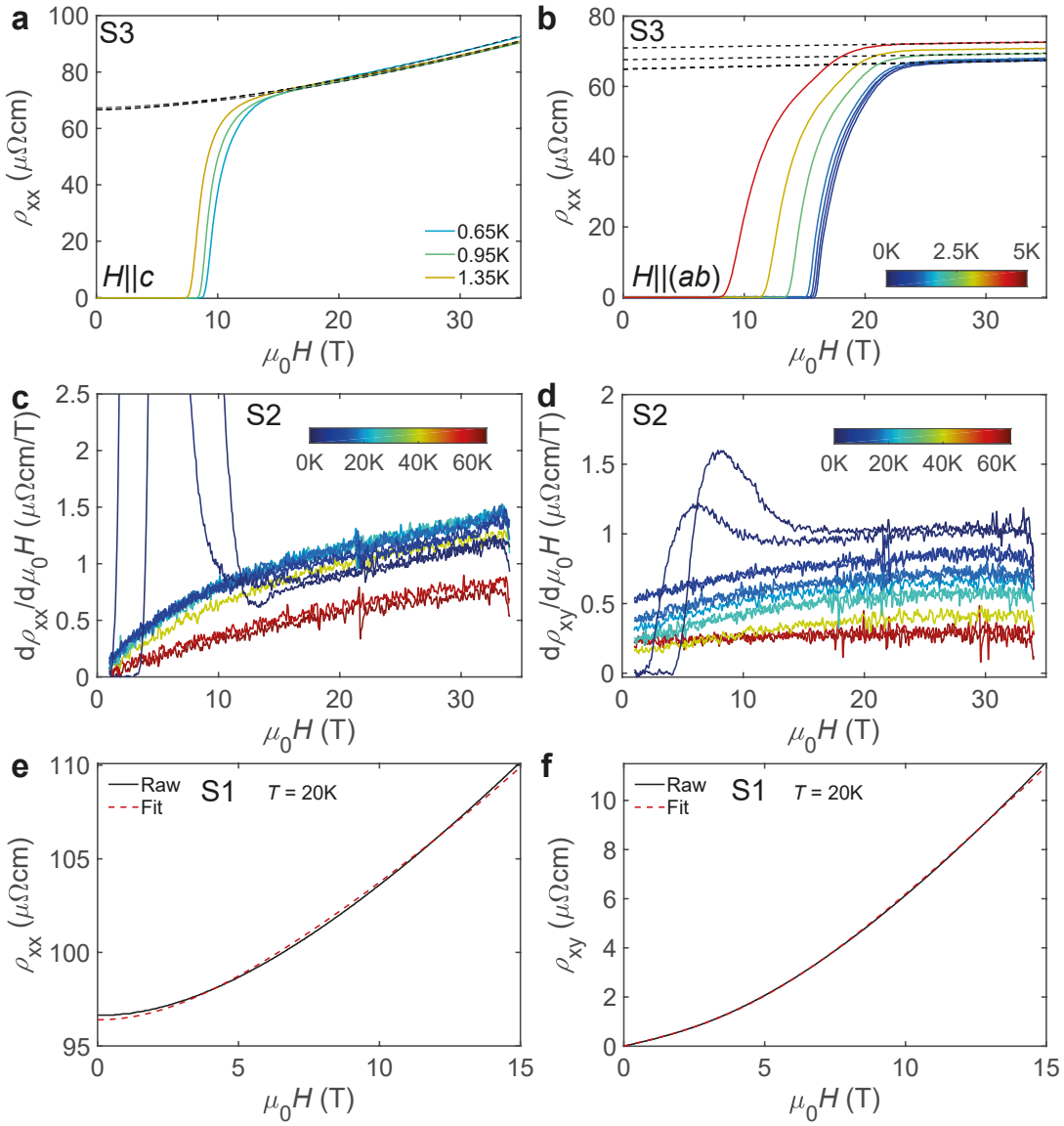

Figure 3.8: Magnetotransport behaviour of $Fe_{1-x}Cu_xSe$, $x = 0.0025$. (a) Longitudinal resistivity, ρ_{xx}, with the magnetic field $H||c$ for sample S3. Dashed lines are fits to a $(\mu_0 H)^{1.6}$ field dependence, in the normal state, to extrapolate the zero-field resistivity at low temperatures in Figure 3.3c. (b) Longitudinal resistivity, ρ_{xx} with $H||(ab)$ for sample S3. Dashed lines are fits to a linear dependence in magnetic field, in the normal state, to extrapolate the zero-field resistivity in magnetic field in Figure 3.3c. (c) The derivatives of ρ_{xx} and (d) ρ_{xy} in magnetic field of sample S2 (raw data in Figure 3.2(c) and (d)). An example of simultaneous fitting to a three-carrier model of the resistivity component ρ_{xx} in (e) and ρ_{xy} in (f) (red dashed lines) measured at $T = 20\,\mathrm{K}$.

4

Pressure effects in $Fe_{1-x}Cu_xSe$

This next chapter investigates the phase diagram of $Fe_{1-x}Cu_xSe$ $x = 0.0025$ under applied pressure to understand the changes induced by the impurity scattering. The superconductivity of FeSe is enhanced under applied pressure, and its rich phase diagram contains different phases competing with superconductivity, such as the nematic electronic phase and spin density wave phase. From the previous chapter, I reported the strong impurity scattering effects from the Cu substitution on the superconducting and nematic phases. Here, I investigate how an impurity inside the Fe plane induced by the Cu substitution can alter the balance between competing electronic phases of FeSe at high pressures. At low pressures, the nematic and superconducting phases remain suppressed compared to FeSe. At high pressures, above 10 kbar, the superconductivity becomes comparable to FeSe, but the resistivity shows no signatures of magnetic order, which in FeSe presented as an upturn in resistivity and assigned to a spin density wave phase. However, with large magnetic fields the resistivity does shows an upturn in 15 T, which displays hysteretic behaviour. Hence, the high pressure superconducting phase of FeSe is demonstrated to be robust even in the presence of a disruptive Cu impurity, whereas the magnetic phase is suppressed. This could suggest the high pressure superconducting phase has a sign-preserving order parameter due to the robustness of this phase. In addition, I will analyse the magnetotransport across the pressure

phase diagram to show a reduction of the charge carrier mobilities at high pressure, which is accompanied by an increase in the charge carrier densities[1].

4.1 Introduction

Hydrostatic pressure is an invaluable tool to stabilize novel electronic phases as well as to enhance superconductivity towards room temperature [14]. Among unconventional superconductors, FeSe displays the signature of a nematic electronic phase before becoming superconducting at low temperatures below 9 K [155]. However, with applied pressure the nematic phase is suppressed and the superconducting transition temperature is enhanced towards 37 K close to 6.3 GPa [16, 69, 72, 85, 90–92]. This enhanced superconductivity at high pressures occurs in a region in which a new electronic phase, believed to be of magnetic origin is present [86]. The volume and the local magnetic field of this magnetic phase is strongly dependent on the applied pressure [86] and it coincides with a first-order structural transition at high pressures, suggesting a potential magnetoelastic coupling and phase coexistence [93].

Another tuning parameter for the superconducting and nematic phases of FeSe is the chemical substitution either inside or outside the conducting Fe plane. As shown in the previous chapter, the Cu substitution is highly disruptive due to the larger size of the Cu relative to the Fe ions inside the conducting planes. This introduces significant impurity scattering that mainfests in most of the electronic properties probed by transport measurements. The nematic and superconducting phases are quickly suppressed, fully by 3% Cu substitution, and the carrier mobilities are quickly reduced even with a small amount of Cu substitution [75, 76, 149]. With increasing Cu substitution the system undergoes a metal-to-insulator transition and it could lead to the stabilization of local magnetic moments at Fe sites [75, 157, 173]. However, under applied hydrostatic pressure the superconductivity could be restored by suppressing the insulating behaviour in powder samples [158] or quenching from high pressures in single crystals [160]. Theoretical studies suggest

[1]This chapter is adapted from work published in Physical Review Research **4**, 043123 [185]

that non-magnetic disorder has the potential to enhance superconductivity in a multiband system [186], and thus the Cu substitution can be used to assess this proposal and to understand its unusual manifestation.

This chapter will first look at the results in the absence of an applied magnetic field. The transport measurements up to 20 kbar present the zero-field phase diagram and reveal the evolution of the homogeneity of the superconducting state. Following that, magnetotransport measurements will be presented and used to analyse the presence of the magnetic phase, and changes to the charge carrier mobilities and densities. The upper critical field is extracted from the in-field measurements and compared to FeSe under pressure. Finally, the temperature-pressure phase diagram of Cu substituted FeSe is presented and compared to FeSe in zero-field, in high-field and when scaled in temperature by the nematic transition.

4.2 Methods

Single crystals of $Fe_{1-x}Cu_xSe$ were grown by Shiv Singh, with the nominal composition of $x = 0.0025(4)$ were grown using the $KCl/AlCl_3$ chemical vapour transport method [102, 162], as reported in the previous chapter. Magnetotransport and Hall effect measurements under pressure using a 5-contact configuration were carried out in a 16 T Quantum Design PPMS and an ElectroLab High Pressure Cell, using Daphne Oil 7373 which ensures hydrostatic conditions up to about 21 kbar. The pressure inside this cell was determined via the superconducting transition temperature of Sn after cancelling the remanent field in the magnet. In-plane transport measurements ($I||(ab)$) were performed in a 16 T Quantum Design PPMS, with the magnetic field applied along the c-axis, for ambient and pressure measurements. The resistivity ρ_{xx} and Hall ρ_{xy} components were measured using a low-frequency five-probe technique and were separated by (anti)symmetrizing data measured in positive and negative magnetic fields. Good electrical contacts were achieved by In soldering along the long edges of the single crystals, and electrical currents up to 1 mA (peak-to-peak) were used to avoid heating. Errors in estimating the exact contact positions and their size result in errors in the absolute values of

resistivity being up to 13% of the total value. The superconducting transition, T_c, is defined as the offset temperature or field, unless stated otherwise. The nematic structural transition, T_s, and the high pressure magnetic phase transition, T_m, are defined by the minimum in the derivative of the resistivity as a function of temperature. All experimental preparation and measurements, and the analysis of said results, in this chapter was performed by the author.

4.3 Transport studies under applied pressure

Figure 4.1a shows the temperature dependence of the resistivity in the absence of a magnetic field for pressures up to 20 kbar for a sample of $Fe_{0.9975}Cu_{0.0025}Se$ (see shifted curves in Figure 4.2a). Recalling from Chapter 3, due to the presence of Cu, the nematic transition T_s, at 80 K, and superconducting transition, T_c, at 6.2 K are suppressed, as compared with FeSe. The structural transition into the nematic phase is linearly suppressed with applied pressure up to 15 kbar, similar to FeSe [94]. In contrast, the superconductivity is continually enhanced with applied pressure up to 20 kbar, without showing any dome like-feature inside the nematic phase, as is visible for FeSe under pressure [94]. The superconducting transition width at low pressures, $\Delta T_c = T_{on} - T_{off}$, is around 1.3(2) K, before increasing by a factor of 2 at higher pressures above 10 kbar, as shown in Figure 4.1b. Whilst in FeSe under pressure the superconducting transition width is narrower at low pressures (1 K), this increases significantly towards 7 K for higher pressures where the magnetic phase is present [187]. This suggests that either the high pressure superconducting phase becomes inhomogeneous through competition with another phase, or that strong superconducting and/or magnetic fluctuations are present in this high pressure regime [94].

The resistivity behaviour reveals additional information about the normal electronic phases as a function of pressure. The resistivity at room temperature initially decreases with applied pressure, indicating that the pressure increases in-plane transfer integrals, increasing the bandwidth, and the system becomes a better metal, as shown in Figure 4.1b. However, at pressures above 15 kbar

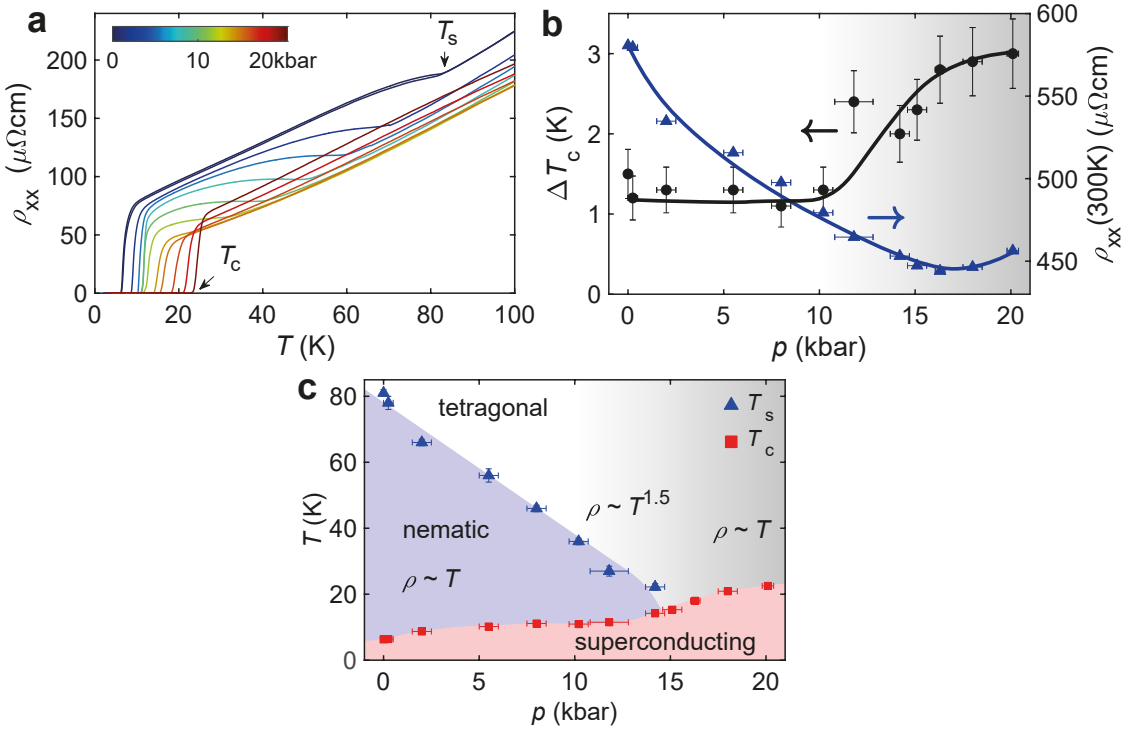

Figure 4.1: Zero-field transport properties of $Fe_{1-x}Cu_xSe$ $x = 0.0025$ under pressure. (a) Temperature dependence of the resistivity as a function of applied pressure. (b) The evolution of the superconducting transition width, $\Delta T_c = T_{on} - T_{off}$ (black circles), and the resistivity at 300 K (blue triangles) with pressure. (c) Temperature-pressure phase diagram in zero magnetic field tuned by pressure. The nematic phase occurs at T_s (blue triangles) and the superconducting phase at T_c (red squares). The phase diagram can be divided into different regions: the low pressure region up to $p_1 = 10$ kbar, inside the nematic phase, the high-pressure region above $p_2 = 15$ kbar, once the nematic phase is fully suppressed, and the intermediate pressure region between p_1 and p_2. Shaded regions indicate the different phase boundaries.

this trend reverses with resistivity increasing, and matches the trends observed in the low temperature behaviour with ρ_0 (Figure 4.2b). The substitution of Cu in FeSe increases the impurity scattering and the residual resistivity, leading to the suppression of superconductivity and inducing a linear dependence down to 0.4 K, see Chapter 3.

Figure 4.2b shows the mean free path, $\ell = \frac{\pi c\hbar}{Ne^2 k_F \rho_0}$, calculated with a constant value for c and k_F. For 0 to 20 kbar, c for FeSe changes at a rate of -0.0088 Å/kbar, from a starting value of 5.5237 Å, which is not a significant change. Similarly, k_F will change with pressure as is known from FeSe quantum oscillation measurements [87], however the exact change is not known for Cu-FeSe and so is assumed to

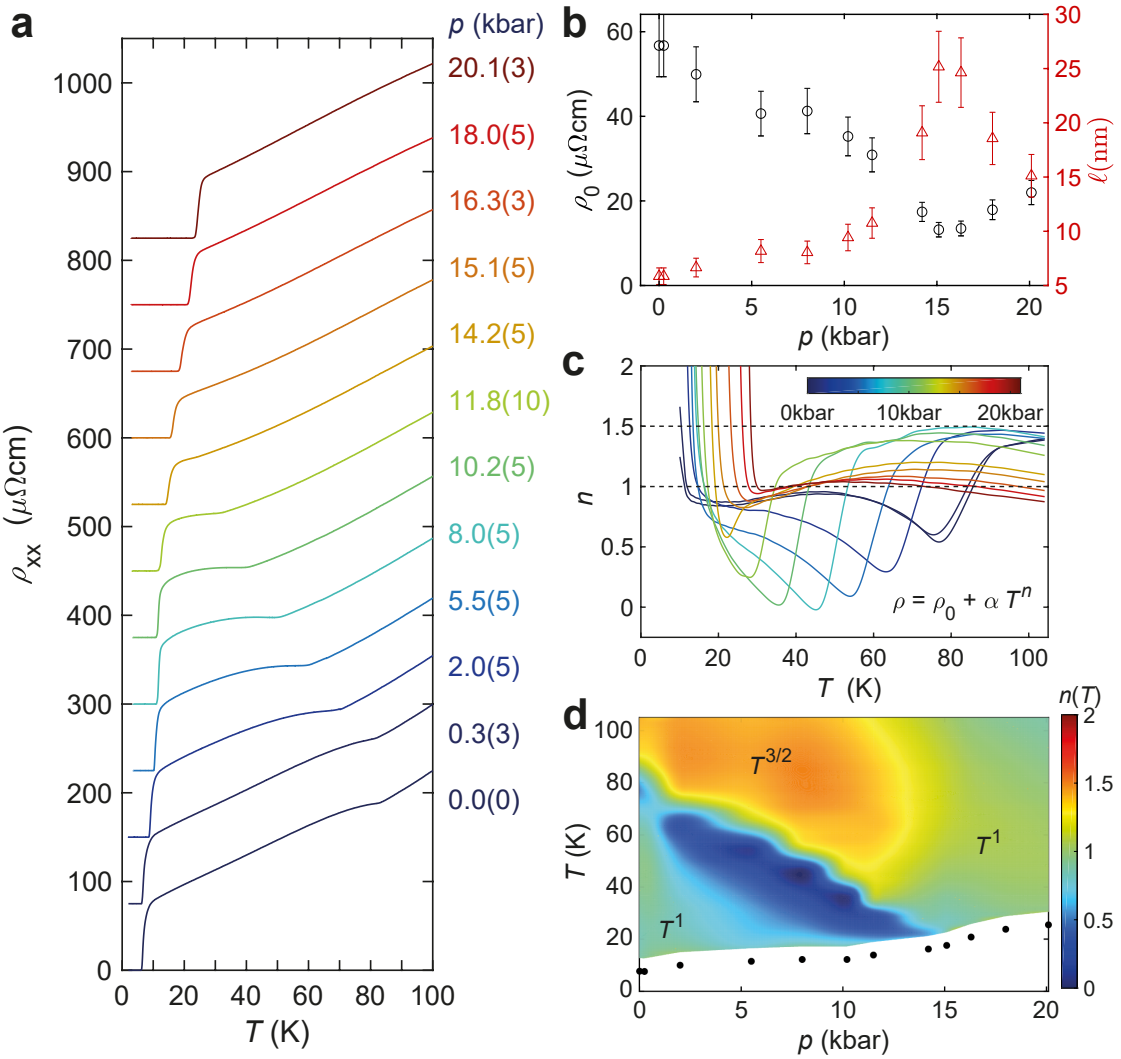

Figure 4.2: The zero-field resistivity and the local resistivity exponent of $Fe_{1-x}Cu_xSe$ $x = 0.0025$ under pressure. (a) Resistivity temperature dependence in 0 T for each pressure, curves are shifted for clarity. Figure 4.1a shows the curves not shifted. (b) The pressure dependence of the zero-temperature resistivity, ρ_0, extracted from a linear extrapolation of the zero-field resistivity above the onset of superconductivity similar to the ambient pressure dependence [149]. The red triangles are the mean free path, calculated from the ρ_0 values. (c) The temperature dependence of the local resistivity exponent, n, for different pressures in zero magnetic field and (d) its interpolated colour map as a function of temperature and pressure.

be constant for this analysis. Additionally, it is unknown exactly how large the Fermi surface is for Cu-FeSe inside the magnetic phase.

To check the resistivity temperature dependence, the resistivity can be expressed using the form $\rho = \rho_0 + \alpha T^n$, where n is the local resistivity temperature exponent. At ambient pressure the zero-temperature resistivity, ρ_0, is obtained by using high

magnetic fields to suppress the superconductivity at temperatures below T_c and extrapolating the high-field dependence at zero-field for each temperature [149]. Here, under pressure a linear temperature dependence ($n = 1$) is found both inside the nematic phase at low pressures, as well as in the high pressure phase, as illustrated by the temperature dependence of the resistivity exponent, n, shown in Figures 4.2c and d. In the tetragonal phase at high temperatures, a power law of $T^{1.5}$ describes the resistivity well, which is similar to that found in both $FeSe_{1-x}S_x$ tuned by the isoelectronic substitution or applied pressure [71, 105].

Interestingly, in the high pressure regime above 10 kbar the resistivity of Cu-substituted FeSe shows no additional anomaly associated to other phase transitions, see Figures 4.1a or 4.2a. This is in contrast to FeSe where an anomaly of a clear upturn in the resistivity was associated with the presence of a magnetic transition, at temperatures higher than T_c [69, 94, 187, 188].

From these transport measurements, the zero-field temperature-pressure phase diagram of $Fe_{0.9975}Cu_{0.0025}Se$ up to 20 kbar is presented in Figure 4.1c. The superconducting transition temperature at high pressure increases once the nematicity is suppressed even in the presence of the Cu impurity. This behaviour is in agreement with previous studies in powder samples of Cu substituted FeSe ($x = 0.04$), where insulating behaviour is transformed into superconducting behaviour with applied pressure, although not to a zero resistance state [158]. Furthermore, the phase diagram in zero-magnetic field in the presence of the Cu impurity inside the conducting plane is remarkably similar to that of $FeSe_{1-x}S_x$ under pressure for various x, in which the isoelectronic substitution takes place outside the conducting plane [104–107], as will be shown in Chapter 6. The phase diagram is split into three regions here. First, the low pressure region up to $p_1 = 10$ kbar, inside the nematic phase up to the point where the superconducting transition width increases. Second, from p_1 up to $p_2 = 15$ kbar at the nematic phase boundary. Finally, above p_2, where the nematic phase is fully suppressed.

4.4 The high-pressure electronic phase in high magnetic fields

Next, high magnetic fields are used to suppress the superconductivity to reveal if there are any hidden electronic phases under the superconducting dome, and to explore the normal electronic behaviour at lower temperatures. Figure 4.3a shows the temperature dependence of resistivity in different magnetic fields at 17 kbar ($>p_2$). At this pressure, the nematicity has been suppressed already. Here, an upturn in resistivity occurs at T_m as the superconducting transition temperature is reduced in large enough magnetic field. This anomaly shows hysteretic behaviour between the cooling and warming curve, independent of the temperature sweep rate, indicative of a first-order phase transition, as shown in Figure 4.3b. In FeSe, the high pressure magnetic phase displays evidence of hysteresis in heat capacity and NMR studies implying the existence of a concomitant structural transition via a spin-lattice coupling [94, 99]. The temperature dependence of the resistivity in 15 T shows smooth changes in the upturn anomaly as a function of the applied pressure, as shown in Figure 4.3c and the corresponding derivatives in Figure 4.3d. As the pressure increases, this anomaly shifts to higher temperatures and it tracks closely the zero field superconducting transition temperature. In FeSe, this anomaly in transport was associated to a magnetic phase and it occurs already in zero-field at temperatures higher than where superconductivity is stabilized ($T_m > T_c$) but its appearance in resistivity seems to vary strongly with pressure, either as an increase, decrease or change in slope [69].

4.5 Magnetotransport behaviour

The magnetotransport behaviour can provide insightful details related to the evolution in the electronic structure and scattering with applied pressure. Figures 4.4a and b show the field dependence of the longitudinal and Hall resistivity, ρ_{xx} and ρ_{xy}, at 13.3 kbar. A linear field dependence of the Hall component is a hallmark sign of two-band behaviour, which seems to manifest at high pressures, as shown

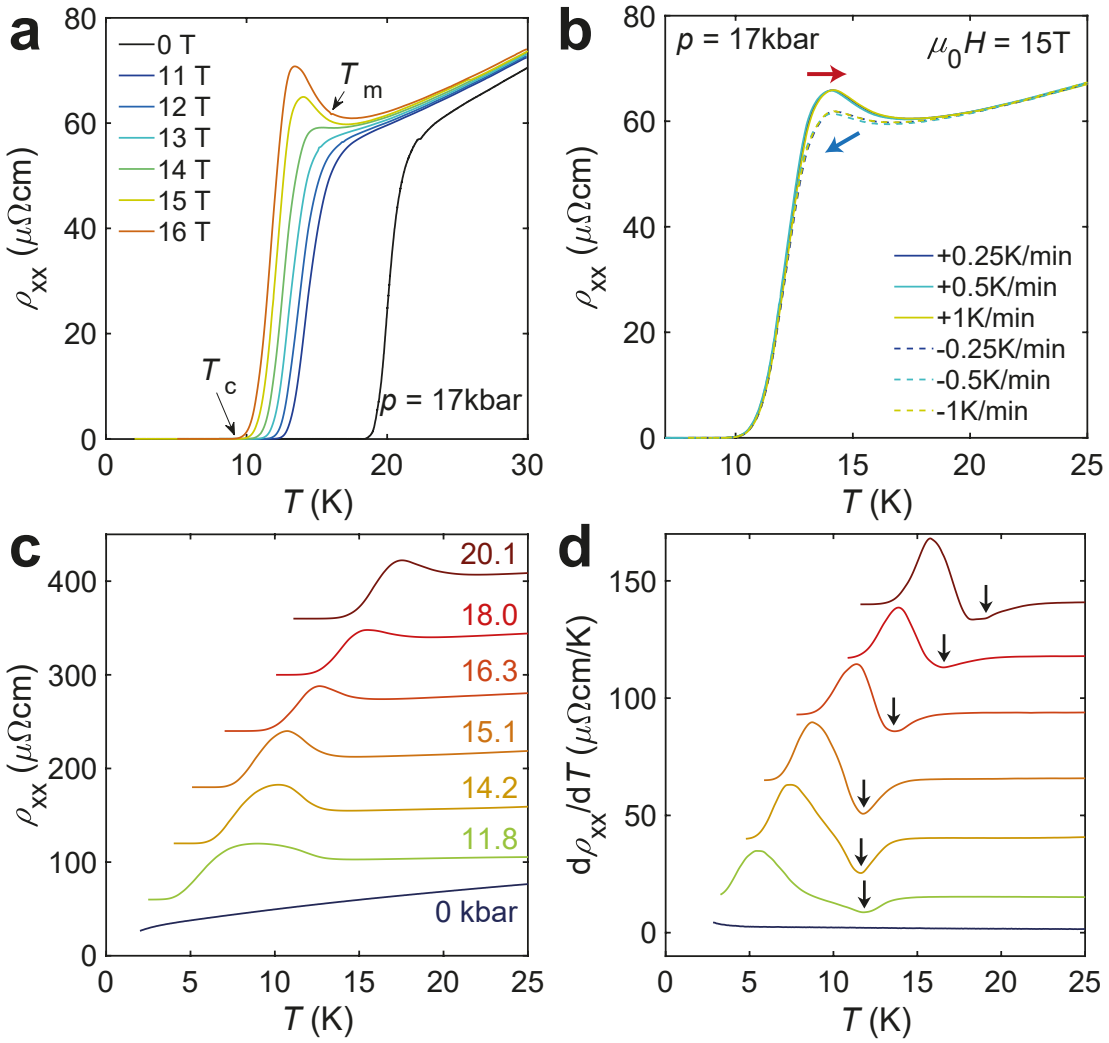

Figure 4.3: The transport behaviour in magnetic field of the $Fe_{1-x}Cu_xSe$ $x = 0.0025$ under pressure. (a) The temperature dependence of the longitudinal resistivity in different magnetic fields at $p = 17$ kbar. (b) The resistivity upturn at T_m in 15 T at 17 kbar using various temperature sweep rates. The solid lines correspond to the warming sweeps whereas the dashed lines correspond to the cooling sweeps. (c) The temperature dependence of resistivity in a magnetic field of 15 T ($H||c$) for different applied pressures and (d) their corresponding derivatives. The value of T_m is defined as the minimum in the derivative and indicated by arrows, similar to FeSe [104]. Curves are offset for clarity.

in Figure 4.5 and in the tetragonal phase, as shown in Figure 4.10 in Section 4.10. Figure 4.12f shows the Hall coefficient, R_H, for different pressures extracted from the slope of the Hall resistivity, ρ_{xy}, in low fields, which is positive and generally increases with decreasing temperature. This is in stark contrast to FeSe where R_H is negative at low temperatures inside the nematic phase, and only becomes

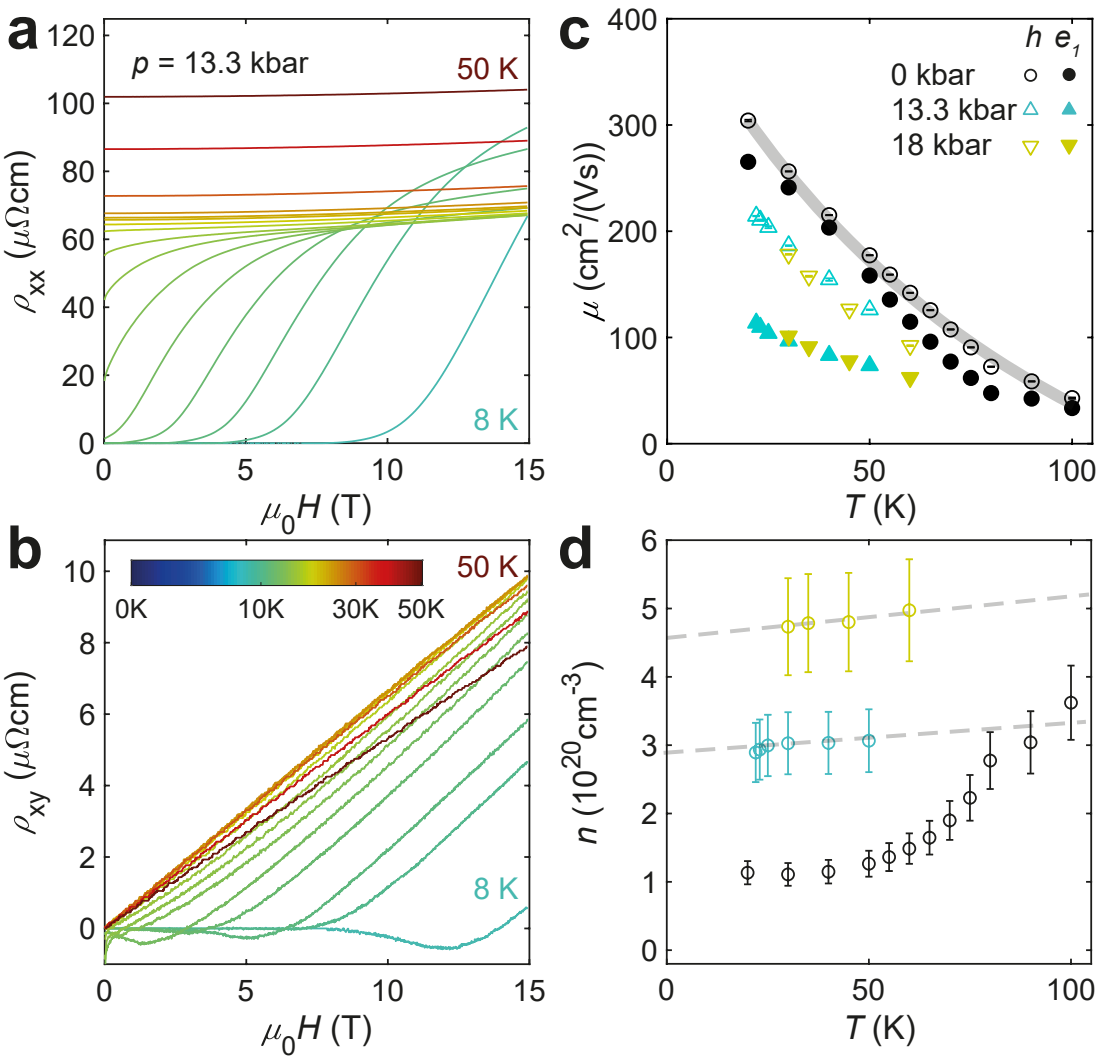

Figure 4.4: Magnetotransport of $Fe_{1-x}Cu_xSe$ $x = 0.0025$ under pressure. Field dependence of (a) the longitudinal resistivity, ρ_{xx}, and (b) the Hall resistivity, ρ_{xy} at a pressure of $p = 13.3$ kbar. (c) Mobility and (d) carrier density of each charge carrier (holes, h, and electrons, e_1) at different pressures considering a two-band compensated model ($n_h = n_e$). For 0 kbar only data up to 7 T is used in the two band model, and results from a three band model up to 15 T, as shown in Chapter 3, and shown for comparison in Figure 4.12 in Section 4.10. Solid and dashed grey lines are guides to the eye.

positive at quite high pressures ($\sim$3.8 GPa and above) [77, 170, 189].

Magnetotransport measurements enable construction of the mobility spectrum, where peaks appear at the mobilities of different hole and electron carriers. The mobility peaks shift to slightly lower mobilities with increasing pressure, as shown in Figure 4.6. However, by simultaneously fitting the ρ_{xx} and ρ_{xy} to a two-band compensated model the charge carrier density and mobilities can be extracted

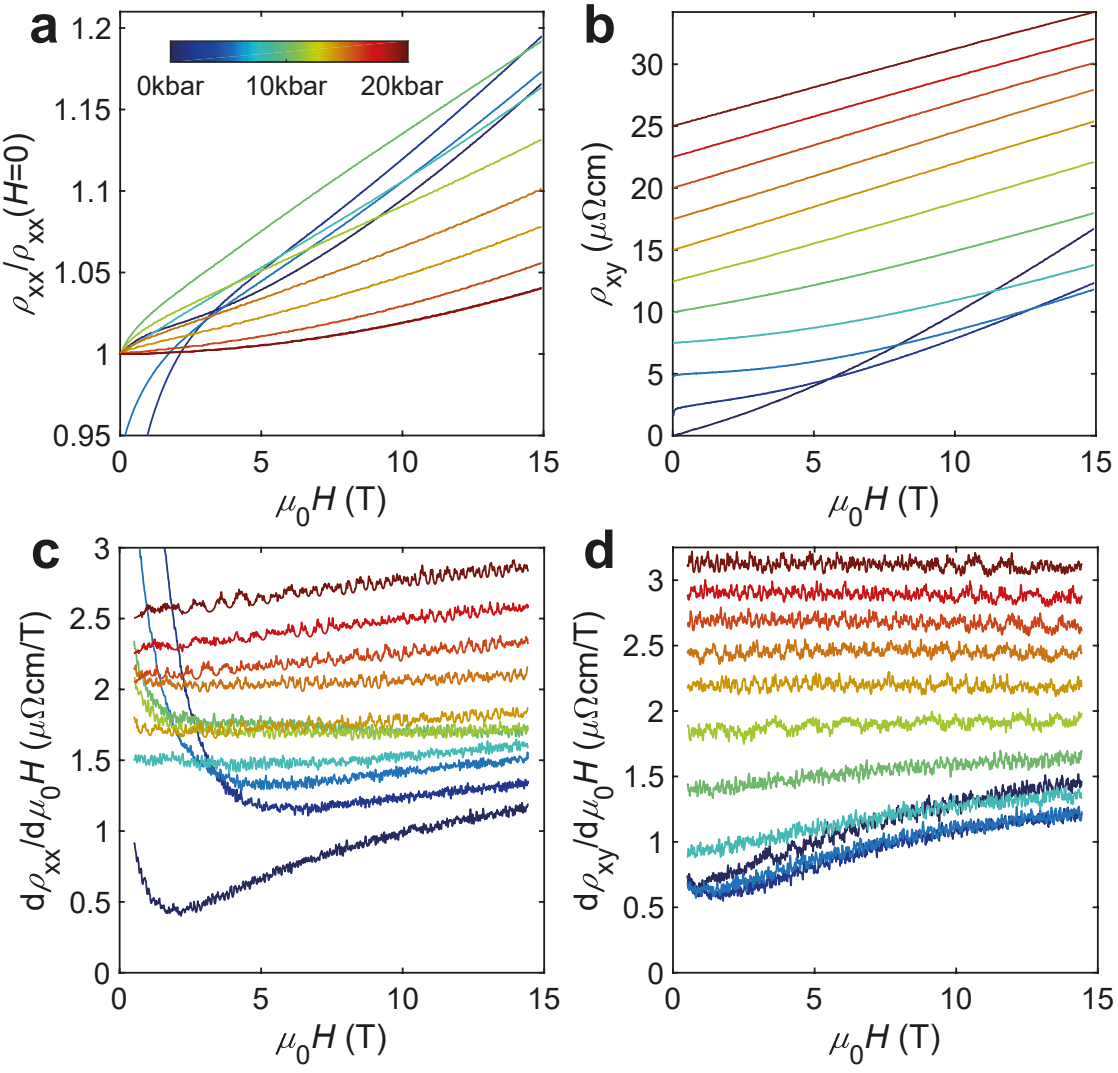

Figure 4.5: Magnetotransport behaviour in the normal phase of $Fe_{1-x}Cu_xSe$ $x = 0.0025$ under pressure. The field dependence of (a) ρ_{xx} and (b) ρ_{xy} at a fixed temperature just above the onset of superconductivity for different pressures and their corresponding derivatives in relation to the magnetic field in (c) and (d), respectively. The derivatives of ρ_{xy} show a constant behaviour at high-pressures above 10 kbar indicative of two-band behaviour. Note, for the three lowest pressures the highest temperature sweep available is used, which is not above the onset of superconductivity.

as a function of temperature and pressure. At ambient pressure a three-band compensated model can account for the non-linear Hall resistivity, as in the previous chapter, and similar to FeSe [77, 149, 190], whereas at high pressures a two-band compensated model is more appropriate. Here, a two-band compensated model is used in the low-field regime (< 7 T) for ambient pressure for comparison to the high pressure results. Figures 4.4c and d compare the temperature dependence

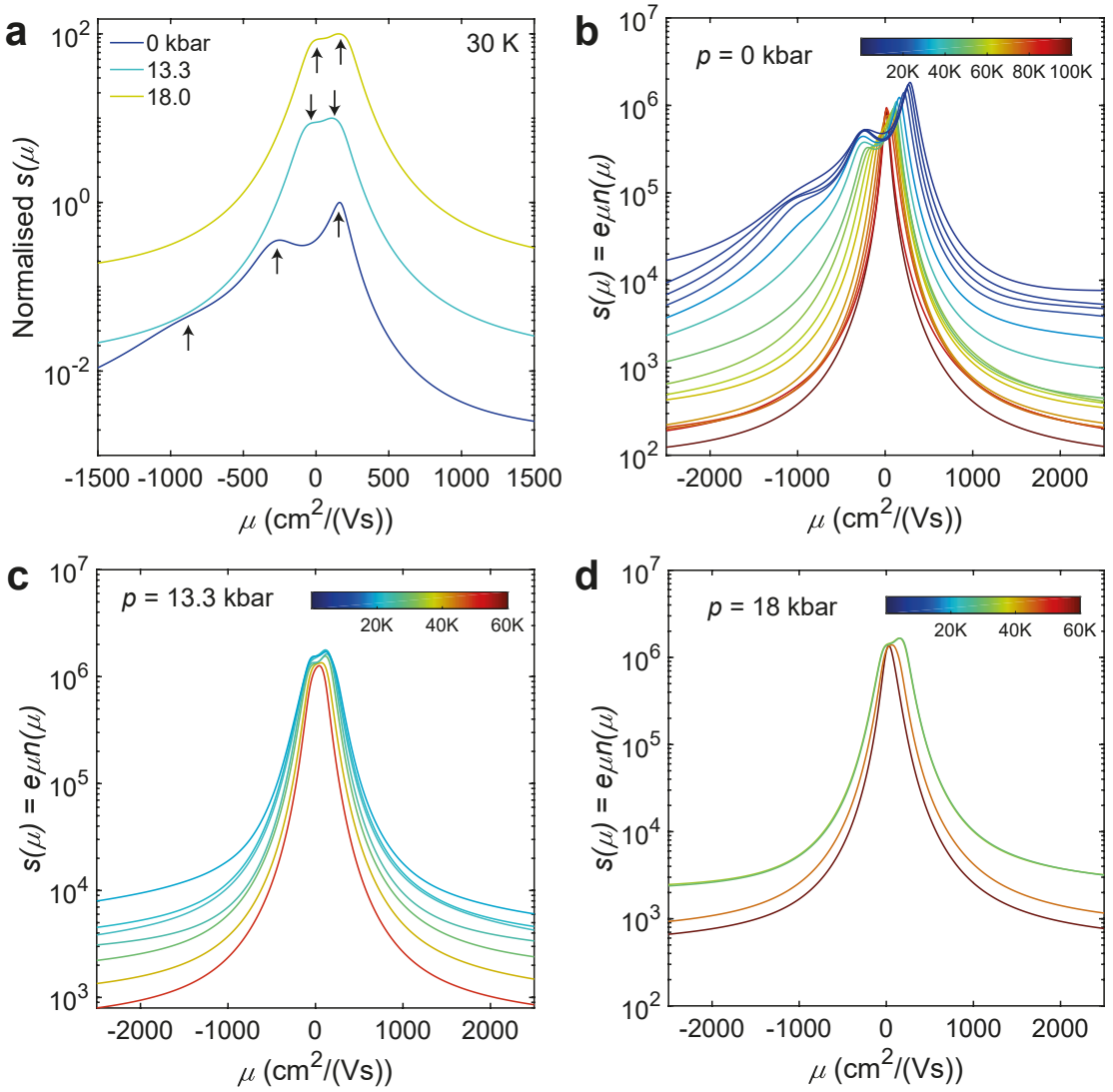

Figure 4.6: Mobility spectrum at different pressures of $Fe_{1-x}Cu_xSe$ $x = 0.0025$. (a) The mobility spectrum extracted from magnetotransport data [129] for different pressures at 30 K. Arrows indicate the positions of mobilities the positive and negative charge carriers. Mobility spectrum are extracted for constant temperatures at different pressures of (b) 0 kbar, (c) 13.3 kbar and (d) 18 kbar, respectively.

of the charge carrier mobilities and carrier densities at various pressures. As the system enters the nematic phase from high temperatures there is a significant decrease in the carrier density due to the development of anisotropic scattering, as found with FeSe [77, 190]. In the high pressure phase, above p_2, the carrier density is significantly larger, indicative of an increase of the Fermi surface size similar to findings for $FeSe_{1-x}S_x$ [105]. Furthermore, the mobilities of both holes and electrons are suppressed with applied pressure, with stronger suppression for

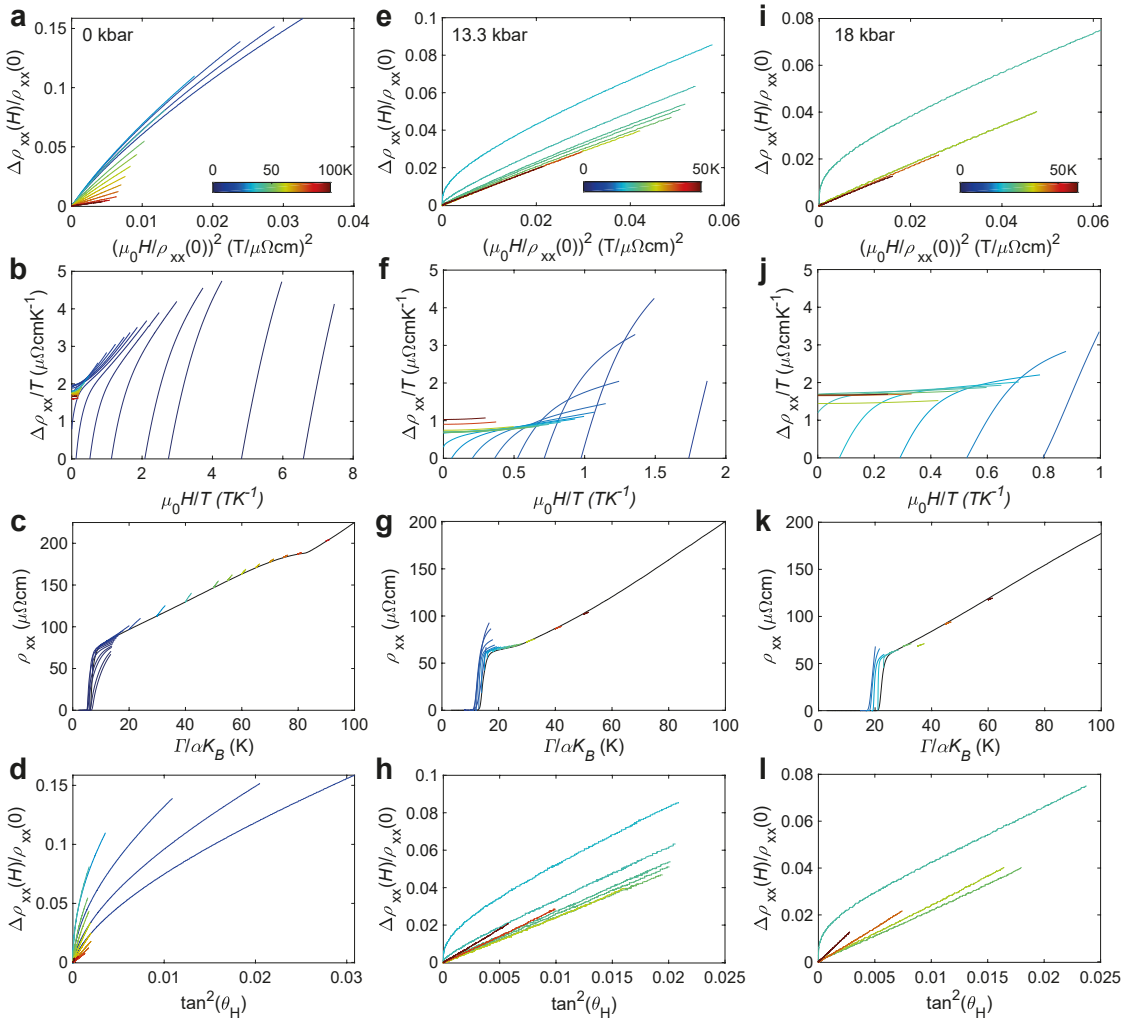

Figure 4.7: Different scaling rules applied to $Fe_{1-x}Cu_xSe$ ($x = 0.0025$) at different pressures. These are all for the longitudinal magnetoresistance with $H||c$. (a) - (d) 0 kbar, (e) - (h) 13.3 kbar, (i) - (l) 18 kbar. (a, e, i) Kohler's rule scaling, $\Delta\rho_{xx}(\mu_0 H)/\rho_{xx}(0) \sim (\mu_0 H/\rho_{xx}(\mu_0 H = 0))^2$, with $\Delta\rho_{xx}(\mu_0 H, T) = \rho_{xx}(\mu_0 H, T) - \rho_{xx}(0, T)$. For all three pressures Kohler's rule is violated, indicating the transport is not dominated by a single scattering time. (b, f, j) Field-temperature scaling using $\Delta\rho_{xx}(\mu_0 H)/\rho_0 \sim \mu_0 H/T$, where $\Delta\rho_{xx}(\mu_0 H) = \rho_{xx}(\mu_0 H) - \rho_0$ and ρ_0 is the zero-temperature zero-field resistivity. (c, g, k) Energy scaling varying Γ, where $\Gamma = \alpha k_B T\sqrt{1 + (\beta/\alpha)^2(\mu_B\mu_0 H/(k_B T))^2}$, as used in $BaFe_2(As_{1-x}P_x)_2$ [178]. (d, h, l) Modified Kohler's rule scaling with the Hall angle, $\tan\theta_H = \rho_{xy}/\rho_{xx}$.

the negative charge carriers, similar to findings in thin flakes of FeSe [77]. This could indicate an increased scattering rate of spin fluctuations at high pressures and/or an increase in effective mass, which is consistent with the enhanced resistivity found in the high pressure phase of Cu-substituted FeSe shown in Figure 4.1b. This behaviour is rather similar to that of FeSe under pressure, where a three-band

model is required to explain its low temperature behaviour for all pressures, but in this case the carrier densities are enhanced and the mobilities decreased with increasing pressure by about 30% for an intermediate pressure (where the nematic and magnetic phases both stabilise) [96].

To elucidate further the role of scattering, one can look for scaling of the longitudinal magnetoresistance. Most simply, if a single scattering process dominates the transport behaviour then Kohler's rule should be obeyed, but in these systems this is not the case, as detailed in Figure 4.7. Violation of Kohler's rule is found in many unconventional superconductors, and often a modified Kohler's rule is employed where the magnetoresistance is related to the Hall angle, $\theta_H = \arctan(\rho_{xy}/\rho_{xx})$ [191]. However, no suitable scaling law describes the magnetoresistance data here for Cu-FeSe (Figure 4.7) including the energy scaling employed to describe the anti-ferromagnetic critical region of $BaFe_2(As_{1-x}P_x)_2$ [178]. This suggest a complex scattering dominates the magnetotransport behaviour of this multi-band system, which may be influenced by the nematic and magnetically-dependent scattering.

4.6 Upper critical field

Figure 4.8a shows the temperature dependence of the upper critical field extracted from the longitudinal resistance studies under pressure up to 15 T (Figures 4.10 and 4.11 in Section 4.10). The upper critical field shows a linear temperature dependence for $H||c$ for all measured pressures, similar to FeSe [79, 180, 192] and $FeSe_{1-x}S_x$ [107] under pressure. The upper critical field curves at different pressures collapse onto a single curve when scaled to the zero resistivity critical temperature T_c as a function of the reduced temperature $t = T/T_c$, as shown in Figure 4.8b. A similar dependence is found for FeSe for $H||c$ only [79, 192]. The full temperature dependence of the upper critical field can be modelled using a clean two-band model at 0 kbar, as discussed in the previous chapter, and one can extract the zero-temperature orbital upper critical field $\mu_0 H_{c2}(0)$ at each pressure from the slope, as shown in Figure 4.8c. From this, the in-plane coherence length ξ_{ab} is found to decrease from 60 Å towards 35 Å close to 20 kbar.

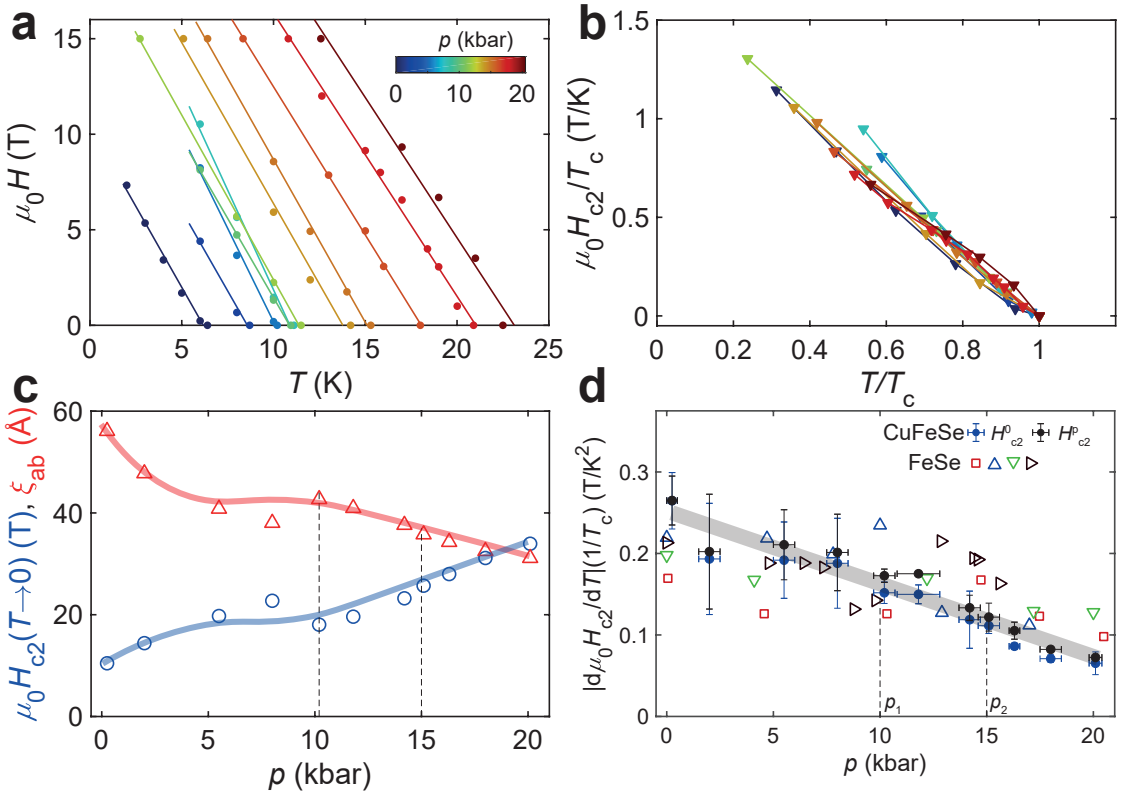

Figure 4.8: Upper critical field of $Fe_{1-x}Cu_xSe$ ($x = 0.0025$) under pressure. (a) The temperature dependence of the upper critical field for different pressures. (b) Scaling of the upper critical field in reduced units, $\mu_0 H_{c2}/T_c$ versus $t = T/T_c$. (c) Orbital field ($\mu_0 H_{c2}(0)$) and coherence length (ξ_{ab}) pressure dependence. (d) Pressure dependence of the ratio $1/T_c|d\mu_0 H_{c2}/dT|$ for Cu-FeSe compared to that of FeSe. The ratio is calculated using both the offset zero resistance, $\mu_0 H^0_{c2}$ (blue solid circles), and midpoint, $\mu_0 H^p_{c2}$ (black solid circles), defined through the peak in the derivative for the transition. The symbols corresponding to FeSe are the red squares (from reference [96]), blue up and green down triangles (from reference [88]), and black right triangles (from reference [95]). Solid lines are guide to the eye only.

The slope of the critical magnetic fields close to T_c, $|d\mu_0 H_{c2}/dT|$, shows little pressure dependence, being around 1.8(2) T/K up to 20 kbar and it is comparable to that of FeSe [87, 88]. In a two-band model the ratio $1/T_c|d\mu_0 H_{c2}/dT_c|$ is inversely proportional to the sum over each band of $n_i \lambda_{ii} v^2_{F,i}$, with n_i the density of states, λ_{ii} the normalised coupling constant, and $v_{F,i}$ the Fermi velocity [28], see Section 1.2.2. Similarly, it is proportional to the quasiparticle effective mass (squared) in a clean single band system. Figure 4.8d shows this ratio continuously decreases with pressure as the critical temperature increases, and so could indicate that the quasiparticles effective masses decrease with pressure. On the other hand, in FeSe

as the critical temperature has a two-dome structure this ratio changes across the three different regions under pressure, with a peak where T_c reaches a minimum [87, 95, 107], similar to changes observed in the heat capacity under pressure [94]. In Cu-FeSe, no such dome is found as T_c monotonically increases with pressure. No differences were found between when the gradient was determined from the peak in the derivative of the transition ($\mu_0 H_{c2}^{p}$), or from the offset critical fields ($\mu_0 H_{c2}^{0}$), which is verified to account for the width variation of the superconducting transition with pressure (see Figure 4.11 in Section 4.10).

4.7 The pressure-temperature p-T phase diagrams

The findings are now summarised in detail through the comparison of the temperature-pressure phase diagram of Cu-FeSe with that of FeSe [187] in 0 T and 15 T, as shown in Figures 4.9a and b respectively. The phase diagram can be split into three distinct regions: firstly, the low pressure region, $p < p_1 \sim 10$ kbar, where the superconducting phase emerges from the nematic phase, secondly at intermediate pressures, $p_1 < p < p_2 \sim 15$ kbar, where signatures of the magnetic phase are detected in FeSe in zero-field, and finally, at higher pressures, $p > p_2$ where the magnetic and superconducting phases coexist and the nematic phase is suppressed at p_2. Interestingly, as the pressure increases beyond p_1, the superconducting transition temperature, T_c, displays a broadly similar pressure dependence for the two systems, indicating a strong robustness to impurity scattering. Unlike the low pressure region, the superconductivity of Cu-FeSe is no longer suppressed relative to FeSe. On the other hand, the magnetic phase above p_2 is highly sensitive to impurity scattering being washed out by the Cu substitution and its signatures are only visible in strong magnetic fields, as discussed earlier and shown in Figure 4.9b.

In order to account for the relative changes in superconductivity due to the Cu substitution, the temperature-pressure diagrams are scaled by the ambient value of $T_s(0\,\text{kbar})$ for each system, as shown in Figure 4.9c. A remarkable scaling occurs for the nematic and superconducting transitions between FeSe and Cu-FeSe, up to p_1. Thereby suggesting that the impurity scattering affects the nematic and

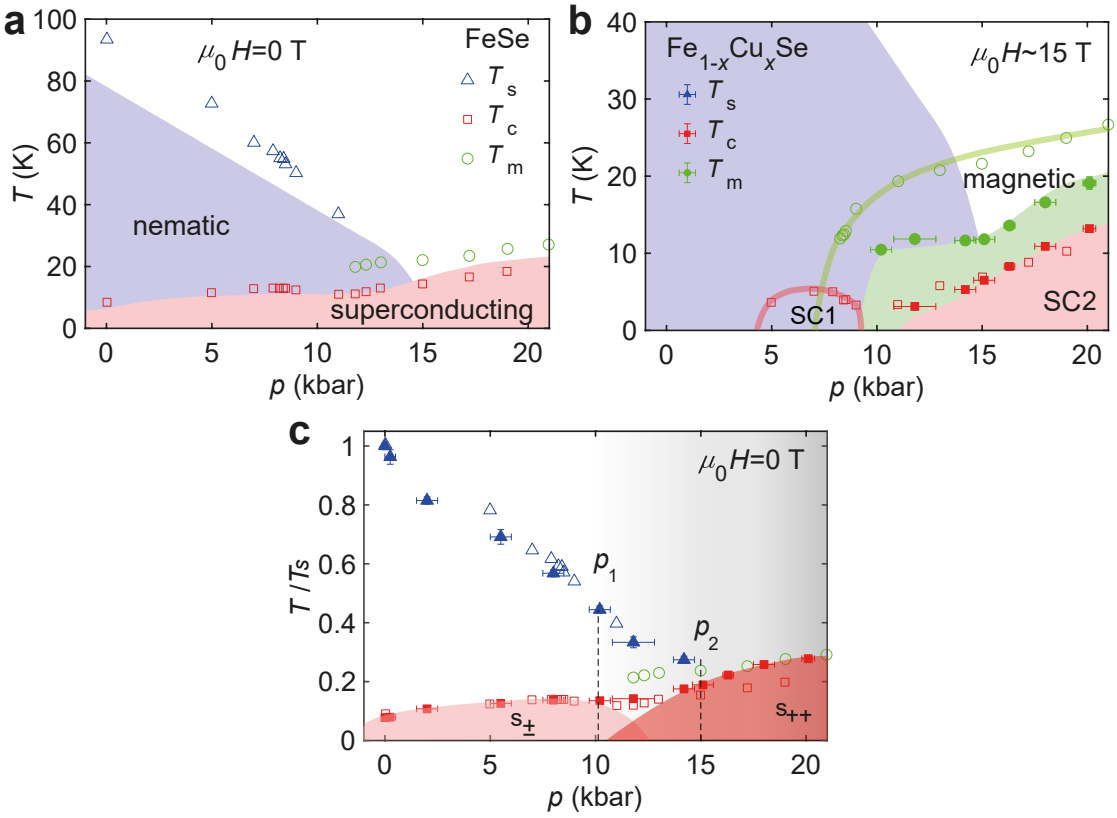

Figure 4.9: The pressure-temperature phase diagrams of Cu substituted FeSe. The comparison between the different electronic phases of FeSe (open symbols) from Chen et al. [187] and Cu-FeSe ($x = 0.0025$) (solid symbols) measured in (a) 0 T and (b) in magnetic field, 15 T for Cu-FeSe and 16 T for FeSe. Solid lines in (b) are guides to the eye for the phase boundaries of FeSe. Shaded regions in (a) and (b) denote the difference phase regions of Cu-FeSe, in (b) the nematic phase boundary is assuming a field-independent T_s. (c) Scaling of the pressure-temperature phase diagram from (a) by using the reduced temperature $t = T/T_s$, where T_s is the nematic transition at ambient pressure for each system. The two shaded regions schematically show two proposed superconducting regions.

superconducting phases in the same manner, as found also for Cu substitution in $Fe_{1-x}Cu_xSe$ in Chapter 3. As the superconductivity at low pressures remains strongly suppressed, like for ambient $Fe_{1-x}Cu_xSe$, this is indicting a sign-changing $s_{\pm}$-type of order parameter in the low pressure regime, as presented in Chapter 3.

Interestingly, at high pressure above p_2 the magnetic and superconducting phases enhance their transition temperatures with a similar behaviour, suggestive of a cooperative relationship between them. However, the very small Cu substitution is sufficient to break this trend, where in Cu-FeSe the upturn in resistivity, a signature of the magnetic phase, is not present in the absence of magnetic fields. Instead, the

requirement of a magnetic field to detect, and possibly for the stabilising of, the magnetic phase highlights the fragility of this phase. As seen for high magnetic fields of $\sim 15\,\mathrm{T}$, the magnetic phase is strongly suppressed as compared to FeSe, whereas the high pressure superconducting dome shows similar behaviour and absolute value, as seen in Figure 4.9b.

Significant disruption of the high pressure magnetic phase was also detected under pressure for FeSe single crystals with higher amounts of disorder, where no signatures of magnetic order were found in zero field [35, 193]. Similar results occur in thin flakes of FeSe under pressure, in which the magnetic phase occurs above T_c for thick flakes down to $140\,\mu\mathrm{m}$, but the signatures of the magnetic phase are suppressed as the thickness decreases further [194]. In the presence of sulphur substitution outside the Fe planes, the magnetic phase is also suppressed at lower pressures in $\mathrm{FeSe}_{1-x}\mathrm{S}_x$, although it has been suggested that the magnetic phase could be stabilized at higher pressures around 50 kbar [104]. The superconductivity at high temperatures is recovered in systems with larger amounts of Cu substitution ($x = 0.04$) for a power sample, and in this scenario no signatures of the magnetic phase in zero-field were detected [158]. This implies that the impurity scattering affects strongly the interplay between the magnetism and superconductivity in the high pressure phase. The robustness of the superconducting phase to impurity scattering is consistent with a sign preserving s_{++} pairing symmetry. In such a system the superconductivity can be enhanced even in the presence of large disorder, if the disorder can induce spatial modulations where the coherence length is a few nanometers [186, 195]. Another scenario is that the high pressure phase is inhomogeneous, which would be consistent with a sign changing $s_{\pm}$ symmetry because connected emergent disorder regions are unable to provide large-momentum transfer interband scattering connecting opposite signs of the superconducting gap function of electron and hole pockets. Therefore strongly limiting any substantial pair-breaking processes from the inhomogeneous disordered state. Although, the expected response in a sign changing order parameter system is that T_c is quickly suppressed with impurity scattering, as found for $\mathrm{Fe}_{1-x}\mathrm{Cu}_x\mathrm{Se}$ in Chapter 3. Figure

4.9c indicates the separation into two superconducting domes describing the pressure-temperature phase diagram of Cu-FeSe. Notably, two superconducting domes are also found in the isoelectronic substitution outside of the conducting Fe-plane in $FeSe_{0.89}S_{0.11}$ under pressure, where no magnetic phase was detected [105].

4.8 Discussion

The increase in resistivity in the high pressure phase, combined with the reduction of mobilities despite the increase in the charge carrier densities, suggests that either the high-pressure phase is highly inhomogeneous, or that there are very strong spin fluctuations that do not permit the stabilization of the long-range magnetic order. These effects are also evident in the evolution of the superconducting transition width which becomes extremely broad above p_1, both in FeSe and Cu-FeSe, as shown in Figure 4.1b [187]. Evidence of short-range static local magnetism was found in FeSe under pressure using μSR, as well as Mössbauer spectroscopy, up to very high pressures with its volume fraction dependent on temperature and pressure [86, 89, 93]. The hysteresis effects in resistivity, for different cooling rates in high magnetic fields at high pressure, could suggest the local short-range magnetic order is affected by the presence of Cu by freezing of dynamical spin fluctuations of the Fe magnetic moments in the presence of the Cu non-magnetic disorder [196].

Theoretically, the non-magnetic impurities in FeSe are expected to locally induce magnetic order and the structure of the induced magnetization cloud can be modified by orbital selectivity [197, 198]. The Cu substitution into the Fe-plane in the SDW phase can lead to increased phase fragmentation, or glassy behaviour. A SDW glass was proposed to arise for systems with weak non-magnetic disorder [199]. For iron-based superconductors, microscopic calculations suggest that inside the SDW phase strong non-magnetic potentials can generate extended magnetic nematogens, a region of competing magnetic order centred on the impurity site, such as the Cu in this system [198]. These features could short-circuit the transport of the system, and hide or suppress the SDW signature in transport measurements, despite the tiny amount of Cu present. The observation of the SDW signature with a strong

external magnetic field, could be induced by the magnetic field re-aligning the magnetic regions and result in additional spin-dependent scattering which enhances the resistivity, as found in the systems without Cu impurities. Spatially-resolved probes to investigate the electronic structure of Cu-FeSe would provide invaluable insights to understand the interplay between the magnetic and superconducting phases, and disorder, in the high pressure phase of FeSe.

4.9 Conclusions and Outlook

This study provides insight into the nature of superconductivity and the sensitivity to impurity scattering in $Fe_{1-x}Cu_xSe$ $x = 0.0025$. In particular at high pressures, the magnetic phase is profoundly affected by the impurity scattering, where fragmentation of the magnetic order can lead to phase separation of the superconducting and magnetic phases. The magnetic phase transition is found to be a hysteretic first-order transition. The low pressure region with suppressed nematic and superconducting phases continues to suggest a sign-changing pairing mechanism, as seen with ambient $Fe_{1-x}Cu_xSe$. Conversely, the robust high pressure superconducting phase instead implies a non-sign changing mechanism through the robustness of this phase, or a very inhomogeneous phase with suppressed pair-breaking effects for $s_{\pm}$ superconductivity. Future measurements using spatially resolved probes, particularly focusing on the magnetic phase, are required.

Future work to explore the low substituted Cu-FeSe ($x = 0.005$ and 0.1 in particular), using piston cylinder cells for new substitutions and anvil cells for higher pressures of this substitution, could further provide valuable insights in to the stability of this superconducting phase, to build upon this work. A previous study on powder samples of $x = 0.04$ at high pressures could be repeated with single crystals measuring the magnetotransport, to map out the phase diagram and determine if any magnetic order stabilises. In particular, determining the peak value of T_c and the pressure this occurs at for all Cu substituted FeSe. Additionally, whilst only 0.25% Cu in this work has significantly disrupted the magnetic phase, the question then arises on how a slightly larger substitution, for example 0.5%

Cu, affects the overall phase diagram. It may be that the suppressed nematic phase and magnetic phase lead to a larger T_c at lower pressures. Finally, pressure experiments on $Fe_{1-x}Co_xSe$ would provide a fascinating comparison to the work presented here on $Fe_{1-x}Cu_xSe$, due to the similarities and differences that were found between the two substitution series in Chapter 3.

4.10 Additional Figures

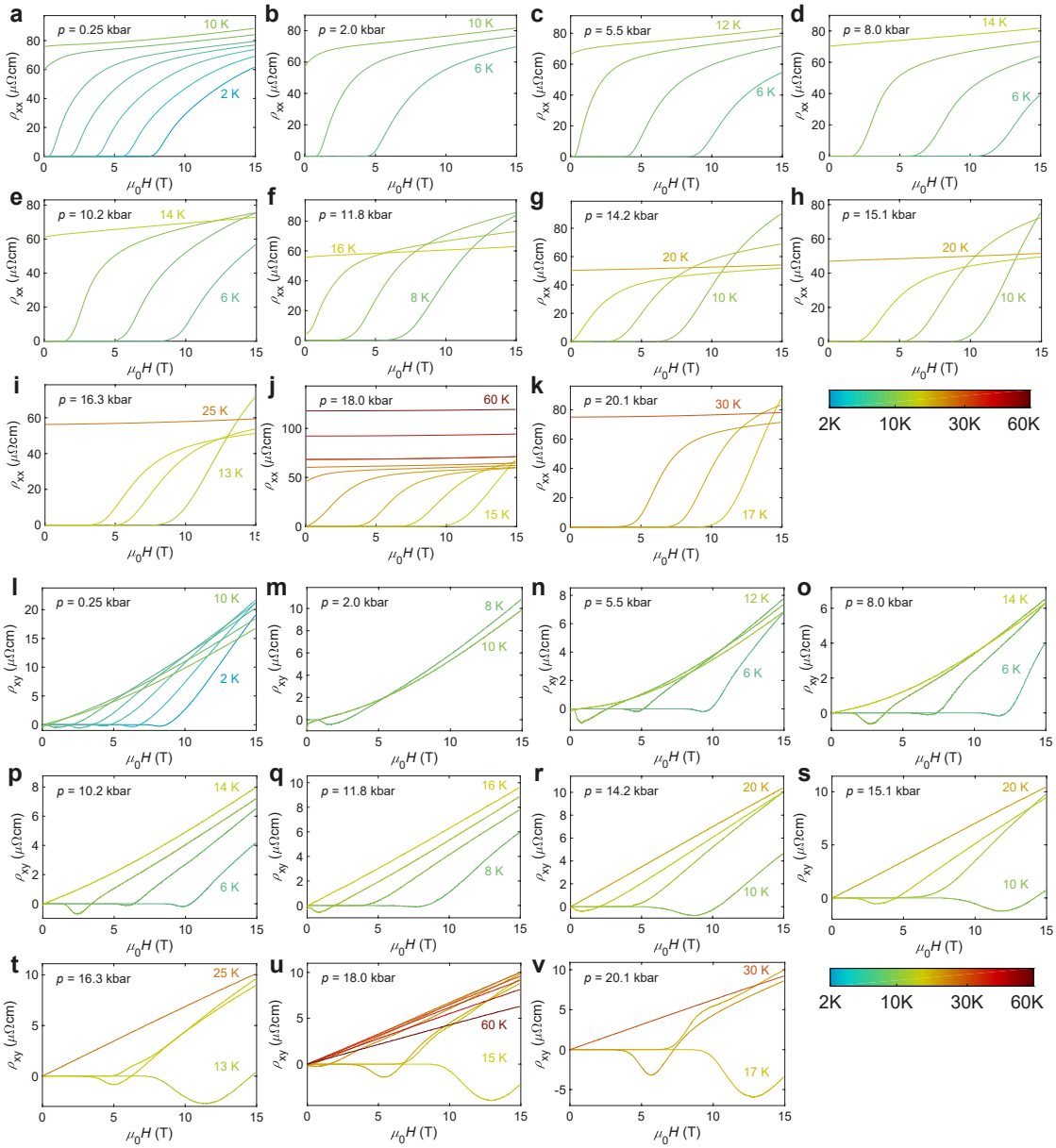

Figure 4.10: Magnetotransport behaviour at different pressures of $Fe_{1-x}Cu_xSe$ $x = 0.0025$. The field-dependence of (a) ρ_{xx} and (b) ρ_{xy} measured a different constant temperatures. Each panel corresponds to a different applied pressure.

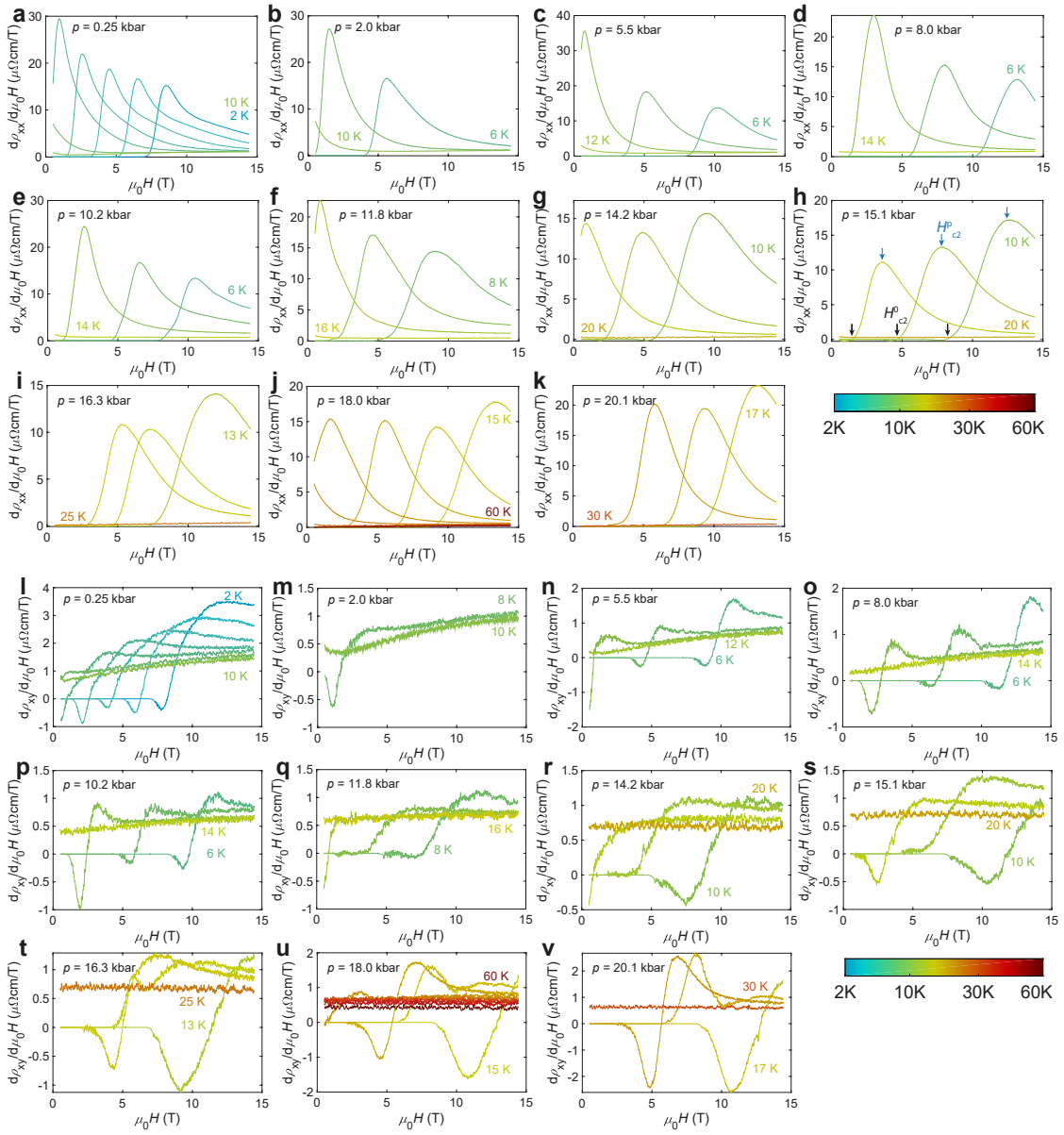

Figure 4.11: The derivative of magnetotransport curves in relation to magnetic field at different pressures for $Fe_{1-x}Cu_xSe$ $x = 0.0025$. Derivatives with respect to magnetic field for (a) ρ_{xx} and (b) ρ_{xy} as a function of magnetic field measured at different constant temperatures. Each panel corresponds to a different applied pressure. Examples of how the critical field is defined are shown in (h). The peak of the derivative is referred to as $\mu_0 H^{\mathrm{p}}_{\mathrm{c2}}$, and the zero extrapolation as $\mu_0 H^{0}_{\mathrm{c2}}$.

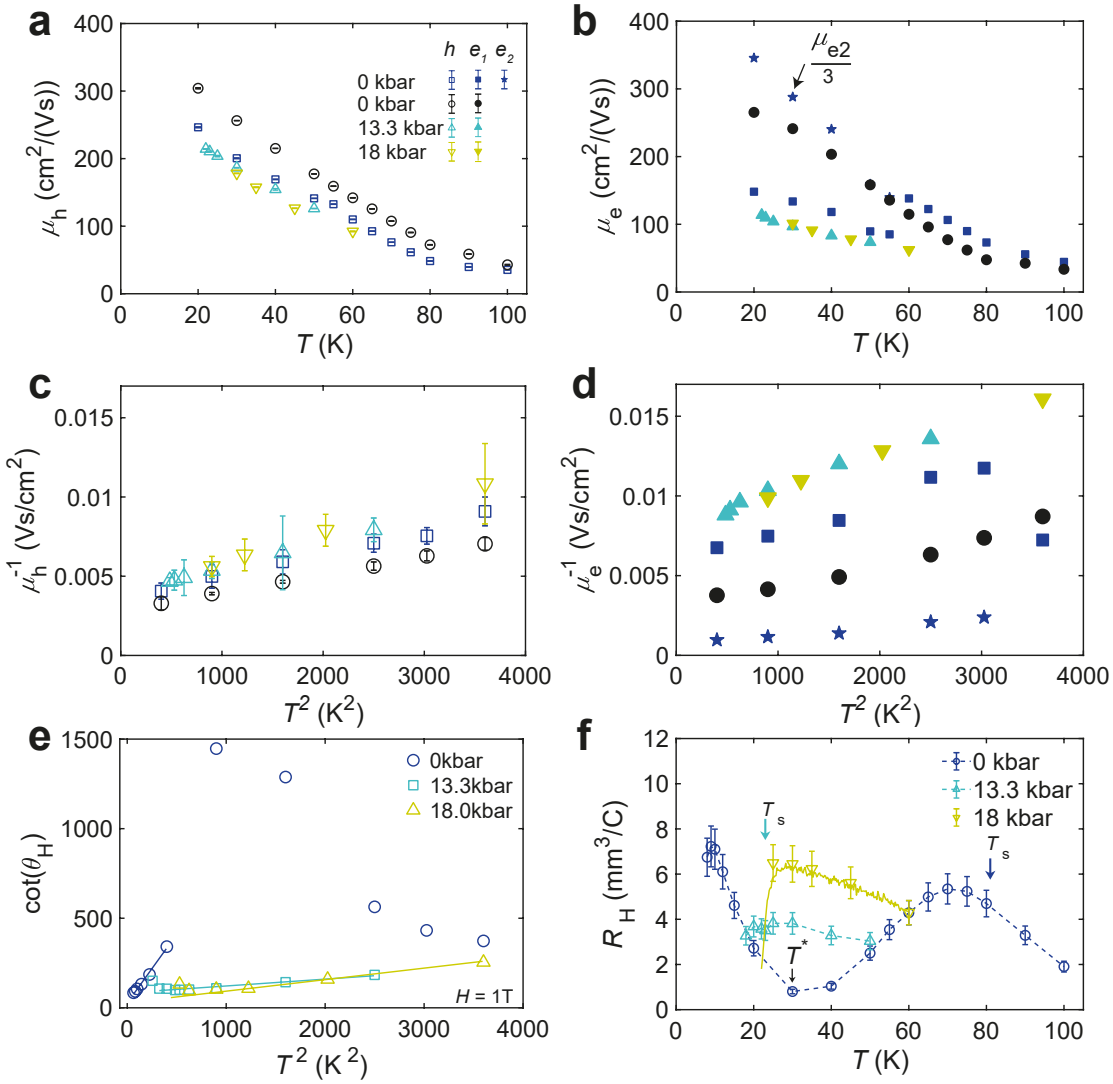

Figure 4.12: Mobility spectrum at different pressures for $Fe_{1-x}Cu_xSe$ $x = 0.0025$**.** The mobility temperature dependence for (a) holes and (b) electrons. The 0 kbar is modelled in a high field 3 band model and shown from Chapter 3, whilst the 2 band is taken from low field (<7 T) only. The mobility of the second electron, e_2, in (b) is scaled by a factor 1/3. The inverse mobility against a T^2 dependence for (c) holes and (d) electrons. (e) $\cot(\theta_H)$, cotangent of the Hall angle defined, temperature dependence. Solid lines are fit to linear regions at higher temperatures. The values are taken from field sweep measurements and chosen at a fixed field value for all temperatures. (f) The Hall coefficient, R_H, temperature dependence for different pressures of Cu-FeSe. The dashed lines are guide to the eye. The solid line for 13.3 kbar is from a temperature sweep. T^* marks the minimum in R_H for 0 kbar.

5

Signatures of the high-pressure phase of $FeSe_{1-x}S_x$

In contrast to the previous chapters investigating substitution inside the Fe-plane in FeSe, this chapter investigates a system with isovalent substitution of sulphur for the selenium ions in $FeSe_{0.82}S_{0.18}$. The sulphur substitution suppresses the nematic phase at ambient pressure, with full suppression around $x = 0.18$ where the system then remains tetragonal to the lowest temperatures. Thus, this allows access to the superconducting state in the absence of any nematic or magnetic ordering. Low magnetic field transport measurements produce the temperature-pressure phase diagram of the tetragonal $FeSe_{0.82}S_{0.18}$. The superconducting critical temperature remains around 6(1) K up to 10 kbar, before increasing threefold towards 19 K at 21 kbar. The electronic transport can be described by a non-Fermi liquid behaviour with a temperature exponent that varies slightly with pressure around $T^{3/2}$ at higher pressures before crossing towards Fermi liquid behaviour at low temperatures. Additionally, magnetotransport measurements show that the charge carrier density continuously increases with pressure, and the mobilities of both holes and electrons similarly increase with pressure. In high magnetic fields, quantum oscillations are detected for pressures up to 22 kbar. The quantum oscillations show that the Fermi surfaces expand with increasing pressure, much

like the charge carrier density from the magnetoresistance analysis. The electronic correlations show little variation with pressure, despite the enhancement of the superconductivity. This suggests that this phase is weakly correlated and the large sizes of the Fermi surfaces promotes nesting, and potentially heading towards stabilization of a magnetically-ordered phase at high pressures.

5.1 Introduction

In conventional superconductors one route to enhance superconductivity towards room temperature is the use of extremes of applied pressure in the hydride systems, which increases the density of states at the Fermi level and phonon energies [13–15]. FeSe, an unconventional iron-based superconductor, under applied pressure exhibits a strong enhancement in superconductivity from 9 K to 37 K, with the peak T_c around 60 kbar [16, 69, 89, 90]. In this system, applied pressure stabilises a magnetically ordered state above 8 kbar, which persists up to pressures close to the vicinity of the peak T_c [69, 97]. FeSe is unique in iron-based superconductors with no magnetic order in the absence of applied pressure. Instead, in the low pressure regime, a nematic electronic phase exists that is driven by orbital degrees of freedom, and strong electronic correlations give rise to highly anisotropic electronic and superconducting behaviour [50]. For FeSe, due to the small Fermi surface, it is predicted there is competition between the different electronic nematic, magnetic and superconducting orders on similar energy scales [200]. For small Fermi pockets inside the nematic phase a spontaneous orbital order is stabilized before $s_{\pm}$ superconductivity, whereas, outside the nematic phase, the magnetic phase is potenetially more stable due to the increase in the Fermi energy [200].

Chemical pressure has many effects analogous to applied pressure. Isovalent substitution of seleneium for sulphur introduces chemical pressure in $FeSe_{1-x}S_x$ and suppresses nematicity. Once the nematic phase is suppressed, around $x = 0.18$, the system remains tetragonal for all temperatures [55]. Inside the tetragonal phase the superconductivity is not enhanced, no magnetic order is detected and electronic correlations are strongly suppressed [55, 70, 71, 201]. Across the nematic end

point, the superconducting pairing states and the gap structure change [202, 203]. A topological transition into an ultranodal phase with Bogoliubov Fermi surface phases has been postulated [204]. Interestingly, by applying pressure to different $FeSe_{1-x}S_x$ systems the magnetic order seems to be stabilized at higher pressures for higher sulphur substitution [104]. Hence, whilst the magnetic and nematic phases overlap in FeSe, combining chemical and applied pressure can decouple the two phases to identify their role on superconductivity, and explore the region of a possible quantum nematic phase transition [105–107, 205, 206].

One puzzling aspect of the superconducting behaviour of FeSe is that T_c decreases and remains relatively unchanged when the nematic phase is suppressed with chemical substitution but it is strongly enhanced by applied pressure [55, 104]. Despite the differences in superconductivity, the normal electronic state displays certain common features in the vicinity of the nematic critical point, with non-divergent behaviour of the quasiparticle effective masses and a similar temperature dependence of resistivity, found both in $FeSe_{1-x}S_x$ [55, 71] and $FeSe_{0.89}S_{0.11}$ under pressure [105]. In the latter system, the presence of a quantum Griffiths phase stabilised with applied pressure is linked to the distribution of sulphur ions and local strain [205]. An empirical relationship between the anion height and T_c has been found in iron-based superconductors, with a potential *optimal* value of the anion height of 1.38 Å [35]. In $FeSe_{1-x}S_x$ the height of the Se/S above the Fe-plane for pressures at the maximum T_c differs slightly with 1.42 Å for FeSe, and 1.44 Å for $x = 0.20$ [207]. Anion height is considered as a key determining factor in increasing superconductivity under pressure with a lower Se height leading to a more enhanced T_c with the maximum stabilizing around the optimum anion height of 1.38 Å[35].

This work also presents measurements of quantum oscillations under pressure up to 22 kbar into the high-T_c phase. The quantum oscillations are a direct measure of the Fermi surface and are used to help understand the changes in electronic structure, electronic correlations, and pairing interactions, which can play significant roles in the enhancement of superconductivity. An advantage of quantum oscillations compared to other spectroscopic techniques, such as angle resolved photoemission

(ARPES) and scanning tunneling microscopy (STM), is that quantum oscillations can be measured in extreme conditions under high pressure and can access the high pressure high-T_c phase of $FeSe_{1-x}S_x$. Due to the high quality of these single crystals, quantum oscillations have been observed at ambient pressure in FeSe [60, 208, 209] and $FeSe_{1-x}S_x$ [67, 100], revealing the presence of multiple Fermi surface pockets with relatively large effective masses [55]. Results with chemical pressure suggests the Fermi surfaces continuously expand with sulphur substitution up to FeS, based on quantum oscillations [67, 100] and ARPES [190, 201]. Additionally, a Lifshitz-transition was detected by these quantum oscillations in $FeSe_{1-x}S_x$ and $FeSe_{0.89}S_{0.11}$ under pressure, coinciding with the nematic end point [67, 105]. Under pressure, quantum oscillations studies of $FeSe_{0.96}S_{0.04}$ (Chapter 6) and FeSe [87] have a sudden change from high frequency oscillations to low frequency only, consistent with a Fermi surface reconstruction in the presence of the magnetic phase.

5.2 Materials and Methods

Single crystals of $FeSe_{0.82}S_{0.18}$ were grown by Amir-Abbas Haghighirad using the $KCl/AlCl_3$ chemical vapor transport method, as reported previously [101, 102]. Single crystals from this batch were found to have large residual resistivity ratios (RRR) up to 25 between room temperature and the onset of superconductivity. Crystals from the same batch were previously used in quantum oscillations and ARPES studies [67, 201]. All samples measured are from the same batch and EDX measurements measured the composition to contain a suplhur content of $x = 0.18(1)$, which places the batch in the vicinity of the nematic end point [201]. Magnetotransport and Hall effect measurements under pressure using a 5-contact configuration were carried out on samples S1 and S2, in two different experiments, in low fields up to 16 T in an Oxford Quantum Design PPMS and an ElectroLab High Pressure Cell using Daphne Oil 7373 which ensures hydrostatic conditions up to about 21 kbar. The pressure inside this cell was determined via the superconducting transition temperature of Sn after cancelling the remanent field in the magnet. The magnetic field was applied along the crystallographic c axis for all samples.

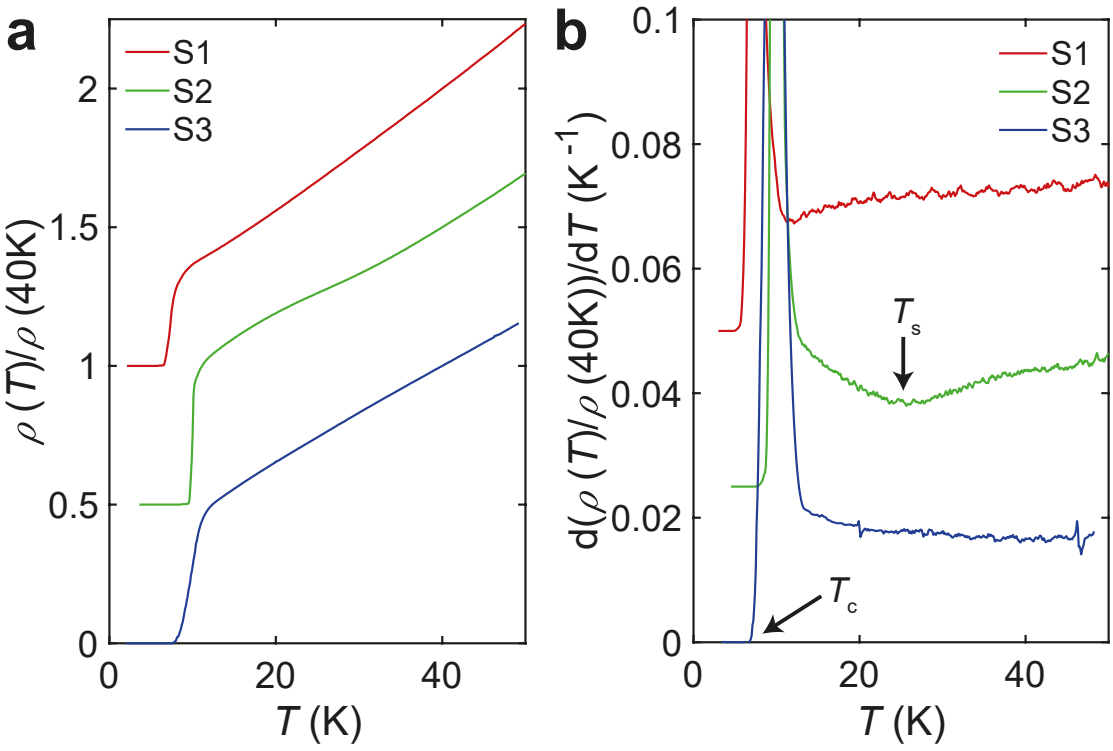

Figure 5.1: The low temperature resistivity of different crystals. (a) The temperature dependence of the resistivity normalised at 40 K and (b) the corresponding first derivative of the resistivity for the different single crystals of $FeSe_{0.92}S_{0.18}$ from the same batch. The arrow at T_s indicates the position of the nematic transition for sample S2.

A maximum current of up to 2 mA flowing in the conducting tetragonal *ab* plane was used. The pressure cell with sample S1 was prepared by Pascal Reiss. This author performed that experiment alongside Pascal Reiss. The author of this thesis analysed all the data and produced all the figures presented in this chapter.

High magnetic field measurements up to 45 T at ambient pressure and under hydrostatic pressure were performed using the hybrid magnet d.c. facility at the NHMFL in Tallahassee, Florida, USA on sample S3. Pressures up to 22 kbar were generated using a piston cylinder cell made of a NiCoCrMo alloy (MP35N), using Daphne Oil 7575 as pressure medium. The pressure inside the cell was determined by means of ruby fluorescence at low temperatures where quantum oscillations were observed. This experiment was prepared and perform by Pascal Reiss, Amalia Coldea, and David Graf. All analysis presented was performed by this author.

Figure 5.1a shows the zero-field resistivity temperature dependence at low

Table 5.1: Sample details for single crystals of $FeSe_{0.82}S_{0.18}$. Extracted parameters for the different single crystals of $FeSe_{0.82}S_{0.18}$ measured at ambient pressures. Sample S3 was measured in the hybrid magnet only at low temperatures.

Sample	Label	Experimental Details	max p (kbar)	RRR	T_s (K)	T_c (K)
T3C	S1	Oxford, 16 T, 2 K	21	36	–	6.5
P1	S2	Oxford, 16 T, 2 K	9.2	21.5	26	9.2
T3B	S3[1]	Tallahassee, 45 T, 0.4 K	22	–	–	7.5

temperatures for each of the three samples at 0 kbar. Sample S2 enters the nematic phase below a structural transition at $T_s = 26$ K, as shown in Figure 5.1b. The 0 kbar transport properties for each sample are described in Table 5.1.

5.3 Temperature dependence of resistivity with applied pressure

Figure 5.2a shows the temperature dependence of the longitudinal resistivity, ρ_{xx}, of sample S1 for a range of applied pressures. At ambient pressure ($p = 0$ kbar), the resistivity has no anomaly, indicating that the system is in the tetragonal phase and the nematic order has been suppressed fully by the isoelectronic substitution of sulphur for selenium. For a second crystal from the same batch, sample S2, there is an anomaly associated with the structural transition at 26 K, which is suppressed at low pressures ($\sim$ 0.6 kbar), as shown in Figure 5.1a and in Figure 5.15 in Section 5.8. The superconducting transition temperature, T_c, is defined through the offset as 6.5 K, and with increasing pressure the transition temperature, T_c, remains relatively unchanged up to 11 kbar, with a minimum of 6 K around 5 kbar. However, further increasing pressure enhances superconductivity by a factor of 3 to 19 K at 21 kbar. The superconducting transition region becomes broader at high pressures, shown in Figure 5.2b. This occurs in the region where T_c is enhanced, above 12 kbar. Here, the increased transition width is found despite the lack of any signatures of another competing phase at low temperatures, as is the case for $FeSe_{0.96}S_{0.04}$ in Chapter 6 and Cu-FeSe in Chapter 4. In both those cases, and for

[1]For sample S3 the dimensions are not available for conversion to resistivity, so the resistance is reported for this sample only.

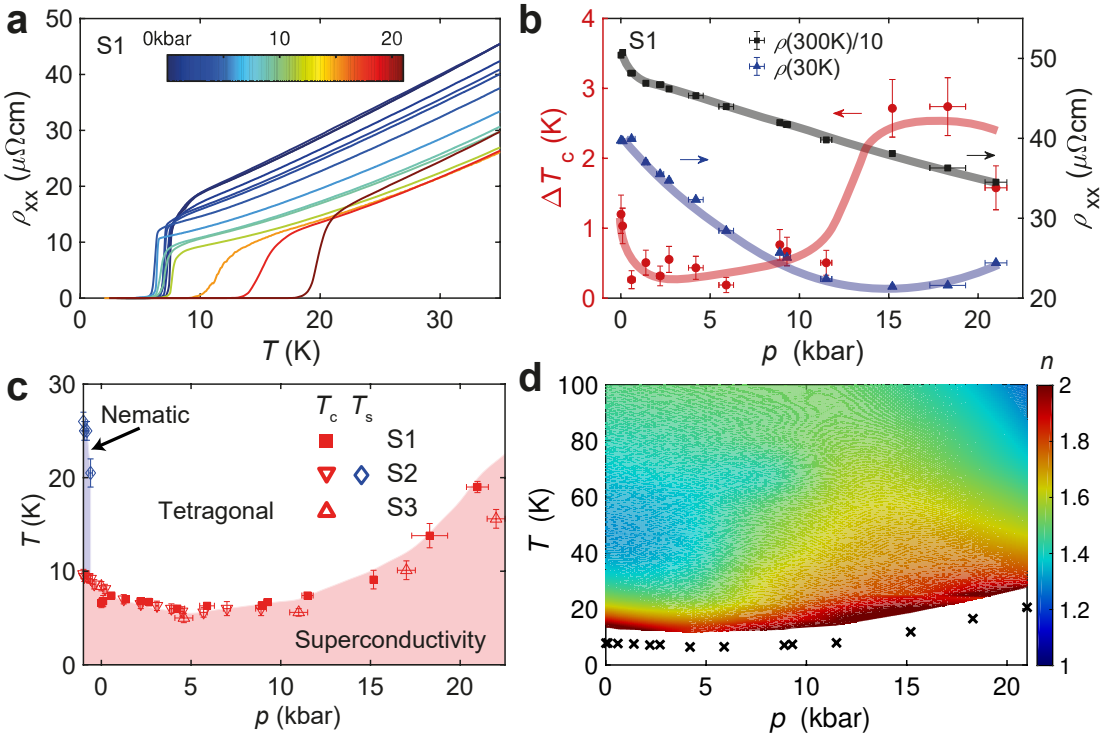

Figure 5.2: Transport under pressure in $FeSe_{0.82}S_{0.18}$ Sample S1. (a) Temperature dependence of resistivity in $FeSe_{0.82}S_{0.18}$ for different applied pressures up to 21 kbar. T_c is defined as the temperature at which the system reaches zero resistivity. (b) The superconducting transition width, $\Delta T_c = T_{on} - T_{off}$ (red circles), and resistivity at 300 K (black squares, scaled by a factor 1/10), and at 30 K (blue triangles) as functions of pressure. Solid lines are guide to the eye only. (c) Temperature-pressure phase diagram of $FeSe_{0.82}S_{0.18}$. 0 kbar is ambient for samples S1 (red solid squares) and S3 (upwards open triangles), whilst sample S2 (downwards triangles for T_c and blue diamonds for T_s) is shifted by -1 kbar. (d) Pressure-temperature phase diagram with a colour map representing the local resistivity temperature exponent, n from $\rho = \rho_0 + AT^n$. The crosses represent the offset of superconductivity from (a).

FeSe and $FeSe_{1-x}S_x$ under pressure generally, the superconducting transition width increases in the vicinity of where magnetic phase signatures have been detected [69, 94, 105, 187]. At much higher pressures around 50 kbar, tetragonal $FeSe_{1-x}S_x$ under pressure displayed anomalies in transport that have been assigned to a spin-density wave, close to the maximum $T_c = 35$ K, for $x = 0.17$ [104].

In the normal state and at high temperatures, the resistivity reaches values of the order $\rho(300\,\text{K}) = 500\,\mu\Omega$cm, which decreases strongly with applied pressure having a linear slope in the high pressure regime of $6.5\,\mu\Omega$cm/kbar, as shown in Figure 5.2b. This suggests that the tetragonal system becomes a better metal

with increasing pressure and its bandwidth increases. In the low temperature regime around 30 K, the resistivity decreases initially with pressure before slightly increasing again in the region where superconductivity is enhanced, see Figure 5.2b. This disparity between the high and the low temperature normal states suggests that besides changes in the bandwidth, the pressure tunes across different electronic phases from which superconductivity emerges.

Figure 5.2c presents the temperature-pressure phase diagram as constructed from the transport measurements of samples S1 (from Figure 5.2a), S2 (from Figure 5.15a) and S3 (from Figure 5.3). The pressure for sample S2 is shifted by −1 kbar, such that the first pressure measurement without the nematic anomaly coincides with 0 kbar. The superconducting transition temperature smoothly evolves for S2 through the nematic end point and is in good agreement with the other samples.

In order to understand the nature of the electronic normal behaviour, the resistivity temperature dependence is investigated. The resistivity exponent, n, is defined through the relationship, $\rho = \rho_0 + AT^n$, and can be used to determine the value locally both with temperature and pressure (see Section 2.1.3 for more details). The exact dependence of the resistivity exponent is heavily influenced by the value of ρ_0 (Figure 5.16c) which is extracted from low temperature resistivity measurements in high magnetic fields.

In the low temperature regime below 50 K, the resistivity exponent varies both with temperature and pressure. Figure 5.2d shows the temperature and pressure evolution of the resistivity exponent. It is found to be close to 4/3 up to 5 kbar before increasing slightly towards 3/2 and eventually close to a linear ($n = 1$) dependence at the highest pressures, in close agreement with previous findings in $FeSe_{1-x}S_x$ [71, 105]. For both samples (S1 and S2) the behaviour of n is found to be similar (the individual n curves are shown in Figure 5.16d for sample 1 and Figure 5.16e for sample 2 in Section 5.8). While previous studies of $FeSe_{1-x}S_x$ found $n = 3/2$ to describe the resistivity over a larger temperature region in the tetragonal phase [71, 105], here with applied pressure there is a slight deviation

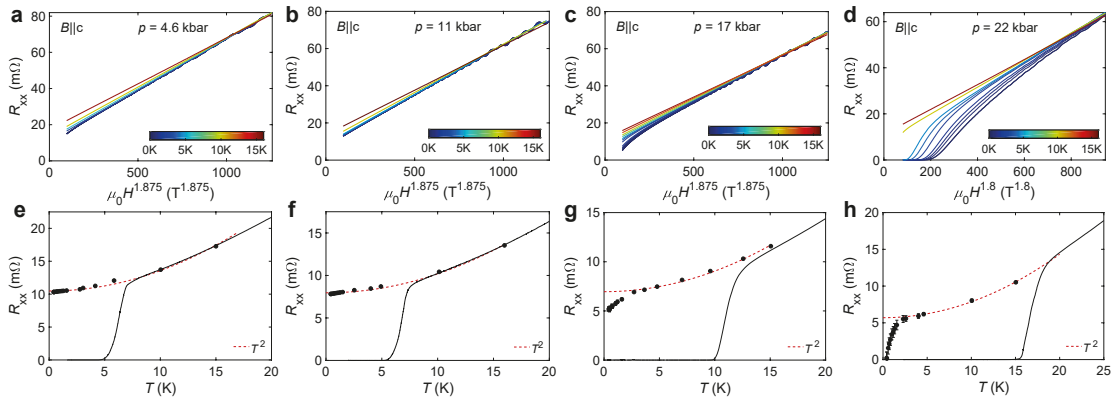

Figure 5.3: High magnetic field longitudinal magnetoresistance power laws of $FeSe_{0.82}S_{0.18}$ Sample S3. (a)-(d) ρ_{xx} magnetic field dependence of $\mu_0 H^{1.875}$ ($\mu_0 H^{1.8}$ for 22 kbar) of each high pressure. (e)-(h) The zero field resistivity at low temperatures for each pressure (black solid curve). Black circles are the corresponding extrapolated zero field values at low temperatures from (a)-(d). Red dashed lines are fits at low temperatures to a T^2 dependence. The coefficient of the T^2 term, A, is shown in Figure 5.14h.

towards $n = 4/3$, which can describe a two-dimensional system in the vicinity of a Pomeranchuk instability [114].

5.4 Magnetotransport

Figures 5.3a-d show the magnetotransport of a third sample, S3, measured in high magnetic fields up to 45 T, which allows access to the normal state at lower temperatures. The power law that best models the measurements is $\mu_0 H^{1.875}$, but slightly reduced at highest pressures to $\mu_0 H^{1.8}$. From these, the resistivity can be extrapolated down to 0 T and then used to extend the normal state of the resistivity below the superconducting transition in Figures 5.3e-h. Following these extrapolated points a Fermi liquid dependence, T^2, is found at low temperatures for each pressure. At 22 kbar, the critical field, $\mu_0 H_{c2}$, is large enough to be seen in the hybrid magnet (>11.5 T) at low temperatures. Here, it is difficult to consistently define an on-set after the superconducting transition where the sample enters the normal state. The resistivity is quite linear in field at the lowest temperatures, before recovering towards $\mu_0 H^{1.8}$ and closer to that of the lower pressures.

The field dependence of the resistivity at low temperatures is shown for both ρ_{xx} and ρ_{xy} respectively in Figures 5.4 and 5.5 for sample S1. For all measured

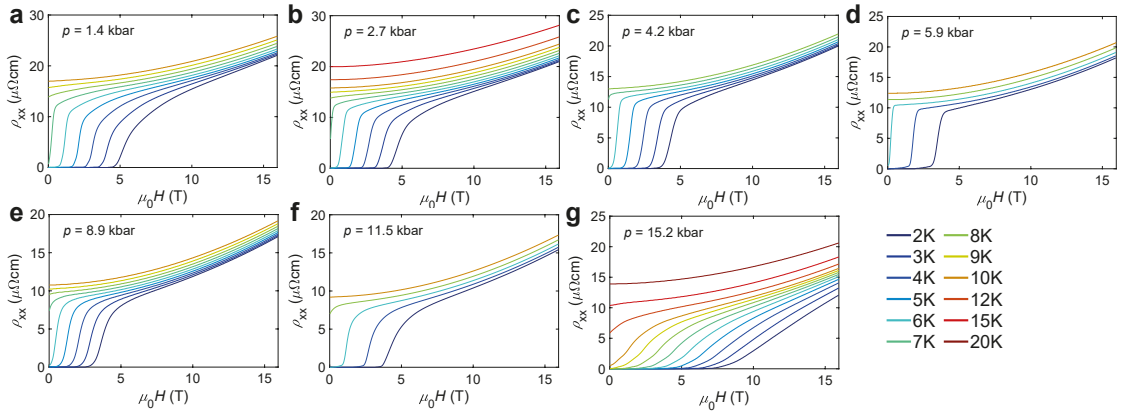

Figure 5.4: Longitudinal resistivity of $FeSe_{0.82}S_{0.18}$ Sample S1. (a)-(g) Longitudinal resistivity field dependence measured at fixed temperatures for a range of pressures for $FeSe_{0.82}S_{0.18}$ Sample S1.

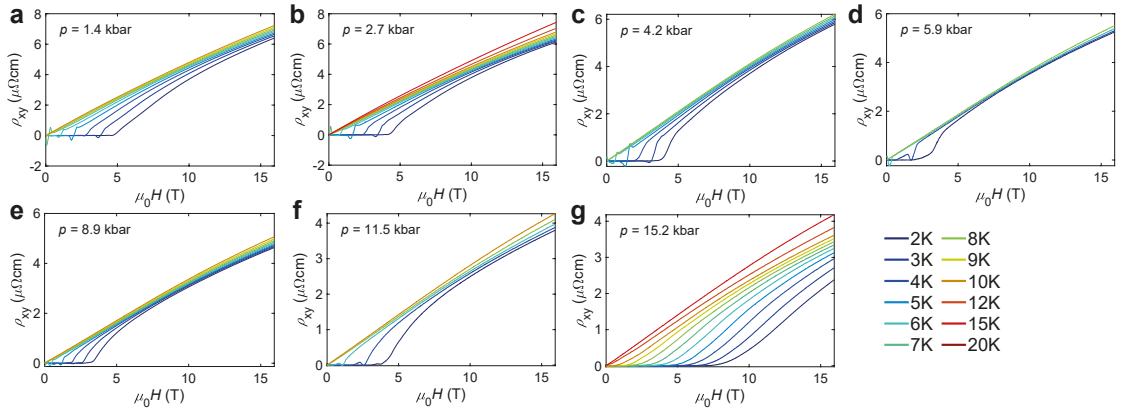

Figure 5.5: Hall resistivity of $FeSe_{0.82}S_{0.18}$ Sample S1. (a)-(g) Hall resistivity field dependence measured at fixed temperatures for a range of pressures for $FeSe_{0.82}S_{0.18}$ Sample S1.

pressures here ρ_{xx} increases with increasing field and increasing temperature, with no kinks or anomalies that might be associated with another phase transition. Additionally, Figure 5.6 shows temperature sweeps in fixed magnetic fields that display no upturn at low temperatures for any pressure. This upturn is found for FeSe and $FeSe_{1-x}S_x$ under pressure and is suggested as the transport signature of the magnetic transition [69, 96, 104, 107]. Hence, for these pressures the only phase transition is the superconducting transition for sample S1.

Next the superconducting transition width is considered, a measure of the homogeneity of the system. Figure 5.2b considers the transition in the absence of an applied magnetic field and shows that the transition becomes very sharp with

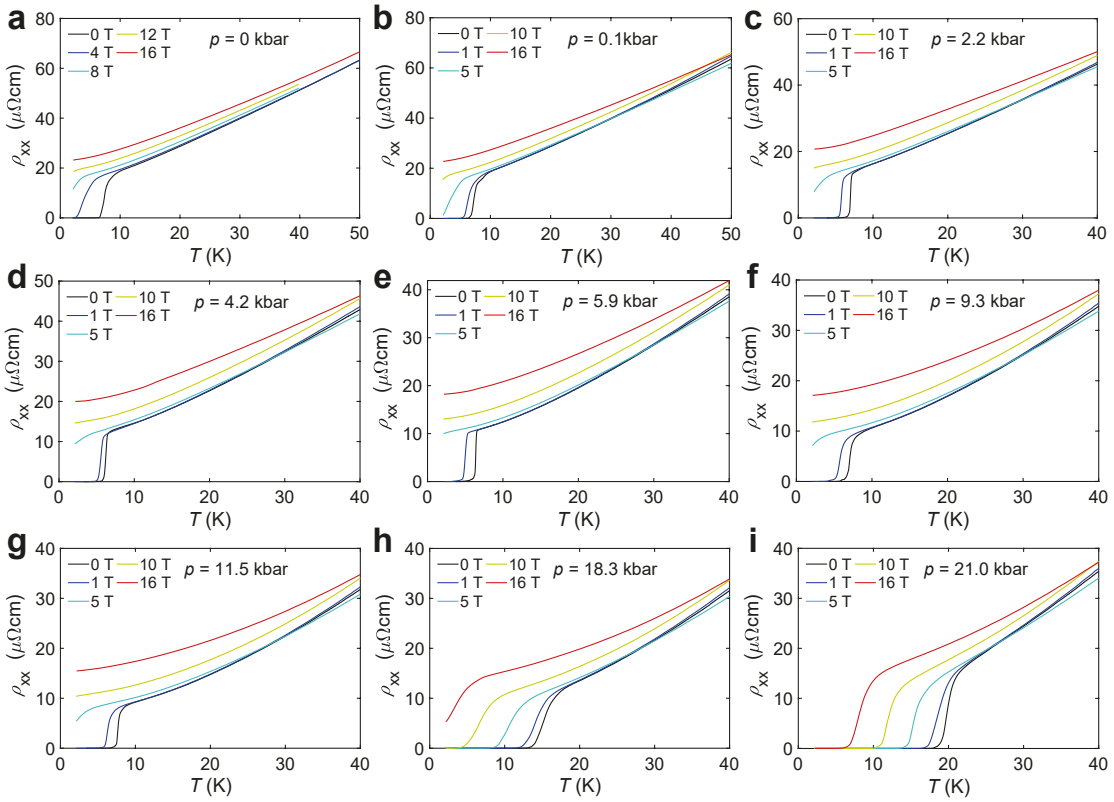

Figure 5.6: Longitudinal resistivity of $FeSe_{0.82}S_{0.18}$ Sample S1. (a)-(i) Longitudinal resistivity temperature dependence in fixed fields for different pressures.

only a small applied pressure, but broadens significantly above 15 kbar. Meanwhile, a similar trend is found for the temperature sweeps in magnetic fields where the superconducting transitions for the highest pressures are much broader, shown in Figure 5.6 (and see derivatives in Figure 5.19 in Section 5.8). The superconducting transition in field, at fixed temperatures, becomes broader at low temperatures. Figure 5.18 shows the derivatives of ρ_{xx} in field for each pressure. As the temperature is lowered, the peak of the derivative through the transition decreases in amplitude and becomes broader in field. In particular, the transition in magnetic field is barely detectable in Figure 5.4g at the lowest temperatures for 15.2 kbar. For the transitions in temperature, the superconducting transition becomes broader in the region of the phase diagram where $T_c(p)$ increases fastest (1.2 K/kbar around 15-20 kbar).

A mobility spectrum can be constructed for a particular temperature and pressure using the ρ_{xx} and ρ_{xy} field dependence, as described in section 1.4.3. Figure 5.7a shows the mobility spectrum for each pressure at 10 K (the 4.2 and

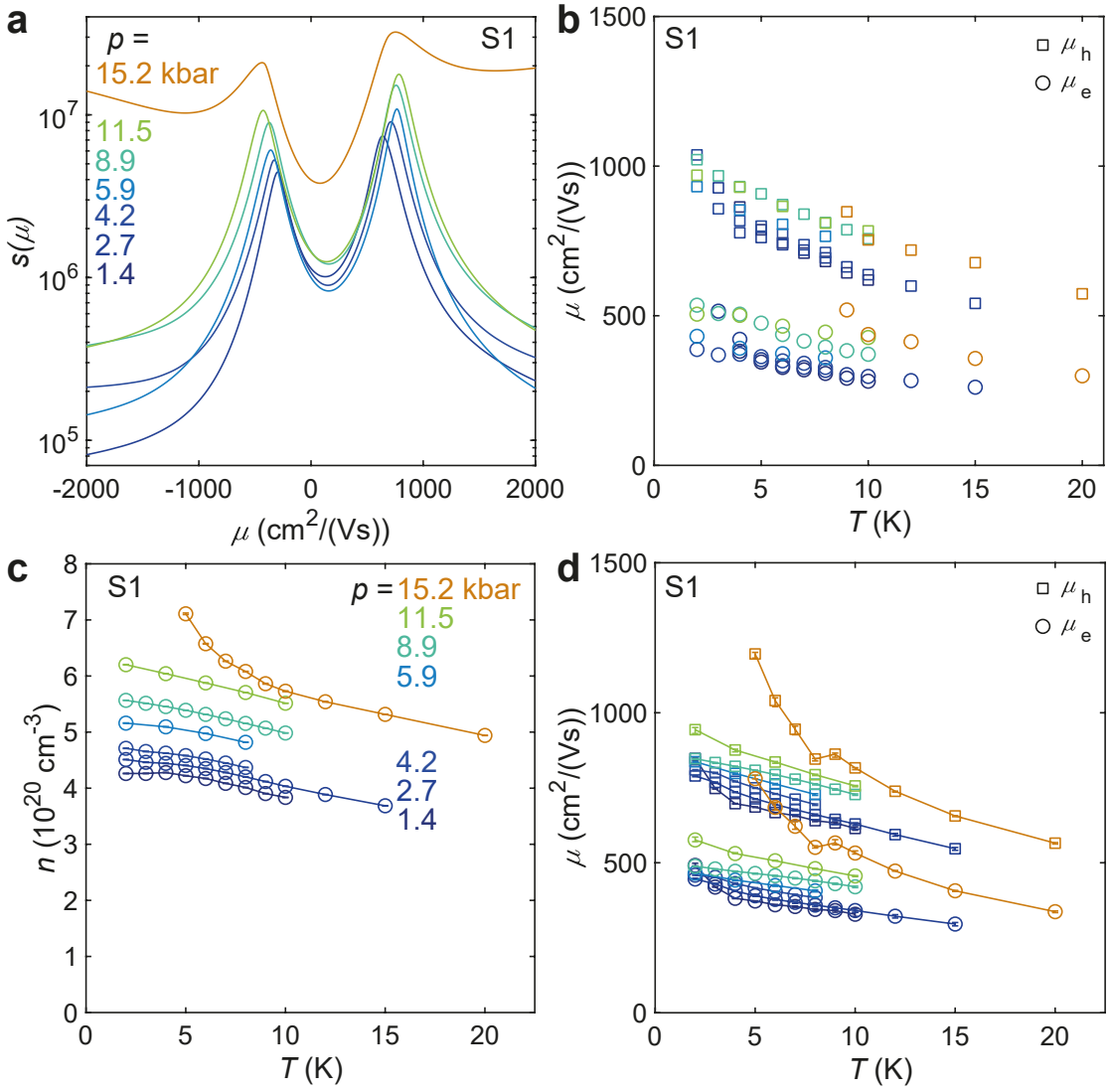

Figure 5.7: Mobility analysis of $FeSe_{0.82}S_{0.18}$ Sample S1. (a) Mobility spectrum at 10 K, using the field dependence of Figures 5.4 and 5.5. For 4.2 and 5.9 kbar, the spectrum is calculated at 8 K (the highest available temperature). (b) The position of the peaks in the mobility spectrums in (a), where peaks with $\mu > 0$ are holes (squares), and $\mu < 0$ are electrons (circles). (c) Charge carrier density and (d) mobility for each pressure at low temperatures from simultaneous fits to ρ_{xx} and ρ_{xy} at fixed temperatures to a compensated two carrier model (see equations 1.39 and 1.40). Colour denotes the pressure across all panels, and the symbols the type of charge carrier. As $n_h = n_e$ only one symbol is shown in (c).

5.9 kbar spectrums are taken at 8 K, as no measurements were performed at 10 K). For all pressures, a single positive mobility peak and a single negative mobility peak are found, corresponding to hole-like and electron-like charge carriers respectively. As the pressure increases the peaks move away from $\mu = 0$, indicating both charge

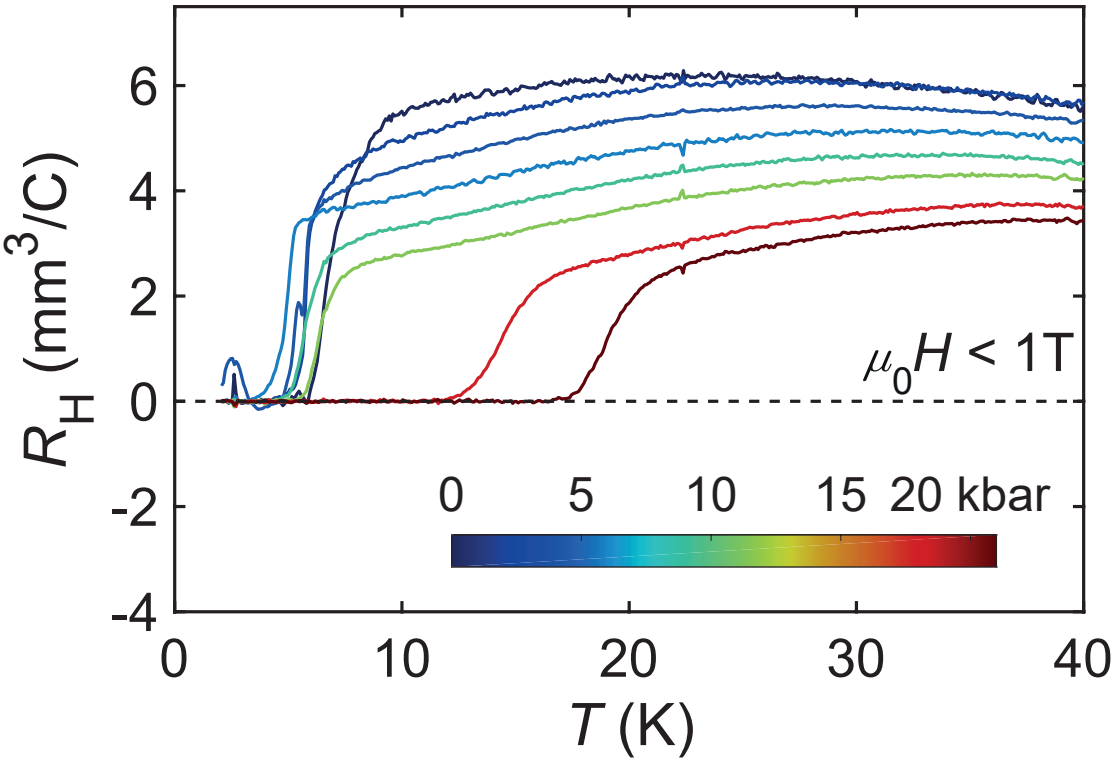

Figure 5.8: Hall coefficient of $FeSe_{0.82}S_{0.18}$ Sample S1. The Hall coefficient measured in magnetic fields of 1 T at different applied pressures.

carriers become more mobile, as shown in Figure 5.7b.

The behaviour in field of ρ_{xx} and ρ_{xy} can be modelled using an appropriate magnetoresistance model, as described in section 1.4.3. Here, a two band compensated model is used for all pressures and temperatures, using the mobility spectrums as a starting point for the fits. From these fits, the charge carrier density and charge carrier mobility can be found and the temperature and pressure evolutions are shown in Figures 5.7c and d respectively. The mobilities from this method follow that of the mobility spectrum, with the electron and holes becoming more mobile at lower temperatures and at higher pressures. At all temperatures and pressures measured here, the holes are always more mobile than the electrons. Similarly, the charge carrier density for each carrier increases as the temperature decreases or the pressure increases, for these low temperatures. The behaviour is similar to Cu-FeSe (Chapter 4 and $FeSe_{0.96}S_{0.04}$ (Chapter 6) under pressure with the charge carrier densities increasing, and the holes being more mobile than electrons.

In Figure 5.8 the Hall resistivity is extracted from ρ_{xy} in low fields (1 T) for various pressures, and found to be positive for all measured values at low temperatures around T_c. The Hall coefficient has the same temperature behaviour for the full pressure range, but the magnitude of R_H decreases with pressure. When considering the changes in the mobility, this is expected. For the two band compensated magnetoresistance, R_H is expected to vary with $(\mu_h - \mu_e)/(\mu_h + \mu_e)$. From Figure 5.7d, the mobilities of both holes and electron-like carriers increase with pressure by a similar amount. Therefore, $\mu_h - \mu_e$ is approximately pressure invariant, and the absolute increase in mobilities as pressure increases will reduce the Hall coefficient. No significant changes occur to R_H, even as T_c begins to increase. The Hall coefficient is negative at low temperatures for FeSe, but with sulphur substitution this negative region is reduced and eventually (around $x = 0.16$) becomes positive at low temperatures [171, 210]. A positive R_H is consistent between the applied pressure of $FeSe_{0.82}S_{0.18}$ reported here, and the chemical pressure in tetragonal $FeSe_{1-x}S_x$ [171, 210], indicating the similar hole dominated transport of the tetragonal phase.

5.5 The evolution of the Fermi surface with pressure.

This next section uses high magnetic fields at very low temperatures to suppress the superconductivity, and reveal the normal state magnetoresistance which displays oscillations as a function of magnetic field on top, as shown in Figure 5.10a. These are quantum oscillations, which arise due to Landau quantization of allowed energy levels for a metallic system in an external magnetic field [133]. The frequency of these oscillations are directly related to the (extremal) cross-sectional areas, A_k, on each Fermi surface by the Onsager relation: $F_k = \frac{\hbar}{2\pi e} A_k$ [132]. From examining the changes in amplitude with temperature and field due to damping effects, insights can be made into the effective mass of quasiparticles and scattering times, see section 1.5. As $FeSe_{1-x}S_x$ is a multiband system, there are contributions to the quantum oscillations from the minimum and maximum orbits of each Fermi surface, leading to a complex superposition of many frequencies.

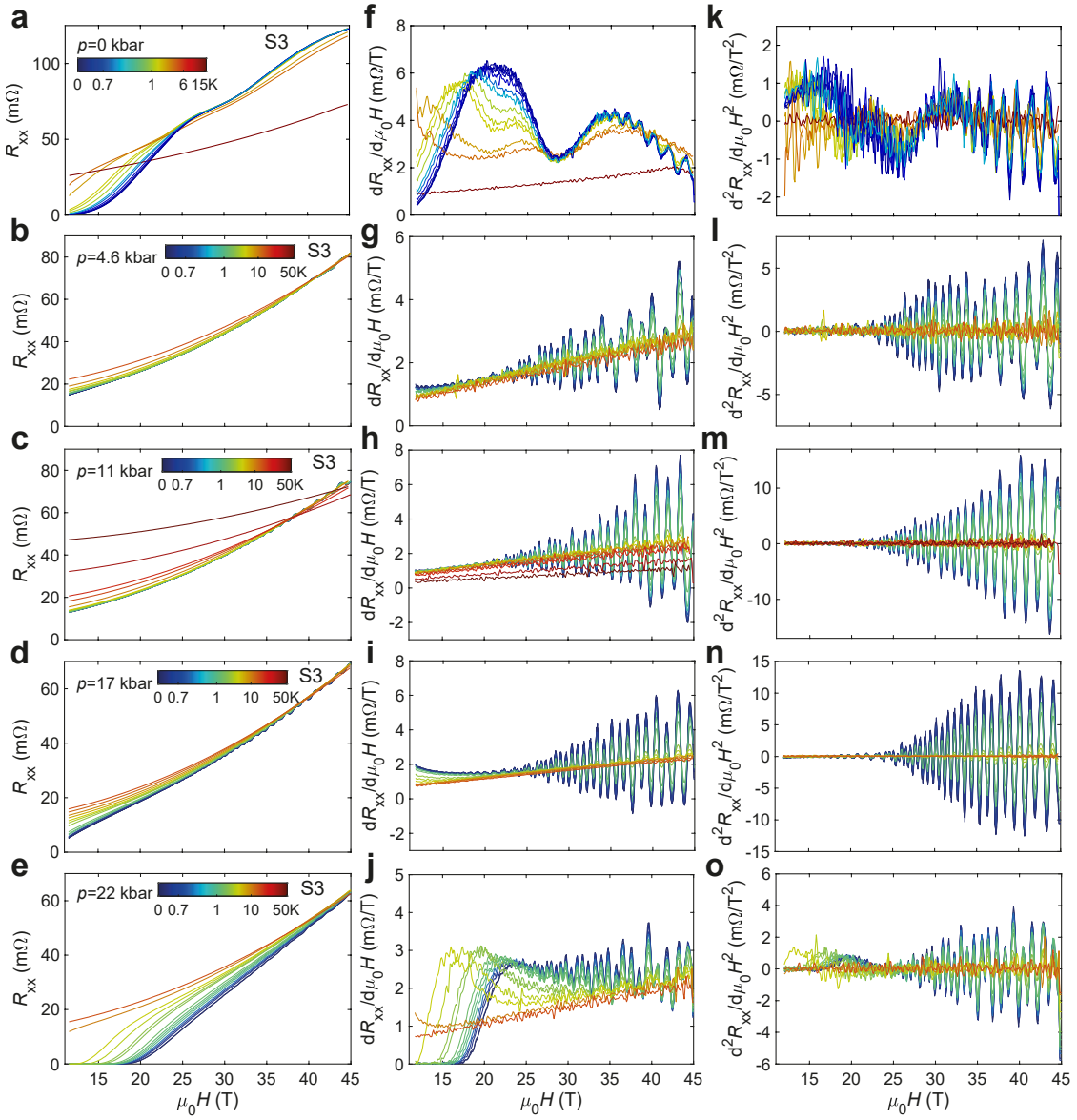

Figure 5.9: High-magnetic field longitudinal magnetoresistance of $FeSe_{0.82}S_{0.18}$ Sample S3. The field dependence of the (a - e) magnetoresistance, (f - j) first derivative in field, and (k - o) second derivative in field. Each row is a different pressure, and the colour scale applies across each row.

Figures 5.9a-e shows the resistance up to 45 T for 5 pressures up to 22 kbar from 0.4 K to high temperatures for $FeSe_{0.82}S_{0.18}$ sample S3. For every pressure the quantum oscillations emerge at high magnetic fields and low temperatures. The first and second derivative emphasise these oscillations being largest at lower temperatures and higher magnetic fields, see Figures 5.9f-j and 5.9k-o. Notably, Figure 5.9j suggests that for the highest pressure, 22 kbar, the oscillations begin

before the system reaches the normal state because the low temperature derivatives remain higher valued than the high temperature derivatives acting as a normal state baseline. At 0 kbar, the resistance in field is dominated by a low frequency oscillations, whereas the measurements under pressure only show higher frequency oscillations. The low frequency dominates the signal for $FeSe_{1-x}S_x$ for systems inside the nematic phase [67], suggesting that sample S3 is inside the nematic phase for 0 kbar. Although, no signature of the nematic phase was seen in the 0 T resistance curve in Figure 5.1, which likely places S3 very close to the nematic end point (the 0 T curve was measured at around -0.5 K/min, which is unlikely to smooth out a strong structural transition resistance kink). The change in oscillations appearance is consistent with the evolution of the Fermi surface and a possible Lifshitz transition between the nematic and tetragonal phases, tuned by both chemical and applied pressure [67, 105].

Figure 5.10 describes how to isolate the oscillatory signal, beginning with the resistance up to 45 T for different pressures up to 22 kbar at a base temperature of 0.4 K in Figure 5.10a. To isolate the quantum oscillations from the normal state background, the background is estimated using a polynomial fit of order 7, the oscillatory signal is shown in Figure 5.10b. The frequencies of the multiple oscillations are determined using a fast Fourier transform (FFT) on the oscillatory signals to produce a frequency spectrum, as shown for base temperature in Figure 5.10c. Each frequency, F, corresponds to a minimum or maximum orbit for a Fermi surface, where a larger F is for a larger area orbit. From Figure 5.10c, individual frequency peaks can be tracked as the pressure increases. Figure 5.14d shows that, with increasing pressure, all the frequencies increase in size linearly. According to Luttinger's theorem, the carrier density is directly proportional to the volume enclosed by a systems Fermi surface [211], and therefore the carrier density is growing approximately linearly with pressure.

Figure 5.10d shows a schematic of the Fermi surface, cut at $k_z = 0$, with orbits assigned to each surface. The two largest frequencies are assigned to the frequencies γ and δ, which correspond to the maximal orbit of the electron and

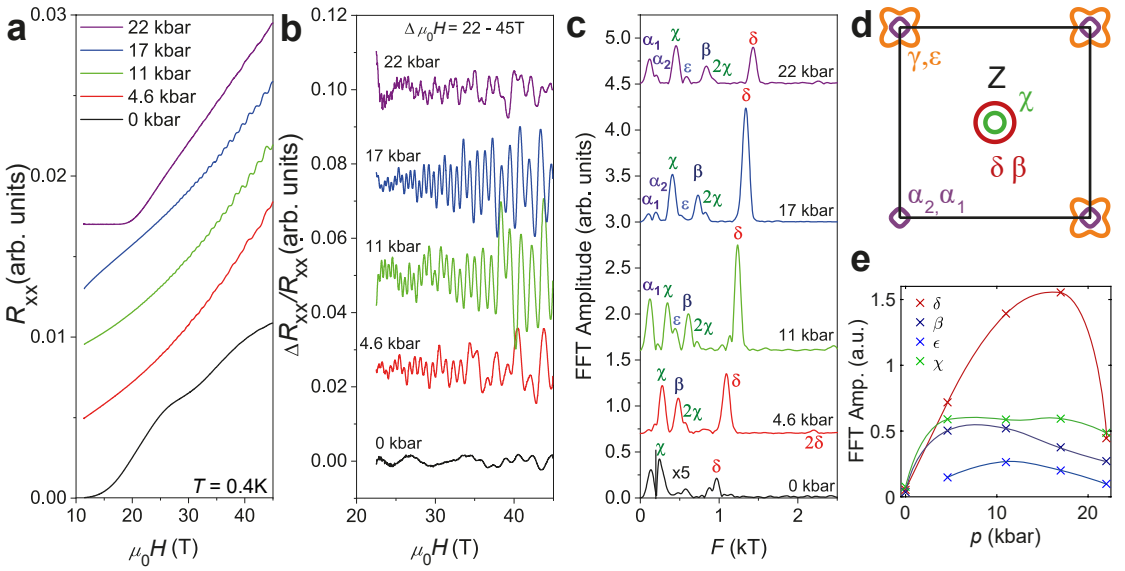

Figure 5.10: Evolution of quantum oscillations with pressure in $FeSe_{0.82}S_{0.18}$. (a) Magnetotransport at 0.4 K for a range of pressures, shifted for clarity. (b) Shubnikov de Haas oscillations obtained as the residuals from fitting the magnetoresistance to a polynomial order seven over a field window of $\Delta\mu_0 H = 22 - 45$ T (c) Fast Fourier transforms (FFT) using a Hanning windowing function of each signal. The ambient signal is amplified above 200 T for clarity. Several peaks are tracked across the different pressures and labelled, as are observed harmonics. (d) Schematic Fermi surface of $FeSe_{0.82}S_{0.18}$ (0 kbar) cut at $k_z = 0$. The bottom left outer electron orbit is intentionally omitted to highlight the inner orbit. Labels correspond to the Fermi surface that orbit is on (both minimum and maximum). (e) Pressure dependence of the FFT amplitude at base temperature for each orbit, extracted from the FFT spectrums in (c).

hole outer surfaces respectively. The next largest frequency, β, is the outer hole minimum, at the Γ point, and the minimum of the outer electron is the ϵ orbit. Next, the χ frequency corresponds to the maximal orbit of the three-dimensional inner hole [201]. Finally, the two low frequencies, α_1 and α_2, are assigned to the inner electron. Figure 5.10e shows how the amplitude of the high frequency δ peak increases significantly with pressure up to 17 kbar but then decreases significantly at 22 kbar. In contrast, the other orbit amplitudes remain relatively stable in the tetragonal phase, with small changes, and a consistent, small, decrease at 22 kbar. Note that the lowest frequencies assigned to the α_1 and α_2 orbits are determined both from the frequency spectrum, and investigating the oscillations with a low pass filter. A quasi-two dimensional cylinder is expected here for $FeSe_{0.82}S_{0.18}$ from ARPES measurements [201]. Table 5.2 contains all the experimentally determined

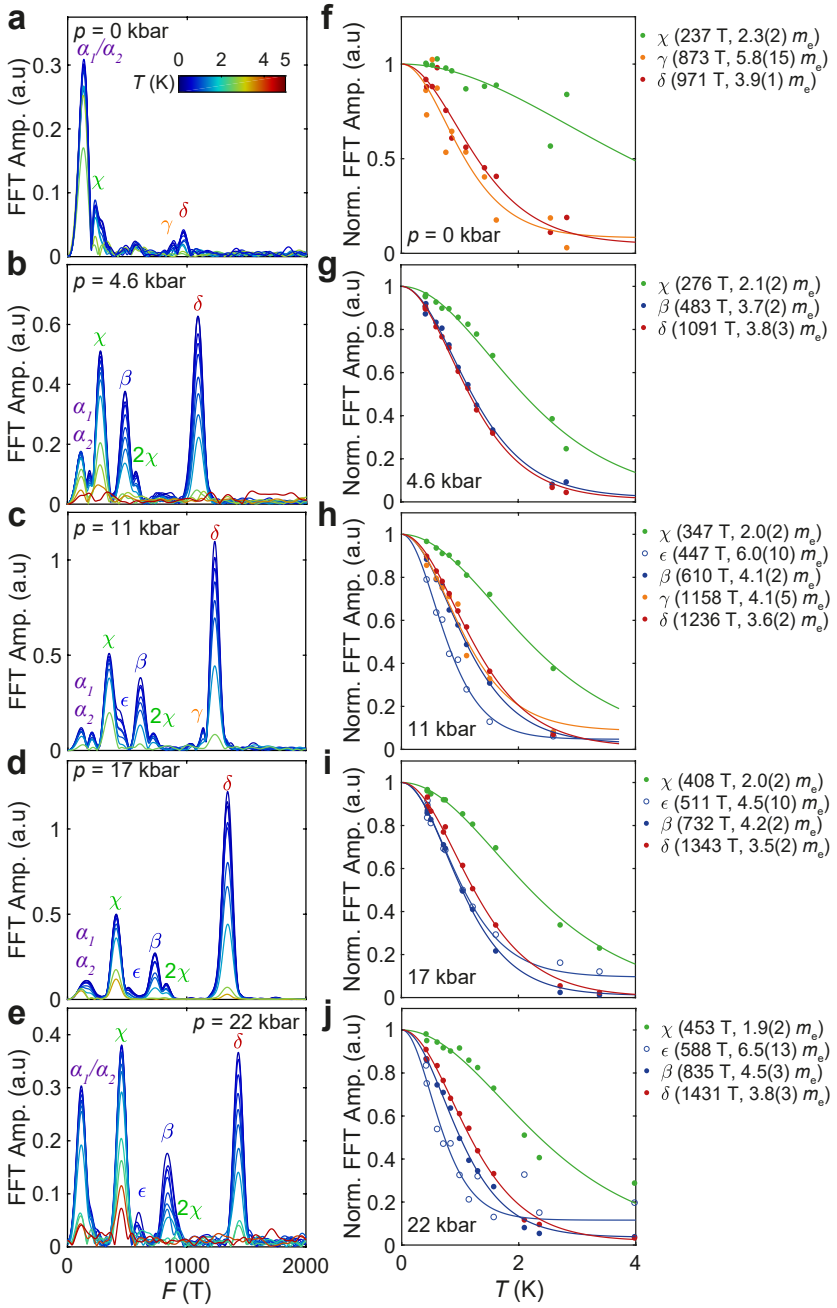

Figure 5.11: Frequency spectrum of oscillations and amplitude temperature dependence. (a-e) Quantum oscillations at each pressure for a range of temperatures where a background of polynomial order seven has been removed and the remaining oscillatory signal fast Fourier transformed (FFT). The signals are from a field window of 22 to 44.5 T, with the average inverse field used in the LK formula, and a Hanning window was used for every FFT. (f-j) The temperature dependence of the amplitude of the main peaks. The solid lines are fits to the Lifshitz-Kosevich formula to extract the effective mass of that orbit. Each plot is normalised at $T = 0$. The second harmonic of the χ orbit is labelled 2χ.

frequencies for each orbit and pressure.

5.5.1 Quasiparticle masses

The effective mass of the quasiparticles can be extracted from the thermal damping term describing changes in the quantum oscillations due to smearing of the Fermi surface as the temperature increases. This is governed by the Lifshitz Kosevich (LK) formula, equation 1.64 [133]. Figures 5.11a-e show the temperature dependence of the amplitude for each orbit at different pressures in the FFT frequency spectrums. To determine the effective mass of a particular orbit and pressure the LK formula is applied to the FFT amplitude temperature dependence, as shown for each orbit and pressure in Figures 5.11f-j. An orbit with strong electronic correlations has a heavier effective mass, and the FFT amplitude will decrease faster as the temperature increases than for a lighter effective mass. Here, the χ orbit has a lighter effective mass than the, quite similar, δ and β orbits. The heaviest effective masses are found in the γ and ϵ orbits, although these are hard to track across each pressure due to the low amplitude, and/or proximity in frequency to larger amplitude orbits. Additionally, this suggests the effective masses for the outer electron pocket are heavier than for the outer hole pocket, as found for FeSe with the γ orbit effective mass at $7\,m_e$ [67]. The pressure dependence for the effective mass of each orbit is shown in Figure 5.14f. Perhaps surprisingly, the effective masses of each orbit show only small changes under applied pressure, despite the significant increase in T_c at high pressures (see $\mu_0 H_{c2}$ for 22 kbar in Figure 5.10a). The χ orbit effective mass has a weak linear decrease under pressure, whilst there is a small increase for the β effective mass. The δ orbit effective mass shows no changes under pressure within experimental errors. The effective mass can be enhanced by both electron-electron coupling and electron-phonon coupling, $m^*{=}m_b(1+\lambda_{el-ph})(1+\lambda_{e-e})$ [133]. For FeSe, the electron-phonon coupling was predicted to increase with pressure from $\lambda_{el-ph} = 0.98$ at 0 kbar to 1.159 at 26 kbar [212]. Such an increase would increase the effective mass of δ by $0.4\,m_e$, and χ by $0.2\,m_e$, these changes are within the experimental errors of the measurements. However, the β orbit effective mass increases by $0.8\,m_e$ from 4.6 to 22 kbar, which is larger than the increase predicted just from changes in the electron-phonon coupling of $0.4\,m_e$, hence other

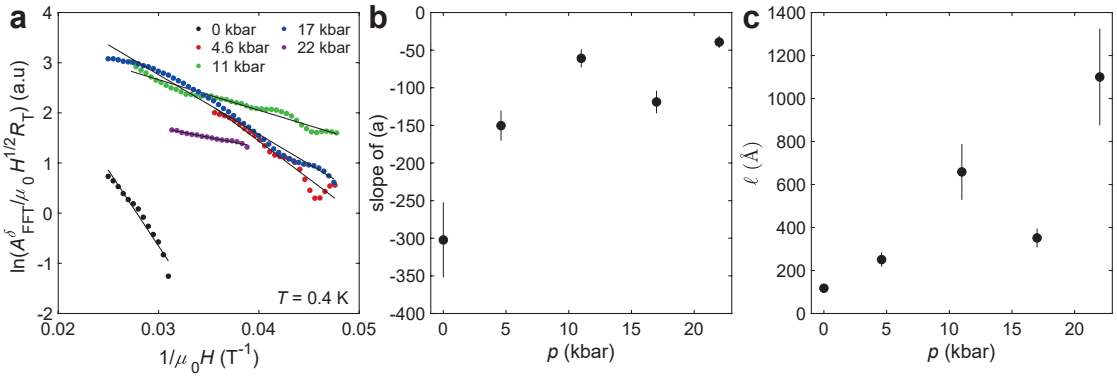

Figure 5.12: Dingle analysis of the δ orbit. (a) Dingle plot for each pressure focused on the δ orbit. The amplitude, $A^{\delta}_{\mathrm{FFT}}$, for each point is for the δ peak in the FFT centred at that $1/\mu_0 H$. Black lines are linear fits. (b) The slope of the fits in (a). (c) Pressure dependence of the mean free path, ℓ, assuming a circular orbit for the Dingle damping with the values in (b) equivalent to $-1140\sqrt{F}/\ell$.

contributions, such as electron-electron interactions may also be increasing with pressure. Ideally, to fully understand the effect of electron-electron correlations comparisons would be made between the effective masses from quantum oscillations and the band masses from DFT calculations. However, DFT calculations are very challenging in these systems because of the strong correlations and the DFT band structure requires orbital dependent band shifts to match experimental results. Notably, for FeS at 0 kbar, which has weaker correlations, there is a ratio of the effective mass to band mass around 2.0(2) for all bands [213].

The impurity level is not expected to change between different pressures because the same sample, with a well-defined impurity content, is pressurized. As such, any further changes in scattering could be caused by additional type of fluctuations coupled to the electronic system. The Dingle term refers to damping of quantum oscillations from broadening of quantum levels due to impurity scattering. Figure 5.12a is a Dingle plot for the δ orbit of each pressure at the lowest temperature (0.4 K). By plotting $\ln(A^{\delta}_{\mathrm{FFT}}/\mu_0 H^{1/2} R_{\mathrm{T}})$ against the inverse field, the slope reveals the Dingle temperature, T_{D}. For a circular orbit, the slope is equal to $-1140\sqrt{F}/\ell\mu_0 H$ (see Section 1.5.3), where F is the frequency and ℓ the mean free path. Figure 5.12b shows the value of the slope for each pressure, which is used to calculate ℓ in Figure 5.12c. It should be noted that the curves have a weak oscillation,

which is expected for two closely spaced frequencies, as expected here for the nearby γ orbit[2]. With increasing pressure, in general, the mean free path increases. At 22 kbar, the amplitude of the δ orbit decreases significantly (see Figure 5.10e), although it now appears the mean free path is largest here which should help the observation of quantum oscillations. A possible explanation is that the oscillations for 22 kbar are observed near to the superconducting transition, inside the vortex state. From Figure 5.9j the low temperature resistivity derivatives do not return to the values of the high temperature derivatives until very high magnetic fields, unlike at lower pressures, an indication the system is not fully in the normal state. In this scenario, a damping effect due to the opening of the superconducting gap is expected close to H_{c2} [214], but such analysis is complicated by the complex spectrum here. In contrast, $FeSe_{0.89}S_{0.11}$ under pressure, the scattering time of the δ orbit showed little pressure dependence across the nematic end point, within experimental errors [105].

5.5.2 Fermi surface simulations

Using the experimentally measured values of the quantum oscillation frequencies, the evolution of the Fermi surface of $FeSe_{0.82}S_{0.18}$ up to 22 kbar is simulated[3], where the constraints of the model are these frequencies. The model expands the Fermi surface, $\mathbf{k}_F$ into symmetric parameters which are allowed by the symmetry of the system with cylindrical coordinates:

$$\mathbf{k}_F(\psi, \kappa) = k_{00} + k_{04} \cos 4\psi + k_{10} \cos \kappa \tag{5.1}$$

where ψ is the radial angle, and $\kappa = ck_z$, with c the lattice constant. The coefficients, k_{00}, k_{04}, and k_{10}, are varied such that the extremal orbit areas of the Fermi surface model match the observed frequencies. The aim is to replicate the Fermi surface distortions seen in ARPES [190, 201], where a Lifshitz transition is seen at the Γ point [67]. It is assumed that, due to curvature effects, the outer electron surface (the γ and ϵ orbits) is harder to observe than the others [190]. As the pressure is increased,

[2] An attempt to bandpass the signal around the high frequency and fit directly the Lifshitz-Kosevich formula for two frequencies was attempted, but has too many variables to be reliably successful.

[3] Thank you to Roemer Hinlopen for access to the software used to model the Fermi Surface.

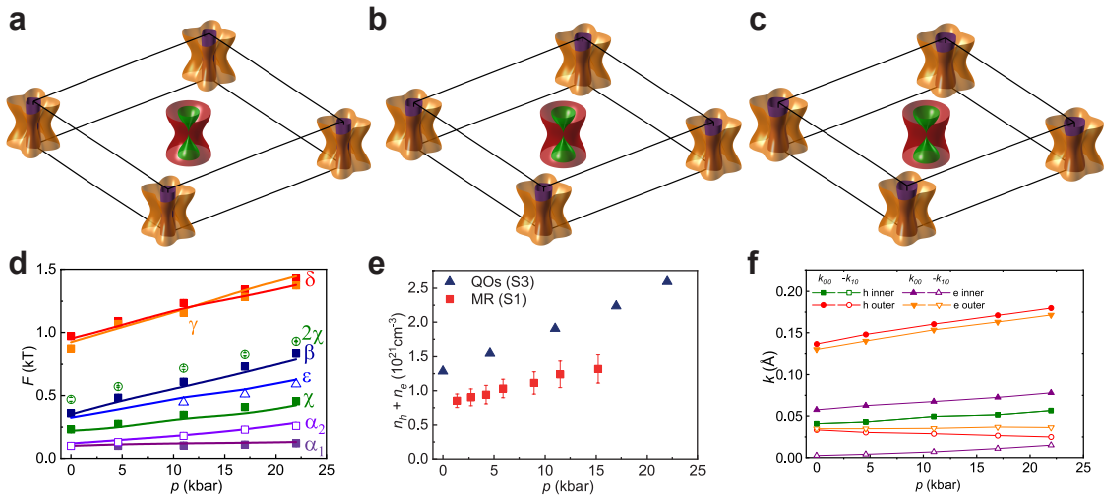

Figure 5.13: Model of the Fermi surface of $FeSe_{0.82}S_{0.18}$ evolution with pressure. Fermi surface model of $FeSe_{0.82}S_{0.18}$ at (a) 0 kbar, (b) 11 kbar, and (c) 22 kbar. (d) Pressure dependence of the frequencies from experiments (symbols) and the model (solid lines). (e) The carrier density, n, using the Fermi surface model (blue triangles), and compared to the fitted magnetoresistance at 2 K (sample S1) (red squares, error bars correspond to 8 K difference). (f) The k_{00} and $(-1)k_{10}$ changes with applied pressure from the model. The values are included in Table 5.3.

the surfaces all expand in size to match the linear expansion of the frequencies measured. Additionally, the k_{04} values which affect the shape for the electron surfaces are fixed in pressure and estimated from ARPES [67, 190]. As $FeSe_{1-x}S_x$ systems are compensated metals, and no signatures of a Fermi surface reconstruction under pressure for this system have been found, the models are compensated with slight adjustments to the size of orbits to maintain compensation at all pressures.

The $\mathbf{k}_F$ values describing the surfaces are included in Table 5.3. The pressure dependence of the parameters, frequencies and the model itself are included in Figure 5.13. As expected, the value of k_{00}, which affects the overall surface size, increase with pressure with a similar evolution for the inner and outer surfaces, as would be expected to maintain compensation. The k_{10} values show more differentiation. For the inner hole orbit, $k_{10} = -k_{00}$, and so is increasing in magnitude. Similarly, k_{10} increases for the inner electron, as the surface becomes more three-dimensional. Likewise, the outer electron becomes more three-dimensional, whereas the outer hole becomes more two-dimensional with less warping (compare Figures 5.13a and c). A natural comparison is with FeS due to the similarities between chemical

pressure with sulphur substitution and applied pressure. The inner electron in particular for FeS has quite different minimum and maximum frequencies [213], which is the direction the inner electron is heading in here with pressure.

By having an overall shape of the Fermi surface, the evolution of the charge carrier densities can be estimated, and appears to increase linearly, doubling from 0 to 22 kbar, see Figure 5.13e. The density at 0 kbar is larger than that found in FeSe from ARPES ($0.7 \times 10^{21}\,\mathrm{cm}^{-3}$) [170], despite T_c being lower here. The magnetoresistance analysis on sample S1 is shown with the fitted carrier densities at 2 K displaying the same behaviour and similar values as the simulation carrier densities. Notably, in FeSe the carrier density decreased inside the nematic phase, but recovered the high temperature tetragonal value at lowest temperatures [170]. Here, the carrier densities increases for all pressures inside the tetragonal phase are in broad agreement for the different methods.

5.6 Discussion

Figure 5.14 compares changes to the electronic structure and effective masses of $FeSe_{0.82}S_{0.18}$ under pressure to that of the chemical substitution in $FeSe_{1-x}S_x$ [67]. Figure 5.14a shows the $FeSe_{1-x}S_x$ phase diagram as a function of isoelectronic substitution where the superconducting transition temperature decreases across the nematic end point, around $x = 0.18$. This study examines systems around this substitution under pressure in Figure 5.14b. The superconductivity is very stable up to around 10 kbar, before a strong enhancement up to 21 kbar. Firstly, Figure 5.14d shows the frequencies expand linearly with applied pressure in $FeSe_{0.82}S_{0.18}$, similar to trends observed in the tetragonal phases of $FeSe_{1-x}S_x$ [67, 105]. This rules out any reconstruction of the Fermi surface at high pressures (up to the measured 22 kbar) in $FeSe_{0.82}S_{0.18}$, in contrast to the magnetic phase in FeSe under pressure [87], and in $FeSe_{0.96}S_{0.04}$ under pressure in Chapter 6. Next, the effective masses for $FeSe_{0.82}S_{0.18}$ under pressure are lighter than the effective masses found in the nematic phase of $FeSe_{1-x}S_x$ [67] (comparing Figures 5.14e and f). For FeSe under pressure, the effective masses increased inside the nematic phase before the Fermi surface

reconstruction, and were slightly heavier compared to the same orbit values found here [87]. These changes indicate there are weaker correlations in the tetragonal phase, if the band mass is not significantly altered itself. Notably, a previously discussed correlation between the effective mass of the δ orbit (outer hole) and T_c in the nematic phase of $FeSe_{1-x}S_x$ and $FeSe_{0.89}S_{0.11}$ under pressure, which persists at least somewhat across the nematic end point, is not found to persist significantly into the tetragonal phase here (Figures 5.14a and e). Whilst the δ effective mass shows little pressure variation here, T_c increases three fold at high pressures (Figures 5.14b and f). Similarly, NMR measurements found that AFM fluctuations strongly correlated with T_c in the nematic $FeSe_{1-x}S_x$ [169], whereas the AFM fluctuations displayed little pressure dependence in FeSe up to 20 kbar, into the tetragonal phase [168, 169].

Figure 5.14h shows the pressure dependence of the T^2 coefficient in resistivity, A, which corresponds to Fermi liquid behaviour, and is linked to electron-electron interactions such that $A \propto (m^*/m_e)^2$. With increasing pressure up to 10 kbar A decreases, and plateaus at higher pressures, this behaviour is consistent across all three samples measured here, and two similar ones in literature [206]. It is expected that A would show little pressure dependence if solely related to the effective masses, which all show minimal pressure dependence (Figure 5.14f). Instead, A plateaus in the region that T_c increases significantly. This may indicate additional scattering effects, which do not alter the electronic correlations as measured by the thermal damping of quantum oscillations.

Next, I consider the similarity between chemical pressure and applied pressure in $FeSe_{1-x}S_x$ in the tetragonal phase where the Fermi surface expands in both cases [55, 67], but the enhancement in superconductivity is only found under applied pressure, such as here [104, 105]. The size of the Fermi energy, E_F, in a multiband superconductor is a parameter that provides important clues about the stabilization of different ground states competing with superconductivity [200]. In the case of a small Fermi energy, a Pomeranchuk instability is favoured, whereas a spin-density wave is stabilized for large Fermi energies. For this study, Figure 5.14g shows the

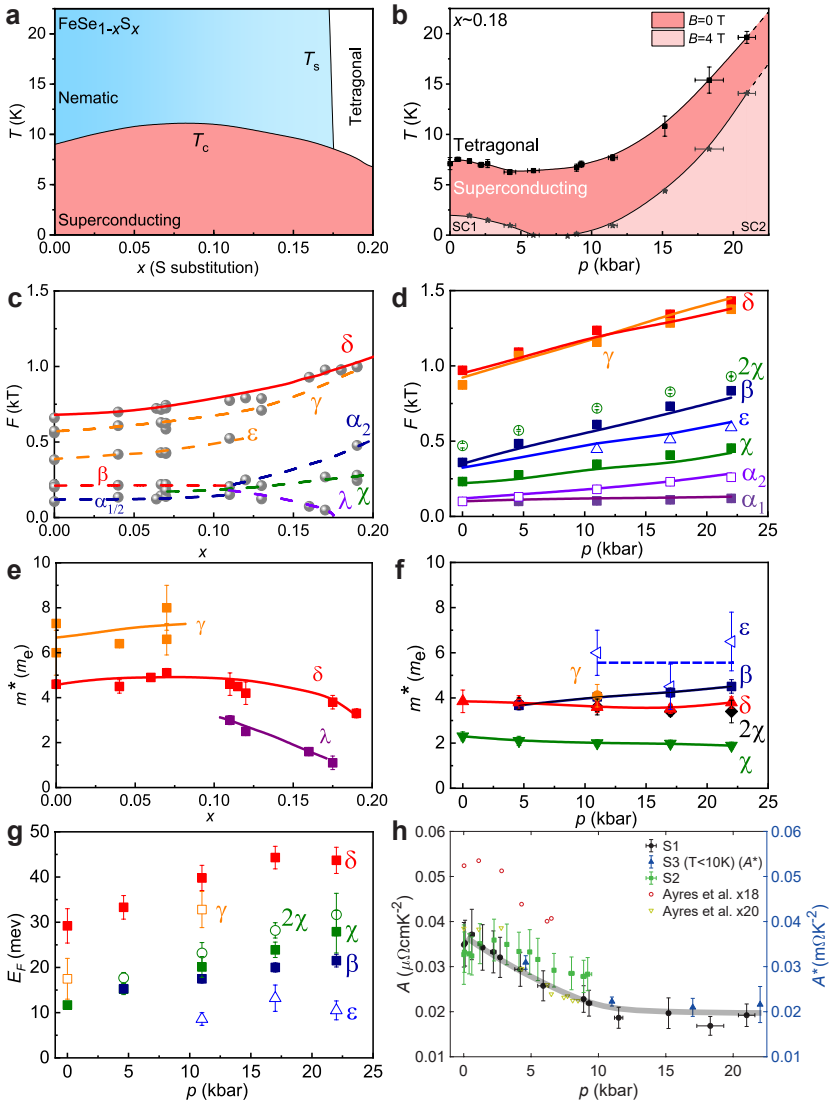

Figure 5.14: Pressure-temperature phase diagrams. (a) Sulphur substitution-temperature phase diagram of $FeSe_{1-x}S_x$, the nematic and superconducting phases are highlighted. (b) Pressure-temperature phase diagram of $FeSe_{0.82}S_{0.18}$ for different applied pressures up to 21 kbar, in no magnetic field and a 4 T field. Frequencies from quantum oscillation measurements of (c) $FeSe_{1-x}S_x$ and (d) $FeSe_{0.82}S_{0.18}$ with applied pressure. Quasiparticle effective masses from quantum oscillation measurements of (e) $FeSe_{1-x}S_x$ and (f) $FeSe_{0.82}S_{0.18}$ with applied pressure. (g) Fermi energy of each Fermi surface using the values in (d) and (f). (h) A pressure dependence with A extracted from low temperature Fermi liquid behaviour ($\rho = \rho_0 + AT^2$). Values for samples S1 and S2 are calculated in zero field, for a temperature range of $T_{on} + 2\,K$ to $T_{on} + 10\,K$. Sample S3 values are extracted from Figure 5.3 with $T < 10\,K$, these are in resistance and labelled A^*. Data is reproduced from Ayres et al. [206] for $FeSe_{1-x}S_x$ with $x = 0.18$ and 0.20. Values for the frequencies, effective masses and Fermi energies are included in Table 5.2. Data for figures (a), (c), and (e) reproduced from [67].

Fermi energy, E_F, calculated for each orbit using the frequencies (Figure 5.14d) and effective masses (Figure 5.14f) with the relation: $E_F = e\hbar F/m^*$, assuming parabolic dispersions. With increasing pressure, the Fermi energies increase steadily in the tetragonal phase for all orbits, towards 50 meV, because the frequencies increase but the quasiparticle effective masses show little pressure dependence. For the high pressure phase of FeSe, the Fermi energy seems to remain around 10 meV, although this is in the magnetic phase [87]. A previous study on $FeSe_{0.89}S_{0.11}$ highlighted an increase in E_F from the nematic to tetragonal phase under pressure [105], to comparable values found here at low pressures. It is expected that large hole and electron Fermi surface sheets at high pressures enhance nesting, which could enhance spin fluctuations and which promotes the stabilization of magnetically ordered states. This does not explain why such order is stabilised across the $FeSe_{1-x}S_x$ pressure phase diagrams as both the chemical and applied pressure expand the Fermi surfaces, but the smallest pressure required to stabilise magnetic order is found in FeSe (8 kbar) and not a higher substitution [104]. A possible explanation is that how well the Fermi surfaces overlap through the nesting vector may change since both the chemical and applied pressure alter the shape and size of the Fermi surfaces to affect nesting.

A crystallographic study of $FeSe_{0.80}S_{0.20}$ showed the lattice constants all decrease with pressure [207], and hence in reciprocal space $k_z = 2\pi/c$ will increase. Extensive structural studies of FeSe under pressure have shown the interlayer compressibility ($\mathrm{d}\ln c/\mathrm{d}P$) is a factor 2.5 larger than the compressibility in the (ab) plane [16]. This suggests the Se-Se interlayer interactions will be most strongly affected, and therefore interplane distortions of the Fermi surface ($k_z = 2\pi/c$) must be accounted for. The Fermi surface simulation does this with the k_{10} parameter of each surface (Figure 5.13f). These simulations showed that with pressure the small inner pockets are sensitive to the distortion and k_{10} increases. The outer hole becomes less warped and more two-dimensional in shape, whereas the outer electron surface became more three dimensional for the high pressure phase. These trends are also found

with chemical pressure. For FeS the hole cylinders are more two-dimensional as compared with the more distorted electron pockets [100, 213].

An additional consideration is the increase in the charge carrier density, n, from the expansion of the Fermi surface. Figure 5.13e shows from 0 to 22 kbar a doubling of n (calculated from the quantum oscillations), whereas the superconductivity increases by a factor 3 over the same pressure range. Interestingly, for FeS even though the Fermi surface continues to expand T_c is only 5 K [100, 213]. Enhancements in the density of states should lead to an increase in T_c. For a conventional superconductor described by the BCS theory, the critical temperature is related to the electron-phonon coupling, $\lambda = |g_{\text{eff}}|^2 g(E_F)$. The Fermi surfaces here are not quite two-dimensional, so the density of states will not be constant in energy, and therefore increases in E_F should increase $g_{3D}(E) \propto \sqrt{(E)}$, the density of states. This increases λ, and therefore enhances superconductivity. In the unconventional iron-based superconductors an empirical relationship has been found between the anion (chalcgoen/pnictogen) height above the Fe-plane, h, and T_c, with an optimum height of 1.38 Å [35]. Additionally, in $FeSe_{1-x}Te_x$ the value of h was closely linked to magnetism in these systems, and thus the nesting between surfaces, where the system becomes more magnetic as h increases towards FeTe [215]. With chemical pressure the chalcogen height in $FeSe_{1-x}S_x$ decreases towards FeS [216], which shows some differences to that for FeSe and $FeSe_{0.80}S_{0.20}$ under pressure [16, 207]. This may explain the shift in the pressure range where the magnetic phase is stabilised, and hence enhance spin fluctuations and enhance T_c [104].

The increase in T_c shows no correlation to the changes in effective mass, as shown between Figures 5.14b and f. The effective masses in the high pressure tetragonal phase of $FeSe_{1-x}S_x$ are similar both for $x \sim 0.18$ reported here, and $x \sim 0.11$ [105], as well as for the tetragonal $FeSe_{1-x}S_x$ [67] and FeS at ambient pressure [100]. As the resistivity at low temperatures generally decreases with pressure, the bandwidth should become wider and lead to weaker correlations. The smoothly varying transition temperature, T_c, at low pressure can be linked to the collapse of nematic fluctuations as the resistivity exponent varies strongly below

5 kbar [116]. However, the strong rise of T_c in $FeSe_{1-x}S_x$ under pressure cannot be explained only by modifications of the phonon spectrum and thus being only mediated by a conventional electron-phonon interaction [217].

5.7 Conclusions

This study explored the high pressure tetragonal phase of $FeSe_{1-x}S_x$. The phase diagram of $FeSe_{0.82}S_{0.18}$ has been constructed up to 22kbar, and, after the suppression of nematicity, no other phases are found. The superconducting transition temperature is very stable at low pressures, but exhibits a three-fold enhancement by 21 kbar. The electronic normal behaviour was found to display non-Fermi liquid behaviour evolving with pressure, and recovering Fermi liquid behaviour at low temperatures. The A coefficient linked to T^2 Fermi liquid behaviour decreased with pressure but levels off at high pressures where T_c is enhancing, and the quantum oscillations amplitude of the large pocket, δ decreases. The magnetoresistance showed that at low temperatures both the charge carrier densities and mobilities continuously increased with applied pressure. Furthermore, the high magnetic field measurements showed the Fermi surfaces expand linearly with pressure, from the frequency evolution in the quantum oscillations, matching the behaviour of the charge carrier density from the magnetoresistance analysis. The effective quasi-particle masses of the main frequencies, a measure of the electronic correlations, remain relatively constant in the high pressure phase, despite the threefold enhancement of superconductivity. The effective masses in the tetragonal phase here are lighter than those in the nematic state of $FeSe_{1-x}S_x$, and their evolution with pressure may be explained by a combination of electron-phonon coupling enhancement and nearest-neighbour Coulomb repulsion weakening.

5.8 Additional Figures and Tables

Table 5.2: Quantum oscillation results for $FeSe_{0.82}S_{0.18}$ Sample S3. Table of Fermi surface orbit frequencies, effective masses and Fermi energies extracted from quantum oscillation measurements under pressure. Frequencies for γ are extracted from bandpass filtered fits to the oscillations. All other frequencies extracted from FFTs.

p	0 kbar			4.6 kbar		
Orbit	F (T)	m^* (m_e)	E_F (meV)	F (T)	m^* (m_e)	E_F (meV)
α_1				100(10)		
α_2	100(10)			130(10)		
χ	237(6)	2.3(2)	11.7(10)	276(5)	2.1(2)	15(2)
ϵ						
β	359(4)			483(6)	3.7(2)	15(1)
2χ	470(15)			572(6)	3.8(3)	18(1)
γ	873(24)	5.8(15)	18(5)	1068		
δ	971(11)	3.9(1)	29(4)	1091(7)	3.8(3)	33(3)

p	11 kbar			17 kbar		
Orbit	F (T)	m^* (m_e)	E_F (meV)	F (T)	m^* (m_e)	E_F (meV)
α_1	103(12)			110(8)		
α_2	180(15)			230(15)		
χ	347(10)	2.0(2)	20(2)	408(4)	2.0(2)	24(2)
ϵ	447(3)	6.0(10)	8.6(14)	511(6)	4.5(10)	13(3)
β	610(8)	4.05(20)	18(1)	732(10)	4.2(2)	20(1)
2χ	719(10)	3.6(4)	23(2)	828(12)	3.4(2)	28(2)
γ	1158(18)	4.1(5)	33(4)	1285(11)		
δ	1236(10)	3.6(2)	40(3)	1343(5)	3.5(2)	44(3)

p	22 kbar		
Orbit	F (T)	m^* (m_e)	E_F (meV)
α_1	120		
α_2	260		
χ	453	1.9(2)	28(2)
ϵ	588	6.5(13)	11(2)
β	835	4.5(3)	22(2)
2χ	930	3.4(5)	32(5)
γ	1376		
δ	1431	3.8(3)	44(3)

Table 5.3: Table of Fermi surface simulation parameters. These are the input parameters used for the simulations. Beyond 3 significant figures the changes to the frequencies is within the error of experimentally determined frequencies.

	Electron					
	Inner			Outer		
p (kbar)	k_{00}	k_{04}	k_{10}	k_{00}	k_{04}	k_{10}
0	0.0575	0.005	−0.0025	0.13	−0.04	−0.035
4.6	0.0625	0.005	−0.004	0.14	−0.04	−0.035
11	0.0675	0.005	−0.007	0.154	−0.04	−0.0355
17	0.0725	0.005	−0.011	0.163	−0.04	−0.037
22	0.078	0.005	−0.015	0.171	−0.04	−0.0365

	Hole			
	Inner		Outer	
p (kbar)	k_{00}	k_{10}	k_{00}	k_{10}
0	0.041	−0.041	0.137	−0.0335
4.6	0.043	−0.043	0.148	−0.0305
11	0.0495	−0.0495	0.161	−0.029
17	0.0515	−0.0515	0.171	−0.0268
22	0.0566	−0.0566	0.180	−0.025

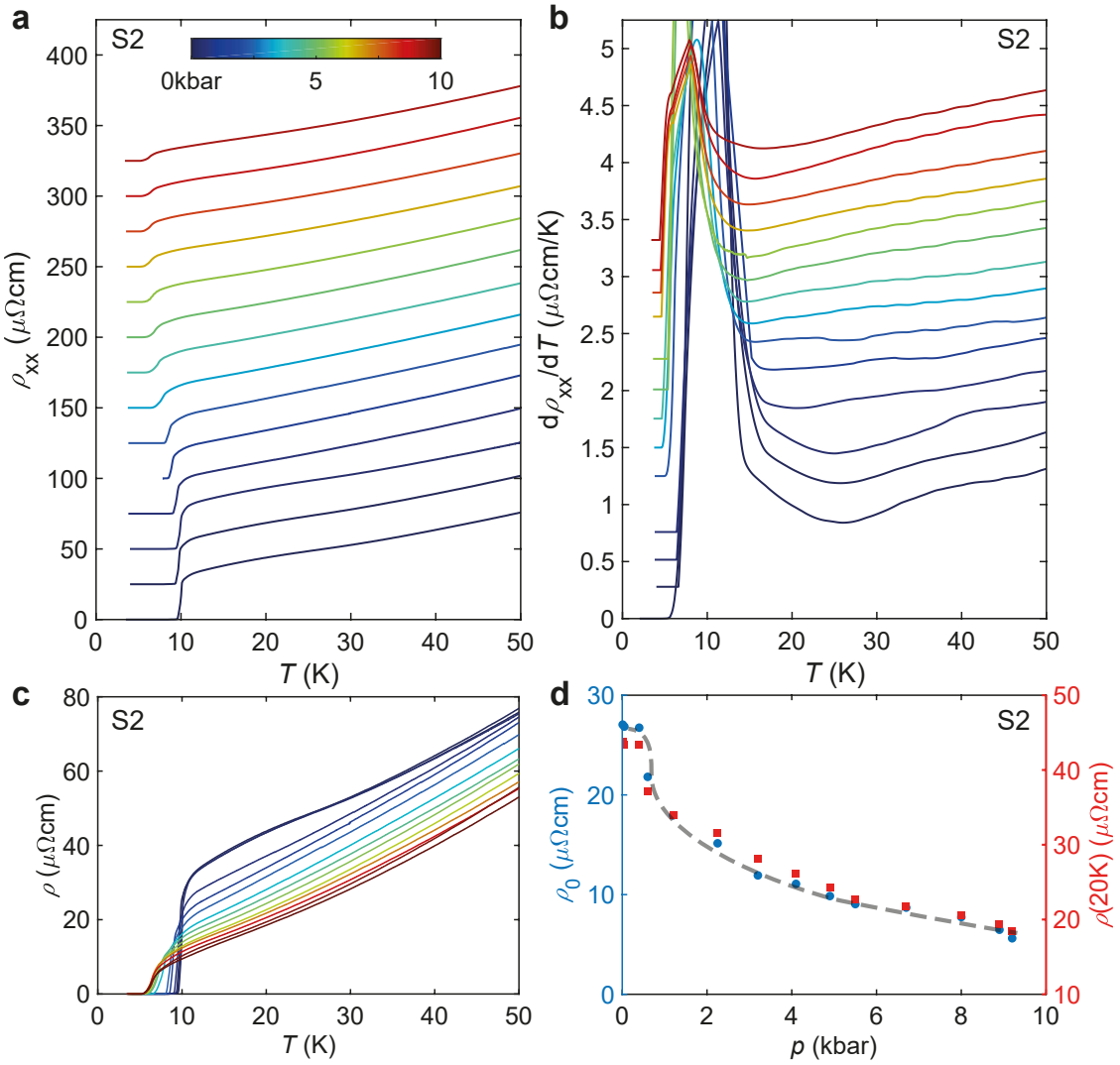

Figure 5.15: Transport of $FeSe_{0.82}S_{0.18}$ Sample S2. (a) Temperature dependence of the resistivity up to 9 kbar and (b) the derivative for determining transition temperatures. Curves are shifted for clarity. (c) The same as (a) without a shift for clarity. (d) The resistivity extrapolated to zero temperature, ρ_0 (blue circles), and at 20 K, ρ(20 K) (red squares), as a function of applied pressure. The dashed line is a guide to the eye.

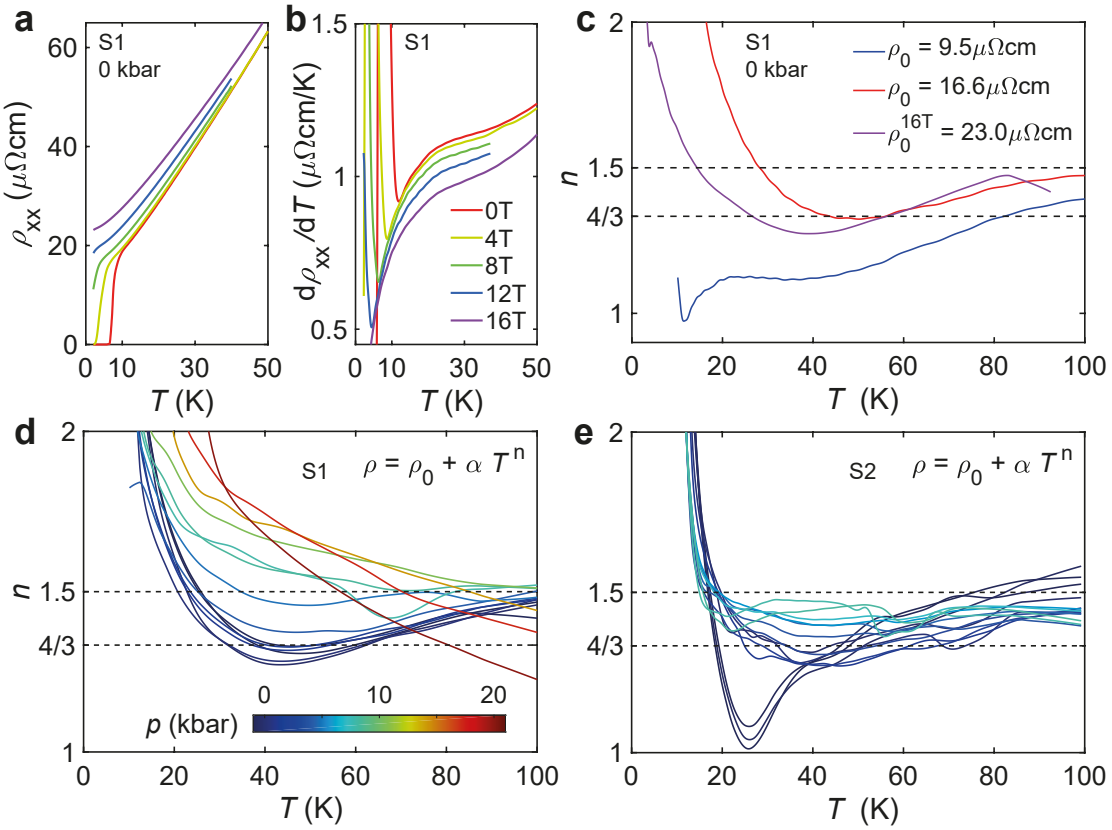

Figure 5.16: Variation of the n exponent with temperature. (a) Resistivity and (b) derivative of $FeSe_{0.82}S_{0.18}$ Sample S1. The zero field and 16 T measurements are used in (c). (c) Temperature dependence of the resistivity exponent, n, according to $\rho = \rho_0 + \alpha T^n$ in 0 kbar. The blue (n=1) and red (n=2) curves are both for zero field and use different ρ_0 values to extract $n(T)$. (d) and (e) are the temperature dependence of resistivity exponent for a range of pressures of samples S1 and S2 respectively. The colour scale is the same for both, with S2 shifted by −1 kbar. The exponents in (d) are used to produce the colour map in Figure 5.2d. The exact dependence of the resistivity exponent n is heavily influenced by the value of ρ_0 which is extracted from low temperature resistivity measurements in high magnetic fields.

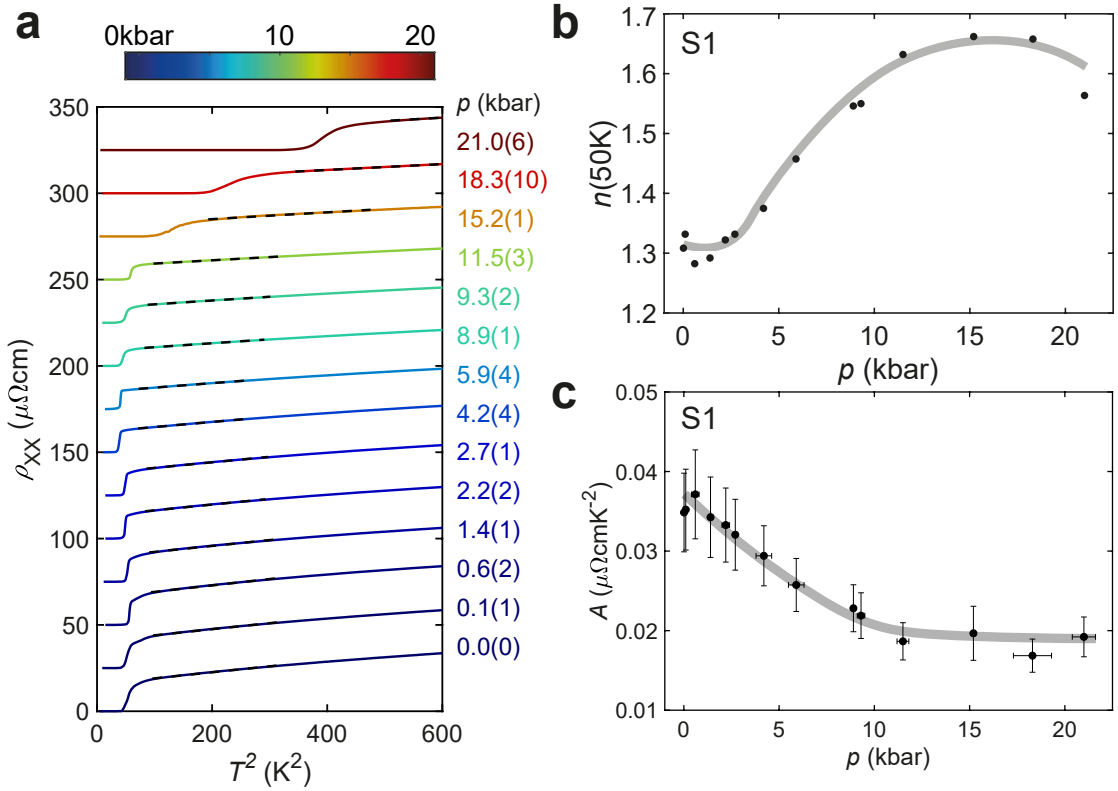

Figure 5.17: Low temperature Fermi liquid behaviour. (a) Resistivity low temperature behaviour for $FeSe_{0.82}S_{0.18}$ Sample S1, curves are shifted for clarity. Dashed lines are fits to T^2 behaviour for a range of 8 K above the onset of superconductivity (T_{on} + 2 K). (b) The local resistivity exponent at 50 K. (c) The coefficient of the T^2 resistivity dependence in (a) for sample S1 at low temperatures.

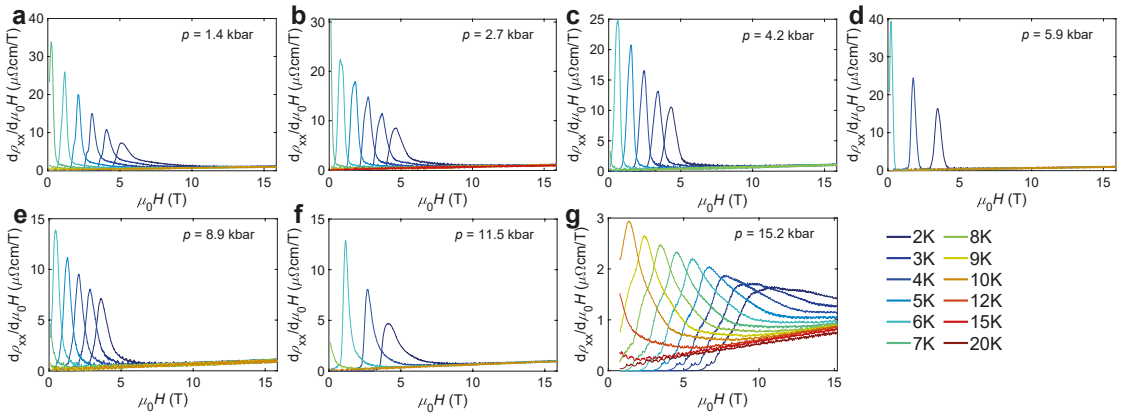

Figure 5.18: Longitudinal resistivity of $FeSe_{0.82}S_{0.18}$ Sample S1. (a)-(g) The derivative in field of the longitudinal resistivity of $FeSe_{0.82}S_{0.18}$ Sample S1 at various pressures, corresponding to (a)-(g) measures in Figure 5.4.

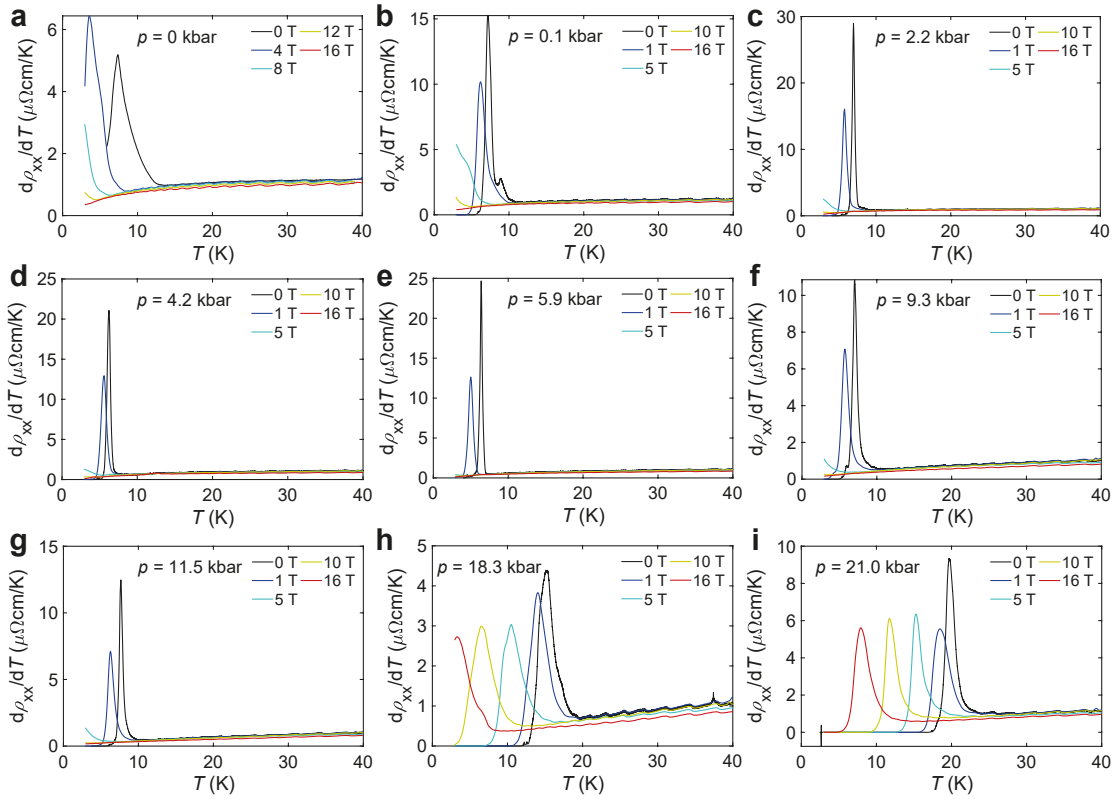

Figure 5.19: Longitudinal resistivity derivative of $FeSe_{0.82}S_{0.18}$ Sample S1. (a)-(i) Longitudinal resistivity derivative in temperature for several fixed fields for different pressures.

6

Interplay between different phases in $FeSe_{0.96}S_{0.04}$ under pressure

This chapter discusses the electronic and superconducting behaviour of $FeSe_{0.96}S_{0.04}$ under pressure, which enables investigations of the interplay of nematicity, magnetism and superconductivity. This work shows how with the modest sulphur substitution out of the Fe-plane in $FeSe_{0.96}Se_{0.04}$ the nematic phase is suppressed, but the superconductivity is slightly enhanced, as opposed to the effect of Cu substitution. Applying hydrostatic pressure suppresses the nematic phase, and enhances superconductivity at low pressures. On the other hand, at intermediate pressures close to the nematic end point, a small dome of magnetic-like order emerges, which coincides with a region where superconductivity is reduced. However, at higher pressures no signatures of this magnetic phase are visible in zero field, similar to Cu substitution, but applying an external magnetic field induces an upturn in resistivity associated to a magnetic-like order. Quantum oscillations in magnetic fields up to 45 T, using both transport and tunnel diode oscillator (TDO) measurements at low pressures, reveal a complex multi-band Fermi surface with a range of high frequency orbits, slightly higher than those at ambient pressure. At higher pressures where signatures of the magnetic phase are found, the oscillations change significantly and only low frequencies are observed, which is consistent with either a Fermi surface

reconstruction due to magnetic order, or increased phase inhomogeneity which only allows small orbits to be detected due to increased scattering. Magnetotransport measurements show that the charge carrier density remains constant with pressure in the tetragonal phase, but is reduced inside the nematic phase, and the magnetic phase. The mobilities of charge carriers show little pressure dependence. The phase diagram of the upper critical field as a function of temperature displays close to linear behaviour, and the behaviour at different pressures can be scaled together in reduced units (of T_c). The gradient of the slope of the critical field near T_c shows a small decrease with pressure, as the superconductivity is enhanced, and suggests the Fermi surface changes at high pressures where magnetic order is found.

6.1 Introduction

The phase diagrams of high-T_c superconductors are often complex with different regions stabilising multiple competing phases. Hydrostatic pressure as a tuning parameter allows precise exploration into these different regions of the phase diagrams. In particular, FeSe at ambient pressure stabilises a nematic phase at 90 K, a superconducting phase below 9 K, and no magnetic order [54]. Applied pressure suppresses the nematic phase, and can stabilise magnetic order above 8 kbar which persists to high pressures [16, 69, 72, 85, 90–92]. Without applied pressure in the absence of long range magnetic order, competition between Néel and stripe spin fluctuations exists in FeSe, and which both couple to the nematic order [83]. Overall, the superconductivity is enhanced by pressure, reaching a maximum T_c of 37 K at high pressures where the magnetic phase is suppressed, suggesting the superconductivity is driven by spin fluctuations [69, 90].

The nematic phase is sensitive to chemical substitution in the FeSe family [56, 67, 165]. The isovalent substitution of sulphur for selenium in $FeSe_{1-x}S_x$ suppresses the nematic phase with $x = 0.18$, and forms a small superconducting dome inside the nematic phase [67]. With increasing sulphur substitution for selenium in $FeSe_{1-x}S_x$, the nematic phase is suppressed with both the chemical and applied pressure [104]. Anomalies in resistivity, associated to a spin density

wave (SDW), occur over a broad region in FeSe (∼8 to 63 kbar) [69], but with increasing x this region narrows, centred around 50 kbar [104]. Focusing on the low pressure region where the nematic phase suppression happens, magnetic order in $FeSe_{1-x}S_x$ is suggested to exist at low pressure for low x inside the nematic phase [107], which may be distinct to that found at higher pressure in the tetragonal phase [104]. In order to best disentangle the different phases in the pressure region below 20 kbar, to allow use of piston cylinder cells, a small sulphur substitution of $FeSe_{0.96}S_{0.04}$ is chosen. The magnetotransport can reveal changes to the electronic structure, and in high magnetic fields reveal quantum oscillations to directly probe the Fermi surface. The pairing mechanism behind the superconductivity has been suggested to most likely be driven by nematic or spin fluctuations, due to the close proximity of nematic and/or magnetic order to superconducting domes [31, 41, 200]. Therefore, $FeSe_{0.96}S_{0.04}$ offers an ideal opportunity to investigate the effect of small isoelectronic substitution on the different phases which can be stabilised with pressure. At 0 kbar, the suppression of the nematic phase due to the S substitution is comparable to that from Cu substitution in Chapter 4, which allows comparisons of the effects of in and out of the conducting Fe-plane.

6.2 Methods

Single crystals of $FeSe_{0.96}S_{0.04}$ were prepared by Shiv Singh using the chemical vapour transport method with $KCl/AlCl_3$ [102, 162], all single crystals in this study originate from this growth. High quality single crystals, as considered by their sharp superconducting transitions and high RRR values, were selected for the pressure measurements, as detailed in Table 6.1.

The author analysed all the data and prepared all the figures presented in this chapter. Two experiments were performed in Oxford using a piston cylinder cell, up to 20 kbar, on samples A and B. These used a commercially available BeCu pressure cell from Quantum Design, inside a Quantum Design 16 T PPMS (Physical property measurement system), measured down to 2 K. A maximum a.c. current of 1 mA (RMS) was applied to the sample. Daphne 7373 was used as the pressurising

medium for hydrostatic conditions, which is hydrostatic up to 2.2 GPa [136]. The pressure was determined in-situ through the reduction in superconducting transition temperature of tin. The tin was measured using a four-probe technique, with contacts made using silver paint. The superconducting transition of tin was measured in cooling and warming at 0.02 K/min. Due to the small critical field on tin, any remanent magnetic field in the superconducting magnet of the PPMS will suppress T_c. Therefore, to determine accurately the T_c of the tin manometer by removing any remanent magnetic field, a high resolution technique alternated the magnetic field by ± 100 Oe at fixed temperatures (every 0.02 K) around the transition.

High magnetic field measurements were performed at the d.c. magnet facility at the NHMFL in Tallahassee, Florida. One experiment used the hybrid magnet up to 45 T on sample C. The pressure cell was prepared by Pascal Reiss and David Graf, the experiments performed by Pascal Reiss, Amalia Coldea, and David Graf. For this experiment, the temperature of the magnetic field sweeps was extrapolated using the magnetoresistance of a cernox and a RuOx thermometer, as detailed in section 2.3.4. A second experiment used the fully resistive magnet up to 41 T in both polarisations on sample D (transport) and sample E (TDO) in a single pressure cell. This experiment used samples prepared by the author in a pressure cell prepared by David Graf, who also performed the experiment locally whilst the author remotely monitored the experiment[1]. For both experiments, a piston cylinder cell, made from a nickel-cobalt base alloy (MP35N), was measured up to 22 kbar, with a pressurising medium of Daphne Oil 7575. The pressure was determined at low temperatures through the ruby fluorescence technique. Sample C used a maximum a.c. current of 2 mA (RMS), whilst sample D used a maximum a.c. current of 1 mA (RMS). For both experiments, the magnetic field sweep rate was 2 T/min when increasing the magnetic field strength at low temperatures, and 4 T/min for decreasing the field strength at low temperatures, and always at higher temperatures (over 5 K). No difference was found between field sweeps taken in up sweeps ($\mathrm{d}|\mu_0 H|/\mathrm{d}T >$

[1]Due to the Covid-19 pandemic, the original magnet time was delayed from April 2020. Whilst travel from the UK was not possible in November 2020, this author sent the prepared samples to David Graf to measure locally.

Table 6.1: Properties of the $FeSe_{0.96}S_{0.04}$ single crystals measured under pressure. Samples A-D were measured using transport, whilst sample E was measured using XRD (X-ray diffraction) and TDO.

Sample	Method	Measured	T_s (K)	T_{on} (K)	T_c (K)	T_m (K)	*RRR*
A (MB1)	ρ_{xx}	16 T, 2 K	80(2)	10.4	10.0	9.5	17.5
B (TZ1)	ρ_{xx}, ρ_{xy}	16 T, 2 K	80(1)	10.3	10.0	9.5	20.9
C (P1)	ρ	45 T, 0.38 K	82(2)	10.4	10.0	9.6	20.6
D (TZ2)	ρ_{xx}, ρ_{xy}	41 T, 0.38 K	80(1)	10.2	10.0	9.4	21.1
E (XZ5)	ΔF	41 T, 0.38 K					

0) and those in down sweeps ($\mathrm{d}|\mu_0 H|/\mathrm{d}T < 0$). For sample D, the ρ_{xx} and ρ_{xy} components were isolated by symmetrising and anti-symmetrising field sweeps in positive and negative magnetic fields. For the single crystal measured using the TDO technique, five crystals were screened using x-ray diffraction (XRD). The crystal with the most point like diffraction pattern was chosen as sample E, and the results are shown earlier in Figure 2.7. Sample E was placed inside a coil in the pressure cell at the end of an LC tank circuit driven by a tunnel diode, where the resonant frequency was recorded and analysed here. The measurement frequency was found around 42 MHz. The coil contained 35 turns of 40 μm copper wire with a diameter of 1.2 mm and an approximate length of 1.5 mm.

The upper critical field for transport measurements (in both field sweeps and temperature sweeps) is defined where the resistivity is first found to be finite as the magnetic field or temperature is increased, classified as the offset. Similarly, the superconducting transition temperature in zero field is defined through the highest temperature of zero resistance.

6.3 Transport behaviour

Figure 6.1a shows the evolution of resistivity with applied pressure for $FeSe_{0.96}S_{0.04}$ sample A. At ambient pressure, there is a kink in the resistivity at $T_s = 80(2)$ K as the system undergoes a structural transition upon entering the nematic phase. The resistivity continues to decrease with temperature, displaying metallic like behaviour, until the systems enters the superconducting state at $T_c = 9.3$ K in Figure 6.1a. Applying pressure up to 7.5 kbar, the slope of the resistivity as a function of temperature is significantly reduced just below the structural transition over a broad temperature range of ~ 25 K. For intermediate pressures (7.5 to 12.5 kbar), an anomaly leading to an upturn in resistivity occurs at low temperatures, found below the structural transition at T_s. The nematic phase is fully suppressed for pressures above 12.5 kbar. The resistivity for each pressure decreases smoothly as the temperature decreases before entering a superconducting state at T_c, which increases with pressure up to 23.4 K at 20 kbar. For the resistivity under pressure, the curves can be split into two bunches/regions separated by being in the nematic phase, or being tetragonal, labelled ρ_{nem} and ρ_{tet} respectively in Figure 6.1a.

Next, the behaviour of the upturn in resistivity is discussed, which has been associated to a magnetic phase transition in FeSe for resistivity data [69]. Here, the upturn is found only for pressures between $p_1 = 7.5$ kbar and $p_2 = 12.5$ kbar, defined by a minimum in the derivative in Figure 6.1c. The boundaries of this region split the pressure phase diagram into three regions: the low pressure regime where $p < p_1 = 7.5$ kbar, the intermediate pressure regime $p_1 < p < p_2$ with the upturn in resistivity at low temperatures, and the high pressure regime for $p > p_2$ where the nematic phase has been suppressed. In FeSe, the magnetic phase is detected from above similar pressures ($\sim$8 kbar) [94] and persists to pressures of several GPa [69]. In Cu-FeSe (Chapter 4) and $FeSe_{1-x}S_x$ with $x \geq 0.11$ no upturn is found at any pressures in zero-magnetic field, suggesting this magnetic phase is highly sensitive to impurity and isoelectronic substitutions [105].

Figure 6.1b is the pressure phase diagram of $FeSe_{0.96}S_{0.04}$, for all measured samples. The superconducting transition temperature increases with pressure up to

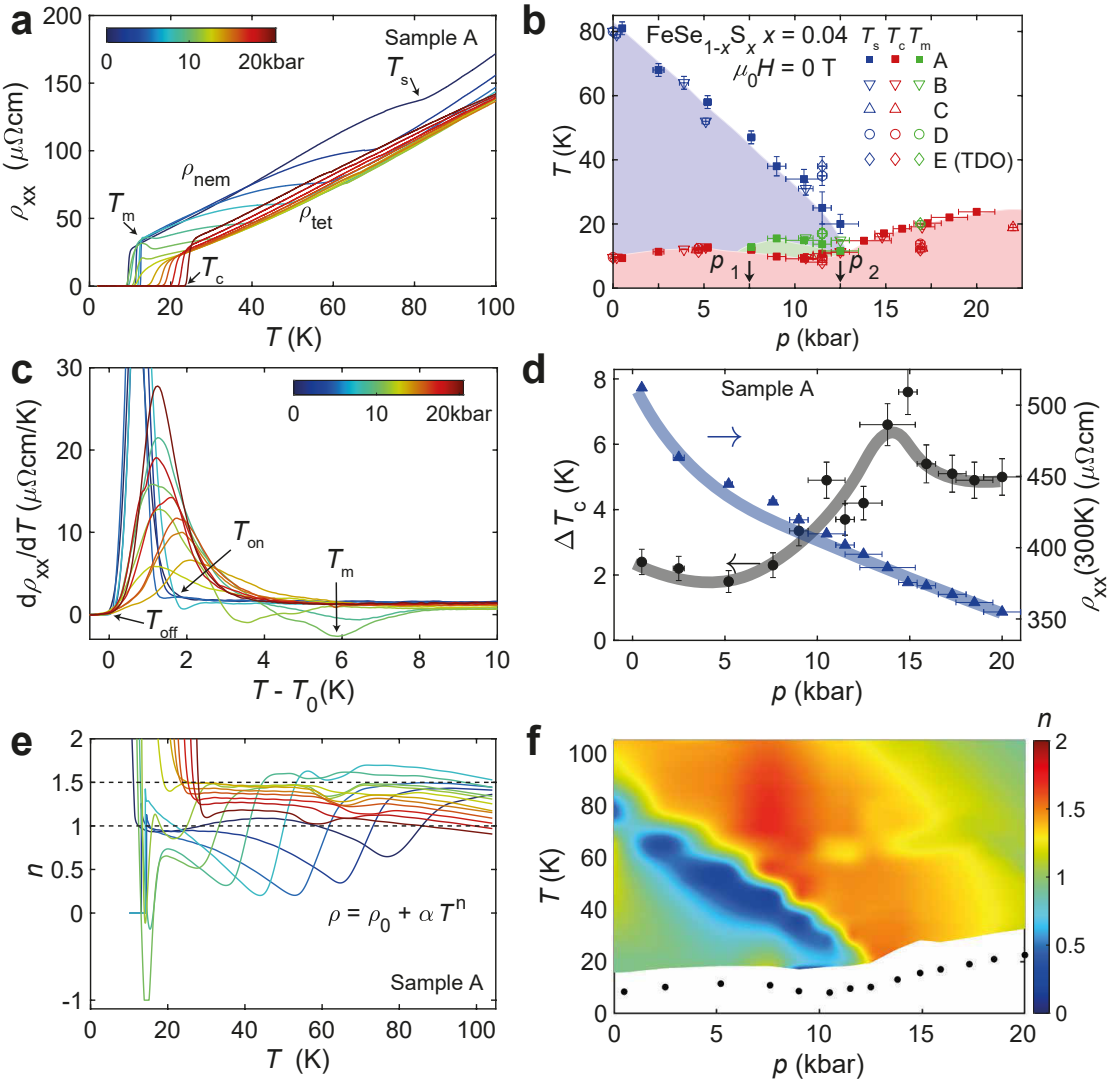

Figure 6.1: Transport under pressure in $FeSe_{0.96}S_{0.04}$. (a) Temperature dependence of resistivity for sample A at different pressures. T_s and T_m are defined as the minimum in the derivative. T_c is defined as the temperature at which the system reaches zero resistivity. (b) Temperature-pressure phase diagram of $FeSe_{0.96}S_{0.04}$ for several samples indicated by different symbols. Background colours indicate phase boundaries between different electronic phases. (c) Differential resistivity with respect to temperature close to the superconducting transition, shifted by T_0 for each pressure. (d) Superconducting transition width, $\Delta T_c = T_{on} - T_{off}$ (black circles), and resistivity at 300 K (blue triangles) as the pressure changes. (e) Local resistivity exponent, n, calculated using the method described in section 2.1.3, and uses the same colour scale for pressure as (c). (f) Colour map of n against pressure and temperature using the results of (d).

p_1, and after p_2. However, in the intermediate pressure region, T_c decreases where T_m increases, suggesting a competition between the two phases. This phase diagram is consistent with a pressure study measuring the inter-plane resistance ρ_c on a

similar composition, $x = 0.043$ [107]. On the other hand, a cubic anvil cell study of $x = 0.04$, up to 80 kbar, found a magnetic phase at high pressures, well above p_2, which stabilises at high temperatures, above T_c [104], similar to FeSe [69, 94]. The anomalies associated to the magnetic phases found from these two studies occur in different regions of the phase diagram, and therefore may be of different origins.

The reduction of the nematic transition temperature with pressure is quite linear (−4.8 K/kbar), and similar to Cu-FeSe with a similar nematic transition T_s (−4 K/kbar) in Chapter 4. However, in FeSe a slower reduction of the nematic transition temperature is found (−2.5-3.5K/kbar) [69, 95, 188], compared to a quicker suppression as seen for $FeSe_{1-x}S_x$ with $x > 0.04$ [105, 107]. Both substitutions, inside (Fe to Cu, $x = 0.0025$) and outside (Se to S, $x = 0.04$) the Fe-plane lead to a similar suppression of T_s at ambient pressure, and a similar suppression rate of T_s with pressure, suggesting the nematic phase is sensitive to changes from both in-plane and out-of-plane impurity scattering potentials.

The width of the superconducting transition changes significantly with pressure, as represented by the derivative in Figure 6.1c where the curves are shifted by T_0. In the low pressure regime, $p < p_1$, the superconducting transitions are sharp at < 2 K. However, in the intermediate pressure regime, where signatures of magnetic order are found, the superconducting transition broadens significantly, see Figure 6.1d. The broader transition persists into the high pressure regime above p_2, despite the absence of signatures of any magnetic order. The broader transitions suggest the presence of strong superconducting fluctuations, or that the superconducting phase becomes inhomogeneous at high pressures, where the transition width reaches $\Delta T_c = T_{on} - T_{off} = 6$ K.

To understand the trends of the electronic structure under pressure, the resistivity at 300 K is shown to decrease with pressure in Figure 6.1d. However, at low temperatures, the resistivity does not continuously decrease with pressure and increases at the higher pressures, see Figure 6.1a. This trend in the resistivity with pressure is similar to FeSe, and S [69, 105, 107] and Cu (Chapter 4) substituted FeSe systems.

Figures 6.1e and f explore the normal state of the system through the local resistivity exponent, n, from $\rho(T) = \rho_0 + AT^n$. At low pressures where the system enters the nematic phase, $p < p_2$, $n = 1.5$ in the tetragonal phase, which drops to $n = 1$ inside the nematic phase. At pressures above p_2, n evolves towards 1 by 20 kbar, which is linear behaviour in temperature, for the whole temperature range (up to 100 K). The pressure and temperature dependence of n is reminiscent of that of $FeSe_{1-x}S_x$ inside and outside the nematic phase [71], and of $FeSe_{0.89}S_{0.11}$ under pressure [105]. For $Fe_{1-x}Cu_xSe$, $x = 0.0025$, under pressure similar behaviour was found, albeit with an enhanced linearity at low temperatures inside the nematic phase, and for all temperatures above p_2 (Chapter 4).

6.4 Magnetotransport and the Magnetic Phase

The anomaly present in the zero magnetic field at T_m for intermediate pressures, associated to magnetic order, can be explored further using an applied magnetic field to suppress the superconductivity and reveal the normal state at lower temperatures. Figure 6.2 describes the evolution of the resistivity temperature dependence in different magnetic fields, at intermediate and high pressures. Interestingly, at high pressure and high magnetic fields an upturn in the resistivity is found, as shown in Figures 6.2c and d. The transitions are extracted from the corresponding derivatives shown in Figures 6.2e-h. From Figure 6.2a the magnetoresistance, the increase in resistivity with magnetic field, increases from the tetragonal to nematic to magnetic phases. For example in Figure 6.2a, the ratio of resistivity in 0 T to 15 T at 20 K (nematic) is only 1.5, but increases to 2.75 at 14 K inside the magnetic phase.

Next, differences between the resistivity upturn in the intermediate and high pressure regimes are considered. For intermediate pressures, Figures 6.2e and f show that the differential resistivity upon cooling has a sharp minimum and then a plateau before the superconducting transition at lower temperatures, such a magnetic phase and magnetic phase transition are pointed out in Figure 6.2s. On the other hand, Figures 6.2g and h at high pressure have no plateau feature in the derivative, even in high magnetic fields. This is likely because in the intermediate

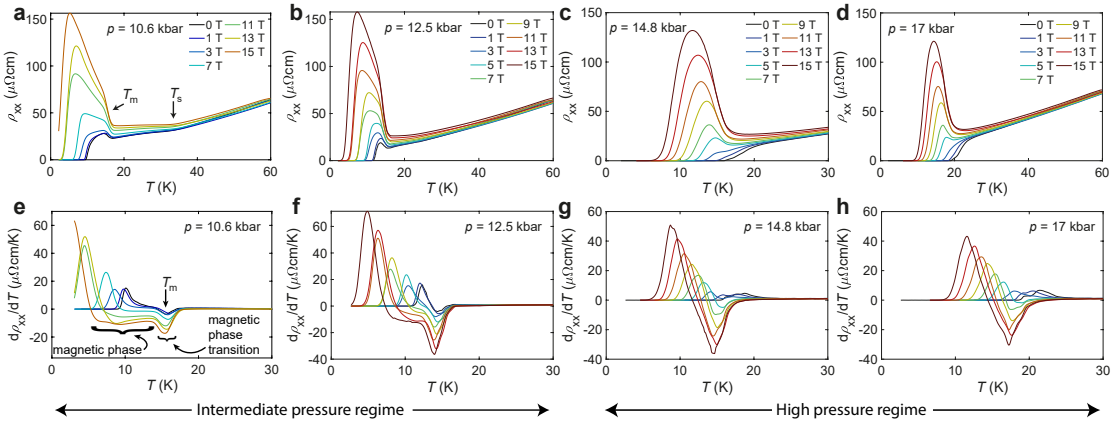

Figure 6.2: High pressure longitudinal resistivity of $FeSe_{0.96}S_{0.04}$ sample B. (a) - (d) Temperature dependence of the longitudinal resistivity under pressure in $FeSe_{0.96}S_{0.04}$ for sample B at pressures 10.6 kbar and above. (e) - (h) The derivative with respect to temperature for ρ_{xx} from the panels above. The magnetic phase transition T_m is defined through the derivative and shown as an example in (e).

pressure regime upon cooling in high magnetic fields the system fully completes the magnetic phase transition before the onset of superconductivity, whereas in the high pressure phase access to high enough magnetic fields to suppress T_c sufficiently below T_m are not available here. Thus, no plateau in the derivative develops as the system is either in the magnetic or superconducting phase transitions throughout. Alternatively, the magnetic order is changing between these two regions, potentially from being in coexistence to being in competition.

The magnetic order is expected to be a first-order phase transition, as seen in x-ray diffraction measurements measuring the crystallographic axis through the transition, and therefore hysteresis effects would be expected [89, 93]. Figure 6.3a finds no significant hysteresis for the superconducting phase transition in zero field, between cooling and warming at the same temperature sweep rate, for sample B, as expected. Notably though, some hysteresis is seen at 12.5 kbar through the upturn. Furthermore, Figure 6.3b shows the resistivity temperature dependence in 15 T displaying modest hysteresis of 0.5(1) K between cooling and warming, which is present from the initial upturn in resistivity down to zero resistance. For FeSe, transport measurements attributed small thermal hysteresis to instrumental effects [89]. Other experimental techniques such as heat capacity (up to 0.2 K when

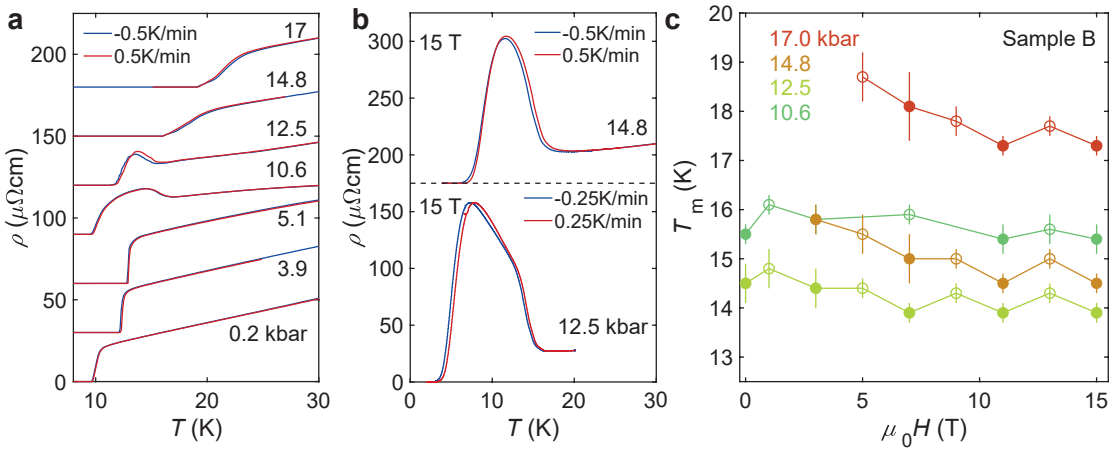

Figure 6.3: Hysteresis checks near the upturn in resistivity. (a) Resistivity temperature dependence in 0 T for cooling and warming at the same temperature sweep rate for each pressure through the superconducting and magnetic transitions for $FeSe_{0.96}S_{0.04}$ Sample B. (b) Cooling and warming in field through the magnetic transition. (c) The position of the minimum in the derivative associated with the magnetic phase, T_m, taken in different fixed applied fields from Figures 6.2e-h. The errorbars are from the width of the minimum in the derivative. Solid points were measured through cooling, and open points from warming.

measured at 0.25 K/min) and NMR (1.5K when measured at 0.1 K/min) did observe small hysteresis, consistent with a first order phase transition and a simultaneous structural transition [94, 99]. A significant hysteresis was found in Cu-FeSe between cooling and warming measurements through the magnetic transition, again in high magnetic fields at high pressures, in Chapter 4.

Figure 6.3c shows T_m to be field invariant for both 10.6 and 12.5 kbar, varying within 1 K as the magnetic field increases. For higher pressures (14.8 and 17.0 kbar) T_m decreases slightly as the field increases, and plateaus above 10 T. I explain this apparent decrease in T_m as the magnetic field increases through the two transitions being near each other in temperature. The upturn in resistivity at T_m appears as a minimum in the derivative, in contrast the superconducting transition increases the value of the derivative (to a maximum). When these two transitions are close by, the superconducting transition onset can begin before the transition at T_m completes, which cuts off the minimum in the derivative at a higher temperature for low magnetic fields. When the magnetic field is large enough to suppress superconductivity sufficiently (>9 T), the value of T_m at all pressures is found

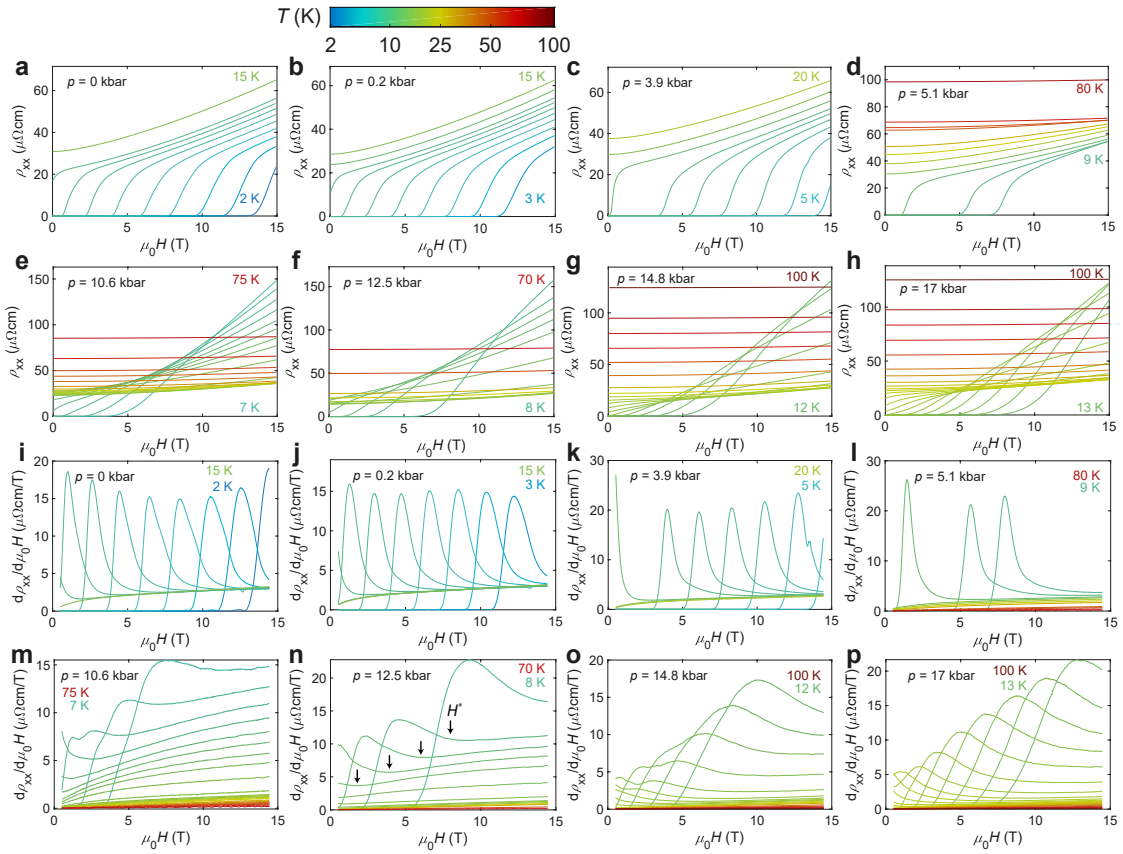

Figure 6.4: Longitudinal resistivity field dependence of $FeSe_{0.96}S_{0.04}$ sample B. (a) - (h) Longitudinal resistivity magnetic field dependence at different fixed temperatures, for pressures up to 17 kbar. (i) - (p) Differential longitudinal resistivity with respect to magnetic field for (a) - (h) respectively. The colour scale applies to all figures for the temperature of each curve.

to be field invariant. The increase in resistivity for temperatures below T_m are consistent between the intermediate and high pressure regions. Therefore, the signatures of magnetic order are found to have been suppressed below the zero-field superconductivity ($T_m < T_c(0\,T)$) for $p > p_2$, compared to the intermediate pressure region where the magnetic phase transition occurs before superconductivity ($T_m > T_c(0\,T)$). The high pressure region is similar to Cu-FeSe in Chapter 4 where the upturn is only revealed in high magnetic fields. A study of FeSe under pressure found that around 8 kbar, at the very edge of the magnetic dome, T_m is just below T_c, such that a magnetic field of 16 T was required to suppress T_c and reveal the signature of an upturn in the resistivity [187].

The increase in the magnetoresistance inside the magnetic phase can also

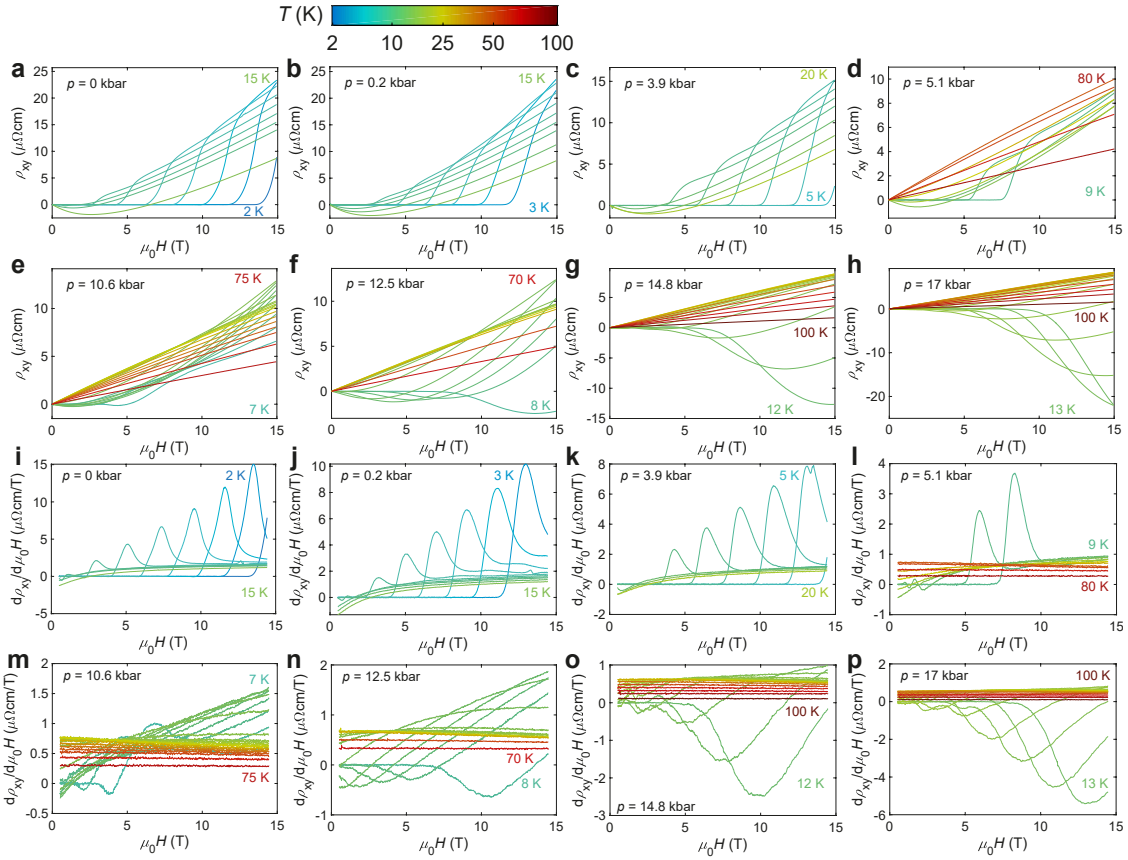

Figure 6.5: Hall resistivity field dependence of $FeSe_{0.96}S_{0.04}$ sample B. (a) - (h) Hall resistivity magnetic field dependence at different fixed temperatures, for pressures up to 17 kbar. (i) - (p) Differential Hall resistivity with respect to magnetic field for (a) - (h) respectively. The colour scale applies to all figures for the temperature of each curve.

be further visualised through the field dependence of the resistivity. Figure 6.4 shows the field dependence of ρ_{xx} at various temperatures for several pressures of $FeSe_{0.96}S_{0.04}$ sample B. For all pressures, the high temperature ($T > 50$ K) field dependence shows little magnetoresistance. Figures 6.4a-d show the low pressure field dependence of ρ_{xx}, with no signatures of magnetic order, where the superconducting transition is well-defined, and the transition width does not change significantly with temperature, as shown by the derivatives in Figures 6.4i-l. Figures 6.4e-h show that for intermediate and high pressures there is a strong increase in the resistivity at low temperatures, inside this low temperature magnetic phase, such that the largest resistivity, strongest scattering, occurs for low temperatures and high magnetic fields (note the change in scale of the vertical axis). At low pressures, the superconducting transition in the derivative is a narrow peak with

a large amplitude above a small background, the normal state of the system (see Figures 6.4i-l). On the other hand, increasing the pressure above p_1 and examining the derivatives (Figures 6.4m-p), the absolute height of the superconducting peak does not change significantly compared to the lower pressures ($\sim$20 $\mu\Omega$cm/T), but the high field normal state background at low temperatures increases significantly when compared to the corresponding derivatives from high temperatures (from $< 5\,\mu\Omega$cm/T to $\sim$15 $\mu\Omega$cm/T). At this point, the well-defined transitions in the resistivity (see Figures 6.4a-d) are smeared out and a superconducting transition onset temperature is hard to define consistently. Figure 6.4n shows the position of $\mu_0 H^*$ which is the onset of the superconducting transition from in high field magnetic phase. Whilst the value of the derivative in the normal state is almost temperature independent at low pressures, the derivative in the magnetic-normal state is highly temperature dependent.

Figure 6.5 shows the field dependence of ρ_{xy} for $FeSe_{0.96}S_{0.04}$ sample B. For the Hall resistivity, a linear field dependence is found consistently at high temperatures for all pressures, whereas a non-linear dependence is found at low temperatures. Figure 6.6a shows the temperature dependence of the Hall coefficient for various pressures, extracted from ρ_{xy} in low magnetic fields ($\mu_0 H < 1$ T). At low temperatures for all pressures, the Hall coefficient is negative, and becomes positive with increasing temperature at T^* (See Figure 6.6b). Increasing the temperature above T^* results in a peak in R_H, with the magnitude of the peak reduced with increasing pressure. At 10.6 kbar, where a structural transition occurs at 31(2) K, there is no change in the behaviour of R_H across the structural transition. The difference between T_c and T^* decreases with increasing pressure, to only 2 K at 17 kbar. In high pressure FeSe, this negative region was found to have been fully suppressed at 38 kbar and above [189]. For $FeSe_{1-x}S_x$, with sulphur substitution the absolute value of R_H at low temperatures decreases but remains negative until $x \sim 0.16$, alluding to a change in the scattering favouring hole-like carriers for higher x [171]. FeSe under pressure sees the low temperature negative R_H region suppressed with

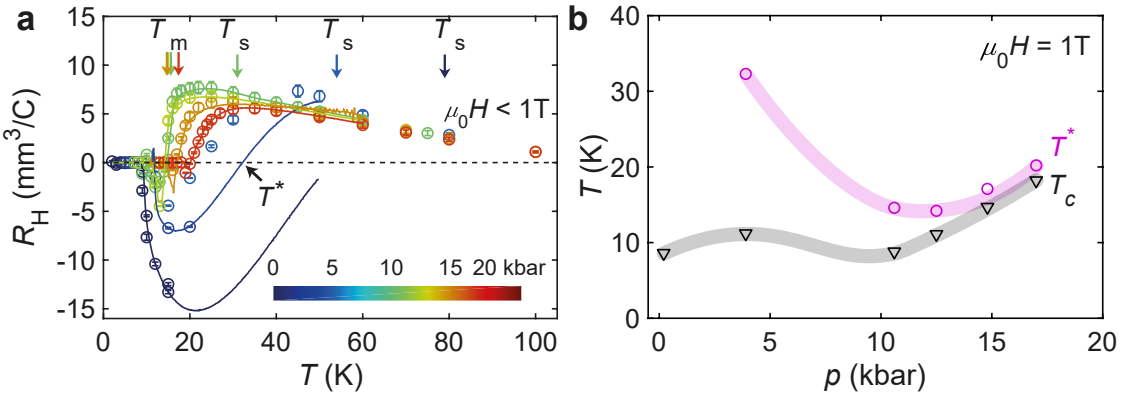

Figure 6.6: Hall coefficient of $FeSe_{0.96}S_{0.04}$ sample B. (a) The Hall coefficient, R_H, as a function of temperature and pressure. Each point is extracted from the slope of ρ_{xy} below 1 T, shown in Figure 6.5. Solid lines are from the Hall resistivity measured in 1 T. (b) Pressure dependence of the offset superconductivity in 1 T (T_c) and the temperature at which R_H is negative below (T^*). Solid lines are guides to the eye.

pressure, and transitions to a strongly positive R_H at high pressures (4 to 8 GPa) indicating the dominance of hole carriers on transport properties [189].

Concerning the presence of additional anomalies and features in the resisitivity, around T_m, this work is compared to a pressure experiment on $FeSe_{0.96}S_{0.04}$ using an inter-planar current (ρ_c), which found similar magnetic transitions in anomaly appearance and T_m [107]. However, they identified a second anomaly at T_m^* just above T_m, which appears as a small kink and increase in the resistivity which is weaker than found at T_m in their work or this work. No signatures of a second anomaly are found here in any sample. It may be that their second anomaly is a feature of the inter-planar resistivity.

6.5 Charge Carrier Mobilities

The resistivity is a measure of the scattering in a system, and from the temperature and field dependencies of the Hall and longitudinal resistivities, one can reveal changes in the electronic structure. A mobility spectrum can be extracted at a particular temperature using the technique described in section 1.4.3. Subsequently, by simultaneously fitting ρ_{xx} and ρ_{xy} to an n-carrier model, the quasi-particle carrier density and mobilities are found as a function of temperature and pressure.

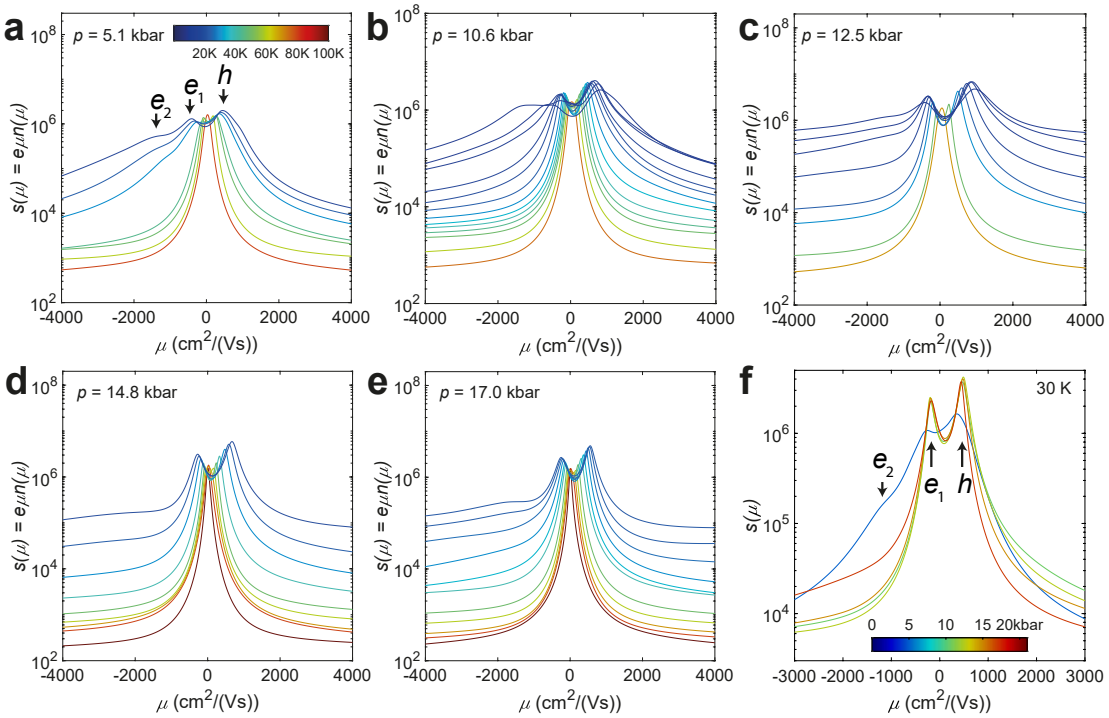

Figure 6.7: Mobility spectrum for $FeSe_{0.96}S_{0.04}$ sample B at various pressures. Temperature dependence of the mobility spectrum for (a) 5.1 kbar (b) 10.6 kbar (c) 12.5 kbar (d) 14.8 kbar and (e) 17 kbar. The colour scale in (a) applies to all of (a) - (e). (f) The mobility spectrum at 30 K for each pressure in (a) - (e).

Figure 6.7 shows the temperature dependence of the mobility spectrum for each pressure, where $s = en\mu$, with n and μ the charge carrier density and mobility respectively. For all pressures at high temperatures there is only a single peak centred close to $\mu = 0$, which indicates the mobilities of the holes and electrons are relatively small. By decreasing the temperature, this peak splits into one of positive mobility for the hole, h, and one of negative mobility for the electron, e_1. In Figure 6.7a, as the temperature is decreased significantly below $T_s = 54$ K, a second electron peak of high mobility appears, labelled e_2. Small signatures which could be e_2 appear at lowest temperatures in each spectrum, but are of too small amplitude to be confirmed. The shape of the mobility spectrum does not change drastically as the pressure is increased from Figure 6.7a to e. To compare these, the mobility spectrums at 30 K are shown together for each pressure in Figure 6.7f. The peak of the second electron is only found at 5.1 kbar for this temperature, which is the only pressure where the system is nematic at 30 K. The mobility

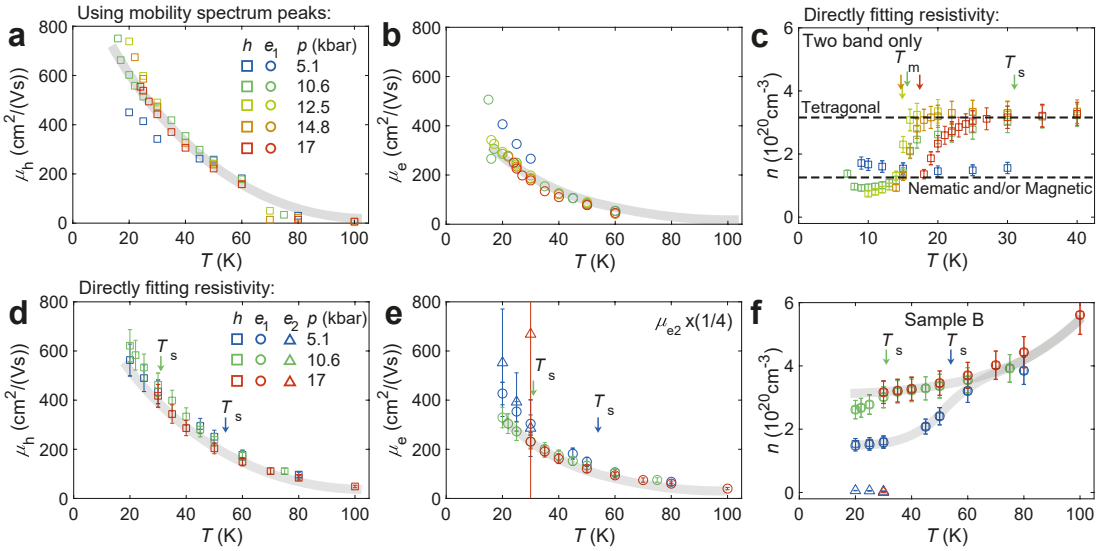

Figure 6.8: Quasiparticle properties for $FeSe_{0.96}S_{0.04}$ sample B. (a) Hole mobility, and (b) electron mobility temperature dependence at different pressures extracted from the mobility spectrum peaks in Figure 6.7. (c) Charge carrier density of a 2 band compensated system (per carrier), extracted from fits to temperatures below the superconducting transition and using the high field resistivity measurements only. (d) Hole mobility, (e) electron mobilities (note: μ_{e2} is scaled down by a factor 4), and (f) charge carrier density temperature dependence at different pressures extracted from simultaneously fitting ρ_{xx} and ρ_{xy}. A two band model is used at high temperatures, and a three band model at low temperatures as necessary. All grey lines and dashed lines are guides to the eye.

spectrum peaks show only modest pressure changes in the two well defined peaks. Figures 6.8a and b show the extracted hole and electron mobilities respectively from the peaks in the mobility spectrums. There are small but consistent changes to the mobilities under pressure, where the hole mobilities increase and the electron mobilities decrease with increasing pressure.

Next, simultaneous fits to the field dependence of ρ_{xx} and ρ_{xy} are performed to reveal the charge carrier properties further. The starting point for the fits use the values of the mobilities given by the mobility spectrums (Figures 6.8a and b), and ensure charge compensation. In the tetragonal phase, at temperatures above T_s, a compensated two band model successfully captures the field dependence of both ρ_{xx} and ρ_{xy}, meanwhile inside the nematic phase a three band model is required. The non-linearity of ρ_{xy} (Figure 6.5) at low temperatures would require either a non-compensated model, or at least a third charge carrier. In this analysis, all models assume a compensated system, a reasonable assumption because FeSe is a

compensated metal, the sulphur substitution is isovalent, and the pressure tuning parameter should not lead to any doping effects, despite the fact that it changes the volume of the unit cell. Figure 6.8f shows the pressure dependence of the charge carrier densities for a representative pressure in the low (5.1 kbar), intermediate (10.6 kbar), and high (17 kbar) pressure regimes. The charge carrier densities at high temperatures are similar for each pressure region, which are all tetragonal. On cooling through T_s for the lower and intermediate pressures a clear reduction in n occurs. A similar factor of ∼3 decrease in the carrier density through T_s was also found in thin flakes of FeSe [130], and under applied pressure in FeSe [96], and Cu-FeSe in Chapter 4. In FeSe, this reduction has been attributed to anisotropic scattering [170], because even though the nematic transition distorts the Fermi surface it should not alter the volume. The high mobility electron, e_2, appears at 30 K for 5.1 kbar, with an increase in carrier density at lower temperatures. It is likely that e_2 is found at low temperatures for each of these pressures, but the carrier densities are too small to be noticeable.

To investigate the charge carrier density at lower temperatures, below T_c, fits are made using a compensated two band model for all temperatures in the high field regime, and presented in Figure 6.8c. For temperatures close to and below T_c, only the high field resistivities are used in the model that are clearly in the normal state, far away from any superconducting fluctuations. A clear decrease of factor 3 in the carrier density from 3.2(0.3) to $1.0(0.2)\times10^{20}$ carriers cm^{-3} is observed on cooling through T_m for each pressure, similar to the decrease seen upon entering the nematic phase (Figure 6.8f). The decrease would be expected with a Fermi surface reconstruction in the magnetic phase.

Figures 6.8d and e show the temperature dependence of the mobilities below 100 K for hole-like and electron-like carriers respectively from fits to the magneto-transport. Reducing the temperature increases the mobility for all three carriers, however, the holes become much more mobile at low temperatures than the main electron-like carrier. Where present, the second electron-like carrier mobility is roughly 4 times larger than that of the main electron, μ_{e1}. The hole mobilities show

a weak increase with pressure, whereas the electrons become slightly less mobile with pressure. Thus the enhanced superconductivity region is dominated by the more mobile hole-like carriers, and this change leads to the positive R_{H} from earlier. For FeSe under pressure up to 20 kbar, the mobilities of all carriers decrease with pressure for temperatures above the magnetic phase [96]. However, the charge carrier mobilities increase as the temperature decreases for the tetragonal, nematic and magnetic phases, but the rate of increase is fastest inside the magnetic phase [96]. Interestingly, for Cu-FeSe under pressure, the mobilities of both electrons and holes were reduced at high pressure, from Chapter 4. In thin flakes of FeSe, the hole mobilities remained relatively unchanged with decreasing thickness, whereas the electron mobilities became temperature independent at low temperatures [130].

6.6 Upper Critical Field

This section considers the upper critical field, $\mu_0 H_{c2}$, of the superconducting phase for $FeSe_{0.96}S_{0.04}$ under pressure. The upper critical field is defined in the methods section earlier (Section 6.2) as the offset value. Figures 6.9a and c show the field-temperature phase diagram for samples B and A of $FeSe_{0.96}S_{0.04}$ respectively. Generally, as the superconductivity is enhanced, so is $\mu_0 H_{c2}$. Figures 6.9b and d highlight an unusual temperature scaling for different pressures using reduced units, $\mu_0 H_{c2}/T_{\mathrm{c}}$ v. T/T_{c}, with T_{c} being the critial temperature in 0 T. At low pressures, the curves are linear. However, at high pressures the curves develop a non-linear temperature dependence, particularly in low fields close to T_{c}. For a single-band superconductor, the upper critical field behaviour is expected to be linear close to T_{c}, and saturate at low temperatures, from the WHH model [25]. Here, the linear behaviour extending to lowest measured temperatures suggests multiband effects are important [218], as found for FeSe with $H||c$ at ambient pressure [79, 180], and under applied pressure [192].

In order to understand the effect of pressure, the slope of the upper critical field near T_{c}, $|\mathrm{d}\mu_0 H_{c2}/\mathrm{d}T|_{T=T_{\mathrm{c}}}$, is shown in Figure 6.9e. There is a small decrease in the slope only at the highest pressures, above roughly 10-15 kbar. As discussed in

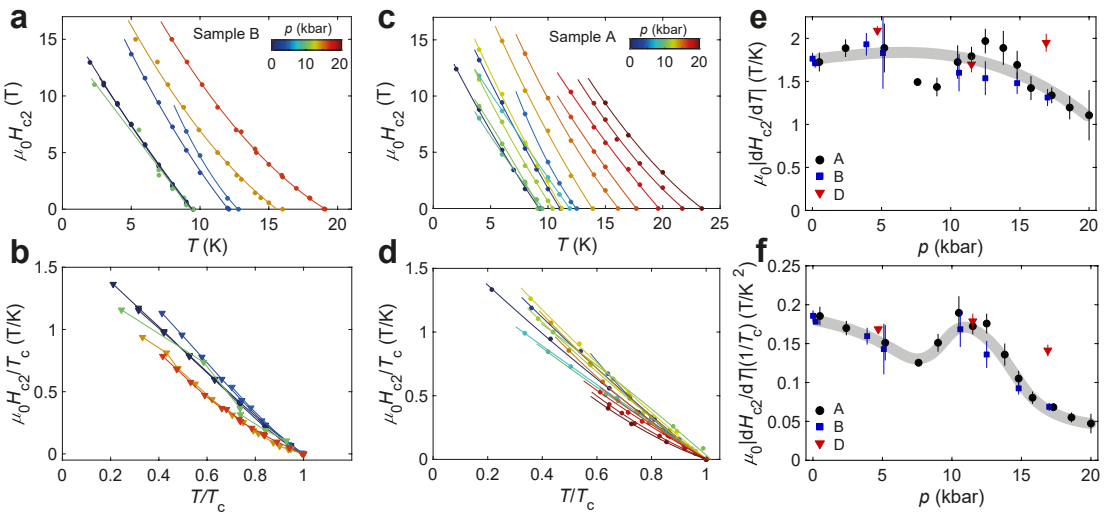

Figure 6.9: Upper Critical field, $\mu_0 H_{c2}$, of $FeSe_{0.96}S_{0.04}$ under pressure. Temperature and pressure dependence for $\mu_0 H_{c2}$ as determined from the offset value for (a) sample B and (c) sample A. Solid lines are fits to a second order polynomial as guides to the eye. (b) and (d) are the same as (a) and (c), but in reduced units using T_c. Due to the hysteretic nature of the resistivity curves at 12.5 kbar for sample B these are not included in (a). (e) The slope of the gradient of $\mu_0 H_{c2}$ pressure dependence for several samples. (f) The slope of the gradient divided by T_c. Solid grey curves are guides to the eye.

Section 1.2.2, the upper critical field close to T_c is, in general, determined by orbital pair breaking effects. For a clean limit multiband system, the normalised upper critical field close to T_c is a useful metric to consider: $R_{Hc2} = 1/T_c|d\mu_0 H_{c2}/dT|_{T=T_c}$, and changes can be related to changes in the Fermi surface [28]. Figure 6.9f shows the pressure dependence of R_{Hc2} being quite constant in the low and intermediate pressure regions, up to 12.5 kbar, but decreasing sharply with pressure in the high pressure regime up to 20 kbar. As the slope itself does not change significantly, the decrease in R_{Hc2} is related to the enhancement of T_c. This pressure behaviour is similar to FeSe, where the slope remains relatively constant but the ratio decreases at higher pressures, highlighting the potential decrease in the dominant effective mass for $FeSe_{1-x}S_x$ [87, 88, 95].

Next, I compare the behaviour of the upper critical field for different samples investigated using different techniques, all the samples are from the same batch and have similar transition temperatures and superconducting properties at ambient pressure (see Table 6.1). Figures 6.10a-c examine the critical field in

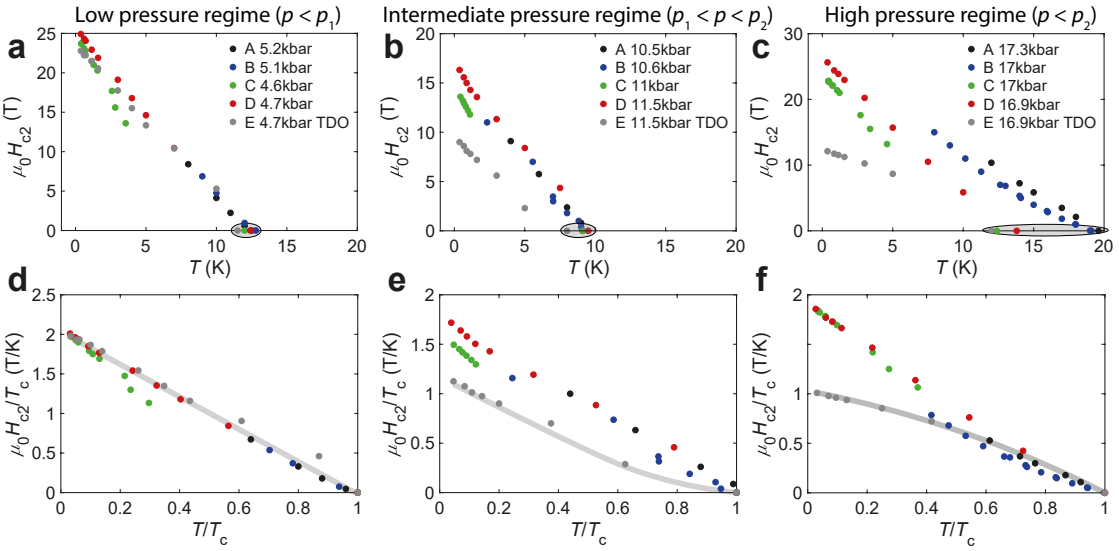

Figure 6.10: Upper Critical field, $\mu_0 H_{c2}$, of $FeSe_{0.96}S_{0.04}$ under pressure. (a), (b), and (c) are field-temperature phase diagrams for each sample at nearest measured pressures to 5 kbar, 11 kbar and 17 kbar respectively. (d), (e), and (f) are the reduced units of the panels above them, scaled by T_c of each sample respectively. Solid lines are guides to the eye for Sample E. Large grey circles in (a), (b), and (c) represent the spread of T_c in each pressure region.

the three different pressure regimes. Figure 6.10a shows the low pressure regime, displaying a good agreement between all samples and measurement techniques. However, at higher pressures in Figures 6.10b and c the spread in values of $T_c(0\,\mathrm{T})$ increases, particularly around 17 kbar in the high pressure regime, indicating the superconducting phase in the high pressure regime is more inhomogeneous. To account for the variance of T_c in 0 T, the upper critical field curves are scaled by T_c, and shown for each pressure regime in Figure 6.10d-f. Here, in the low pressure regime, the different samples and measurement techniques continue to scale together. Notably, differences are found in the scaled curves in both the intermediate and high pressure regimes when comparing sample E (TDO) to the transport measured samples. For sample E, $\mu_0 H_{c2}$ is extracted as the intercept of linear fits through the superconducting transition, and the low field response, which is similar to the extraction in resistivity, but the transition is more rounded at the onset and offset in the TDO measurements. As the TDO technique measures the penetration depth inside the superconducting state, differences may be expected compared to bulk measurements such as transport. Focusing on the transport measured samples, the

two samples measured in Oxford (A and B) scale well together for all pressures, when accounting for the small differences in T_c from variation in pressure and exact composition. Meanwhile, the two transport samples measured in Tallahassee (C and D) scale together well in Figure 6.10d (low pressure regime, $p < p_1$) and Figure 6.10f (high pressure regime, $p > p_2$). However, differences between these samples in Figure 6.10e could be attributed to the larger pressure difference between samples (0.5 kbar), and the hysteresis effects at intermediate pressures as discussed earlier. The regions where dT_c/dp is largest is where small pressure differences will be most important to be accounted for. The pressure for all measurements were verified at low temperatures using either the superconducting transition of tin (A, B) or the ruby fluorescence pressure method (C, D, E).

To explain differences in temperatures between samples, such as T_c at high pressures, it is crucial to first consider instrument effects. One check for consistency is to compare the $\mu_0 H_{c2}$ and T_c values from field sweeps and temperature sweeps for agreement. If the temperature sweep rate was too fast, one would expect to see differences between measurements taken in warming to those taken in cooling, and between the field sweeps at a fixed temperature. For Figure 6.9a about Sample B, the transitions are defined from Figures 6.2 and 6.4. Only for pressures in the intermediate pressure regime (10.6 and 12.5 kbar) were significant differences found, and not for higher or lower pressures. This suggests that, for this sample, temperature lags do not affect the extracted parameters. Overall, the differences in T_c occur between two groups, the pressure cells in Oxford and the pressure cells in Tallahassee. The pressurising medium in Oxford was Daphne oil 7373, meanwhile in Tallahassee Daphne oil 7575 was used. Both pressurising mediums should provide hydrostatic conditions to pressures beyond those measured in this study [136, 137]. In iron-based superconductors, strain can substantially alter phase diagrams, affecting superconducting, magnetic and nematic phases [167]. In $BaFe_2As_2$ the pressurising medium has been shown to have profound effects on the temperature-pressure phase diagram, in particular the SDW suppression and enhancement of superconductivity [219]. In high pressure magnetisation measurements of FeSe

significant differences were found above 5-6 GPa in the superconducting transition when using different pressure-transiting mediums of Ar or He (which should ensure hydrostatic conditions for these pressures), suggesting extreme care is required at high pressures to ensure hydrostatic conditions in the high pressure inhomogeneous superconducting phase [220].

6.7 Quantum Oscillations in High Magnetic Fields

In this section, quantum oscillations are used to examine the changes in the Fermi surface under pressure across the different regions of the phase diagram of $FeSe_{0.96}S_{0.04}$. FeSe is a multiband system with a quasi-two-dimensional hole-like pocket at the centre of the Brillouin zone, and two electron-like pockets at the corner of the Brillouin zone [55, 66, 155]. Inside the nematic phase of $FeSe_{1-x}S_x$ the sulphur substitution expands the hole and two electron surfaces, according to ARPES [55, 221] and low temperature quantum oscillations [67]. Substitution also leads to the appearance of a second, three-dimensional, hole pocket crossing the Fermi energy, around $x = 0.11$ [67, 190, 201]. For each Fermi surface, up to two frequencies will be observed depending on the angle and unique frequency values, which can lead to a superposition of many frequencies overall. The frequency is related to the cross-sectional area, A, of quasi-particle orbits on Fermi surfaces by the Onsager relation: $F_{\mathrm{i}} = \frac{\hbar c}{2\pi e} A_{\mathrm{i}}$ [132].

Figures 6.11a-d present quantum oscillations from three samples of $FeSe_{0.96}S_{0.04}$ - C (R), D (ρ_{xx} and ρ_{xy}) and E (F) - in the low pressure regime, $p \sim 5$ kbar $< p_1$, where the systems are nematic. The amplitude of the oscillations at high field increases with magnetic field, and are largest at low temperatures and high magnetic fields, as shown in the derivatives in Figures 6.11e-h. After removing the background with a polynomial of order 3 inside the normal phase, the now isolated oscillatiory signal has a fast Fourier transform (FFT) applied, and the resulting frequency spectrums are shown in Figures 6.11i-l. Two frequencies with large amplitudes appear in each signal, around 250 and 850 T, for the β and δ orbits, corresponding to the hole surface minimum (around the Γ point) and maximum (around the Z

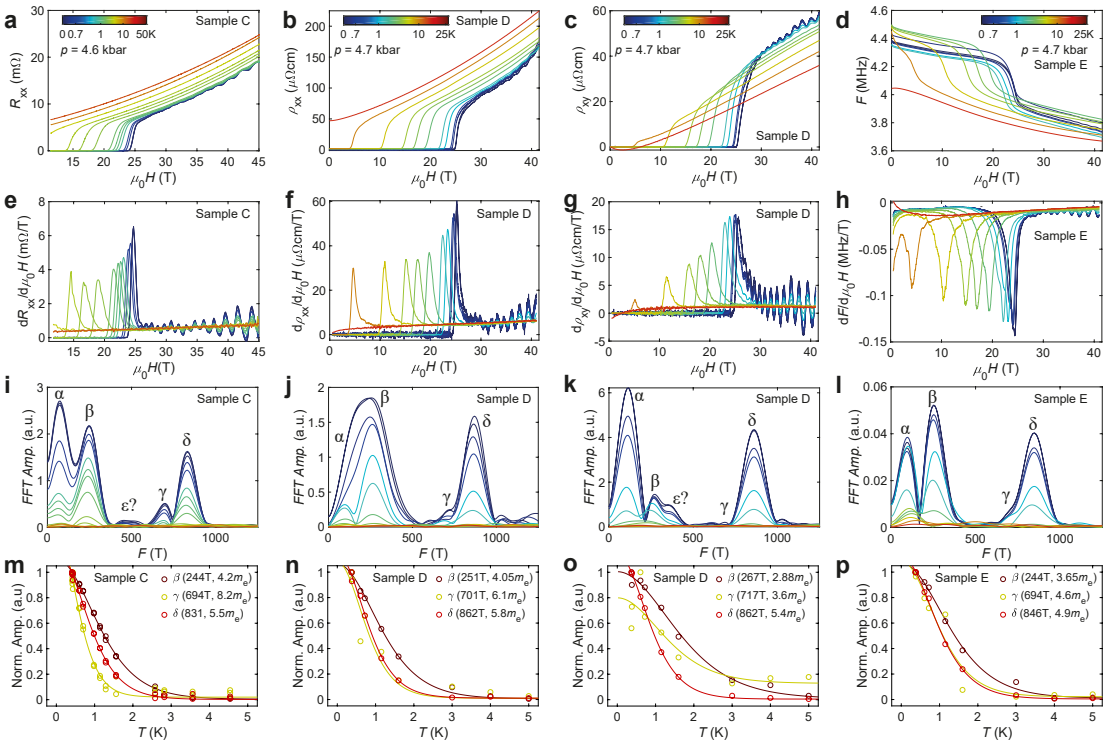

Figure 6.11: Quantum oscillations at $p \sim 4.6$ kbar for $FeSe_{0.96}S_{0.04}$ (a) - (d) Raw data for samples C, D, D and E respectively. (e) - (h) Derivative with respect to field for the above panels. (i) - (l) FFT of the quantum oscillations using a third order polynomial to remove the background. For sample C a field window of $\Delta\mu_0 H = 26 - 44.5$ T is used for the FFT, and for samples D and E a window of $\Delta\mu_0 H = 26.5 - 41.4$ T. (m) - (p) Fits of the normalised amplitudes temperature dependence to the Lifshitz-Kosevich formula [133].

point). Smaller amplitude frequencies are assigned to the electron surfaces, notably the γ orbit as the outer electron maximum orbit, which is of a slightly smaller frequency than the δ. The small amplitude of these oscillations leads to higher variance in their appearance in the frequency spectrum of each sample. At around the 300-500 T region in each frequency spectrum, at least one peak is observed. From Coldea et al. [67], the ϵ orbit is expected to have an area corresponding to a frequency of 417 T at 0 kbar. If a similar increase in this frequency is found as is found for the frequency change in the other orbits from 0 kbar to here, around 14-20%, then a peak for ϵ is expected around 485(25) T. In this region, there are possible small peaks in two of the signals (Figures 6.11i and k), but not for the other signals (Figures 6.11j and l). Additional consideration is the possibility of a second harmonic of the β orbit ($F_\beta = 244 - 267$ T). The lowest frequency peak is tentatively

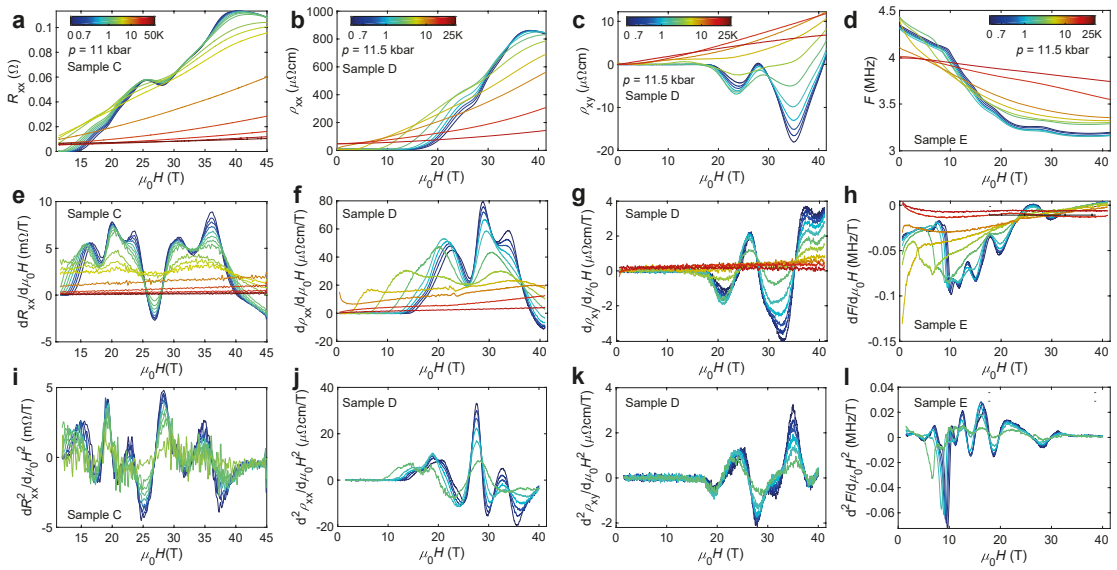

Figure 6.12: Quantum oscillations at $p \sim 11$ kbar for $FeSe_{0.96}S_{0.04}$ (a) - (d) Resistivity data for samples C, D (ρ_{xx}), and D (ρ_{xy}), and frequency change for sample E in high magnetic fields at fixed temperatures. (e) - (h) The derivative and (i) - (l) second derivative of resistivity or frequency with respect to magnetic field, where minimums and maximums in the oscillations in the signal are enhanced relative to the background.

labelled as the α orbit, as they are consistent across the four measurements and literature [67, 87]. However, at such low frequencies the effects from removing the background with a polynomial can be significant.

In the intermediate pressure regime ($p_1 < p \sim 11\text{kbar} < p_2$), where both nematic and magnetic phase transitions occur, the high frequency oscillations are no longer found. Instead, only low frequency oscillations ($F < 200$ T) are observed, where only a few complete oscillations are observed in the magnetic field range available. Figures 6.12a-c for the two transport samples, C and D, present very similar oscillations in the resistivity which are found above 17 T, with the derivative in Figures 6.12e-g. However, for the TDO sample (E) the oscillations are detected in lower magnetic fields, from 10 T. Due to the low frequency and amplitude, it is hard to remove the background without heavily influencing the oscillatory signal through fitting an n^{th} order polynomial. Therefore, the second derivative is used to locate the minimum and maximums of the oscillations, from Figures 6.12i-l. At lowest temperatures, a frequency around 150(30) T is found for samples C and D (both ρ_{xx} and ρ_{xy}), whereas a lower frequency around 60 T is found for sample E. However,

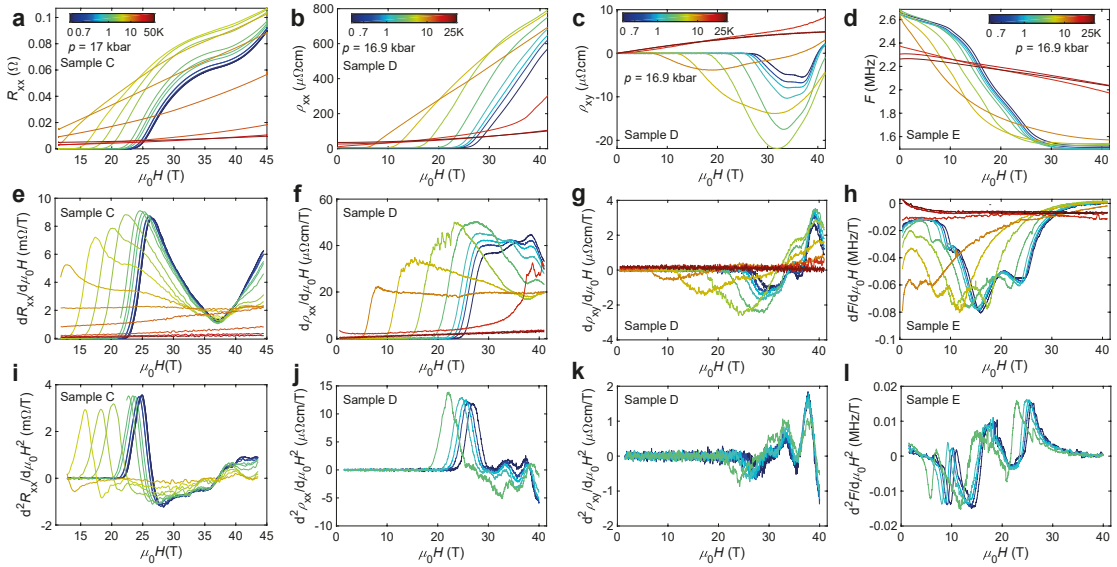

Figure 6.13: Quantum oscillations at $p \sim 17$ kbar for $FeSe_{0.96}S_{0.04}$ (a) - (d) Resistivity data for samples C, D (ρ_{xx}), and D (ρ_{xy}), and frequency change for sample E in high magnetic fields at fixed temperatures. (e) - (h) The derivative and (i) - (l) second derivative of resistivity or frequency with respect to magnetic field, where minimums and maximums in the oscillations in the signal are enhanced relative to the background.

looking at temperatures around 3 to 5 K, the position of minimum and maximums is different to that at lowest temperatures, suggesting there are two frequencies in the signal. Such a scenario can be explained by the thermal damping of the LK formula (see equations 1.62 and 1.64) by a higher frequency with a heavier effective mass that is only found at lowest temperatures, and a lower frequency with a lighter effective mass that can be observed up to ∼5 K, and will be discussed shortly.

The quantum oscillations in the high pressure regime ($p \sim 17$ kbar), where superconductivity is enhanced, only contain low frequency oscillations. Figure 6.13a-c show the small amplitude, low frequency oscillations in resistivity. Figure 6.13c shows the peculiar form of the Hall resistivity, making reliably separating the background and oscillatory signal almost impossible. Again, the second derivative is used to determine the frequency of oscillations, see Figures 6.13i-k. Meanwhile, Figures 6.13d, h and l, show the TDO measurement oscillatory signal. The second derivative of the frequency signal (Figure 6.13l) shows that the oscillations primarily occur in the mixed state (10 to 30 T), based on $\mu_0 H_{c2}$ of sample D from resistivity in the same experiment (see Figure 6.13b around 25 T at 0.4 K). Additionally, the

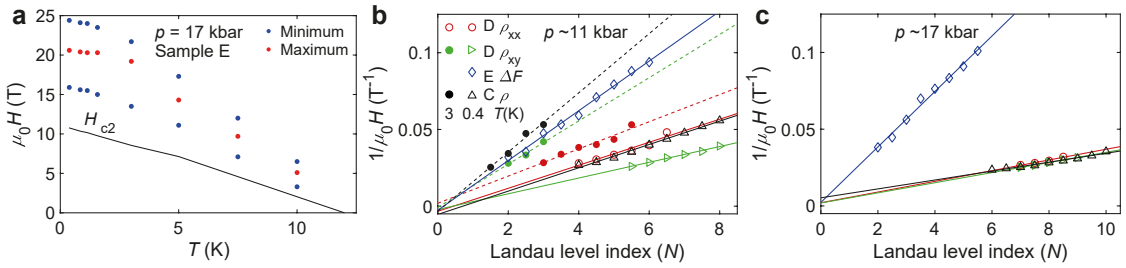

Figure 6.14: Frequency of high pressure oscillations. (a) Position of minimum and maximum in the second derivative of the signal from Figure 6.13 for sample E of $FeSe_{0.96}S_{0.04}$ at 17 kbar. Solid line is $\mu_0 H_{c2}$ from field sweeps (Figure 6.10c). Landau level index plots at (b) ∼11 kbar and (c) ∼17 kbar for samples C, D ρ_{xx}, D ρ_{xy}, and E from field sweeps at lowest measured temperatures. Linear fits are made to the minimum and maximums together. For (b) the dashed lines and solid points are minimum and maximums in the second derivative from field sweeps at higher temperatures (∼ 3 K).

positions of the minimum and maximums shift in field as the temperature increases. Figure 6.14a shows the changing position of the minimums and maximum in the second derivative with temperature, which is not typically expected for quantum oscillations. Above 30 T, in the normal state, no oscillations exist (see high field of Figure 6.13l), even at the lowest temperature where amplitudes would be largest [133]. The Fermi surface may become strongly polarised in high magnetic fields in this high pressure regime, which would lead to a strong temperature dependence of the oscillations. This would explain the TDO signal where the oscillation peaks shift to lower fields at higher temperatures but the oscillatory signal retains the same general shape. However, the transport signals do not show such shifts in where the minimums and maximums occur in field as the temperature increases in high magnetic fields (Figures 6.13i-k).

Figures 6.14b and c extract the oscillation frequency in the intermediate and high pressure regimes respectively using the position of the minimums and maximums from the second derivative of the signal. Typically, quantum oscillations are periodic in inverse field. Thus, by assigning (half)integer Landau level index numbers to each (minimum)maximum and plotting the inverse field against index number the frequency of that oscillation can be determined from the slope. A higher(lower) frequency will correspond to a shallower(steeper) slope. Figure 6.14b considers this for the intermediate pressure regime at low temperatures. As discussed earlier, the

transport samples for these pressures show a change in the oscillation pattern from 0.4 to 3 K which may indicate two orbits of different frequency and effective mass, and so both are considered in Figure 6.14b (see in particular the region of 30 to 40 T in Figure 6.12e where the two maximums at low temperatures become one at a different field as the temperature increases). Firstly, for the low temperatures the transport signals all show a similar frequency around 150(30) T, which is now labelled the Ω_2 orbit. At higher temperatures, 3 K, a different frequency is found with frequency of 65(15) T, labelled the Ω_1 orbit. In contrast, only a single small frequency is found in the TDO signal at 58 T, now assigned to the low frequency Ω_1 orbit. Figure 6.14c considers the position of peaks in the high pressure regime ($p \sim 17$ kbar) to determine the value of the frequencies. The transport samples all show a decreased slope compared to at ∼11 kbar, indicating the frequency has increased, and all are in good agreement with a value around 330(30) T, indicating the Fermi surface is expanding with pressure. Similarly to before, the oscillations seen in sample E are of a lower frequency of 50 T, which is not a significant change from the 58 T at intermediate pressures. Therefore, the transport signals frequency is assigned to the Ω_2 orbit, whilst the TDO signal is tentatively suggested to be an Ω_1 orbit. It could be that the Ω_2 signal is particularly weak for TDO measurements, and not resolvable in this study.

Figure 6.15a shows the frequencies as a function of pressure, and compares these to FeSe from Terashima et al. [87], and 0 kbar results for $FeSe_{0.96}S_{0.04}$ from Coldea et al. [67]. At low pressures, the frequencies all increase with pressure indicating the cross-sectional areas of the Fermi surfaces are increasing in size. Inside the magnetic phase, only low frequencies are found, indicative of a Fermi surface reconstruction as previously suggested form FeSe quantum oscillation measurements [87]. These frequencies appear to increase with pressure in the magnetic phase; likewise, in the low pressure regime the frequencies increased with pressure. The frequency change from 0 to 4.7 kbar is around 14-21% for the major orbits. This is compared to an increase of roughly 50% from 11 to 17 kbar for the low frequency Ω_2 orbit, suggesting the frequencies increased faster in this regime. In $FeSe_{0.89}S_{0.11}$ the frequencies for

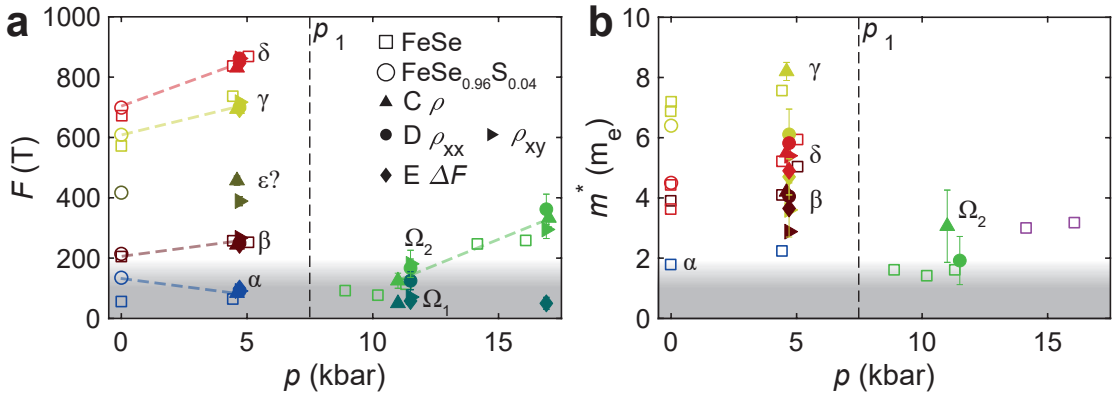

Figure 6.15: Results from quantum oscillations. (a) Frequency and (b) effective mass pressure dependence for $FeSe_{0.96}S_{0.04}$ under pressure (solid circles) and ambient (open circles [67], compared to FeSe (open squares) [87]. The dashed line marks p_1. The shaded area at low frequencies highlights the uncertainty in resolving well defined frequencies below 200 T.

Table 6.2: Quantum oscillations results for $FeSe_{0.96}S_{0.04}$ under pressure. The frequency assigned to each orbit for the four different sets of quantum oscillations. The possible frequencies for the ϵ orbit are all included.

Orbit	F (T)	Low Pressure Regime		
	Sample C (ρ)	D (ρ_{xx})	D (ρ_{xy})	E (ΔF)
α	84(5)	91(5)	91(5)	99(5)
β	244(10)	251(10)	267(10)	244(10)
ϵ?	457(15)		389(15)	
γ	694(10)	701(10)	717(10)	694(10)
δ	831(10)	862(10)	862(10)	846(10)
		Intermediate Pressure Regime		
Ω_1	50(10)	125(30)	71(25)	58(10)
Ω_2	125(25)	167(30)	181(45)	—
		High pressure Regime		
Ω_1	—	—	—	50(20)
Ω_2	333(30)	362(50)	295(30)	—

each orbit increased inside the nematic phase, except for the smallest frequency which decreases with pressure and possibly vanishes at a Lifshitz transition at the nematic end point [105]. Interestingly, in that same work, in the tetragonal phase at high pressures a low frequency was detected in TDO but not transport measurements [105]. This low frequency in the tetragonal phase could be similar to the low frequency found in TDO here inside the magnetic phase.

The amplitude of quantum oscillations will decrease as the temperature increases

and the Landau levels broaden. The temperature dependence of the amplitude of the FFT amplitude can be fitted to the Lifshitz-Kosevich (LK) formula (equation 1.64 in Chapter 1) to determine the effective mass, m^*, of quasiparticles on that orbit [133]. The insets of Figures 6.11i-l show fits to the LK formula for the three main orbits in each sample at low pressures. The background for the fits is estimated from the FFT amplitude at high temperatures ($T > 10\,\mathrm{K}$). The effective mass follows this formula: $m^*/m_\mathrm{b} = (1 + \lambda_{\mathrm{el-el}})(1 + \lambda_{\mathrm{el-ph}})$, where m_b is the band mass, $\lambda_{\mathrm{el-el}}$ and $\lambda_{\mathrm{el-ph}}$ are the electron-electron and electron-phonon coupling constants respectively. If the band mass remains constant, a heavier effective mass indicates stronger correlations, and the amplitude will decrease faster as the temperature increases. The effective masses cannot be estimated for the high pressures due to the inability to remove just the background signal to isolate the oscillatory signal. Figure 6.15b shows the effective masses for the different frequencies, compared to FeSe and $FeSe_{0.96}S_{0.04}$ [67, 87]. Inside the nematic phase, the effective mass for the γ, and δ orbits show increases of approximately 30 and 20% respectively with pressure. There is a spread of masses for each orbit between the different samples, which is an additional proxy of the error on estimating masses using the LK formula [133]. Errors arise from the possibility of multiple orbits having similar frequencies that cannot be distinguished without a very large field window, and from the weak amplitude of the oscillations relative to the background. For $FeSe_{0.89}S_{0.11}$ the effective masses for every orbit showed no significant change, within errors, with pressure inside the nematic phase up to 5 kbar [105]. The effective mass of the Ω_2 orbit is cautiously calculated for the intermediate pressure regime to be around $2\,m_\mathrm{e}$. At high pressures inside the magnetic phase for FeSe the effective mass increased with pressure from around $2\,m_\mathrm{e}$ to around $3\,m_\mathrm{e}$ between the two orbits identified by Terashima et al. [87]. Interestingly, the frequencies and effective masses appear to increase continuously with pressure inside and outside the magnetic phase for FeSe and $FeSe_{0.96}S_{0.04}$ [87]. This is further evidence that in the high pressure phase the low temperature Fermi surface of $FeSe_{0.96}S_{0.04}$ has similar features to FeSe. Hence,

whilst magnetic fields were required to reveal the upturn in resistivity here, but not in FeSe, in both cases the systems enter the same high pressure phase.

I now consider the puzzling disappearance of oscillations in the TDO sample at high pressure and high field, as the oscillations usually have frequencies matching that from transport and are probing the same Fermi surface [105]. In the mixed state of other superconductors, such as 2H-NbSe2 [222] or URu_2Si_2 [223], the oscillation amplitudes are damped within the mixed state. Inside the magnetic phase additional scattering may occur due to the increased resistivity at low temperatures and high magnetic fields. Therefore, the scattering rates increase in the high pressure phase at low temperatures, such that the high frequency quantum oscillations are not observed because the requirement to observe quantum oscillations, $\omega_c\tau > 1$, is not satisfied. From the mobility spectrum analysis in Figure 6.7, the mobilities for temperatures above the magnetic phase show only small changes in pressure, but are not able to probe the low temperature magnetic phase, where the quantum oscillations are observed, to consider this possibility.

6.8 Discussion

Figure 6.16a is the phase diagram of $FeSe_{0.96}S_{0.04}$ under pressure in zero-magnetic field, compared to that of FeSe from Chen et al. [187]. At low pressures, both systems display enhanced superconductivity and suppressed nematicity with pressure. A magnetic phase is found in intermediate pressures for both systems, beginning at a similar pressure p_1, coinciding with a reduced T_c. Above p_2 where the nematic phase has been suppressed in both systems, the magnetic phase is only found in FeSe. Here, the superconducting transition temperature of both systems are of similar value, and small differences may be sample specific rather than system specific.

Figure 6.16b shows the low temperature phase diagram in an applied magnetic field of $\sim$16 T, to suppress the superconductivity and stabilise the magnetic phase at high pressures. Interestingly, the magnetic phase displays two different domes in high magnetic fields which coincide around $p_2 = 12.5$ kbar, with one dome inside the nematic phase, and the other emerging at the nematic phase boundary, p_2. This

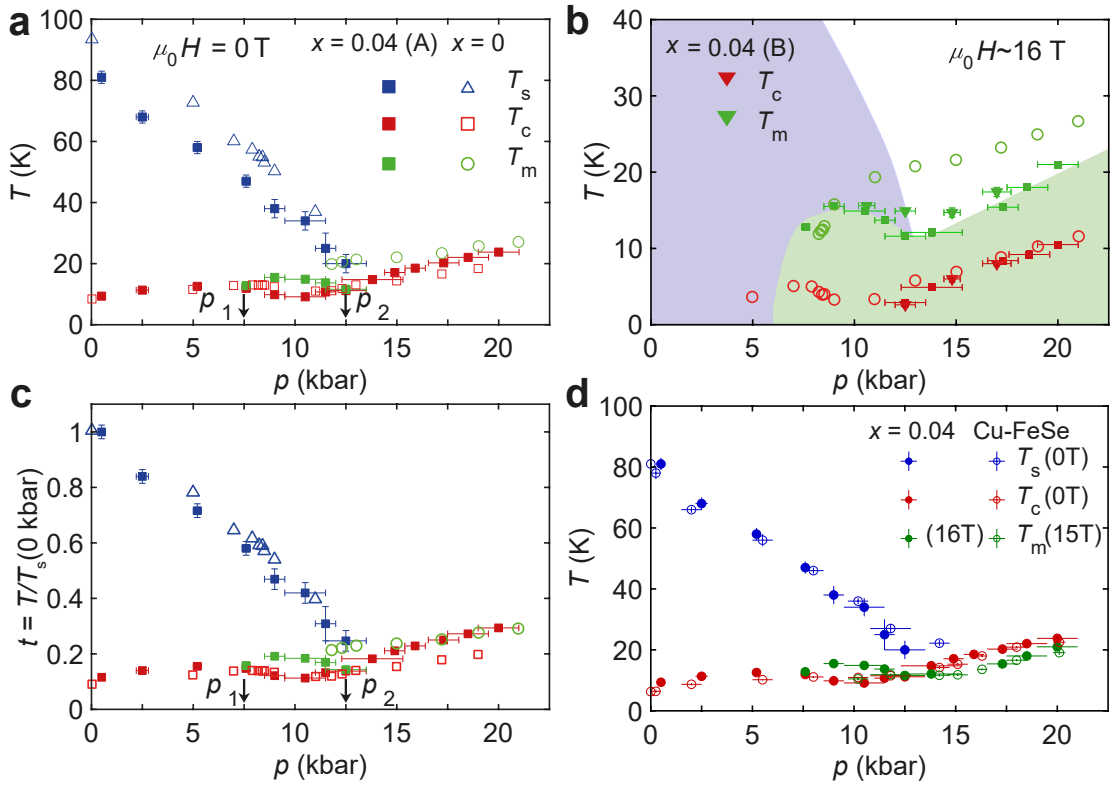

Figure 6.16: Pressure-temperature phase diagrams of $FeSe_{0.96}S_{0.04}$. (a) Pressure-temperature phase diagram in 0 T for $FeSe_{0.96}S_{0.04}$ sample A (solid squares), compared to FeSe under pressure (open symbols) from Reference [187]. (b) Pressure-temperature phase diagram in magnetic field. The blue background is a guide to the eye for the nematic phase. Solid green squares and triangles are $FeSe_{0.96}S_{0.04}$ samples A and B in a 16 T and 15 T magnetic field respectively. The green shaded region represents the magnetic phase in field. Open circles are FeSe data from reference [187] in a 16 T magnetic field. (c) The same as (a) but all temperatures are scaled by the respective T_s(0 kbar) of that system. (d) Pressure-temperature phase diagram from $FeSe_{0.96}S_{0.04}$ sample A (solid symbols) compared to $Fe_{0.9975}Cu_{0.0025}Se$ (open symbols) from Chapter 4.

is different from FeSe where the magnetic phase evolves more smoothly without a clear distinction between two domes seperated by the nematic phase boundary [69, 95, 187]. Notably, in a high magnetic field of $\sim$16 T the superconducting temperature of both FeSe and $FeSe_{0.96}S_{0.04}$ are the same, despite the reduction in T_m of up to 10 K. At low pressures inside the nematic phase, the peak in T_c around 7.5 kbar coincides with the onset of the magnetic phase (see Figure 6.16a). Increasing the pressure above p_2, a second dome of superconductivity emerges and T_c is enhanced, even as T_m increases too. Surprsingly, the superconducting transition temperature does not peak at the nematic end point, as could be expected due to

enhanced critical fluctuations. More generally in iron-based superconductors, domes of superconductivity often emerge around the points of suppression of nematic and magnetic phases [31]. Meanwhile, in $FeSe_{0.89}S_{0.11}$ under pressure a similar two domes of superconductivity emerge, even in the complete absence of a magnetic phase [105].

To further compare the changes induced by the sulphur substitution, the temperatures of the zero field phase diagram are scaled by $T_s(p = 0\,\text{kbar})$ for each composition in Figure 6.16c. For the low and intermediate pressure regimes, up to the nematic phase boundary at p_2, the nematic and superconducting phases scale well between FeSe and $FeSe_{0.96}S_{0.04}$. In the high pressure regime above p_2, the scaled T_c of $FeSe_{0.96}S_{0.04}$ is slightly enhanced relative to FeSe. Next, due to the similarity in the ambient T_s ($\sim$80 K), the phase diagram is compared to that of Cu-FeSe (from Chapter 4) in Figure 6.16d. Recall that at 0 kbar the sulphur substitution in $FeSe_{0.96}S_{0.04}$ slightly enhanced T_c compared to FeSe, whereas the copper substitution in Cu-FeSe suppressed T_c. This difference remains between the two phase diagrams in the low pressure regime. In the intermediate pressure regime, the dome of magnetic order in $FeSe_{0.96}S_{0.04}$ is absent in Cu-FeSe. Remarkably, in the high pressure phase above $p_2 = 12.5$ kbar, the superconducting phase of both systems are completely comparable. Additionally, the magnetic phase transition for both systems in high fields is shown for comparison, and again shows a remarkable similarity. This emphasises the similarity in disrupting the magnetic phase through both sulphur and copper substitution in FeSe. Furthermore, the presence of two separate domes of superconductivity in both systems suggests the mechanism behind the superconductivity changes between the low pressure region, below p_2, and the high pressure region above p_2. As discussed for Cu-FeSe in Chapter 4, the robustness of the high pressure superconducting phase to these different substitutions is suggestive of a sign preserving s_{++} pairing. Interestingly, in FeSe thin flakes under pressure, the superconductivity and magnetism are both suppressed as the thickness decreases and disorder increases [194]. Similarly, in thin films of Fese under pressure no signatures of magnetic order were found in transport, even with applied magnetic fields up to 14 T and 27 kbar [224].

Next, the pressure phase diagram of $FeSe_{0.96}S_{0.04}$ is compared to the substitution phase diagram of $FeSe_{1-x}S_x$ (See Figure 1.4 in Chapter 1). In $FeSe_{1-x}S_x$ inside the nematic phase, there are two regions, separated above and below the peak in T_c, named nematic A ($x \lesssim 0.11$) and nematic B ($0.11 \lesssim x \lesssim 0.175$) [71]. There are many similarities in the transport properties of the nematic B phase of $FeSe_{1-x}S_x$ and the high pressure magnetic phase of $FeSe_{0.96}S_{0.04}$. In the nematic B phase, the magnetotransport shows a large increase at low temperatures and high magnetic fields, similar to the intermediate pressure region of $FeSe_{0.96}S_{0.04}$. Additionally, the quantum oscillations in the nematic B phase are dominated by low frequency oscillations, as is the case for $FeSe_{0.96}S_{0.04}$ in the magnetic phase. However, high frequency oscillations with a small amplitude do exist for $FeSe_{1-x}S_x$ [67, 105] (and the 0 kbar results in Chapter 5), whilst no signature of any high frequency oscillations have been detected in $FeSe_{0.96}S_{0.04}$ under pressure in this study. The question remains if the nematic B phase of $FeSe_{1-x}S_x$ contains magnetic-like order, similar to that in FeSe under pressure, or not, and more direct spectroscopic probes will be required to investigate this.

Overall, the high pressure phase has now been found to exhibit enhanced superconductivity in many different environments. In FeSe the high pressure phase contains the magnetic phase, has small Fermi surfaces, and large resistivity at low temperatures [69, 87]. In Chapter 5, for the tetragonal $FeSe_{0.82}S_{0.18}$ the large Fermi surfaces again supports a similarly enhanced superconducting state, in the absence of any magnetic order. Perhaps most surprisingly, as shown for Cu-FeSe in Chapter 4, when the magnetic phase has been suppressed at high pressures, the same enhanced superconductivity is found, despite the mobilities of charge carriers being significantly reduced.

Furthermore, the high pressure phase of $FeSe_{0.96}S_{0.04}$ has shown possible variation in the phase diagram linked to the pressure medium used. If this high pressure phase is inhomogeneous, as suggested by the broadening of the superconducting transition, it is expected to be more sensitive to any non-hydrostatic conditions. A study on FeSe under pressure found differences in the phase diagram based on

the pressure medium and pressure cell type used [220]. An additional consideration should be possible local strain effects induced by the distribution of Se/S ions across the sample, as discussed for a Griffiths phase in $FeSe_{0.89}S_{0.11}$ [205]. Future studies on similar compositions, where T_m and T_c track each other closely as found here at high pressures, should investigate the role of hydrostaticity on these competing phases and any possible uniaxial contribution.

6.9 Conclusions and Outlook

By carefully examining the transport properties of $FeSe_{0.96}S_{0.04}$ under pressure, I have presented the current state of this highly complex system. The competition between the superconducting and magnetic phases at low temperatures is highlighted by the increase in the superconducting transition width. At low temperatures for a small pressure range (7.5 - 12.5 kbar) an upturn in the resistivity indicates the transition to a magnetic phase, likely a spin-density wave, but at higher pressures ($p > 12.5$ kbar) external magnetic fields are required to stabilise this phase, which shows this phase has been suppressed compared to FeSe. The positive Hall coefficient suggests that the normal state of the system is dominated by more mobile hole-like carriers at higher pressure. Meanwhile, the charge carrier densities were shown to decrease inside the nematic and magnetic phases, but showed little pressure dependence. Similarly the mobility of holes and electrons showed only small changes with pressure.

The phase diagram in high magnetic fields showed the magnetic phase is stabilised in different regimes of the phase diagram and appears to consist of two unique domes of magnetic order, either side of the nematic phase boundary around $p = 12.5$ kbar. The similarity in phase diagram for the zero field superconducting phase, and the high field magnetic phase, of $FeSe_{0.96}S_{0.04}$ and Cu-FeSe under pressure is surprising and shows the magnetic phase is highly sensitive to chemical changes both in and out of the Fe-plane. The similarity furthers suggests the high pressure superconducting phase is rather robust to these changes, and supports the sign preserving s_{++} scenario considered with Cu-FeSe. Further work under pressure using more direct probes of the magnetic phase, such as NMR, are required to categorically compare the high

pressure magnetic phase here with the similar upturn in resistivity behaviour of $FeSe_{1-x}S_x$ at low temperatures close to the nematic end point ($x = 0.18$).

Quantum oscillations showed that the Fermi surfaces increase with pressure, both in the low pressure phase, and at high pressures inside the magnetic phase. The high frequency oscillations in the low pressure phase are replaced by low frequency oscillations for $p = 11$ kbar and above, coinciding with the high pressure magnetic phase. Inside the nematic phase the effective masses of each orbit become heavier as the pressure increases, and the effective mass of the low frequency orbit at high pressures seems to be relatively lighter. The slope of the upper critical field close to T_c has been shown to be relatively constant up to p_2, but decreases linearly as the pressure increases further, suggesting that the electronic correlations decrease in the high pressure phase. The upper critical field also highlighted the possible sensitivity of the high pressure phase to conditions, which may be from small non-hydrostatic contributions of the pressurising medium inducing strain and/or the distribution of Se/S ions.

For future work, an angular dependent quantum oscillation study under pressure with the magnetic field applied along different directions would clarify the dimensionality of the Fermi surface in the high pressure magnetic phase, to explore a possible Fermi surface reconstruction [87]. In addition, transport measurements in magnetic fields at higher pressures using a diamond cell could clarify the properties of the possible high pressure magnetic phase from Matsuura et al. [104]. Furthermore, measurements in higher magnetic fields (>45 T), using pulsed fields, could provide a resolution about if the Fermi surface reconstructs, or if the scattering is changed sufficiently in this high pressure phase to suppress the high frequency orbits, such that $\mu B > 1$ requires strong fields to be satisfied. Besides sulphur substitution, another avenue to be explored is with tellurium, which is also isovalent substitution outside the Fe-plane, but with a bigger atom than selenium. Without pressure, $FeSe_{1-x}Te_x$ suppresses the nematic phase, and the superconductivity has a local minimum within the nematic phase and is enhanced past the nematic phase boundary unlike in $FeSe_{1-x}S_x$ [56]. Whilst pressure phase diagrams in zero field for $FeSe_{1-x}Te_x$

have been investigated in the high pressure regime [56], it would be interesting to investigate the region below 20 kbar carefully to map out the evolution of any nematic and magnetic phases, and compare that to $FeSe_{1-x}S_x$ under pressure.

7
Concluding Remarks

In this thesis I have investigated the electronic changes across the phase diagrams of several different iron-chalcogenide systems under applied hydrostatic pressure. Figure 7.1 shows the pressure-temperature phase diagram of different FeSe-substituted systems, in addition to the phase diagram of FeSe the parent compound. The phase diagram of FeSe shows the nematic electronic phase is suppressed with pressure, whereas the superconductivity has a small done, as shown in Figure 7.1a. Just inside the boundary of the nematic phase superconductivity is suppressed, and a magnetic order phase is stabilised. In the high-pressure phase, the transition temperatures associated with the superconducting phase and magnetic order both increase with applied pressure towards a high-T_c phase.

Firstly, in Chapter 3, I explored the role of the impurity scattering due to Cu substitution in $Fe_{1-x}Cu_xSe$, and how this quickly suppresses the superconductivity and leads to a significant increase in resistivity. Subsequently, in Chapter 4, I focused on the temperature-pressure phase diagram of a low substitution of $Fe_{1-x}Cu_xSe$ with $x = 0.0025$ (Figure 7.1b), where superconductivity under high pressures is enhanced to similar values as found in FeSe around 20 kbar despite the presence of the strong impurity scattering. Most notably, in the same pressure regime the magnetic phase of FeSe is found to be suppressed to temperatures below T_c. Thus, an applied magnetic field is required to reveal the upturn in resistivity signature associated with

the magnetic phase. In Chapter 6, I presented the phase diagram of $FeSe_{0.96}S_{0.04}$ (Figure 7.1c). In this case, the low pressure phase diagram is similar to FeSe except for the appearance of a reduced region of magnetic order coinciding with a dip in T_c. Moreover, the magnetic order outside the magnetic phase is only revealed with an applied magnetic field, similar to $Fe_{1-x}Cu_xSe$ $x = 0.0025$. In $FeSe_{0.96}S_{0.04}$, the quantum oscillations study at low temperatures found changes in the Fermi surface at high-pressure, coinciding with the magnetic phase transition. In contrast, Chapter 5 explored the high-pressure phase of tetragonal $FeSe_{0.82}S_{0.18}$ (Figure 7.1d). This system has no signatures of magnetic order, and quantum oscillations confirm the Fermi surface remains relatively large. Despite the lack of any magnetic order, the superconductivity displays a threefold enhancement at high pressures.

In conclusion, these studies show unexpected enhancements in T_c to around 20 K under a pressure of 20 kbar in all three systems investigated here, as well as for FeSe. The enhanced superconductivity occurs despite the different phase diagrams, size of their Fermi surfaces, and charge carrier mobilities. Overall, this detailed study of transport under applied pressure has shown the sensitivity of the magnetic phases and robustness of the superconducting stabilised by high pressures to the effects of chemical substitution both inside and outside the conducting Fe-plane in FeSe.

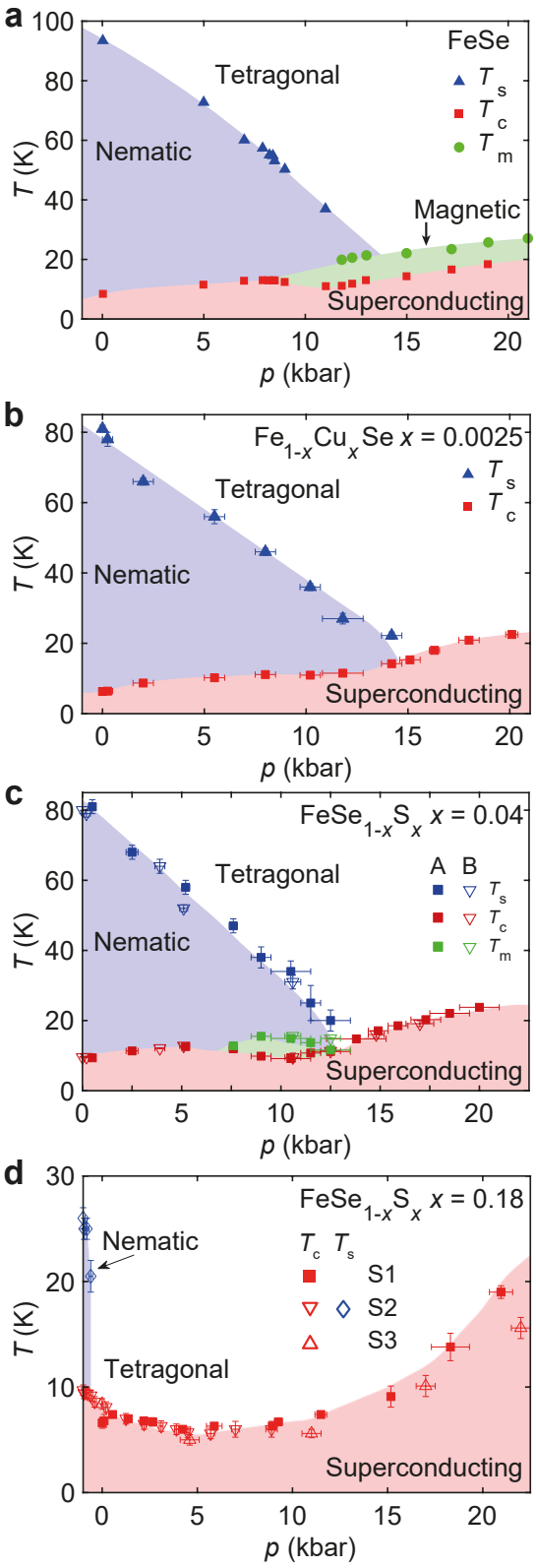

Figure 7.1: Zero-field pressure-temperature phase diagrams of FeSe related systems. The pressure-temperature phase diagram in zero-field for (a) FeSe (data taken from Chen et al. [187] using a piston cylinder cell similar to the measurements in this thesis), (b) $Fe_{1-x}Cu_xSe$ $x = 0.0025$ (Chapter 4), (c) $FeSe_{1-x}S_x$ $x = 0.04$ (Chapter 6), and (d) $FeSe_{1-x}S_x$ $x = 0.18$ (Chapter 5). The shaded regions are guides to the eye for the different phases.

8
Publications

- **Z. Zajicek**, P. Reiss, D. Graf, J. C. A. Prentice, A. A. Haghighirad, and A. I. Coldea, "Unravelling the Fermi surface and quasiparticles inside the pressure-enhanced superconducting phase of a iron-chalcogenide superconductor", *To be submitted* (2023).

- **Z. Zajicek**, T. Chatfield, O. Squire, S. J. Singh, M. Bristow, P. Reiss, D. Graf, and A. I. Coldea, "The interplay between nematic and magnetic states on the superconducting behaviour of $FeSe_{0.96}S_{0.04}$ under pressure", *In preparation* (2023).

- **Z. Zajicek**, S. J. Singh, and A. I. Coldea, "Robust superconductivity and fragile magnetism induced by the strong Cu impurity scattering in the high-pressure phase of FeSe", *Physical Review Research* **4**, 043123 (2022).

- **Z. Zajicek**, S. J. Singh, H. Jones, P. Reiss, M. Bristow, A. Martin, A. Gower, A. McCollam, and A. I. Coldea, "Drastic effect of impurity scattering on the electronic and superconducting properties of Cu-doped FeSe", *Physical Review B* **105**, 115130 (2022).

- P. Reiss, A. McCollam, **Z. Zajicek**, A. A. Haghighirad, and A. I. Coldea, "Collapse of Metallicity and High-T_c Superconductivity in the High-Pressure phase of $FeSe_{0.89}S_{0.11}$", *To be submitted*, arXiv:2212.06824 (2022).

- L. Farrar, **Z. Zajicek**, A.B. Morfoot, M. Bristow, O. S. Humphries, A. A. Haghighirad, A. McCollam, S. J. Bending, and A. I. Coldea, "Unconventional localization of electrons inside of a nematic electronic phase", *Proceedings of the National Academy of Sciences* **119**, e2200405119 (2022).

- M. Bristow, P. Reiss, A. A. Haghighirad, **Z. Zajicek**, S. J. Singh, T. Wolf, D. Graf, W. Knafo, A. McCollam and A. I. Coldea, "Anomalous high-magnetic field electronic state of the nematic superconductors $FeSe_{1-x}S_x$", *Physical Review Research* **2**, 013309 (2020).

References

[1] J. Bardeen, L. N. Cooper, and J. R. Schrieffer, "Microscopic Theory of Superconductivity", Phys. Rev. **106**, 162–164 (1957).

[2] J. Bardeen, L. N. Cooper, and J. R. Schrieffer, "Theory of Superconductivity", Phys. Rev. **108**, 1175–1204 (1957).

[3] J. G. Bednorz and K. A. Müller, "Possible hightc superconductivity in the ba-la-cu-o system", Zeitschrift für Physik B Condensed Matter **64**, 189–193 (1986).

[4] A. Schilling, M. Cantoni, J. D. Guo, and H. R. Ott, "Superconductivity above 130 K in the Hg–Ba–Ca–Cu–O system", Nature **363**, 56–58 (1993).

[5] A. Yamamoto, N. Takeshita, C. Terakura, and Y. Tokura, "High pressure effects revisited for the cuprate superconductor family with highest critical temperature", Nature Communications **6**, 8990 (2015).

[6] F. Steglich, J. Aarts, C. D. Bredl, W. Lieke, D. Meschede, W. Franz, and H. Schäfer, "Superconductivity in the Presence of Strong Pauli Paramagnetism: $CeCu_2Si_2$", Phys. Rev. Lett. **43**, 1892–1896 (1979).

[7] C. Petrovic, P. G. Pagliuso, M. F. Hundley, R. Movshovich, J. L. Sarrao, J. D. Thompson, Z. Fisk, and P. Monthoux, "Heavy-fermion superconductivity in $CeCoIn_5$ at 2.3 K", Journal of Physics: Condensed Matter **13**, L337–L342 (2001).

[8] Y. Kamihara, H. Hiramatsu, M. Hirano, R. Kawamura, H. Yanagi, T. Kamiya, and H. Hosono, "Iron-Based Layered Superconductor: LaOFeP", Journal of the American Chemical Society **128**, 10012–10013 (2006).

[9] Y. Kamihara, T. Watanabe, M. Hirano, and H. Hosono, "Iron-Based Layered Superconductor $La[O_{1-x}F_x]FeAs$ (x = 0.05-0.12) with T_c = 26 K", Journal of the American Chemical Society **130**, 3296–3297 (2008).

[10] W. Qing-Yan, L. Zhi, Z. Wen-Hao, Z. Zuo-Cheng, Z. Jin-Song, L. Wei, D. Hao, O. Yun-Bo, D. Peng, C. Kai, W. Jing, S. Can-Li, H. Ke, J. Jin-Feng, J. Shuai-Hua, W. Ya-Yu, W. Li-Li, C. Xi, M. Xu-Cun, and X. Qi-Kun, "Interface-Induced High-Temperature Superconductivity in Single Unit-Cell FeSe Films on $SrTiO_3$", Chinese Physics Letters **29**, 037402 (2012).

[11] G. Jian-Fen, L. Zhi-Long, L. Canhua, G. Chun-Lei, Q. Dong, X. Qi-Kun, L. Ying, and J. Jin-Feng, "Superconductivity above 100 K in single-layer FeSe films on doped $SrTiO_3$", Nature Materials **14**, 285–289 (2015).

[12] D. Huang and J. E. Hoffman, "Monolayer FeSe on $SrTiO_3$", Annual Review of Condensed Matter Physics **8**, 311–336 (2017).

[13] A. P. Drozdov, M. I. Eremets, I. A. Troyan, V. Ksenofontov, and S. I. Shylin, "Conventional superconductivity at 203 kelvin at high pressures in the sulfur hydride system", Nature **525**, 73–76 (2015).

[14] A. P. Drozdov, P. P. Kong, V. S. Minkov, S. P. Besedin, M. A. Kuzovnikov, S. Mozaffari, L. Balicas, F. F. Balakirev, D. E. Graf, V. B. Prakapenka, E. Greenberg, D. A. Knyazev, M. Tkacz, and M. I. Eremets, "Superconductivity at 250 K in lanthanum hydride under high pressures", Nature **569**, 528–531 (2019).

[15] M. Somayazulu, M. Ahart, A. K. Mishra, Z. M. Geballe, M. Baldini, Y. Meng, V. V. Struzhkin, and R. J. Hemley, "Evidence for Superconductivity above 260 K in Lanthanum Superhydride at Megabar Pressures", Phys. Rev. Lett. **122**, 027001 (2019).

[16] S. Margadonna, Y. Takabayashi, Y. Ohishi, Y. Mizuguchi, Y. Takano, T. Kagayama, T. Nakagawa, M. Takata, and K. Prassides, "Pressure evolution of the low-temperature crystal structure and bonding of the superconductor FeSe T_c=37 K", Phys. Rev. B **80**, 064506 (2009).

[17] A. F. Wang, Z. J. Xiang, J. J. Ying, Y. J. Yan, P. Cheng, G. J. Ye, X. G. Luo, and X. H. Chen, "Pressure effects on the superconducting properties of single-crystalline Co doped NaFeAs", New Journal of Physics **14**, 113043 (2012).

[18] C. Yao and Y. Ma, "Recent breakthrough development in iron-based superconducting wires for practical applications", Superconductor Science and Technology **32**, 023002 (2019).

[19] J. F. Annett, *Superconductivity, Superfluids and Condensates* (Oxford University Press, 2004).

[20] N. W. Ashcroft and N. D. Mermin, *Solid State Physics* (Holt-Saunders, 1976).

[21] P. B. Allen and R. C. Dynes, "Transition temperature of strong-coupled superconductors reanalyzed", Phys. Rev. B **12**, 905–922 (1975).

[22] P. Anderson, "Theory of dirty superconductors", Journal of Physics and Chemistry of Solids **11**, 26–30 (1959).

[23] A. A. Abrikosov and L. P. Gor'kov, "On the theory of superconducting alloys", Sov. Phys. JETP **12**, 1243 (1961).

[24] K. Maki, "Effect of Pauli Paramagnetism on Magnetic Properties of High-Field Superconductors", Phys. Rev. **148**, 362–369 (1966).

[25] N. R. Werthamer, E. Helfand, and P. C. Hohenberg, "Temperature and Purity Dependence of the Superconducting Critical Field, H_{c2}. III. Electron Spin and Spin-Orbit Effects", Phys. Rev. **147**, 295–302 (1966).

[26] E. Helfand and N. R. Werthamer, "Temperature and Purity Dependence of the Superconducting Critical Field, H_{c2}. II", Phys. Rev. **147**, 288–294 (1966).

[27] A. Gurevich, "Upper critical field and the Fulde-Ferrel-Larkin-Ovchinnikov transition in multiband superconductors", Phys. Rev. B **82**, 184504 (2010).

[28] V. G. Kogan and R. Prozorov, "Orbital upper critical field and its anisotropy of clean one- and two-band superconductors", Reports on Progress in Physics **75**, 114502 (2012).

[29] J.-H. Chu, J. G. Analytis, C. Kucharczyk, and I. R. Fisher, "Determination of the phase diagram of the electron-doped superconductor $Ba(Fe_{1-x}Co_x)_2As_2$", Phys. Rev. B **79**, 014506 (2009).

[30] S. Avci, O. Chmaissem, D. Y. Chung, S. Rosenkranz, E. A. Goremychkin, J. P. Castellan, I. S. Todorov, J. A. Schlueter, H. Claus, A. Daoud-Aladine, D. D. Khalyavin, M. G. Kanatzidis, and R. Osborn, "Phase diagram of $Ba_{1-x}K_xFe_2As_2$", Phys. Rev. B **85**, 184507 (2012).

[31] R. M. Fernandes, A. V. Chubukov, and J. Schmalian, "What drives nematic order in iron-based superconductors?", Nat. Phys. **10**, 97 (2014).

[32] A. E. Böhmer, P. Burger, F. Hardy, T. Wolf, P. Schweiss, R. Fromknecht, H. v. Löhneysen, C. Meingast, H. K. Mak, R. Lortz, S. Kasahara, T. Terashima, T. Shibauchi, and Y. Matsuda, "Thermodynamic phase diagram, phase competition, and uniaxial pressure effects in $BaFe_2(As_{1-x}P_x)_2$ studied by thermal expansion", Phys. Rev. B **86**, 094521 (2012).

[33] J. G. Analytis, H.-H. Kuo, R. D. McDonald, M. Wartenbe, P. M. C. Rourke, N. E. Hussey, and I. R. Fisher, "Transport near a quantum critical point in $BaFe_2(As_{1-x}P_x)_2$", Nature Physics **10**, 194 (2014).

[34] Y. Mizuguchi and Y. Takano, "Review of Fe Chalcogenides as the Simplest Fe-Based Superconductor", Journal of the Physical Society of Japan **79**, 102001 (2010).

[35] H. Okabe, N. Takeshita, K. Horigane, T. Muranaka, and J. Akimitsu, "Pressure-induced high-T_c superconducting phase in FeSe: Correlation between anion height and T_c", Phys. Rev. B **81**, 205119 (2010).

[36] S. Jiang, H. Xing, G. Xuan, C. Wang, Z. Ren, C. Feng, J. Dai, Z. Xu, and G. Cao, "Superconductivity up to 30 K in the vicinity of the quantum critical point in $BaFe_2(As_{1-x}P_x)_2$", Journal of Physics: Condensed Matter **21**, 382203 (2009).

[37] C. Proust and L. Taillefer, "The Remarkable Underlying Ground States of Cuprate Superconductors", Annual Review of Condensed Matter Physics **10**, 409–429 (2019).

[38] P. C. Canfield and S. L. Bud'ko, "FeAs-Based Superconductivity: A Case Study of the Effects of Transition Metal Doping on $BaFe_2As_2$", Annual Review of Condensed Matter Physics **1**, 27–50 (2010).

[39] M. D. Watson, P. Dudin, L. C. Rhodes, D. V. Evtushinsky, H. Iwasawa, S. Aswartham Saicharanand Wurmehl, B. Büchner, M. Hoesch, and T. K. Kim, "Probing the reconstructed Fermi surface of antiferromagnetic $BaFe_2As_2$ in one domain", npj Quantum Materials **4**, 36 (2019).

[40] P. J. Hirschfeld, M. M. Korshunov, and I. I. Mazin, "Gap symmetry and structure of Fe-based superconductors", Reports on Progress in Physics **74**, 124508 (2011).

[41] R. M. Fernandes, H. Coldea Amalia I. Ding, I. R. Fisher, P. J. Hirschfeld, and G. Kotliar, "Iron pnictides and chalcogenides: a new paradigm for superconductivity", Nature **601**, 34–44 (2022).

[42] P. J. Hirschfeld, "Using gap symmetry and structure to reveal the pairing mechanism in Fe-based superconductors", Comptes Rendus Physique **17**, 197–231 (2016).

[43] C.-C. Lee, W.-G. Yin, and W. Ku, "Ferro-orbital order and strong magnetic anisotropy in the parent compounds of iron-pnictide superconductors", Phys. Rev. Lett. **103**, 267001 (2009).

[44] F. Krüger, S. Kumar, J. Zaanen, and J. van den Brink, "Spin-orbital frustrations and anomalous metallic state in iron-pnictide superconductors", Phys. Rev. B **79**, 054504 (2009).

[45] H. Kontani and S. Onari, "Orbital-Fluctuation-Mediated Superconductivity in Iron Pnictides: Analysis of the Five-Orbital Hubbard-Holstein Model", Phys. Rev. Lett. **104**, 157001 (2010).

[46] R. T. Scalettar, D. J. Scalapino, R. L. Sugar, and S. R. White, "Antiferromagnetic, charge-transfer, and pairing correlations in the three-band Hubbard model", Phys. Rev. B **44**, 770–781 (1991).

[47] S. M. O'Mahony, W. Ren, W. Chen, Y. X. Chong, X. Liu, H. Eisaki, S. Uchida, M. H. Hamidian, and J. C. S. Davis, "On the electron pairing mechanism of copper-oxide high temperature superconductivity", Proceedings of the National Academy of Sciences **119**, e2207449119 (2022).

[48] J. Kang and R. M. Fernandes, "Superconductivity in FeSe Thin Films Driven by the Interplay between Nematic Fluctuations and Spin-Orbit Coupling", Phys. Rev. Lett. **117**, 217003 (2016).

[49] S. Onari and H. Kontani, "Violation of Anderson's Theorem for the Sign-Reversing s-Wave State of Iron-Pnictide Superconductors", Phys. Rev. Lett. **103**, 177001 (2009).

[50] P. O. Sprau, A. Kostin, A. Kreisel, A. E. Böhmer, V. Taufour, P. C. Canfield, S. Mukherjee, P. J. Hirschfeld, B. M. Andersen, and J. C. S. Davis, "Discovery of orbital-selective Cooper pairing in FeSe", Science **357**, 75–80 (2017).

[51] K. Kuroki, S. Onari, R. Arita, H. Usui, Y. Tanaka, H. Kontani, and H. Aoki, "Unconventional Pairing Originating from the Disconnected Fermi Surfaces of Superconducting $LaFeAsO_{1-x}F_x$", Phys. Rev. Lett. **101**, 087004 (2008).

[52] A. Subedi, L. Zhang, D. J. Singh, and M. H. Du, "Density functional study of FeS, FeSe, and FeTe: Electronic structure, magnetism, phonons, and superconductivity", Phys. Rev. B **78**, 134514 (2008).

[53] Y. Wang, A. Kreisel, P. J. Hirschfeld, and V. Mishra, "Using controlled disorder to distinguish $s_{\pm}$ and s_{++} gap structure in Fe-based superconductors", Phys. Rev. B **87**, 094504 (2013).

[54] F.-C. Hsu, J.-Y. Luo, K.-W. Yeh, T.-K. Chen, T.-W. Huang, P. M. Wu, Y.-C. Lee, Y.-L. Huang, Y.-Y. Chu, D.-C. Yan, and M.-K. Wu, "Superconductivity in the PbO-type structure α-FeSe", Proceedings of the National Academy of Sciences **105**, 14262–14264 (2008).

[55] A. I. Coldea, "Electronic Nematic States Tuned by Isoelectronic Substitution in Bulk $FeSe_{1-x}S_x$", Frontiers in Physics **8**, 528 (2021).

[56] K. Mukasa, K. Matsuura, M. Qiu, M. Saito, Y. Sugimura, K. Ishida, M. Otani, Y. Onishi, Y. Mizukami, K. Hashimoto, J. Gouchi, R. Kumai, Y. Uwatoko, and T. Shibauchi, "High-pressure phase diagrams of $FeSe_{1-x}Te_x$: correlation between suppressed nematicity and enhanced superconductivity", Nat. Comm. **12**, 381 (2021).

[57] X. Yi, X. Xing, L. Qin, J. Feng, M. Li, Y. Zhang, Y. Meng, N. Zhou, Y. Sun, and Z. Shi, "Hydrothermal synthesis and complete phase diagram of $FeSe_{1-x}S_x$ ($0 \leq x \leq 1$) single crystals", Phys. Rev. B **103**, 144501 (2021).

[58] D.-x. Mou, L. Zhao, and X.-j. Zhou, "Structural, magnetic and electronic properties of the iron-chalcogenide $A_xFe_{2-y}Se_2$ (A=K, Cs, Rb, and Tl, etc.) superconductors", Frontiers of Physics **6**, 410–428 (2011).

[59] T. M. McQueen, A. J. Williams, P. W. Stephens, J. Tao, Y. Zhu, V. Ksenofontov, F. Casper, C. Felser, and R. J. Cava, "Tetragonal-to-Orthorhombic Structural Phase Transition at 90 K in the Superconductor $Fe_{1.01}Se$", Phys. Rev. Lett. **103**, 057002 (2009).

[60] M. D. Watson, T. K. Kim, A. A. Haghighirad, N. R. Davies, A. McCollam, A. Narayanan, S. F. Blake, Y. L. Chen, S. Ghannadzadeh, A. J. Schofield, M. Hoesch, C. Meingast, T. Wolf, and A. I. Coldea, "Emergence of the nematic electronic state in FeSe", Phys. Rev. B **91**, 155106 (2015).

[61] K. Momma and F. Izumi, "*VESTA3* for three-dimensional visualization of crystal, volumetric and morphology data", Journal of Applied Crystallography **44**, 1272–1276 (2011).

[62] S. He, J. He, W. Zhang, L. Zhao, D. Liu, X. Liu, D. Mou, Y.-B. Ou, Q.-Y. Wang, Z. Li, L. Wang, Y. Peng, Y. Liu, C. Chen, L. Yu, G. Liu, X. Dong, J. Zhang, C. Chen, Z. Xu, X. Chen, X. Ma, Q. Xue, and X. J. Zhou, "Phase diagram and electronic indication of high-temperature superconductivity at 65 K in single-layer FeSe films", Nature Materials **12**, 605–610 (2013).

[63] S. Tan, Y. Zhang, M. Xia, Z. Ye, F. Chen, X. Xie, R. Peng, D. Xu, Q. Fan, H. Xu, J. Jiang, T. Zhang, X. Lai, T. Xiang, J. Hu, B. Xie, and D. Feng, "Interface-induced superconductivity and strain-dependent spin density waves in FeSe/SrTiO3 thin films", Nature Materials **12**, 634–640 (2013).

[64] M. Burrard-Lucas, D. G. Free, S. J. Sedlmaier, J. D. Wright, S. J. Cassidy, Y. Hara, A. J. Corkett, T. Lancaster, P. J. Baker, S. J. Blundell, and S. J. Clarke, "Enhancement of the superconducting transition temperature of FeSe by intercalation of a molecular spacer layer", Nat. Mater. **12**, 15 (2013).

[65] M. Yi, H. Pfau, Y. Zhang, Y. He, H. Wu, T. Chen, Z. R. Ye, M. Hashimoto, R. Yu, Q. Si, D.-H. Lee, P. Dai, Z.-X. Shen, D. H. Lu, and R. J. Birgeneau, "Nematic Energy Scale and the Missing Electron Pocket in FeSe", Phys. Rev. X **9**, 041049 (2019).

[66] L. C. Rhodes, M. Escrig, T. K. Kim, and M. D. Watson, "FeSe and the Missing Electron Pocket Problem", Frontiers in Physics **10**, 10.3389/fphy.2022.859017 (2022).

[67] A. I. Coldea, S. F. Blake, S. Kasahara, A. A. Haghighirad, M. D. Watson, W. Knafo, E. S. Choi, A. McCollam, P. Reiss, T. Yamashita, M. Bruma, S. Speller, Y. Matsuda, T. Wolf, T. Shibauchi, and A. J. Schofield, "Evolution of the low-temperature Fermi surface of superconducting $FeSe_{1-x}S_x$ across a nematic phase transition", npj Quantum Materials **4**, 2 (2019).

[68] M. Yi, Z. Liu, Y. Zhang, R. Yu, J. Zhu, J. Lee, R. Moore, F. Schmitt, W. Li, S. Riggs, J.-H. Chu, B. Lv, J. Hu, M. Hashimoto, S.-K. Mo, Z. Hussain, Z. Mao, C.-W. Chu, I. Fisher, Q. Si, Z.-X. Shen, and D. Lu, "Observation of universal strong orbital-dependent correlation effects in iron chalcogenides", Nat. Comm. **6**, 7777 (2015).

[69] J. P. Sun, K. Matsuura, G. Z. Ye, Y. Mizukami, M. Shimozawa, K. Matsubayashi, M. Yamashita, T. Watashige, S. Kasahara, Y. Matsuda, J.-Q. Yan, B. C. Sales, Y. Uwatoko, J.-G. Cheng, and T. Shibauchi, "Dome-shaped magnetic order competing with high-temperature superconductivity at high pressures in FeSe", Nat. Commun. **7**, 12146 (2016).

[70] S. Hosoi, K. Matsuura, K. Ishida, H. Wang, Y. Mizukami, T. Watashige, S. Kasahara, Y. Matsuda, and T. Shibauchi, "Nematic quantum critical point without magnetism in $FeSe_{1-x}S_x$ superconductors", PNAS **113**, 8139 (2016).

[71] M. Bristow, P. Reiss, A. A. Haghighirad, Z. Zajicek, S. J. Singh, T. Wolf, D. Graf, W. Knafo, A. McCollam, and A. I. Coldea, "Anomalous high-magnetic field electronic state of the nematic superconductors $FeSe_{1-x}S_x$", Phys. Rev. Research **2**, 013309 (2020).

[72] Y. Mizuguchi, F. Tomioka, S. Tsuda, T. Yamaguchi, and Y. Takano, "Superconductivity at 27K in tetragonal FeSe under high pressure", Applied Physics Letters **93**, 152505 (2008).

[73] T. Urata, Y. Tanabe, K. K. Huynh, Y. Yamakawa, H. Kontani, and K. Tanigaki, "Superconductivity pairing mechanism from cobalt impurity doping in FeSe: Spin ($s_{\pm}$) or orbital (s_{++}) fluctuation", Phys. Rev. B **93**, 014507 (2016).

[74] T.-W. Huang, T.-K. Chen, K.-W. Yeh, C.-T. Ke, C. L. Chen, Y.-L. Huang, F.-C. Hsu, M.-K. Wu, P. M. Wu, M. Avdeev, and A. J. Studer, "Doping-driven structural phase transition and loss of superconductivity in $M_xFe_{1-x}Se_{\delta}$ ($M = \mathrm{Mn},\ \mathrm{Cu}$)", Phys. Rev. B **82**, 104502 (2010).

[75] A. J. Williams, T. M. McQueen, V. Ksenofontov, C. Felser, and R. J. Cava, "The metal-insulator transition in $Fe_{1.01-x}Cu_xSe$", Journal of Physics: Condensed Matter **21**, 305701 (2009).

[76] C. Gong, S. Sun, S. Wang, and H. Lei, "Normal and superconducting state properties of Cu-doped FeSe single crystals", Phys. Rev. B **103**, 174510 (2021).

[77] L. S. Farrar, PhD thesis, University of Bath (2021).

[78] S. Kasahara, Y. Sato, S. Licciardello, M. Čulo, S. Arsenijević, T. Ottenbros, T. Tominaga, J. Böker, I. Eremin, T. Shibauchi, J. Wosnitza, N. E. Hussey, and Y. Matsuda, "Evidence for an Fulde-Ferrell-Larkin-Ovchinnikov State with Segmented Vortices in the BCS-BEC-Crossover Superconductor FeSe", Phys. Rev. Lett. **124**, 107001 (2020).

[79] J. M. Ok, C. I. Kwon, Y. Kohama, J. S. You, S. K. Park, J.-h. Kim, Y. J. Jo, E. S. Choi, K. Kindo, W. Kang, K.-S. Kim, E. G. Moon, A. Gurevich, and J. S. Kim, "Observation of in-plane magnetic field induced phase transitions in FeSe", Phys. Rev. B **101**, 224509 (2020).

[80] Y. Matsuda and H. Shimahara, "Fulde–Ferrell–Larkin–Ovchinnikov State in Heavy Fermion Superconductors", Journal of the Physical Society of Japan **76**, 051005 (2007).

[81] J. Wosnitza, "FFLO States in Layered Organic Superconductors", Annalen der Physik **530**, 1700282 (2018).

[82] P. Zhang, K. Yaji, T. Hashimoto, Y. Ota, T. Kondo, K. Okazaki, Z. Wang, J. Wen, G. D. Gu, H. Ding, and S. Shin, "Observation of topological superconductivity on the surface of an iron-based superconductor", Science **360**, 182–186 (2018).

[83] Q. Wang, Y. Shen, B. Pan, X. Zhang, K. Ikeuchi, K. Iida, A. D. Christianson, H. C. Walker, D. T. Adroja, M. Abdel-Hafiez, X. Chen, D. A. Chareev, A. N. Vasiliev, and J. Zhao, "Magnetic ground state of FeSe", Nat. Commun. **7**, 12182 (2016).

[84] Q. Wang, Y. Shen, B. Pan, Y. Hao, M. Ma, F. Zhou, P. Steffens, K. Schmalzl, T. R. Forrest, M. Abdel-Hafiez, X. Chen, D. A. Chareev, A. N. Vasiliev, P. Bourges, Y. Sidis, H. Cao, and J. Zhao, "Strong interplay between stripe spin fluctuations, nematicity and superconductivity in FeSe", Nat. Mater. **15**, 159 (2016).

[85] D. Braithwaite, B. Salce, G. Lapertot, F. Bourdarot, C. Marin, D. Aoki, and M. Hanfland, "Superconducting and normal phases of FeSe single crystals at high pressure", Journal of Physics: Condensed Matter **21**, 232202 (2009).

[86] M. Bendele, A. Amato, K. Conder, M. Elender, H. Keller, H.-H. Klauss, H. Luetkens, E. Pomjakushina, A. Raselli, and R. Khasanov, "Pressure Induced Static Magnetic Order in Superconducting $FeSe_{1-x}$", Phys. Rev. Lett. **104**, 087003 (2010).

[87] T. Terashima, N. Kikugawa, A. Kiswandhi, D. Graf, E.-S. Choi, J. S. Brooks, S. Kasahara, T. Watashige, Y. Matsuda, T. Shibauchi, T. Wolf, A. E. Böhmer, F. Hardy, C. Meingast, H. v. Löhneysen, and S. Uji, "Fermi surface reconstruction in FeSe under high pressure", Phys. Rev. B **93**, 094505 (2016).

[88] J. H. Kang, S. G. Jung, S. Lee, E. Park, J. Y. Lin, D. A. Chareev, A. N. Vasiliev, and T. Park, "Pressure dependence of upper critical fields in FeSe single crystals", Superconductor Science and Technology **29**, 10.1088/0953-2048/29/3/035007 (2016).

[89] K. Kothapalli, A. E. Böhmer, W. T. Jayasekara, B. G. Ueland, P. Das, A. Sapkota, V. Taufour, Y. Xiao, E. Alp, S. L. Bud'ko, P. C. Canfield, A. Kreyssig, and A. I. Goldman, "Strong cooperative coupling of pressure-induced magnetic order and nematicity in FeSe", Nat. Comm. **7**, 12728 (2016).

[90] S. Medvedev, T. M. McQueen, I. A. Troyan, T. Palasyuk, M. I. Eremets, R. J. Cava, S. Naghavi, F. Casper, V. Ksenofontov, G. Wortmann, and C. Felser, "Electronic and magnetic phase diagram of β-$Fe_{1.01}Se$ with superconductivity at 36.7 K under pressure", Nat. Mater. **8**, 630 (2009).

[91] G. Garbarino, A. Sow, P. Lejay, A. Sulpice, P. Toulemonde, M. Mezouar, and M. Núñez-Regueiro, "High-temperature superconductivity (T_c onset at 34 K) in the high-pressure orthorhombic phase of FeSe", EPL (Europhysics Letters) **86**, 27001 (2009).

[92] S. Masaki, H. Kotegawa, Y. Hara, H. Tou, K. Murata, Y. Mizuguchi, and Y. Takano, "Precise Pressure Dependence of the Superconducting Transition Temperature of FeSe: Resistivity and 77Se-NMR Study", Journal of the Physical Society of Japan **78**, 063704 (2009).

[93] A. E. Böhmer, K. Kothapalli, W. T. Jayasekara, J. M. Wilde, B. Li, A. Sapkota, B. G. Ueland, P. Das, Y. Xiao, W. Bi, J. Zhao, E. E. Alp, S. L. Bud'ko, P. C. Canfield, A. I. Goldman, and A. Kreyssig, "Distinct pressure evolution of coupled nematic and magnetic orders in FeSe", Phys. Rev. B **100**, 064515 (2019).

[94] E. Gati, A. E. Böhmer, S. L. Bud'ko, and P. C. Canfield, "Bulk Superconductivity and Role of Fluctuations in the Iron-Based Superconductor FeSe at High Pressures", Phys. Rev. Lett. **123**, 167002 (2019).

[95] U. S. Kaluarachchi, V. Taufour, A. E. Böhmer, M. A. Tanatar, S. L. Bud'ko, V. G. Kogan, R. Prozorov, and P. C. Canfield, "Nonmonotonic pressure evolution of the upper critical field in superconducting FeSe", Phys. Rev. B **93**, 064503 (2016).

[96] T. Terashima, N. Kikugawa, S. Kasahara, T. Watashige, Y. Matsuda, T. Shibauchi, and S. Uji, "Magnetotransport study of the pressure-induced antiferromagnetic phase in FeSe", Phys. Rev. B **93**, 180503 (2016).

[97] M. Bendele, A. Ichsanow, Y. Pashkevich, L. Keller, T. Strässle, A. Gusev, E. Pomjakushina, K. Conder, R. Khasanov, and H. Keller, "Coexistence of superconductivity and magnetism in $FeSe_{1-x}$ under pressure", Phys. Rev. B **85**, 064517 (2012).

[98] R. Khasanov, Z. Guguchia, A. Amato, E. Morenzoni, X. Dong, F. Zhou, and Z. Zhao, "Pressure-induced magnetic order in fese: a muon spin rotation study", Phys. Rev. B **95**, 180504 (2017).

[99] P. S. Wang, S. S. Sun, Y. Cui, W. H. Song, T. R. Li, R. Yu, H. Lei, and W. Yu, "Pressure Induced Stripe-Order Antiferromagnetism and First-Order Phase Transition in FeSe", Phys. Rev. Lett. **117**, 237001 (2016).

[100] T. Terashima, N. Kikugawa, H. Lin, X. Zhu, H.-H. Wen, T. Nomoto, K. Suzuki, H. Ikeda, and S. Uji, "Upper critical field and quantum oscillations in tetragonal superconducting FeS", Phys. Rev. B **94**, 100503 (2016).

[101] A. E. Böhmer, F. Hardy, F. Eilers, D. Ernst, P. Adelmann, P. Schweiss, T. Wolf, and C. Meingast, "Lack of coupling between superconductivity and orthorhombic distortion in stoichiometric single-crystalline FeSe", Phys. Rev. B **87**, 180505 (2013).

[102] A. E. Böhmer, V. Taufour, W. E. Straszheim, T. Wolf, and P. C. Canfield, "Variation of transition temperatures and residual resistivity ratio in vapor-grown FeSe", Phys. Rev. B **94**, 024526 (2016).

[103] W. Liu, X. Yi, W. Li, X. Xing, H. Zhao, M. Xu, and Z. Shi, "Transport properties and phase diagrams of $FeSe_{1-x}S_x$ $(0 \leq x \leq 1)$ single crystals", Journal of Alloys and Compounds **919**, 165760 (2022).

[104] K. Matsuura, Y. Mizukami, Y. Arai, Y. Sugimura, N. Maejima, A. Machida, T. Watanuki, T. Fukuda, T. Yajima, Z. Hiroi, K. Y. Yip, Y. C. Chan, Q. Niu, S. Hosoi, K. Ishida, K. Mukasa, S. Kasahara, J.-G. Cheng, S. K. Goh, Y. Matsuda, Y. Uwatoko, and T. Shibauchi, "Maximizing T_c by tuning nematicity and magnetism in $FeSe_{1-x}S_x$ superconductors", Nat. Comm. **8**, 1143 (2017).

[105] P. Reiss, D. Graf, A. A. Haghighirad, W. Knafo, L. Drigo, M. Bristow, A. Schofield, and A. I. Coldea, "Quenched nematic criticality and two superconducting domes in an iron-based superconductor", Nature Physics **16**, 89–94 (2020).

[106] K. Rana, L. Xiang, P. Wiecki, R. A. Ribeiro, G. G. Lesseux, A. E. Böhmer, S. L. Bud'ko, P. C. Canfield, and Y. Furukawa, "Impact of nematicity on the relationship between antiferromagnetic fluctuations and superconductivity in $FeSe_{0.91}S_{0.09}$ under pressure", Phys. Rev. B **101**, 180503 (2020).

[107] L. Xiang, U. S. Kaluarachchi, A. E. Böhmer, V. Taufour, M. A. Tanatar, R. Prozorov, S. L. Bud'ko, and P. C. Canfield, "Dome of magnetic order inside the nematic phase of sulfur-substituted FeSe under pressure", Phys. Rev. B **96**, 024511 (2017).

[108] L. Landau, "The Theory of a Fermi Liquid", J. Exptl. Theoret. Phys. **3**, 920–925 (1957).

[109] L. Landau, "On the theory of the Fermi liquid", Sov. Phys. JETP **8**, 70 (1959).

[110] S. Licciardello, J. Buhot, J. Lu, J. Ayres, S. Kasahara, Y. Matsuda, T. Shibauchi, and N. E. Hussey, "Electrical resistivity across a nematic quantum critical point", Nature **567**, 213–217 (2019).

[111] T. Senthil, "Critical Fermi surfaces and non-Fermi liquid metals", Phys. Rev. B **78**, 035103 (2008).

[112] S. Kasahara, T. Shibauchi, K. Hashimoto, K. Ikada, S. Tonegawa, R. Okazaki, H. Shishido, H. Ikeda, H. Takeya, K. Hirata, T. Terashima, and Y. Matsuda, "Evolution from non-Fermi- to Fermi-liquid transport via isovalent doping in $BaFe_2(As_{1-x}P_x)_2$ superconductors", Phys. Rev. B **81**, 184519 (2010).

[113] J. Paglione, M. A. Tanatar, D. G. Hawthorn, E. Boaknin, R. W. Hill, F. Ronning, M. Sutherland, L. Taillefer, C. Petrovic, and P. C. Canfield, "Field-Induced Quantum Critical Point in $CeCoIn_5$", Phys. Rev. Lett. **91**, 246405 (2003).

[114] D. L. Maslov, V. I. Yudson, and A. V. Chubukov, "Resistivity of a Non-Galilean–Invariant Fermi Liquid near Pomeranchuk Quantum Criticality", Phys. Rev. Lett. **106**, 106403 (2011).

[115] X. Wang and E. Berg, "Scattering mechanisms and electrical transport near an Ising nematic quantum critical point", Phys. Rev. B **99**, 235136 (2019).

[116] V. S. de Carvalho and R. M. Fernandes, "Resistivity near a nematic quantum critical point: Impact of acoustic phonons", Phys. Rev. B **100**, 115103 (2019).

[117] J. M. Ziman, *Electrons and Phonons: the theory of transport phenomena in solids* (Oxford University Press, 2001).

[118] S. J. Blundell and J. Singleton, "Semiclassical description of angle-dependent magnetoresistance oscillations in quasi-one-dimensional metals", Phys. Rev. B **53**, 5609–5619 (1996).

[119] M. Kohler, "Zur magnetischen Widerstandsänderung reiner Metalle", Annalen der Physik **424**, 211–218 (1938).

[120] A. B. Pippard, *Magnetoresistance in Metals* (Cambridge University Press, 1989).

[121] J. S. Kim, "A matrix formulation of magnetoresistance for an arbitrary J-fold multicarrier semiconductor system via the reduced-conductivity-tensor scheme in the nonquantizing regime", Journal of Applied Physics **84**, 292–300 (1998).

[122] J. S. Kim, "A matrix formalism for the Hall effect in multicarrier semiconductor systems", Journal of Applied Physics **86**, 3187–3194 (1999).

[123] J. W. McClure, "Field Dependence of Magnetoconductivity", Phys. Rev. **101**, 1642–1646 (1956).

[124] W. A. Beck and J. R. Anderson, "Determination of electrical transport properties using a novel magnetic field-dependent Hall technique", Journal of Applied Physics **62**, 541–554 (1987).

[125] Q. L. Pei, X. Luo, F. C. Chen, H. Y. Lv, Y. Sun, W. J. Lu, P. Tong, Z. G. Sheng, Y. Y. Han, W. H. Song, X. B. Zhu, and Y. P. Sun, "Mobility spectrum analytical approach for the type-II Weyl semimetal Td-MoTe2", Applied Physics Letters **112**, 072401 (2018).

[126] H. Zhao, W. Li, Y. Chen, C. Xu, B. Li, W. Luo, D. Qian, and Z. Shi, "Transport property of multi-band topological material $PtBi_2$ studied by maximum entropy mobility spectrum analysis (MEMSA)", Scientific Reports **11**, 6249 (2021).

[127] K. K. Huynh, Y. Tanabe, T. Urata, H. Oguro, S. Heguri, K. Watanabe, and K. Tanigaki, "Electric transport of a single-crystal iron chalcogenide FeSe superconductor: Evidence of symmetry-breakdown nematicity and additional ultrafast Dirac cone-like carriers", Phys. Rev. B **90**, 144516 (2014).

[128] K. K. Huynh, Y. Tanabe, T. Urata, S. Heguri, K. Tanigaki, T. Kida, and M. Hagiwara, "Mobility spectrum analytical approach for intrinsic band picture of $Ba(FeAs)_2$", New Journal of Physics **16**, 093062 (2014).

[129] O. Humphries, "Mobility spectrum analysis for multiband superconducting systems", MPhys project, University of Oxford (2016).

[130] L. S. Farrar, Z. Zajicek, A. B. Morfoot, M. Bristow, O. S. Humphries, A. A. Haghighirad, A. McCollam, S. J. Bending, and A. I. Coldea, "Unconventional localization of electrons inside of a nematic electronic phase", Proceedings of the National Academy of Sciences **119**, e2200405119 (2022).

[131] N. Akhiezer and M. Krein, *Some Questions in the Theory of Moments (Translations of Mathematical Monographs)* (American Mathematical Society, 1962).

[132] L. Onsager, "Interpretation of the de Haas-van Alphen effect", The London, Edinburgh, and Dublin Philosophical Magazine and Journal of Science **43**, 1006–1008 (1952).

[133] D. Shoenberg, *Magnetic oscillations in metals* (Cambridge University Press, Cambridge, 1984).

[134] E. Adams and T. Holstein, "Quantum theory of transverse galvano-magnetic phenomena", Journal of Physics and Chemistry of Solids **10**, 254–276 (1959).

[135] N. H. M. F. Laboratory, *Calculated field distributions for the 41.5t magnet*, https://nationalmaglab.org/images/users/dc_field/searchable_docs/magnets/41_5_tesla_cell6/41_5_tesla_Cell_6_Field_Distributions.pdf.

[136] K. Yokogawa, K. Murata, H. Yoshino, and S. Aoyama, "Solidification of High-Pressure Medium Daphne 7373", Japanese Journal of Applied Physics **46**, 3636–3639 (2007).

[137] D. Staško, J. Prchal, M. Klicpera, S. Aoki, and K. Murata, "Pressure media for high pressure experiments, Daphne Oil 7000 series", High Pressure Research **40**, 525–536 (2020).

[138] K. Murata, H. Yoshino, H. O. Yadav, Y. Honda, and N. Shirakawa, "Pt resistor thermometry and pressure calibration in a clamped pressure cell with the medium, Daphne 7373", Review of Scientific Instruments **68**, 2490–2493 (1997).

[139] R. J. Angel, M. Bujak, J. Zhao, G. D. Gatta, and S. D. Jacobsen, "Effective hydrostatic limits of pressure media for high-pressure crystallographic studies", Journal of Applied Crystallography **40**, 26–32 (2007).

[140] N. Tateiwa and Y. Haga, "Evaluations of pressure-transmitting media for cryogenic experiments with diamond anvil cell", Review of Scientific Instruments **80**, 123901 (2009).

[141] A. Eiling and J. S. Schilling, "Pressure and temperature dependence of electrical resistivity of Pb and Sn from 1-300K and 0-10 GPa-use as continuous resistive pressure monitor accurate over wide temperature range. superconductivity under pressure in Pb, Sn and In", Journal of Physics F: Metal Physics **11**, 623–639 (1981).

[142] L. D. Jennings and C. A. Swenson, "Effects of Pressure on the Superconducting Transition Temperatures of Sn, In, Ta, Tl, and Hg", Phys. Rev. **112**, 31–43 (1958).

[143] H. K. Mao, P. M. Bell, J. W. Shaner, and D. J. Steinberg, "Specific volume measurements of Cu, Mo, Pd, and Ag and calibration of the ruby R1 fluorescence pressure gauge from 0.06 to 1 Mbar", Journal of Applied Physics **49**, 3276–3283 (1978).

[144] A. Dewaele, P. Loubeyre, and M. Mezouar, "Equations of state of six metals above 94 GPa", Phys. Rev. B **70**, 094112 (2004).

[145] H. Yamaoka, Y. Zekko, I. Jarrige, J.-F. Lin, N. Hiraoka, H. Ishii, K.-D. Tsuei, and J. Mizuki, "Ruby pressure scale in a low-temperature diamond anvil cell", Journal of Applied Physics **112**, 124503 (2012).

[146] Q. Design, *Quantum Design Physical Property Measurement System*, https://qd-uki.co.uk/material-characterisation/quantum-design-ppms-measurement-system/.

[147] R. W. Shaw, D. E. Mapother, and D. C. Hopkins, "Critical Fields of Superconducting Tin, Indium, and Tantalum", Phys. Rev. **120**, 88–91 (1960).

[148] C. T. Van Degrift, "Tunnel diode oscillator for 0.001 ppm measurements at low temperatures", Review of Scientific Instruments **46**, 599–607 (1975).

[149] Z. Zajicek, S. J. Singh, H. Jones, P. Reiss, M. Bristow, A. Martin, A. Gower, A. McCollam, and A. I. Coldea, "Drastic effect of impurity scattering on the electronic and superconducting properties of Cu-doped FeSe", Phys. Rev. B **105**, 115130 (2022).

[150] S. R. Saha, N. P. Butch, K. Kirshenbaum, and J. Paglione, "Evolution of bulk superconductivity in $SrFe_2As_2$ with Ni substitution", Phys. Rev. B **79**, 224519 (2009).

[151] S. T. Cui, S. Kong, S. L. Ju, P. Wu, A. F. Wang, X. G. Luo, X. H. Chen, G. B. Zhang, and Z. Sun, "ARPES study of the effect of Cu substitution on the electronic structure of NaFeAs", Phys. Rev. B **88**, 245112 (2013).

[152] S. L. Skornyakov, V. I. Anisimov, and I. Leonov, "Orbital-selective coherence-incoherence crossover and metal-insulator transition in Cu-doped NaFeAs", Phys. Rev. B **103**, 155115 (2021).

[153] J. Pelliciari, K. Ishii, L. Xing, X. Wang, C. Jin, and T. Schmitt, "Fluctuating magnetism of Co- and Cu-doped NaFeAs", Applied Physics Letters **118**, 112604 (2021).

[154] A. F. Wang, J. J. Lin, P. Cheng, G. J. Ye, F. Chen, J. Q. Ma, X. F. Lu, B. Lei, X. G. Luo, and X. H. Chen, "Phase diagram and physical properties of $NaFe_{1-x}Cu_xAs$ single crystals", Phys. Rev. B **88**, 094516 (2013).

[155] A. I. Coldea and M. D. Watson, "The Key Ingredients of the Electronic Structure of FeSe", Annual Review of Condensed Matter Physics **9**, 125–146 (2018).

[156] A. Kreisel, P. J. Hirschfeld, and B. M. Andersen, "On the Remarkable Superconductivity of FeSe and Its Close Cousins", Symmetry **12**, 1402 (2020).

[157] B.-L. Young, J. Wu, T.-W. Huang, K.-W. Yeh, and M.-K. Wu, "Magnetic fluctuations in $FeSe_{1-\delta}$ and Cu-doped $FeSe_{1-\delta}$:^{77} Se NMR experiments", Phys. Rev. B **81**, 144513 (2010).

[158] L. M. Schoop, S. A. Medvedev, V. Ksenofontov, A. Williams, T. Palasyuk, I. A. Troyan, J. Schmitt, F. Casper, C. Wang, M. Eremets, R. J. Cava, and C. Felser, "Pressure-restored superconductivity in Cu-substituted FeSe", Phys. Rev. B **84**, 174505 (2011).

[159] S. I. Shylin, V. Ksenofontov, P. G. Naumov, S. A. Medvedev, and C. Felser, "Interplay Between Superconductivity and Magnetism in Cu-Doped FeSe Under Pressure", Journal of Superconductivity and Novel Magnetism **31**, 763–769 (2019).

[160] L. Deng, T. Bontke, R. Dahal, Y. Xie, B. Gao, X. Li, K. Yin, M. Gooch, D. Rolston, T. Chen, Z. Wu, Y. Ma, P. Dai, and C.-W. Chu, "Pressure-induced high-temperature superconductivity retained without pressure in FeSe single crystals", Proceedings of the National Academy of Sciences **118**, 10.1073/pnas.2108938118 (2021).

[161] S. Teknowijoyo, K. Cho, M. A. Tanatar, J. Gonzales, A. E. Böhmer, O. Cavani, V. Mishra, P. J. Hirschfeld, S. L. Bud'ko, P. C. Canfield, and R. Prozorov, "Enhancement of superconducting transition temperature by pointlike disorder and anisotropic energy gap in FeSe single crystals", Phys. Rev. B **94**, 064521 (2016).

[162] D. Chareev, E. Osadchii, T. Kuzmicheva, J.-Y. Lin, S. Kuzmichev, O. Volkova, and A. Vasiliev, "Single crystal growth and characterization of tetragonal $FeSe_{1-x}$ superconductors", CrystEngComm **15**, 1989 (2013).

[163] H. Li, M. W. Ma, S. B. Liu, F. Zhou, and X. L. Dong, "Structural and electrical transport properties of Cu-doped $Fe_{1-x}Cu_xSe$ single crystals", Chinese Physics B **29**, 127404 (2020).

[164] A. Rosch, "Interplay of Disorder and Spin Fluctuations in the Resistivity near a Quantum Critical Point", Phys. Rev. Lett. **82**, 4280–4283 (1999).

[165] Y. Mizuguchi, F. Tomioka, S. Tsuda, T. Yamaguchi, and Y. Takano, "Substitution Effects on FeSe Superconductor", Journal of the Physical Society of Japan **78**, 074712 (2009).

[166] L. S. Farrar, M. Bristow, A. A. Haghighirad, S. J. Bending, and A. I. Coldea, "Suppression of superconductivity and enhanced critical field anisotropy in thin flakes of FeSe", npj Quantum Materials **5**, 29 (2020).

[167] M. Ghini, M. Bristow, J. C. A. Prentice, S. Sutherland, S. Sanna, A. A. Haghighirad, and A. I. Coldea, "Strain tuning of nematicity and superconductivity in single crystals of FeSe", Phys. Rev. B **103**, 205139 (2021).

[168] P. Wiecki, M. Nandi, A. E. Böhmer, S. L. Bud'ko, P. C. Canfield, and Y. Furukawa, "NMR evidence for static local nematicity and its cooperative interplay with low-energy magnetic fluctuations in FeSe under pressure", Phys. Rev. B **96**, 180502 (2017).

[169] P. Wiecki, K. Rana, A. E. Böhmer, Y. Lee, S. L. Bud'ko, P. C. Canfield, and Y. Furukawa, "Persistent correlation between superconductivity and antiferromagnetic fluctuations near a nematic quantum critical point in $FeSe_{1-x}S_x$", Phys. Rev. B **98**, 020507 (2018).

[170] M. D. Watson, T. Yamashita, S. Kasahara, W. Knafo, M. Nardone, J. Béard, F. Hardy, A. McCollam, A. Narayanan, S. F. Blake, T. Wolf, A. A. Haghighirad, C. Meingast, A. J. Schofield, H. v. Löhneysen, Y. Matsuda, A. I. Coldea, and T. Shibauchi, "Dichotomy between the Hole and Electron Behavior in Multiband Superconductor FeSe Probed by Ultrahigh Magnetic Fields", Phys. Rev. Lett. **115**, 027006 (2015).

[171] M. Čulo, M. Berben, Y.-T. Hsu, J. Ayres, R. D. H. Hinlopen, S. Kasahara, Y. Matsuda, T. Shibauchi, and N. E. Hussey, "Putative Hall response of the strange metal component in $FeSe_{1-x}S_x$", Phys. Rev. Research **3**, 023069 (2021).

[172] S. Chadov, D. Schärf, G. H. Fecher, C. Felser, L. Zhang, and D. J. Singh, "Electronic structure, localization, and spin-state transition in Cu-substituted FeSe : $Fe_{1-x}Cu_xSe$", Phys. Rev. B **81**, 104523 (2010).

[173] S. Huh, Z. Lu, Y. S. Kim, D. Kim, S. B. Liu, M. W. Ma, L. Yu, F. Zhou, X. L. Dong, C. Kim, and Z. X. Zhao, "Cu doping effects on the electronic structure of $Fe_{1-x}Cu_xSe$", Phys. Rev. B **105**, 245140 (2022).

[174] N. Zhou, Y. Sun, C. Y. Xi, Z. S. Wang, J. L. Zhang, Y. Zhang, Y. F. Zhang, C. Q. Xu, Y. Q. Pan, J. J. Feng, Y. Meng, X. L. Yi, L. Pi, T. Tamegai, X. Xing, and Z. Shi, "Disorder-robust high-field superconducting phase of FeSe single crystals", Phys. Rev. B **104**, L140504 (2021).

[175] A. Rosch, "Transport near antiferromagnetic quantum-phase transitions in metals", Journal of Magnetism and Magnetic Materials **226-230**, 11–16 (2001).

[176] N. E. Hussey, K. Takenaka, and H. Takagi, "Universality of the Mott–Ioffe–Regel limit in metals", Philosophical Magazine **84**, 2847–2864 (2004).

[177] Y. Werman and E. Berg, "Mott-Ioffe-Regel limit and resistivity crossover in a tractable electron-phonon model", Phys. Rev. B **93**, 075109 (2016).

[178] I. M. Hayes, R. D. McDonald, N. P. Breznay, T. Helm, P. J. W. Moll, M. Wartenbe, A. Shekhter, and J. G. Analytis, "Scaling between magnetic field and temperature in the high-temperature superconductor $BaFe_2(As_{1-x}P_x)_2$", Nature Physics **12**, 916 (2016).

[179] J. Hu and T. F. Rosenbaum, "Classical and quantum routes to linear magnetoresistance", Nature Materials **7**, 697–700 (2008).

[180] M. Bristow, "Iron-based superconductors in high-magnetic fields", PhD thesis, University of Oxford (2020).

[181] S.-H. Baek, J. M. Ok, J. S. Kim, S. Aswartham, I. Morozov, D. Chareev, T. Urata, K. Tanigaki, Y. Tanabe, B. Büchner, and D. V. Efremov, "Separate tuning of nematicity and spin fluctuations to unravel the origin of superconductivity in FeSe", npj Quantum Materials **5**, 8 (2020).

[182] Y. Sun, S. Kittaka, S. Nakamura, T. Sakakibara, P. Zhang, S. Shin, K. Irie, T. Nomoto, K. Machida, J. Chen, and T. Tamegai, "Disorder-sensitive nodelike small gap in FeSe", Phys. Rev. B **98**, 064505 (2018).

[183] Y. S. Kushnirenko, A. V. Fedorov, E. Haubold, S. Thirupathaiah, T. Wolf, S. Aswartham, I. Morozov, T. K. Kim, B. Büchner, and S. V. Borisenko, "Three-dimensional superconducting gap in FeSe from angle-resolved photoemission spectroscopy", Phys. Rev. B **97**, 180501 (2018).

[184] V. Grinenko, R. Sarkar, P. Materne, S. Kamusella, A. Yamamshita, Y. Takano, Y. Sun, T. Tamegai, D. V. Efremov, S.-L. Drechsler, J.-C. Orain, T. Goko, R. Scheuermann, H. Luetkens, and H.-H. Klauss, "Low-temperature breakdown of antiferromagnetic quantum critical behavior in FeSe", Phys. Rev. B **97**, 201102(R) (2018).

[185] Z. Zajicek, S. J. Singh, and A. I. Coldea, "Robust superconductivity and fragile magnetism induced by the strong Cu impurity scattering in the high-pressure phase of FeSe", Phys. Rev. Res. **4**, 043123 (2022).

[186] M. N. Gastiasoro and B. M. Andersen, "Enhancing superconductivity by disorder", Phys. Rev. B **98**, 184510 (2018).

[187] G.-Y. Chen, E. Wang, X. Zhu, and H.-H. Wen, "Synergy and competition between superconductivity and antiferromagnetism in FeSe under pressure", Phys. Rev. B **99**, 054517 (2019).

[188] T. Terashima, N. Kikugawa, S. Kasahara, T. Watashige, T. Shibauchi, Y. Matsuda, T. Wolf, A. E. Böhmer, F. Hardy, C. Meingast, H. v. Löhneysen, and S. Uji, "Pressure-Induced Antiferromagnetic Transition and Phase Diagram in FeSe", J. Phys. Soc. Japan **84**, 063701 (2015).

[189] J. P. Sun, G. Z. Ye, P. Shahi, J. Q. Yan, K. Matsuura, H. Kontani, G. M. Zhang, Q. Zhou, B. C. Sales, T. Shibauchi, Y. Uwatoko, D. J. Singh, and J. G. Cheng, "High-T_c Superconductivity in FeSe at High Pressure: Dominant Hole Carriers and Enhanced Spin Fluctuations", Phys. Rev. Lett. **118**, 1 (2017).

[190] M. D. Watson, T. K. Kim, A. A. Haghighirad, S. F. Blake, N. R. Davies, M. Hoesch, T. Wolf, and A. I. Coldea, "Suppression of orbital ordering by chemical pressure in $FeSe_{1-x}S_x$", Phys. Rev. B **92**, 121108 (2015).

[191] S. Kasahara, T. Yamashita, A. Shi, R. Kobayashi, Y. Shimoyama, T. Watashige, K. Ishida, T. Terashima, T. Wolf, F. Hardy, C. Meingast, H. v. Löhneysen, A. Levchenko, T. Shibauchi, and Y. Matsuda, "Giant superconducting fluctuations in the compensated semimetal FeSe at the BCS-BEC crossover", Nat. Commun. **7**, 12843 (2016).

[192] J.-h. Kim, J. M. Ok, J. Choi, W. Kang, J. S. Kim, and Y. Jo, "Enhanced vortex pinning with possible antiferromagnetic order in FeSe under pressure", Phys. Rev. B **105**, 035133 (2022).

[193] K. Miyoshi, K. Morishita, E. Mutou, M. Kondo, O. Seida, K. Fujiwara, J. Takeuchi, and S. Nishigori, "Enhanced Superconductivity on the Tetragonal Lattice in FeSe under Hydrostatic Pressure", Journal of the Physical Society of Japan **83**, 013702 (2014).

[194] J. Xie, X. Liu, W. Zhang, S. M. Wong, X. Zhou, Y. Zhao, S. Wang, K. T. Lai, and S. K. Goh, "Fragile Pressure-Induced Magnetism in FeSe Superconductors with a Thickness Reduction", Nano Letters **21**, 9310–9317 (2021).

[195] D. V. Efremov, M. M. Korshunov, O. V. Dolgov, A. A. Golubov, and P. J. Hirschfeld, "Disorder-induced transition between $s_{\pm}$ and s_{++} states in two-band superconductors", Phys. Rev. B **84**, 180512 (2011).

[196] B. M. Andersen, S. Graser, and P. J. Hirschfeld, "Disorder-Induced Freezing of Dynamical Spin Fluctuations in Underdoped Cuprate Superconductors", Phys. Rev. Lett. **105**, 147002 (2010).

[197] J. H. J. Martiny, A. Kreisel, and B. M. Andersen, "Theoretical study of impurity-induced magnetism in FeSe", Phys. Rev. B **99**, 014509 (2019).

[198] M. N. Gastiasoro, P. J. Hirschfeld, and B. M. Andersen, "Origin of electronic dimers in the spin-density wave phase of Fe-based superconductors", Phys. Rev. B **89**, 100502 (2014).

[199] D. F. Mross and T. Senthil, "Spin- and Pair-Density-Wave Glasses", Phys. Rev. X **5**, 031008 (2015).

[200] A. V. Chubukov, M. Khodas, and R. M. Fernandes, "Magnetism, Superconductivity, and Spontaneous Orbital Order in Iron-Based Superconductors: Which Comes First and Why?", Phys. Rev. X **6**, 041045 (2016).

[201] P. Reiss, M. D. Watson, T. K. Kim, A. A. Haghighirad, D. N. Woodruff, M. Bruma, S. J. Clarke, and A. I. Coldea, "Suppression of electronic correlations by chemical pressure from FeSe to FeS", Phys. Rev. B **96**, 121103 (2017).

[202] T. Hanaguri, V. Iwaya, Y. Kohsaka, T. Machida, T. Watashige, S. Kasahara, T. Shibauchi, and Y. Matsuda, "Two distinct superconducting pairing states divided by the nematic end point in $FeSe_{1-x}S_x$", Sci. Adv. **4**, eaar6419 (2018).

[203] Y. Sato, S. Kasahara, T. Taniguchi, X. Xing, Y. Kasahara, Y. Tokiwa, Y. Yamakawa, H. Kontani, T. Shibauchi, and Y. Matsuda, "Abrupt change of the superconducting gap structure at the nematic critical point in $FeSe_{1-x}S_x$", Proceedings of the National Academy of Sciences **115**, 1227–1231 (2018).

[204] C. Setty, S. Bhattacharyya, Y. Cao, A. Kreisel, and P. J. Hirschfeld, "Topological ultranodal pair states in iron-based superconductors", Nature Communications **11**, 523 (2020).

[205] P. Reiss, D. Graf, A. A. Haghighirad, T. Vojta, and A. I. Coldea, "Signatures of a Quantum Griffiths Phase Close to an Electronic Nematic Quantum Phase Transition", Phys. Rev. Lett. **127**, 246402 (2021).

[206] J. Ayres, M. Čulo, J. Buhot, B. Bernáth, S. Kasahara, Y. Matsuda, T. Shibauchi, A. Carrington, S. Friedemann, and N. E. Hussey, "Transport evidence for decoupled nematic and magnetic criticality in iron chalcogenides", Communications Physics **5**, 100 (2022).

[207] T. Tomita, H. Takahashi, H. Takahashi, H. Okada, Y. Mizuguchi, Y. Takano, S. Nakano, K. Matsubayashi, and Y. Uwatoko, "Correlation between T_c and crystal structure in S-Doped FeSe superconductors under pressure: Studied by x-ray diffraction of $FeSe_{0.8}S_{0.2}$ at Low Temperatures", Journal of the Physical Society of Japan **84**, 1–8 (2015).

[208] T. Terashima, N. Kikugawa, A. Kiswandhi, E.-S. Choi, J. S. Brooks, S. Kasahara, T. Watashige, H. Ikeda, T. Shibauchi, Y. Matsuda, T. Wolf, A. E. Böhmer, F. Hardy, C. Meingast, H. v. Löhneysen, M.-T. Suzuki, R. Arita, and S. Uji, "Anomalous Fermi surface in FeSe seen by Shubnikov-de Haas oscillation measurements", Phys. Rev. B **90**, 144517 (2014).

[209] A. Audouard, F. Duc, L. Drigo, P. Toulemonde, S. Karlsson, P. Strobel, and A. Sulpice, "Quantum oscillations and upper critical magnetic field of the iron-based superconductor FeSe", Europhys. Lett. **109**, 27003 (2015).

[210] W. K. Huang, S. Hosoi, M. Čulo, S. Kasahara, Y. Sato, K. Matsuura, Y. Mizukami, M. Berben, N. E. Hussey, H. Kontani, T. Shibauchi, and Y. Matsuda, "Non-Fermi liquid transport in the vicinity of the nematic quantum critical point of superconducting $FeSe_{1-x}S_x$", Phys. Rev. Research **2**, 033367 (2020).

[211] J. M. Luttinger and J. C. Ward, "Ground-State Energy of a Many-Fermion System. II", Phys. Rev. **118**, 1417–1427 (1960).

[212] S. Mandal, R. E. Cohen, and K. Haule, "Strong pressure-dependent electron-phonon coupling in FeSe", Phys. Rev. B **89**, 220502 (2014).

[213] T. Terashima, N. Kikugawa, D. Graf, H. T. Hirose, S. Uji, Y. Matsushita, H. Lin, X. Zhu, H.-H. Wen, T. Nomoto, K. Suzuki, and H. Ikeda, "Accurate determination of the Fermi surface of tetragonal FeS via quantum oscillation measurements and quasiparticle self-consistent GW calculations", Phys. Rev. B **99**, 134501 (2019).

[214] A. Wasserman and M. Springford, "Quantum oscillations in the vortex state of a type-II superconductor", Physica B: Condensed Matter **194-196**, 1801–1802 (1994).

[215] J. Kumar, S. Auluck, P. K. Ahluwalia, and V. P. S. Awana, "Chalcogen height dependence of magnetism and Fermiology in $FeTe_xSe_{1-x}$", Superconductor Science and Technology **25**, 095002 (2012).

[216] R. Sun, S. Jin, J. Deng, M. Hao, X. Zhong, Y. Ma, M. Li, and X. Chen, "Chemical Pressure Boost Record-High Superconductivity in van der Waals Materials $FeSe_{1-x}S_x$", Advanced Functional Materials **31**, 2102917 (2021).

[217] V. Ksenofontov, G. Wortmann, A. I. Chumakov, T. Gasi, S. Medvedev, T. M. McQueen, R. J. Cava, and C. Felser, "Density of phonon states in superconducting FeSe as a function of temperature and pressure", Phys. Rev. B **81**, 184510 (2010).

[218] A. Gurevich, "Enhancement of the upper critical field by nonmagnetic impurities in dirty two-gap superconductors", Phys. Rev. B **67**, 184515 (2003).

[219] W. J. Duncan, O. P. Welzel, C. Harrison, X. F. Wang, X. H. Chen, F. M. Grosche, and P. G. Niklowitz, "High pressure study of $BaFe_2As_2$ - the role of hydrostaticity and uniaxial stress", Journal of Physics: Condensed Matter **22**, 052201 (2010).

[220] K. Miyoshi, S. Yamamoto, A. Shiota, T. Matsuoka, M. Ohe, Y. Yamamoto, and S. Nishigori, "Disappearance and Survival of Superconductivity in FeSe under High Pressure", Journal of the Physical Society of Japan **90**, 073706 (2021).

[221] Y. Yang, Q. Wang, S. Duan, H. Wo, C. Huang, S. Wang, L. Gu, D. Qian, J. Zhao, and W. Zhang, "Unusual Band Splitting and Superconducting Gap Evolution with Sulfur Substitution in FeSe", Chinese Physics Letters **39**, 057302 (2022).

[222] R. Corcoran, P. Meeson, Y. Onuki, P. .-.-A. Probst, M. Springford, K. Takita, H. Harima, G. Y. Guo, and B. L. Gyorffy, "Quantum oscillations in the mixed state of the type II superconductor 2H-$NbSe_2$", Journal of Physics: Condensed Matter **6**, 4479–4492 (1994).

[223] C. Bergemann, S. Julian, G. McMullan, B. Howard, G. Lonzarich, P. Lejay, J. Brison, and J. Flouquet, "Quantum oscillations in URu_2Si_2", Physica B: Condensed Matter **230-232**, 348–350 (1997).

[224] R. Schneider, A. G. Zaitsev, A. Beck, D. Fuchs, and R. Hott, "Effect of Hydrostatic Pressure on Superconductivity of FeSe Thin Films", Journal of Superconductivity and Novel Magnetism **32**, 3729–3737 (2019).